


UNIVERSITY OF
BIRMINGHAM

# INDIRECT CONVERSION RADIOISOTOPIC BATTERY FOR BURIED ASSET CONDITION MONITORING

by

**Robert Walton**

A thesis submitted to
The University of Birmingham
for the degree of
**DOCTOR OF PHILOSOPHY**

School of Mechanical Engineering
College of Engineering and Physical Sciences
The University of Birmingham
March 2014

# SUMMARY

An indirect conversion radioisotopic battery (ICRB) and capacitor power source was designed, simulated, manufactured and tested in this research. In an ICRB radioisotopic decay particles produce photons in a scintillating material and then the energy of these photons is converted into electrical energy within a photovoltaic (PV) cell. Finally, the electrical energy is stored within a capacitor. All ICRBs manufactured during this research used tritium ($^3$H) as the radioisotope in the form of gaseous tritium light sources (GTLSs).

The operation of an ICRB was theoretically modelled from the generation of radiation particles right up to the storage of electrical energy in the capacitor. Comparison of the results from this model with laboratory testing found close agreement with the modelling of GTLS light emission, though further improvement was found to be necessary in the area of PV cell modelling.

The ICRB was designed to provide power to a wireless sensor network (WSN) sensor node which would be buried underground and would report on the condition of a buried asset (such as a water pipe). The most powerful ICRB generated 1.6μW which is 60% more than the 1.0μW found to be necessary to power a WSN sensor node. This ICRB would provide useful power to the WSN sensor node for 4.24 years. The highest achieved efficiency of ICRB and capacitor system was 0.6% which compares favourably with ICRBs produced by other researchers such as Deus [1] whose ICRB generated 2.56nW at a 0.17% efficiency. An ICRB was buried on a working water pipe for a duration exceeding two months and continues to function as predicted.

Further improvements to the ICRB design have been identified which might produce a power source capable of providing power to a WSN sensor node for 20 years. Areas where efficiency gains may be made include the use of alternate radioisotopes and PV cells, and different arrangements of components relative to each other (PV cells might be printed directly onto the GTLSs).

I would like to dedicate this thesis to my beautiful wife Azumi, who has put up with the late nights, incessant working and stress that this research has generated. She has been as supportive and loving as any man could wish for in a wife.

# ACKNOWLEDGEMENTS

The author would like to offer his heartfelt thanks to his supervisors Dr Carl Anthony, Dr Nicole Metje and Dr David Chapman for their patience, suggestions and encouragement throughout the development of this work.

The author is especially grateful to the support and encouragement of his friends and officemates. In particular, thanks go to Tom Hoskins whose help, advice and friendship were crucial to completing this work.

Thanks also go to my Mum, Dad and Brother for their love and advice.

Finally the author would like to thank United Kingdom Water Industry Research (UKWIR) for their financial support of this research.

# CONTENTS

**LIST OF FIGURES** ..... **I**

**LIST OF TABLES** ..... **X**

**ACRONYMS AND ABBREVIATIONS** ..... **XI**

**NOMENCLATURE** ..... **XIV**

**1 INTRODUCTION** ..... **1**

1.1 BACKGROUND TO RESEARCH ..... 1

1.2 RESEARCH AIMS AND OBJECTIVES ..... 5

1.3 LIST OF CONTRIBUTIONS TO KNOWLEDGE ..... 6

1.4 LIST OF PUBLICATIONS ..... 7

1.5 REPORT STRUCTURE ..... 8

**2 POWER OPTIONS FOR A WSN SENSOR NODE** ..... **9**

2.1 INTRODUCTION ..... 9

2.2 REGENERATIVE POWER SOURCES ..... 10

*2.2.1 Vibration energy harvesting* ..... *11*

*2.2.2 Thermal energy harvesting* ..... *17*

*2.2.3 Fluid flow energy harvesting* ..... *21*

2.3 NON-REGENERATIVE POWER SOURCES ..... 24

*2.3.1 Electrochemical* ..... *24*

*2.3.2 Micro-engines, turbines and fuel cells* ..... *25*

*2.3.3 Radioisotopic* ..... *28*

2.4 STORAGE OPTIONS ..... 31

2.5 CONCLUSIONS OF POWER OPTIONS REVIEW ..... 33

**3 RADIOISOTOPIC BATTERIES ..... 35**

3.1 INTRODUCTION ..... 35

3.2 RADIOISOTOPES SUITABLE FOR BATTERIES ..... 35

3.3 HEALTH AND SAFETY ..... 38

3.4 THERMAL TYPES OF RADIOISOTOPIC BATTERY ..... 40

*3.4.1 RADIOISOTOPIC THERMOELECTRIC GENERATOR ..... 40*

*3.4.2 ALTERNATIVE THERMAL RADIOISOTOPIC BATTERIES ..... 45*

3.5 NON-THERMAL TYPES OF RADIOISOTOPIC BATTERY ..... 47

*3.5.1 DIRECT CHARGE ..... 48*

*3.5.2 MECHANICAL AND DIRECT CHARGE ..... 51*

*3.5.3 DIRECT CONVERSION ..... 53*

*3.5.4 INDIRECT CONVERSION ..... 59*

3.6 GASEOUS TRITIUM LIGHT SOURCES ..... 67

3.7 CHOICE OF RADIOISOTOPIC BATTERY TYPE ..... 69

3.8 THEORETICAL MODELLING OF INDIRECT CONVERSION RADIOISOTOPIC BATTERIES ..... 71

*3.8.1 First stage: Kinetic energy of radioisotopic decay ..... 73*

*3.8.2 Second stage: Conversion into light energy ..... 76*

*3.8.3 Third stage: Transport of light energy into photovoltaic cell ..... 77*

*3.8.4 Fourth stage: Conversion of light into electricity in the photovoltaic cell ..... 78*

*3.8.5 Fifth stage: Storage of electrical energy in a capacitor ..... 81*

3.9 CONCLUSIONS OF THE LITERATURE REVIEW ..... 82

**4 INDIRECT CONVERSION RADIOISOTOPIC BATTERY ..... 83**

4.1 INTRODUCTION ..... 83

4.2 POTENTIAL CONFIGURATIONS ..... 83

4.3 INITIAL EXPERIMENTATION ..... 84

4.4 SELECTED DESIGN ..... 90
4.5 AREAS OF INVESTIGATION ..... 90
4.6 CHALLENGES ..... 91
4.7 CASING DESIGNS ..... 93
4.8 FABRICATION ..... 94
*4.8.1 Gaseous tritium light sources ..... 94*
*4.8.2 Photovoltaic cells ..... 95*
*4.8.3 Contacts ..... 96*
*4.8.4 Casings ..... 98*
*4.8.5 Coatings ..... 99*
*4.8.6 Capacitors ..... 102*
*4.8.7 Dielectric between the PV cells and the GTLSs ..... 104*
4.9 TESTING ..... 104
*4.9.1 Testing of battery power into capacitor ..... 104*
*4.9.2 Measurement of the PV cells current and power output ..... 113*
*4.9.3 Testing of GTLS spectral intensity ..... 114*
*4.9.4 Burial and duration testing ..... 115*
4.10 CONCLUSIONS ..... 118
**5 THEORY OF ENERGY CONVERSION IN AN ICRB ..... 119**
5.1 INTRODUCTION ..... 119
5.2 MODEL OF ENERGY CONVERSION AND TRANSPORT IN BATTERY ..... 119
5.3 FIRST STAGE: KINETIC ENERGY OF RADIOISOTOPIC DECAY ..... 120
*5.3.1 Description of the process ..... 120*
*5.3.2 Model of the process ..... 121*
5.4 SECOND STAGE: CONVERSION INTO LIGHT ENERGY ..... 123

*5.4.1 Description of process ..... 124*

5.5 THIRD STAGE: TRANSPORT OF LIGHT ENERGY INTO PHOTOVOLTAIC CELL ..... 126

*5.5.1 Transmission of light from a single GTLS ..... 131*

*5.5.2 Efficiency of light emitted from adjacent GTLSs ..... 148*

*5.5.3 Light reflected from the casing to the solar cell surface ..... 165*

5.6 FOURTH STAGE: CONVERSION OF LIGHT INTO ELECTRICITY IN THE PHOTOVOLTAIC CELL ..... 173

*5.6.1 Calculated photocurrent in a photovoltaic cell ..... 173*

5.7 FIFTH STAGE: STORAGE OF ELECTRICAL ENERGY IN A CAPACITOR ..... 175

*5.7.1 Efficiency of charging a capacitor ..... 176*

*5.7.2 Leakage loss of the capacitor ..... 178*

*5.7.3 Calculated operational lifetime of a capacitor ..... 180*

5.8 COMPLETE MODEL ..... 181

**6 ICRB PRACTICAL AND THEORETICAL COMPARISON ..... 182**

6.1 INTRODUCTION ..... 182

6.2 EFFICIENCY ..... 182

*6.2.1 Efficiency of radioactive flux ..... 182*

*6.2.2 Efficiency of photon generation in phosphors ..... 185*

*6.2.3 Efficiency of light transport within an ICRB ..... 186*

*6.2.4 Efficiency of electricity generation by PV cells ..... 203*

*6.2.5 Efficiency of capacitor charging ..... 214*

*6.2.6 Overall efficiency of ICRB and capacitor system ..... 220*

6.3 POWER ..... 222

*6.3.1 Overall power in ICRB and capacitor system ..... 222*

*6.3.2 Long-life buried testing of ICRB ..... 224*

*6.3.3 Suitability of ICRB system for powering a WSN sensor node ..... 226*

6.4 CONCLUSIONS ..... 227

**7 CONCLUSIONS ..... 229**

7.1 THESIS SUMMARY ..... 229

7.2 KEY CONCLUSIONS ..... 230

7.3 RECOMMENDATIONS FOR FUTURE WORK ..... 231

*7.3.1 Battery design improvements ..... 231*

*7.3.2 Theoretical modelling ..... 232*

*7.3.3 Alternative uses of the battery ..... 233*

**APPENDIX A: CALCULATION OF GTLS ACTIVITY ..... 234**

A.1 MANUFACTURER DATA ON GTLS ACTIVITY LEVELS ..... 234

**APPENDIX B: THEORETICAL MODELLING ..... 235**

B.1 STAGE 1: KINETIC ENERGY OF RADIOISOTOPIC DECAY ..... 235

*B.1.1 Power flux per unit surface area from gas in cylindrical form ..... 235*

*B.1.2 Efficiency of power flux for gas in cylindrical form ..... 238*

B.2 STAGE 3: EFFICIENCY OF LIGHT TRANSPORT IN ICRB ..... 238

*B.2.1 Derivation of Equation (5-8) ..... 238*

*B.2.2 Simulink model of transmission losses from a single GTLS ..... 240*

*B.2.3 Transmission losses between GTLSs ..... 246*

*B.2.4 Derivation of Equation (5-50) ..... 249*

*B.2.5 Light reflected from GTLSs onto casing and then to PV cells ..... 251*

*B.3 Stage 4: Model of PV cells ..... 257*

B.4 STAGE 5: EFFICIENCY OF CHARGING A CAPACITOR ..... 258

*B.4.1 MATLAB® code for curve fit of power loss during discharge ..... 260*

*B.4.2 MATLAB® code for efficiency of charging a capacitor ..... 261*

**APPENDIX C: DESIGN, FABRICATION AND TESTING ..... 262**

C.1 AUTOMATED TESTING USING LABVIEW ..... 262

C.2 BURIED TESTING ..... 263

**APPENDIX D: RESULTS ..... 266**

D.1 PV CELL TEST RESULTS ..... 266

D.2 PV CELL CHARACTERISTICS ..... 266

**REFERENCES ..... 269**

# LIST OF FIGURES


FIGURE 1-1: SCHEMATIC REPRESENTATION OF THE POWER REQUIREMENTS OF A WSN SENSOR NODE SHOWING TWO CYCLES OF OPERATION ..... 3

FIGURE 1-2: POWER REQUIREMENTS OF A WSN SENSOR NODE DEPENDENT ON FREQUENCY OF READINGS ..... 3

FIGURE 1-3: BESPOKE WSN SENSOR NODE REQUIRING ONLY 1μW OF POWER DESIGNED AND MANUFACTURED IN A PARALLEL PROJECT TO THIS THESIS (SHOWN WITH ANTENNA DETACHED) ..... 5

FIGURE 2-1: TREE OF AVAILABLE POWER SOURCES ..... 10

FIGURE 2-2: COMMON LAYOUT OF A PIEZOELECTRIC ENERGY HARVESTING DEVICE ..... 12

FIGURE 2-3: TYPICAL DESIGN OF AN ELECTROMAGNETIC ENERGY HARVESTING DEVICE ..... 13

FIGURE 2-4: DIAGRAM OF THERMOCOUPLE UTILIZING THE SEEBECK EFFECT (REPRODUCED FROM [43]) ..... 18

FIGURE 2-5: THERMOELECTRIC WATCH DEVELOPED BY KISHI ET AL. (REPRODUCED FROM [46]) ..... 19

FIGURE 2-6: EFFICIENCY OF THERMOELECTRIC MATERIALS AT VARYING TEMPERATURE AND ZT VALUE (REPRODUCED FROM [49]) ..... 20

FIGURE 2-7: LAYOUT OF FLUID FLOW PIEZOELECTRIC ENERGY HARVESTER REPRODUCED FROM [51]) ..... 22

FIGURE 2-8: DESIGN OF AN ELECTROMAGNETIC FLUID FLOW ENERGY HARVERSTER (REPRODUCED FROM [53]) ..... 22

FIGURE 2-9: COMPONENTS AND FINISHED ROTORS OF MICRO TESLA TURBINES (REPRODUCED FROM [57]) ..... 23

FIGURE 2-10: DESIGN OF MICRO-TURBINE CREATED AT MIT (REPRODUCED FROM [66]) ..... 26

FIGURE 2-11: MICRO WANKEL ENGINE FABRICATED AT THE UNIVERSITY OF BIRMINGHAM (REPRODUCED FROM [67]) ..... 26

FIGURE 2-12: MICRO FUEL CELL COMPONENTS AND HOUSING (REPRODUCED FROM [71]) ..... 27

FIGURE 2-13: CUT-AWAY OF RADIOISOTOPE THERMOELECTRIC GENERATOR USED BY NASA (REPRODUCED FROM [81]) ..... 29

FIGURE 2-14: LAYOUT OF A DIRECT CONVERSION RADIOISOTOPIC BATTERY (REPRODUCED FROM [83]) ..... 30

FIGURE 3-1: THE SNAP-27 RTG ON THE SURFACE OF THE MOON AS A SOURCE OF ELECTRICAL ENERGY DURING THE APOLLO 16 MISSION (REPRODUCED FROM [102]) ..... 41

FIGURE 3-2: MARS CURIOSITY ROVER SELF PORTRAIT TAKEN ON MARS (REPRODUCED FROM [107]) ..... 42

FIGURE 3-3: PELLET OF $^{238}PuO_2$ FOR USE IN A NASA RTG (REPRODUCED FROM [80])_ ..... 42

FIGURE 3-4: $^{238}$PU RTG PACEMAKER MANUFACTURED BY ARCO IN 1974 (REPRODUCED FROM [112]) ..... 44

FIGURE 3-5: SCHEMATIC OF SUNPOWER 88W ADVANCED STIRLING CONVERTER FOR NASA SPACE PROGRAM (REPRODUCED FROM [119]) ..... 46

FIGURE 3-6: PROCESS OF THERMOPHOTOVOLTAIC CONVERSION (REPRODUCED FROM [123]) ....47
FIGURE 3-7: SCHEMATIC OF A DIRECT CHARGE RADIOISOTOPIC BATTERY ....48
FIGURE 3-8: HONEYCOMB CONFIGURATION OF PROPOSED DIRECT CHARGE RADIOISOTOPIC BATTERY (REPRODUCED FROM [124]) ...49
FIGURE 3-9: DIRECT CHARGE RADIOISOTOPIC BATTERY CONTAINING 24 TRITIUM SOURCES OF TOTAL 4000GBQ ACTIVITY (REPRODUCED FROM [128]) ....50
FIGURE 3-10: OSCILLATING CANTILEVER BASED DIRECT CHARGE RADIOISOTOPIC BATTERY (REPRODUCED FROM [97]) ....52
FIGURE 3-11: ENERGY CYCLE OF THE OSCILLATING DIRECT CHARGE RADIOISOTOPIC BATTERY (REPRODUCED FROM [130]) ....52
FIGURE 3-12: SCHEMATIC OF DIRECT CONVERSION RADIOISOTOPIC BATTERY (REPRODUCED FROM [132]) ....53
FIGURE 3-13: OPERATING PRINCIPLE OF A DIRECT CONVERSION RADIOISOTOPIC BATTERY (REPRODUCED FROM [134]) ....54
FIGURE 3-14: PM INDIRECT CONVERSION BATTERY DESIGN FROM 1964 (REPRODUCED FROM [139]) ....55
FIGURE 3-15: THE BETACEL-400 BATTERY USED IN PACEMAKERS DURING THE 1970S (REPRODUCED FROM [141, 142]) ....56
FIGURE 3-16: NANOTRITIUM™ P100 BATTERY SOLD BY CITY LABS, INC. (REPRODUCED FROM [156]) ....57
FIGURE 3-17: FOUR CONFIGURATIONS OF INDIRECT CONVERSION RADIOISOTOPIC BATTERY, (A) PV CELLS SURROUNDING A POLYMER CONTAINING PHOSPHOR AND RADIOISOTOPE, (B) SPHERES ON A PV CELL, (C) SANDWICH FORMATION, (D) AEROGEL SURROUNDED BY PV CELLS (REPRODUCED FROM [158-160]) ....60
FIGURE 3-18: ELGIN-KIDDE INDIRECT CONVERSION RADIOISOTOPIC BATTERY SCHEMATIC (REPRODUCED FROM [161]) ....61
FIGURE 3-19: ALPHA POWERED INDIRECT CONVERSION BATTERY POWER CURVES RELATIVE TO VOLTAGE (U) WITH AND WITHOUT (WO) REFLECTIVE FOILS. (REPRODUCED FROM [162]) ....62
FIGURE 3-20: CURRENT/VOLTAGE AND POWER/VOLTAGE CURVES MEASURED FOR ALGAAS PHOTOVOLTAIC CELLS ILLUMINATED BY GREEN GTLSS OF TOTAL ACTIVITY 48.84GBQ (REPRODUCED FROM [163]) ....64
FIGURE 3-21: AN INDIRECT CONVERSION RADIOISOTOPIC BATTERY THEORETICALLY MODELLED USING MCNP (REPRODUCED FROM [164]) ....65
FIGURE 3-22: EXAMPLES OF COMMERCIAL GTLS USAGE: (A) A SELF-LUMINOUS EXIT SIGN, (B) A "GLOW IN THE DARK" WATCH AND (C) GUN SIGHTS (REPRODUCED FROM [167-169]) ....67
FIGURE 3-23: GTLSS RADIATING LIGHT PREDOMINANTLY IN THE GREEN SPECTRUM OF VARIOUS SIZES ....68
FIGURE 3-24: COMPUTER PREDICTED SURFACE POWER FLUX OF TRITIUM AGAINST GAS THICKNESS (REPRODUCED FROM [158]) ....72
FIGURE 3-25: ENERGY PATHWAYS IN AN INDIRECT CONVERSION RADIOISOTOPIC BATTERY ....73
FIGURE 3-26: ENERGY SPECTRUM OF TRITIUM BETA DECAY PARTICLES (REPRODUCED FROM [173]) ....74

FIGURE 3-27: EMISSION SPECTRA OF ZNS PHOSPHORS CONTAINING DIFFERENT PERCENTAGES OF ACTIVATOR CU (REPRODUCED FROM [177]) ..... 76
FIGURE 3-28: EQUIVALENT CIRCUIT DIAGRAM FOR A PHOTOVOLTAIC CELL (REPRODUCED FROM [191]) ..... 79
FIGURE 3-29: EQUIVALENT MODEL OF A CAPACITOR ..... 81
FIGURE 4-1: POTENTIAL CONFIGURATIONS OF ICRBS WITH TWO GTLSS AND (A) ONE PV CELL WITHOUT REFLECTIVE MATERIAL, (B) ONE PV CELL WITH REFLECTIVE MATERIAL, (C) TWO PV CELLS, (D) THREE PV CELLS, AND (E) FOUR PV CELLS 83
FIGURE 4-2: TEST RESULTS OF SINGLE PV CELL WITHOUT REFLECTIVE FOIL SHOWING VOLTAGE IN THE CONNECTED 1MF 50V ALUMINIUM ELECTROLYTIC CAPACITOR CHANGING OVER TIME ..... 85
FIGURE 4-3: POWER REQUIRED TO CHARGE THE 1MF CAPACITOR BY THE SINGLE P-N JUNCTION WITHOUT REFLECTIVE FOIL SET AGAINST TIME ..... 85
FIGURE 4-4: COMPARISON OF INITIAL BATTERY RESULTS WITH P-V JUNCTIONS CONNECTED IN SERIES ..... 86
FIGURE 4-5: COMPARISON OF INITIAL BATTERY RESULTS WITH P-V JUNCTIONS CONNECTED IN PARALLEL ..... 87
FIGURE 4-6: SELECTED LAYOUT OF INDIRECT CONVERSION RADIOISOTOPIC BATTERY (WITHOUT REFLECTIVE COVER) ..... 90
FIGURE 4-7: RESULTS OF TWO BATTERIES CONSTRUCTED USING TWO PV CELLS AND TWO GTLSS ..... 91
FIGURE 4-8: CASING DESIGN IN SOLIDWORKS® [199] SHOWING (A) BASE AND (B) TOP ..... 93
FIGURE 4-9: CASING DESIGN IN SOLIDWORKS® [199] SHOWING (A) LID AND (B) TROUGH ..... 94
FIGURE 4-10: SELECTION OF (GREEN UNLESS STATED OTHERWISE) GTLSS USED IN ICRB CONSTRUCTION SHOWING (A) 30MMX4MMX2MM, (B) 25MMX3MMØ, (C) GREEN, BLUE AND WHITE 10MMX2.5MMØ, (D) 15MMX3MMØ, (E) 22.5MMX3MMØ, (F) 12MMX2MMØ, (G) 80MMX5MMØ ..... 95
FIGURE 4-11: PV CELLS USED IN ICRB CONSTRUCTION SHOWING (A) 103.0MMX15.5MM A-SI, (B) 54.5MMX4.5MM A-SI, (C) 29.6MMX11.7MM A-SI, (D) 72.3MMX15.0MM A-SI, (E) 107.7MMX28.0MM A-SI, (F) 34.9MMX13.8MM A-SI, (G) 39.8MMX26.0MM M-SI, (H) 59.9MMX30.0MM M-SI, (I) 49.8MMX19.9MM P-SI ..... 96
FIGURE 4-12: MODIFIED CASING DESIGN FOR REMOVABLE CONTACTS SHOWING (A) TROUGH, (B) LID ..... 97
FIGURE 4-13: REMOVABLE CONTACTS, SHOWING (A) CLIP CONTACT, (B) CLIP CONTACT ATTACHED TO ICRB ..... 97
FIGURE 4-14: SELECTION OF CASINGS MANUFACTURED TO CONTAIN THE ICRBS SHOWING (A) TROUGH AND LID FOR 103.0MMX15.5MM A-SI PV CELLS, (B) TROUGH AND LID FOR 29.6MMX11.7MM A-SI PV CELLS, (C) TROUGH AND LID FOR

34.9mmX13.8mm a-Si PV cells, (d) top and base for 34.9mmX13.8mm a-Si PV cells, (e) top and base for 59.9mmX30.0mm mono-Si PV cells, (f) top and base for 72.3mmX15.0mm a-Si PV cells .....99
Figure 4-15: Reflectance of aluminium (Al), gold (Au) and silver (Ag) from 200nm to 5000nm (reproduced from [205]).....100
Figure 4-16: Reflectance of $BaSO_4$ and other substances from 200nm to 2700nm (reproduced from [207]) .....101
Figure 4-17: Effect of angle of incidence on reflectance of coated aluminium (reproduced from [208]).....101
Figure 4-18: Casings coated with reflective material, (a) no coating, (b) gold (c) $BaSO_4$.....102
Figure 4-19: Selection of the capacitors used during testing showing (a) front and rear view of AVX niobium oxide 10V 100mF, (b) front and rear view of AVX niobium oxide 10V 47mF, (c) front and rear view of AVX niobium oxide 6.3V 47mF, (d) front and rear view of TDK ceramic 16V 47mF, (e) Taiyo Yuden ceramic 16V 47mF, (f) Taiyo Yuden ceramic 6.3V 10mF, (g) AVX tantalum 6.3V 1000mF, (h) front and rear view of Kemet tantalum 16V 100mF, (i) Radio Spares tantalum 16V 22mF, (j) Rubycon 'button' aluminium electrolytic 25V 100mF, (k) Radio Spares radial aluminium electrolytic 25V 100mF, (l) Vishay radial aluminium electrolytic 25V 1000mF, (m) Jamicon aluminium electrolytic 25V 47mF, (n) Vishay aluminium electrolytic 10V 470mF, (o) Multicomp aluminium electrolytic 16V 1000mF, (p) aluminium electrolytic 6.3V 2700mF, (q) aluminium electrolytic 25V 1000mF, (r) Rubycon aluminium electrolytic 63V 1000mF.....103
Figure 4-20: Test circuit for indirect conversion radioisotopic battery testing using an Arduino.....106
Figure 4-21: LabJack U6-PRO automated test-bed for measurement of voltage in capacitors .....106
Figure 4-22: Graphical user interface of automated measurements run through LabVIEW [210] .....107
Figure 4-23: Darkened environment for the testing of ICRBs.....109
Figure 4-24: Results of control experiment on ICRB without GTLSs in the test environment .....109
Figure 4-25: Voltage measurements against time of discharged capacitors showing dielectric absorption measured by Pease (reproduced from [212]) .....110
Figure 4-26: Measured dielectric absorption in a 1mF aluminium electrolytic capacitor.....111
Figure 4-27: Measured voltage rise in capacitor during control test and soakage test.....112
Figure 4-28: Test circuit in order to generate IV curves of the PV cells at various light intensities .....113
Figure 4-29: ICRB prepared for burial in ground, showing potting material and radioactive markings on the protective casing.....116

FIGURE 4-30: ICRB BURRIED AT A DEPTH OF 90CM IN SOIL AND FIXED TO A WATER PIPE ..... 117

FIGURE 5-1: BETA POWER FLUX AT THE SURFACE OF A CYLINDER OF RADIUS 0.85CM AND LENGTH 1CM WITH INCREASING PRESSURE ..... 122

FIGURE 5-2: THE SPECTRAL RADIANCE OF A GREEN LIGHT EMITTING GTLS (REPRODUCED FROM [217]) ..... 124

FIGURE 5-3: DECREASE IN BRIGHTNESS OF GTLSS OVER TIME (1,2,3) AND DECREASE IN TRITIUM POWER (4) (REPRODUCED FROM [218, 219]) ..... 125

FIGURE 5-4: METHOD OF COMBINING VECTORS IN THE TRANSPORT OF LIGHT WITHIN THE ICRB ..... 127

FIGURE 5-5: THE PERCENTAGE OF LIGHT TRANSMITTED AS CALCULATED FROM ACTUAL PATH OF THE LIGHT OR A COMBINATION OF THE COMPONENT PARTS OF THE PATH OF LIGHT ..... 128

FIGURE 5-6: EMISSION OF LIGHT FROM A GTLS ..... 131

FIGURE 5-7: GLASS/PHOSPHOR BOUNDARY DISPLAYED GRAPHICALLY AND SEGMENTED INTO CONSTITUENT PARTS ..... 132

FIGURE 5-8: INFINITELY SMALL ANGLE (ΔB) SEGMENT OF SECTION X AND DEMONSTRATION OF EMISSION, TRANSMISSION AND REFLECTION OF LIGHT ..... 133

FIGURE 5-9: 'X-Z' PLANE OF SECTION X SHOWING (A) TRANSMISSION THROUGH THE SIDE, (B) REFLECTION AND TRANSMISSION THROUGH THE END, AND (C) POINT OF MAXIMUM REFLECTIVE TRANSMISSION ..... 134

FIGURE 5-10: SCHEMATIC OF LIGHT EMISSION IN THE 'X' AND 'Y' DIRECTIONS OF SECTION X ..... 137

FIGURE 5-11: REPRESENTATION OF THE ENDS (SECTION Y) OF THE GTLS ..... 139

FIGURE 5-12: SIMPLIFIED MODEL OF THE 'X-Y' PLANE OF SECTION Y (A) A SINGLE RAY OF LIGHT EMISSION FROM 'G-H' LINE, (B) RELATIVE ANGLES OF EMISSION AND REFLECTION IN THE PLANE ..... 140

FIGURE 5-13: ANGLES OF TRANSMISSION AND INCIDENCE FROM THE 'X-Y' PLANE OF SECTION Y ..... 141

FIGURE 5-14: LIGHT TRANSMISSION FROM THE 'X-Z' PLANE OF SECTION Y ..... 141

FIGURE 5-15: LIGHT TRANSMITTED THROUGH THE SIDE OF THE GTLS ..... 143

FIGURE 5-16: LIGHT TRANSMITTED THROUGH THE END OF THE GTLS ..... 144

FIGURE 5-17: SIMULINK® BLOCK AND BLOCK DIAGRAM OF THE FIRST FRESNEL EQUATION ..... 146

FIGURE 5-18: MASTER BLOCK DIAGRAM FOR SIMULINK® MODEL OF LIGHT TRANSMITTED FROM A GTLS ..... 147

FIGURE 5-19: VIEW OF MULTIPLE GLTSS POSITIONING ..... 148

FIGURE 5-20: TRANSMISSION OF LIGHT IN THE X-Y PLANE OF MULTIPLE GTLSS ..... 149

FIGURE 5-21: LIGHT FROM GTLS1 INCIDENT ON GTLS2 IN THE X-Y PLANE ..... 150

FIGURE 5-22: GEOMETRY OF ANGLE $A$ FOR LIGHT EMITTED FROM GTLS1 AND INCIDENT ON GTLS2 IN THE X-Y PLANE .....150

FIGURE 5-23: GEOMETRY OF ANGLE $B$ FOR LIGHT EMITTED FROM GTLS1 AND INCIDENT ON GTLS2 IN THE X-Y PLANE .....151

FIGURE 5-24: LIGHT EMITTED FROM GTLS1 AND TRANSMITTED THROUGH GTLS2 IN THE X-Y PLANE .....152

FIGURE 5-25: REFLECTION OF LIGHT EMITTED FROM GTLS1 AGAINST GTLS2 .....152

FIGURE 5-26: CALCULATING THE ANGLE OF REFLECTANCE OF LIGHT EMITTED FROM GTLS1 AND INCIDENT ON GTLS2 .....153

FIGURE 5-27: ANGLE FOR WHICH LIGHT FROM GTLS1 IS NOT INCIDENT ON GTLS2 .....154

FIGURE 5-28: LIMITS OF ANGLE $\mu$ FOR LIGHT INCIDENT ON GTLS2 FROM GTLS1 IN THE X-Y PLANE .....155

FIGURE 5-29: GTLS1 LOCATED BETWEEN TWO OTHER GTLSS WITH LIGHT INCIDENT ON BOTH .....157

FIGURE 5-30: CALCULATION OF LIMITS FOR LIGHT EMITTED FROM GTLS1 INTO GTLS3 .....158

FIGURE 5-31: GEOMETRICAL CONSIDERATION OF ANGLES (A) $\theta_5$ AND (B) $\theta_6$ .....158

FIGURE 5-32: TRANSMISSION OF LIGHT IN THE X-Z PLANE OF MULTIPLE GTLSS THROUGH THE ORIGINS .....159

FIGURE 5-33: TRANSMISSION OF LIGHT IN THE X-Z PLANE OF MULTIPLE GTLSS AT A DISTANCE Y1 FROM THE ORIGIN .....160

FIGURE 5-34: X-Z PLANE LOCATION THROUGH TWO GTLSS OFFSET FROM THE LINE OF ORIGIN BY 'Y1' .....160

FIGURE 5-35: REPRESENTATION OF LIGHT LOSSES IN THE X-Z PLANE BETWEEN TWO GTLSS (A) LIGHT INCIDENT ON GTLS2 FROM GTLS1, (B) PATH OF LIGHT AROUND GTLS2, (C) DIMENSIONED PATH OF LIGHT AROUND GLTS2 .....162

FIGURE 5-36: SIDE VIEW OF AN ARRAY OF GTLSS SHOWING QUADRANTS FOR EACH .....164

FIGURE 5-37: TOP DOWN VIEW OF REFLECTION OF LIGHT AGAINST CASING INSIDE RADIOISOTOPIC BATTERY .....165

FIGURE 5-38: SIDE VIEW OF REFLECTIONS IN REGION 1 OF BATTERY .....166

FIGURE 5-39: LIGHT INCIDENT ON CASING FROM SURFACE OF GTLS AT POINT 'E' IN REGION 1 .....166

FIGURE 5-40: LIGHT REFLECTING FROM THE INNER SURFACE OF THE CASING ONTO THE SOLAR CELL .....168

FIGURE 5-41: SIDE VIEW OF THE REFLECTION OF LIGHT IN REGION 2 OF THE BATTERY .....170

FIGURE 5-42: LIGHT INCIDENT ON THE CASING FROM SURFACE OF GTLS AT POINT 'A' IN REGION 2 .....171

FIGURE 5-43: LIGHT REFLECTING FROM THE INNER SURFACE OF THE CASING ONTO THE SOLAR CELL IN REGION 2 .....172

FIGURE 5-44: I-V CURVE GENERATED FROM A MATLAB MODEL FOR A MONO-CRYSTALINE PV CELL EXPOSED TO DIRECT SUNLIGHT .175

FIGURE 5-45: MODELLED EFFICIENCY OF CHARGING A 47μF CAPACITOR FROM A CONSTANT CURRENT SOURCE DEPENDENT ON THE TIME OF CHARGING .....177

FIGURE 5-46: LEAKAGE POWER FROM CAPACITOR DISCHARGING AS PLOTTED FROM MATLAB® SCRIPT .....180

FIGURE 6-1: EFFICIENCY OF POWER FLUX AT THE SURFACE OF A CYLINDER OF RADIUS 0.85CM AND LENGTH 1CM RELATED TO CHANGE IN TRITIUM PRESSURE ..... 183
FIGURE 6-2: MODELLED CHANGE WITH INCREASE OF RADIUS OF BETA FLUX POWER (RELATIVE UNITS) ON THE SURFACE OF A CYLINDER OF LENGTH 1CM WITH A PRESSURE OF 2 ATMOSPHERES ..... 184
FIGURE 6-3: END ON IMAGE OF A 25MMX3MMØ GTLS TAKEN UNDER X25 MAGNIFICATION AND SHOWING THE OUTER RADIUS MEASUREMENT (R3) ..... 186
FIGURE 6-4: IMPRESSION OF THE FIELD OF VIEW ON A SINGLE GTLS GENERATED WITH A MACRO LENS FOR SPECTROSCOPY TESTING 188
FIGURE 6-5: MEASURED SPECTRAL DISTRIBUTION OF RADIANT FLUX FOR A 25MMX3MMØ GREEN GTLS ..... 189
FIGURE 6-6: CALCULATED LOSSES FROM A 3MMØ GTLS INTO AN ADJACENT GTLS OF THE SAME SIZE ..... 190
FIGURE 6-7: PERCENTAGE LOSS OF LIGHT FROM A GTLS INTO ADJACENT GTLSS AS A FUNCTION OF CHANGING INNER RADIUS WITH A FIXED OUTER RADIUS OF 1.5MM ..... 191
FIGURE 6-8: FIELD OF VIEW DURING MEASUREMENTS OF INDIVIDUAL GTLS AND A GTLS ARRAY RADIANCE AND LUMINANCE ..... 192
FIGURE 6-9: MEASURED SPECTRAL RADIANCE RESULTS FOR A SINGLE 15MMX3MMØ GTLS AND AN ARRAY OF 15MMX3MMØ GTLSS ..... 192
FIGURE 6-10: EFFECT OF REFLECTIVE MATERIAL SURROUNDING THE ICRB DEPENDENT ON THE NUMBER OF GTLSS IN THE ICRB ARRAY ..... 194
FIGURE 6-11: INDIRECT CONVERSION RADIOISOTOPIC BATTERY WITH BARIUM SULPHATE AS A REFLECTIVE COATING ..... 195
FIGURE 6-12: POWER AGAINST VOLTAGE OF THREE ICRBS USING DIFFERENT REFLECTIVE MATERIALS ..... 195
FIGURE 6-13: LAYOUT OF GTLSS, PV CELLS AND CASING RELATIVE TO EACH OTHER, (A) WITH THE PV CELLS BEYOND THE GTLSS, (B) WITH THE GTLSS BEYOND THE PV CELLS ..... 196
FIGURE 6-14: REVISED EFFECT OF REFLECTIVE MATERIAL SURROUNDING THE ICRB DEPENDENT ON THE NUMBER OF GTLSS IN THE ICRB ARRAY ..... 197
FIGURE 6-15: REFLECTANCE OF ALUMINIUM (AL), GOLD (AU) AND SILVER (AG) FROM 200NM TO 1000NM (REPRODUCED FROM [205]) ..... 198
FIGURE 6-16: TRANSPORT OF LIGHT BETWEEN THE GTLSS AND PV CELLS ..... 199
FIGURE 6-17: TRANSITION GRAPHS ACROSS THE FULL RANGE OF INCIDENT ANGLES AS CALCULATED USING THE FRESNEL EQUATIONS FOR LIGHT MOVING FROM (A) GLASS TO AIR, (B) AIR TO GLASS ..... 200

FIGURE 6-18: TRANSITION GRAPHS ACROSS THE FULL RANGE OF INCIDENT ANGLES AS CALCULATED USING THE FRESNEL EQUATIONS FOR LIGHT MOVING FROM (A) GLASS TO INDEX MATCHING FLUID, (B) INDEX MATCHING FLUID TO GLASS ..... 200

FIGURE 6-19: EFFECT OF INTRODUCING AN INDEX MATCHING FLUID INTO AN ICRB ON THE OUTPUT POWER ..... 202

FIGURE 6-20: EXPERIMENTAL AND MODELLED I-V AND P-V CURVES OF A P-SI PV CELL ILLUMINATED BY DIRECT SUNLIGHT (~100,000LUX) ..... 206

FIGURE 6-21: EXPERIMENTAL AND MODELLED I-V AND P-V CURVES OF A P-SI PV CELL ILLUMINATED BY INDOOR LIGHTING (~138LUX) ..... 207

FIGURE 6-22: EXPERIMENTAL I-V AND P-V CURVES FOR P-SI PV CELLS ILLUMINATED BY GTLSS (3.8LUX) ..... 208

FIGURE 6-23: MODELLED I-V AND P-V CURVES FOR P-SI PV CELLS UNDER ILLUMINATION BY GTLSS AT 3.8LUX ..... 209

FIGURE 6-24: POWER-VOLTAGE AND CURRENT-VOLTAGE CURVES FOR AN ICRB USING A-SI PV CELLS AND 24 15MMX3MMØ GTLSS (IN A GOLD COATED CASING) ..... 210

FIGURE 6-25: COMPARISON OF EFFICIENCIES OF SELECTED PV CELLS TO THEIR STC AT VARYING INCIDENT LIGHT INTENSITY (REPRODUCED FROM [239]) ..... 212

FIGURE 6-26: SPECTRAL SENSITIVITY OF AMORPHOUS AND CRYSTALLINE SILICON (REPRODUCED FROM [240]) ..... 213

FIGURE 6-27: POWER AGAINST VOLTAGE CURVES MEASURED DIRECTLY AND CHARGING A CAPACITOR FOR AN ICRB (USING A-SI PV CELLS AND TWENTY FOUR 15MMX3MMØ GTLSS) ..... 215

FIGURE 6-28: POWER AGAINST VOLTAGE COMPARISON OF CHARGING DIFFERENT CAPACITORS BY AN ICRB ..... 217

FIGURE 6-29: DC BIAS EFFECT FOR X7R AND X5R TYPES OF CERAMIC CAPACITOR SHOWING CAPACITANCE CHANGE SET AGAINST APPLIED DC VOLTAGE (REPRODUCE FROM [244]) ..... 218

FIGURE 6-30: COMPARISON OF LEAKAGE POWER IN ELECTROLYTIC, TANTALUM AND NIOBIUM OXIDE CAPACITORS ..... 219

FIGURE 6-31: VOLTAGE OF BURIED ICRB MEASURED OVER TIME AND COMPARED WITH THE GROUND TEMPERATURE AND PIPE TEMPERATURE ..... 224

FIGURE B-1: 'X-Y' PLANE OF SECTION X SHOWING (A) TRANSMISSION THROUGH THE SIDE, (B) REFLECTION AND TRANSMISSION THROUGH THE END, AND (C) POINT OF MAXIMUM REFLECTIVE TRANSMISSION ..... 239

FIGURE B-2: SIMULINK BLOCK DIAGRAM: "EFFICIENCY OF LIGHT TRANSMITTED FROM CAP" ..... 241

FIGURE B-3: SIMULINK BLOCK DIAGRAM: "EFFICIENCY OF LIGHT TRANSMITTED FROM CYLINDER WALLS" ..... 242

FIGURE B-4: SIMULINK BLOCK DIAGRAM: "AVERAGE PERCENTAGE TRANSMISSION EFFICIENCY" ..... 243

FIGURE B-5: SIMULINK BLOCK DIAGRAM: "SUBSYSTEM" ..... 244

FIGURE B-6: SIMULINK BLOCK DIAGRAM: "PHOTONS TRANSMITTED" ..... 245
FIGURE B-7: DISCHARGE VOLTAGE OF A *1000MF 25V* ALUMINIUM ELECTROLYTE CAPACITOR ..... 258
FIGURE B-8: LEAKAGE POWER VS VOLTAGE FOR *1000MF 25V* CAPACITOR ..... 259
FIGURE B-9: RESISTANCE VS VOLTAGE FOR A DISCHARGING *1000MF 25V* CAPACITOR ..... 259
FIGURE B-10: LEAKAGE POWER FROM CAPACITOR DISCHARGING CALCULATED IN EXCEL® ..... 261
FIGURE C-1: LABVIEW BLOCK DIAGRAM FOR LOW POWER ICRB MEASUREMENT ..... 263
FIGURE C-2: ICRB FOR BURIAL ON WATER PIPE, VARIOUS VIEWS ..... 263
FIGURE C-3: ICRB LABELLED ACCORDING TO UK LEGISLATIVE REQUIREMENTS ..... 264
FIGURE C-4: WATER PIPE IMMEDIATELY FOLLOWING EXPOSURE (NO ICRB ATTACHED) ..... 264
FIGURE C-5: ICRB IN ENCLOSURE AFFIXED TO THE WATER PIPE ..... 265
FIGURE C-6: ABOVE GROUND CONTAINER OF SENSOR NODE, IN SITU DIRECTLY ABOVE ICRB WHICH HAS BEEN BURIED ON THE PIPE 265
FIGURE D-1: POWER-VOLTAGE AND CURRENT-VOLTAGE CURVES FOR M-SI PV CELLS UNDER ILLUMINATION BY DIRECT SUNLIGHT ... 266
FIGURE D-2: POWER-VOLTAGE AND CURRENT-VOLTAGE CURVES FOR M-SI PV CELLS ILLUMINATED INDOORS AT 138LUX ..... 266
FIGURE D-3: POWER-VOLTAGE AND CURRENT-VOLTAGE CURVES FOR AN ICRB USING M-SI PV CELLS AND 12 25MMX3MMØ GTLSS ..... 267
FIGURE D-4: EXTERNAL QUANTUM EFFICIENCY OF TWO MANUFACTURED A-SI PV CELLS (BLACK LINE THE ORIGINAL, RED LINE A REPLICA) (REPRODUCED FROM [235]) ..... 267
FIGURE D-5: EXTERNAL QUANTUM EFFICIENCY OF CRYSTALLINE SILICON PV CELLS WITH DIFFERENT PRE-DEPOSITION TIMES (REPRODUCED FROM [236]) ..... 268

# LIST OF TABLES

TABLE 2-1: TABLE OF VARIOUS ELECTROSTATIC ENERGY HARVESTERS SHOWING THEIR ELECTRICAL POWER OUTPUTS (REPRODUCED FROM [36]) ..... 16

TABLE 2-2: SUMMARY OF POWER OPTION FINDINGS ..... 33

TABLE 3-1: KEY PROPERTIES OF RADIOISOTOPES FOR RADIOISOTOPIC BATTERIES ..... 37

TABLE 3-2: COMPARISON OF DIRECT CHARGE RADIOISOTOPIC BATTERY CHARACTERISTICS ..... 50

TABLE 3-3: COMPARISON OF DIRECT CONVERSION RADIOISOTOPIC BATTERY CHARACTERISTICS ..... 58

TABLE 3-4: COMPARISON OF INDIRECT CONVERSION RADIOISOTOPIC BATTERY CHARACTERISTICS ..... 66

TABLE 3-5: PROPERTIES OF SELECTED PHOSPHORS [178-183] ..... 77

TABLE 4-1: PEAK POWER, EFFICIENCY AND POWER DENSITY OF INITIAL ICRB DESIGNS ..... 88

TABLE 5-1: LIST OF VARIABLES AND SUGGESTED VALUES FOR TRITIUM FOR THE POINT BETA SOURCE EQUATIONS [175, 176] ..... 121

TABLE 6-1: CALCULATED VALUES OF SURFACE BETA FLUX POWER FOR THE GEOMETRIES OF THE KEY GTLSS USED DURING LABORATORY TESTING ..... 185

TABLE 6-2: MEASURED DIMENSIONS OF SELECTED GTLSS ..... 187

TABLE 6-3: EFFICIENCY OF SELECTED PV CELLS UNDER ILLUMINATION BY ULTRA-LOW BRIGHTNESS LIGHT FROM GTLSS ..... 211

TABLE 6-4: COMPARISON OF PEAK POWER OF SELECTED ICRB SYSTEMS AS A FUNCTION OF THE ACTIVITY, VOLUME AND ACTIVE SURFACE AREA OF THE PV CELLS IN USE. ..... 223

# ACRONYMS AND ABBREVIATIONS

| | |
|---|---|
| a-Si | amorphous silicon |
| AC | alternating current |
| ADC | analogue-to-digital converter |
| AlAs | aluminium arsenide |
| AlGaAs | aluminium gallium arsenide |
| ARC | anti reflective coating |
| $BaSO_4$ | barium sulfate |
| $BaTiO_3$ | barium titanate |
| BOL | beginning of life |
| CDE | Cornell Dubilier Electronics inc. |
| DAQ | data acquisition |
| DC | direct current |
| DCRB | direct charge radioisotopic battery |
| ESA | European Space Agency |
| ESR | equivalent series resistance |
| GaAs | gallium arsenide |
| GaN | gallium nitride |
| GTLS | gaseous tritium light source |
| GUI | graphical user interface |
| HCCI | homogenous charge compression ignition |
| HSE | health and safety executive |

| | |
|---|---|
| I-V | current-voltage |
| ICRB | indirect conversion radioisotopic battery |
| IQE | internal quantum efficiency |
| m-Si | monocrystalline silicon |
| MCNP | monte carlo nuclear program |
| MEMS | microelectromechanical system |
| MFC | microfibre composite |
| MIT | Massachusetts institute of technology |
| MMRTG | multi-mission radioisotopic thermoelectric generator |
| NASA | national air and space association |
| NNL | national nuclear laboratory |
| p-Si | polycrystalline silicon |
| P-V | power-voltage |
| PBSDF | point beta source dose function |
| PCB | printed circuit board |
| PCSDA | partial continuous slowing down approximation |
| PV | photovoltaic |
| PVDF | polyvinylidene difluoride |
| PZT | lead zirconium titanate |
| RCA | radio corporation of America |
| RHS | radioisotopic heat source |
| RTG | radioisotopic thermoelectric generator |
| $S_2O_3$ | disilicon trioxide |

| | |
|---|---|
| SiC | silicon carbide |
| SNAP | systems nuclear auxiliary power |
| STC | standard test conditions |
| USB | universal serial bus |
| WSN | wirelss sensor network |
| ZnS | zinc sulphide |

# NOMENCLATURE

| | |
|---|---|
| $A$ | activity of radioisotope |
| $A_{1Ci}$ | activity of one curie of radioisotope |
| $A_c$ | cross sectional area |
| $A_m$ | specific activity of the beta emitter |
| $A_{pv}$ | surface area of photovoltaic cell |
| $A_s$ | surface area of the phosphor/glass boundary |
| $A_x$ | averaged atomic weight of a phosphor |
| $b$ | density of the beta emitter |
| $C$ | capacitance |
| $c$ | speed of light in a vacuum |
| $c_1$ | gap between PV cell end and casing |
| $D$ | diode |
| $d$ | thickness of glass on sides of GTLS |
| $d_1$ | length of active area of a photocell |
| $d_{31}$ | piezoelectric coefficient |
| $D_C$ | diameter of a cylinder |
| $dP_\beta$ | power of the beta flux |
| $dS$ | an elementary surface area |
| $dS_E$ | unit surface area on the end of a cylinder |
| $dS_L$ | unit surface area along the length of a cylinder |
| $dt$ | an elemental time |

$dv$ voltage difference

$E$ energy

$e$ thickness of PV cell

$E_{eh}$ energy necessary to form an electron-hole pair

$E_g$ bandgap of a p-n junction

$E_0$ initial energy of an alpha particle

$E_R$ energy loss when charging a capacitor

$f$ distance of PV cell overhanging GTLSs in region 2

$f'(x_n)$ derivative of a function of $x$

$f(x_n)$ function of $x$

$FF$ fill factor of PV cell

$g$ number of GTLSs in array

$h$ Planck constant

$H$ distance between end of PV cells and casing in region 2

$I$ current

$I_d$ current across a diode

$I_{mp}$ current at maximum power point of PV cell

$I_o$ reverse saturation current

$I_{ph}$ generated photocurrent

$IQE$ internal quantum efficiency of a photocell

$I_{SC}$ short circuit current

$I_{sh}$ current across a shunt resistance

$J$ energy of one electron volt

$J_{abs}$ absorbtion current of capacitor dielectric

$J_{leak}$ leakage current of capacitor

$J_{SC}(\lambda)$ short circuit current density

$J_{store}$ current resulting in stored charge in capacitor

$k$ Boltzmann constant

$k'$ correction factor

$K_c$ thermal resistance

$L$ length of a cylinder

l external height of GTLS cylinder

$L_1$ light losses from a GTLS in the middle of an array

$L_2$ light losses from a GTLS on the end of an array

$L_b$ operating life of capacitor at max. voltage and temperature

$L_{c1}$ percentage of light incident on casing from GTLS in region 1

$L_{c2}$ percentage of light incident on casing from GTLS in region 2

$L_{op}$ operating life of capacitor

$L_{S1}$ percentage of light incident on PV cell from casing in region 1

$L_{S2}$ percentage of light incident on PV cell in region 2

$L_T$ total percentage of light reflected onto PV cell in region 1

$L_{T2}$ total percentage of light reflected onto PV cell in region 2

$L_{y2}$ total light losses from one GTLS into an adjacent GTLS

$L_{y3}$ total light losses from GTLS1 into GTLS3

$L_{z1}$ light transmitted from GTLS1 into GTLS2 in the x-z plane

$L_{z2}$ light lost into the phosphor layer of GTLS2

$L_{zt}$ total percentage of light transmitted from GTLS1 into GTLS2 in x-z plane

$m$ mass

$M_3$ molecular mass of a radioisotope

$M_v$ voltage based multiplier

$N$ number of radioactive atoms present at a given time

$n$ diode ideality factor

$n_1$ refractive index of material light is transmitted from

$n_2$ refractive index of material light is transmitted into

$N_o$ number of radioactive atoms initially present

$N_p$ number of incident photons

$P$ power

$p$ pressure of radioisotopic gas

$P_0$ specific power of radioisotope

$P_{chg}$ power of charging capacitor

$P_i$ power of radioisotopic decay

$P_{in}$ power of light incident on a surface

$P_{out}$ generated electrical power

$P_r$ radioisotope power flux

$P_\beta$ total beta power flux

$q$ elementary charge

$QE(531nm)$ quantum efficiency at 531nm

$QE(\lambda)$ quantum efficiency at wavelength $\lambda$

$R$ resistance

$R_a$ applied external resistance

$R_{a1}$ Fresnel equations using glass/air parameters and angle γ1

$R_{a2}$ Fresnel equations using glass/air parameters and angle γ2

$R_{AE}$ total percentage of light reflected from glass/air boundary

$R_{A\alpha}$ Fresnel equations using glass/air parameters and angle α

$R_{A\tau}$ Fresnel equations using glass/air parameters and angle τ

$R_B$ Fresnel equations using glass/air parameters and angle γ3

$R_C$ radius of a cylinder

$R_{ca}$ reflectivity of casing

$R_f$ fixed resistance

$r_i$ inner radius of GTLS glass tube

$r_o$ outer radius of GTLS glass tube

$r_p$ distance along decay particle path

$R_p$ parallel resistance

$R_{PE}$ total percentage of light reflected from phosphor/glass boundary

$R_{P\alpha}$ Fresnel equations using phosphor/glass parameters

$R_{P\tau}$ Fresnel equations using phosphor/glass parameters and angle τ

$R_{P\theta}$ Fresnel equations using phosphor/glass parameter and angle Θ

$R_s$ series resistsnce

$R_v$ variable resistance

$R_\theta$ percentage of light reflected

$R_x$ range of a particle

$s$ distance from base of end of GTLS in region 2

$t$ time

$T$ absolute temperature

$T_{1/2}$ half-life of radioisotope

$T_a$ actual internal operating temperature of capacitor

$T_A$ transmission of light from an array of GTLSs

$T_{amb}$ ambient temperature

$T_c$ cold temperature

$T_{ends}$ overall percentage of light transmitted through the ends of the GTLS

$T_{eX}$ percentage of light transmitted through ends of section X

$T_{EX}$ total percentage of light transmitted from end of section X

$T_{EY}$ total percentage of light transmitted from end of section Y

$T_{gtls}$ percentage of light transmitted from GTLS without reflections

$T_{GTLS}$ total percentage of light transmitted from a GTLS

$T_h$ hot temperature

$T_\infty$ total transmission at a single point and a single angle

$ti$ thickness of glass at top and bottom of GTLS

$T_m$ maximum allowed internal temperature of capacitor

$tP_\beta$ total beta power flux without attenuation losses

$T_{sides}$ overall percentage of light transmitted through the sides of the GTLS

$T_{sX}$ percentage of light transmitted through side of section X

$T_{SX}$ total percentage of light transmitted from side of section X

$T_{SY}$ total percentage of light transmitted from side of section Y

$T_{TX}$ total percentage of light transmitted from section X

$T_{TY}$ total percentage of light transmitted from section Y

$T_{xX}$ percentage of light transmitted in x-y plane of section X

$T_{xyY}$ total percentage of light transmitted in the x-y plane of Section Y

$T_{\theta}$ percentage of light transmitted

$V$ voltage

$v'$ absorbtion coefficient of the beta particle emitting material

$V_a$ voltage applied to capacitor

$V_{mp}$ voltage at maximum power point of PV cell

$V_{oc}$ open circuit voltage

$V_r$ rated voltage of capacitor

$W_0$ stopping power of the beta particle emitting material

$x$ percentage of energy lost during charging

$x_n$ a number

$x_{n+1}$ a new number

z distance from base of GTLS to point of emission

$ZT$ figure of merit (thermoelectricity)

$\alpha$ angle of light incidence

$\alpha_1$ angle of incident light from one GTLS onto an adjacent GTLS

$\alpha_2$ angle of incident light from one GTLS onto an adjacent GTLS

$\alpha_6$ angle of light incident on casing in region 2

$\beta$ angle of light from GTLS incident on casing

$\beta_1$ angle of incident light from one GTLS onto an adjacent GTLS

$\beta_2$ angle of incident light from one GTLS onto an adjacent GTLS

$\beta_3$ angle of incident light from one GTLS onto an adjacent GTLS

$\beta_4$ angle of light reflected onto PV cells in region 2

$\beta_5$ angle of light reflected onto PV cells in region 2

$\beta_6$ angle of light incidence on casing in region 2

$\beta_7$ angle of light incidence on casing in region 2

$\beta_c$ angle of light between GTLSs at which the critical angle has been reached

$\beta_g$ total reflective gains within β region

$\gamma$ angle without incident light from one GTLS onto an adjacent GTLS

$\gamma_1$ angle of light incidence with glass/air boundary 1

$\gamma_2$ angle of light incidence with glass/air boundary 2

$\gamma_3$ angle of incidence of light from one GTLS onto an adjacent GTLS

$\delta$ angle of light interacting between two GTLSs

$\delta_1$ angle of light reflected from casing to casing in region 1

$\delta z$ elemental slice of section X

$\delta z$ elemental slice in x-y plane across two GTLSs

$\delta\beta$ elemental segment of cylinder

$\varepsilon_{avg}$ radioisotope average energy of decay

$\eta$ efficiency

$\eta_c$ efficiency of charging a capacitor

$\eta_p$ efficiency of photon generation in phosphor layer

$\eta_{pc}$ efficiency of photon generation in phosphor layer

$\eta_{pv}$ efficiency of electricity generation in PV cell

$\eta_t$ efficiency of photon transport inside ICRB

$\eta_{total}$ overall efficiency

$\eta_\beta$ efficiency of beta particles leaving radioisotopic source

$\theta$ angle of light emission

$\kappa$ angle of transmission (dependent on geomentry)

$\lambda$ decay constant

$\mu$ angle without incident light from one GTLS onto an adjacent GTLS

$\nu$ flow rate

$\rho$ path length (of decay particle)

$\rho_1$ density

$\rho_x$ density of a phosphor

$\tau$ angle of transmission (geometry dependent)

$\varphi$ angle of light emission inside GTLS2 in x-z plane

$\varphi(r)$ dose function of the beta emitter

$\phi(\lambda)$ photon flux density at wavelength $\lambda$

$\varphi_1$ key angle 1 of light emission inside GTLS2 in x-z plane

$\varphi_2$ key angle 2 of light emission inside GTLS2 in x-z plane

$\varphi_3$ angle of light reflected from casing in region 1

$\Omega$ angle within $\beta 1$ within which some light may be transmitted

$\Omega_1$ angle of light reflected from casing to PV cell in region 1

$\theta_1$ key angle 1 from centre of GTLS1 for light incident on GTLS2

$\theta_2$ key angle 2 from centre of GTLS1 for light incident on GTLS2

$\theta_3$ key angle 3 from centre of GTLS1 for light incident on GTLS2

$\theta_4$ key angle 4 from centre of GTLS1 for light incident on GTLS2

$\theta_5$ key angle 5 from centre of GTLS1 for light incident on GTLS2

$\theta_6$ key angle 6 from centre of GTLS1 for light incident on GTLS2

$\theta_c$ critical angle

# 1 INTRODUCTION

## 1.1 Background to research

Wireless sensor networks (WSNs) consist of a distributed collection of individual autonomously powered sensor nodes (also known as motes) capable of sensing their environment and communicating this data either to each other or to a “mother node”. WSNs have recently attracted a great deal of research interest [2, 3] and may be used to monitor vehicles, buildings, infrastructure and even people. WSNs may be installed in inaccessible and harsh environments where they may be required to operate for extended periods of time independent of human contact. This thesis considers the application of WSNs to monitor infrastructure and specifically where that infrastructure is buried (as is the case with water pipelines). Under these conditions the ability to provide the sensor nodes with power over the useful lifetime of the WSN has proven to be a key challenge [4].

The environment of a buried water pipe has been experimentally investigated and it has been found that at one site the temperature of the pipe (found to be 16-19°C) may differ by 2°C from a location 50cm away from the pipe. This temperature difference is not fixed and is dependent on the temperature of the fluid in the pipe and the temperature of the surrounding medium (which is seasonally variable). At certain times of year the temperature difference may be greater, while at others there may be no temperature difference at all. The flow of fluid through a pipe generates vibrations in the pipe walls. This vibrational energy has been considered as a potential source of power for a WSN sensor node. Shinozuka et al. conducted tests

on water pipes above ground (i.e. un-damped) and measured vibrations at 5 to 10Hz at accelerations of less than 0.01g in the pipe, rising to a peak of 0.1g near to simulated bursts [5]. It is a reasonable assumption that the effect of burial will dampen the vibrations in a pipe, and therefore reduce the acceleration of the pipe wall and the energy available to be harvested from it.

The power requirements of WSN sensor nodes are dependent on the components used in the node and the duty cycle of the device. WSN sensor nodes do not, typically, take readings of their environment and transmit them continuously. Instead, these devices take readings only once every five minutes, every hour or even every day. The period of taking sensor readings and transmitting data may have high power requirements, but may also have a very brief duration (of the order of one second). The “sleep” period between readings and transmissions is commonly far longer than the “on” period of reading and transmitting, and it is this ratio that is referred to as the duty cycle of the network.

WSN sensor nodes continue to consume power even when they are in “sleep” mode (‘S’ period), albeit at a markedly reduced rate compared to their “on” (‘T’ period) mode. The power requirements of a WSN sensor node are presented graphically in Figure 1-1, where the time averaged power required by the sensor node is also displayed.

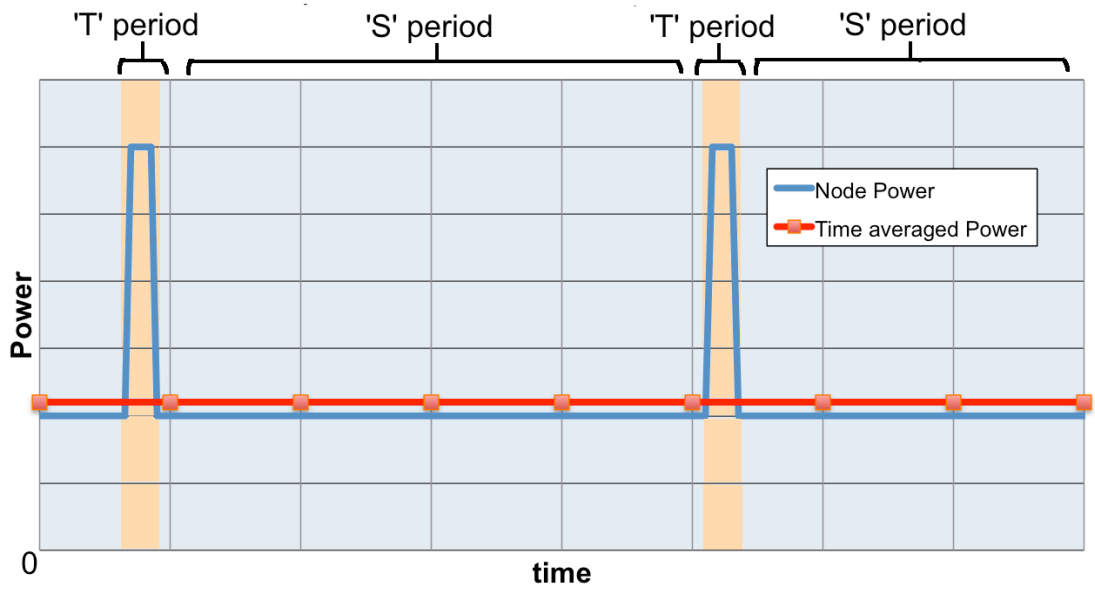



**Figure 1-1: Schematic representation of the** power requirements of a WSN sensor node showing two cycles of operation

It is possible to reduce the power requirements of a WSN sensor node by reducing the duty cycle of the sensor node as shown in Figure 1-2, where the sensor node is modelled to require a sleep power of 20μW. However, the sleep power requirements of the sensor node ultimately act as the lowest power level at which the node may operate.

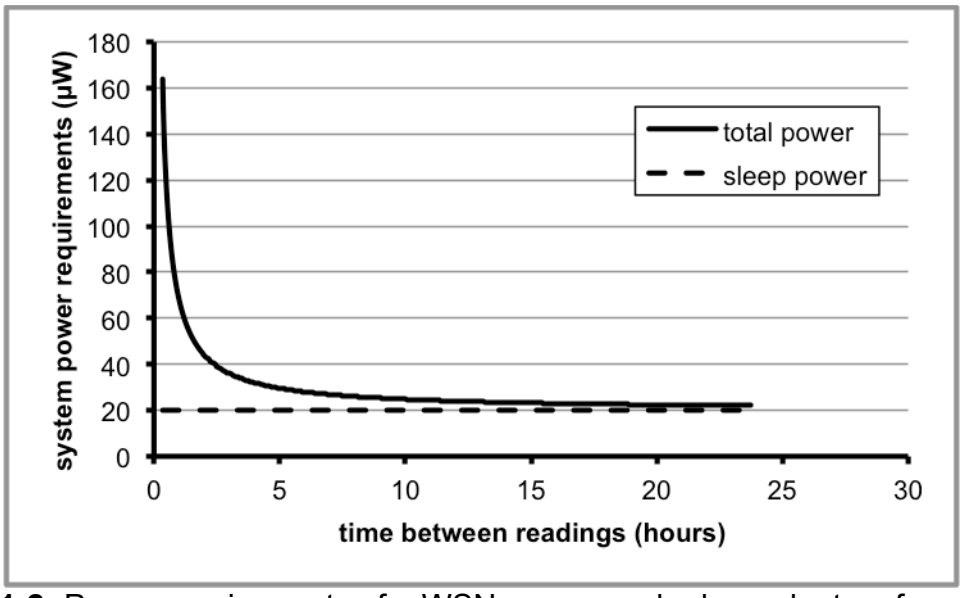



**Figure 1-2:** Power requirements of a WSN sensor node dependent on frequency of readings

From Figure 1-2 it can be seen that reducing the duty cycle beyond one reading and transmission every 8 hours does not have an appreciable effect on the total required power of the WSN sensor node. Wang et al. [6] reported a sensor node taking readings and transmitting every five minutes which had an average operating power of 86μW and a sleep power of 42μW. Their system used the commercially available CC2420 Zigbee™ module from Texas Instruments [7] and was the lowest average power found in the literature. The power issues of WSN sensor nodes have led to researchers attempting to improve the energy efficiency of their networks in an effort to use their available power in the most effective way possible [8, 9].

In parallel to this thesis a project has been undertaken to develop an ultra-low power WSN sensor node capable of operation underground, in order to monitor buried assets. The details of this WSN sensor node are not provided here but its development can be charted in Walton et al. [10] and Metje et al. [11]. The prototype WSN sensor node (shown in Figure 1-3) requires only 1μW of time averaged power to read and transmit once a day. This figure of 1μW therefore provides the power requirement that the power source developed in this thesis will have to provide. This WSN sensor node requires 0.9μW of continuous sleep power and then 34mW of power for reading/transmission (of duration 0.13 seconds). The power requirements of this bespoke sensor node are significantly lower than commercially available systems such as Zigbee™ which has a measured sleep power requirement of 51.8 μW and an active power of 30.7mW, according to Dementyev et al. [12]. It is therefore unlikely that a power source capable of powering the prototype WSN sensor node would be able to power the Zigbee™ node.

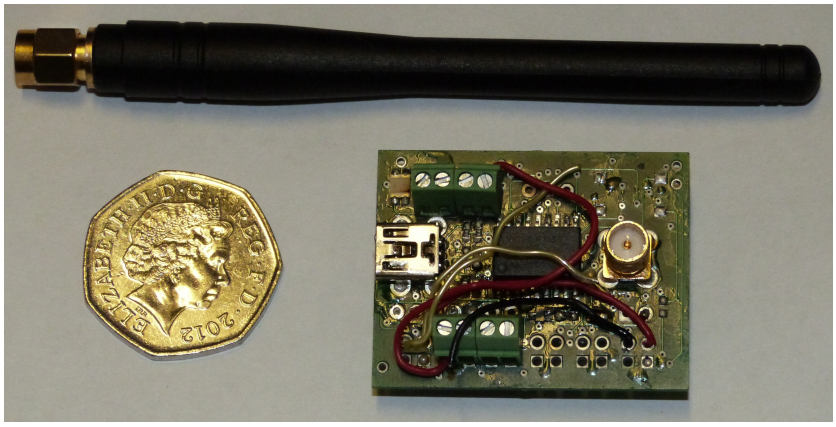


**Figure 1-3:** Bespoke WSN sensor node requiring only 1μW of power designed and manufactured in a parallel project to this thesis (shown with antenna detached)

Previous researchers have used chemical batteries to power their WSN sensor nodes, however these are shown to have major limitations, particularly in their useful operational life. Instead, radioisotopic batteries are identified as a power source worthy of further investigation in this area and multiple prototypes of this type of power source are manufactured and tested. Gaseous tritium light sources (GTLSs) are used as a key component of these radioisotopic batteries and are extensively modelled.

## 1.2 Research aims and objectives

The key aim of this research is to develop a power source capable of powering an autonomous buried wireless sensor network node for the useful lifetime of the network. This useful lifetime has been set at 20 years as after this time period a new generation of technology will have been developed potentially making the sensor node obsolete. The WSN sensor node requires 1μW to power.

The objectives of this research are to:

- Undertake a thorough critical literature review of the available power options to provide a WSN sensor node with $1\mu W$ for 20 years, underground.
- Identify the most suitable power option and theoretically model its operational efficiency with the aim of identifying aspects of its operation where efficiency gains may be obtained.
- Design and fabricate prototypes of the most suitable power option with a view to optimizing the power output and efficiency of the device.
- Design and develop suitable testing regimes in order to accurately measure the power generated by the prototypes.
- Investigate the performance of the selected power source in the ground over an extended period of time in order to determine its suitability for use.

## 1.3 List of contributions to knowledge

The contributions to knowledge made by the research in this thesis are as follows:

- An indirect conversion radioisotopic battery and capacitor system was proposed for the first time as a power source for a buried WSN sensor node.
- Multiple ICRBs manufactured were verified through testing as capable of powering the WSN sensor node.
- A comprehensive theoretical model of the entire battery system was developed and used where previously only partial or simple models had been implemented.
- An ICRB was buried on a live water pipe and its long life suitability verified in practical testing spanning several months.

- The use of barium sulfate as a reflective material was investigated for the first time with ICRBs and demonstrated an improvement in generated power.

## 1.4 List of publications

The following publications are formed in part or in full from research presented in this thesis:

R. Walton, A. M. Sadeghioon, N. Metje, D. Chapman, and M. Ward, "Smart pipes: The future for proactive asset management," in *International Conference on Pipelines and Trenchless Technology 2011: Sustainable Solutions for Water, Sewer, Gas, and Oil Pipelines, ICPTT 2011, October 26, 2011 - October 29, 2011*, Beijing, China, 2011, pp. 1512-1523.

N. Metje, D. N. Chapman, R. Walton, A. M. Sadeghioon, and M. Ward, "Real time condition monitoring of buried water pipes," *Tunnelling and Underground Space Technology,* (2012) vol. 28, pp. 315-320.

R. Walton, C. Anthony, M. Ward, N. Metje, and D. N. Chapman, "Radioisotopic battery and capacitor system for powering wireless sensor networks," *Sensors and Actuators: A Physical,* vol. 203, pp. 405-412*,* 2013.

R. Walton, C. Anthony, M. Ward, D. N. Chapman, and N. Metje, "Radioisotopic battery for long-life, buried autonomous power," PowerMEMS 2013, London, UK, 2013 (in proceedings).

## 1.5 Report structure

This thesis presents the selection, design, fabrication, testing and modelling of a power source for a WSN sensor node. Chapters 2 and 3 investigate the power sources currently available and critiques their suitability based on the design parameters described in section 1.2. The conclusion of these chapters presents the chosen power option and identifies holes in the literature where further investigation is warranted. Chapter 4 presents the results of testing on an initial power source prototype followed by the process of designing, fabricating and testing further practical prototypes., The functioning of all aspects of the power source is extensively described in Chapter 5 alongside theoretical modelling of its internal energy conversion and transfer. Chapter 6 presents the results of this testing along with the output of theoretical modelling and the meaning of these results is discussed. Finally, Chapter 7 concludes the thesis providing a summary of the key findings of the research and giving recommendations for future directions in which this research might be taken. Aspects of this research that do not fit easily into the flow of the main body of the text, but are useful for the reader to be aware of, have been inserted into the appendices.

# 2 POWER OPTIONS FOR A WSN SENSOR NODE

## 2.1 Introduction

A broad range of power options exist which may be used to provide electrical energy to an autonomous buried WSN. These power sources may be defined as being either regenerative or non-regenerative in nature. A regenerative power source generates energy from its environment and therefore could theoretically provide a source of power for as long as the environment is providing the means to do so. These types of power source are often referred to as energy harvesters. Non-regenerative power sources require their own supply of fuel, which will in time be consumed. The size of this fuel supply and the rate at which it is used therefore provides one limiting factor on the useful lifetime of this type of power supply.

An overview of the various key power source options is provided in Figure 2-1. This chapter will examine the available possibilities in both regenerative and non-regenerative power sources, highlighting both positive and negative attributes of each source, with the aim of identifying the most suitable choice to carry forward for further investigation in this research.

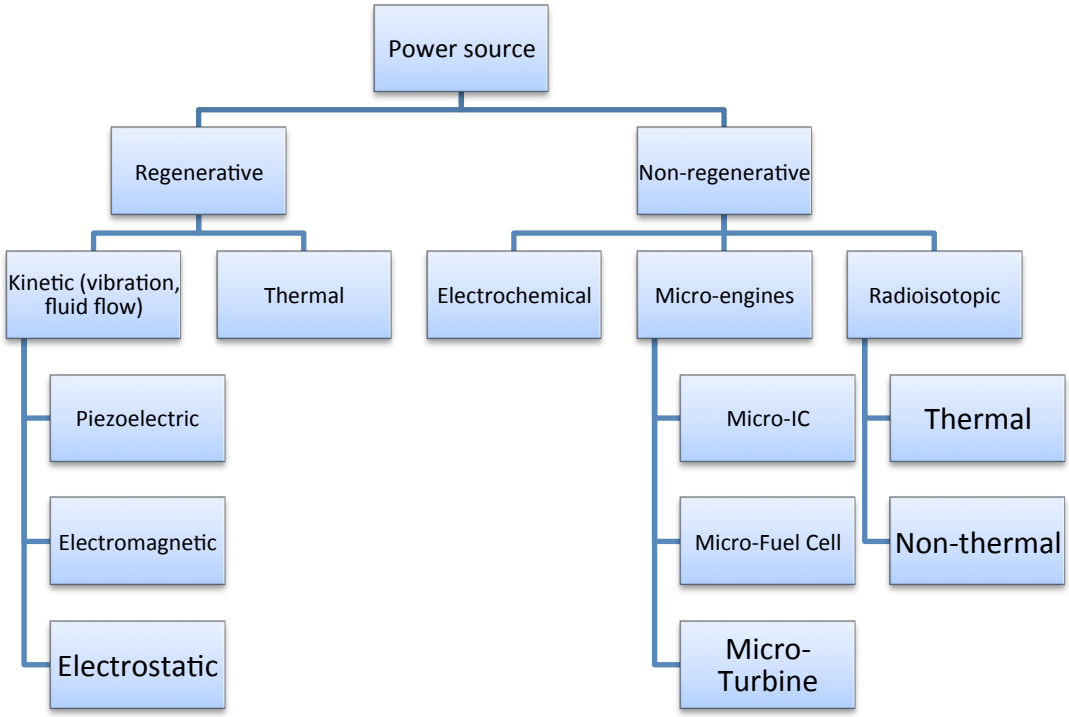



**Figure 2-1:** Tree of available power sources

## 2.2 Regenerative power sources

There is a high likelihood that ambient energy will be present in the environment of a buried sensor node, which may be harnessed and converted into useful electrical energy. This ambient energy may be in the form of thermal energy or kinetic energy. Kinetic energy in the form of vibrations or of a fluid flow may be transformed into electrical energy, and the variety of means that exist to accomplish this will be examined in further detail. Thermal energy may also be converted into electrical energy by the use of thermoelectric and thermionic devices which will also be discussed. Solar radiation, however, will not permeate below the surface of the ground and therefore photovoltaic cells are not an option for this research and hence will not be investigated further.

### 2.2.1 Vibration energy harvesting

There are three common methods for generating electrical energy from environmental vibration (kinetic) energy; piezoelectric systems; electro-magnetic systems; and electrostatic systems [13]. The energy available from these systems may be modelled through consideration of a simplified mechanical model [14].

#### 2.2.1.1 Piezoelectric systems

A property of piezoelectric materials is that they generate electrical current when stressed, while they will also deform if an electric current is applied to them [15]. This property has been utilised by both researchers and in the commercial sphere in order to generate electrical energy from vibration based energy. Physik Instrumente Ltd. [16] are a German company selling piezoelectric actuators while Microstrain Inc. [17] are an American company which produces complete piezoelectric energy harvesting packages and WSN nodes.

A commonly utilised method [18-20] for generating electrical energy from vibrations is to fix a quantity of piezoelectric material to a cantilever beam, which has a proof mass attached to its free end. The device is affixed to the source of the vibrations thus causing the cantilever to oscillate and hence allowing electrical current to be generated in the piezoelectric material, as shown in Figure 2-2. Location of the device is therefore of key importance and will have a significant bearing on the amount of energy harvested. The electrical energy generated in this manner is directly proportional to the frequency and amplitude of the vibration [21] and is greatest at what is known as the resonant frequency of the piezoelectric material.

When the excitation induced by the vibration is not at the resonant frequency the efficiency of electricity generation is greatly reduced. Zhengjun and Lijie [22] have proposed a solution to this issue by utilizing a multi-resonant structure, generating seven resonant peaks and a power output of 20.5μW when attached to a metal beam excited by an electric motor. The cantilever structure consists of 9 beams and as such is larger than would be usual for a piezoelectric device which would generally only have one beam. Similarly there are reportedly reliability issues with the reliability of cantilevers in more complex configurations [23].

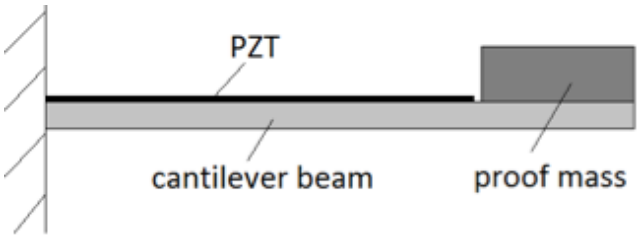



**Figure 2-2:** Common layout of a piezoelectric energy harvesting device

A potential limiting factor of oscillating cantilever beam based piezoelectric energy harvesters is the cycle life of the cantilever itself. Henslee et al. [24] describe testing a piezoelectric microfiber composite (MFC) beam at its resonant frequency of 104Hz (which is within the common range of excitation for piezoelectric energy harvesting) discovering that the fatigue life was heavily dependent on temperature. At 20$^{o}$C the MFC was found to exceed 250 million cycles but at -15$^{o}$C the MFC failed at 135 million cycles. At an operating frequency of 104Hz this would limit the energy harvesting device to only 15 days of continuous operation at its resonant frequency (and 150 days at 10Hz oscillation, as discovered on a water pipe). The exact frequencies of the oscillations generated in a harvester of this type are highly dependent on application (the source of vibrations) however this may well prove to

be a limiting factor on the useful life of this class of device. The practical efficiency of this class of energy harvester was found to be less than 1% by Kubba in 2012 [25].

### 2.2.1.2Electromagnetic systems

Utilizing Faraday's law [26], electromagnetic energy harvesters generate an electric current by subjecting a coiled wire to a varying magnetic flux. Either the coil of wire or the magnets interacting with it are fixed to the main body of the energy harvester while the other component is free to move within the confines of the device. Ambient vibrations then cause the mobile component to move relative to the fixed component and hence electrical power is generated as shown in Figure 2-3. Micro-scale versions of this class of energy harvesting device were first described by Williams and Yates [27] in 1996.

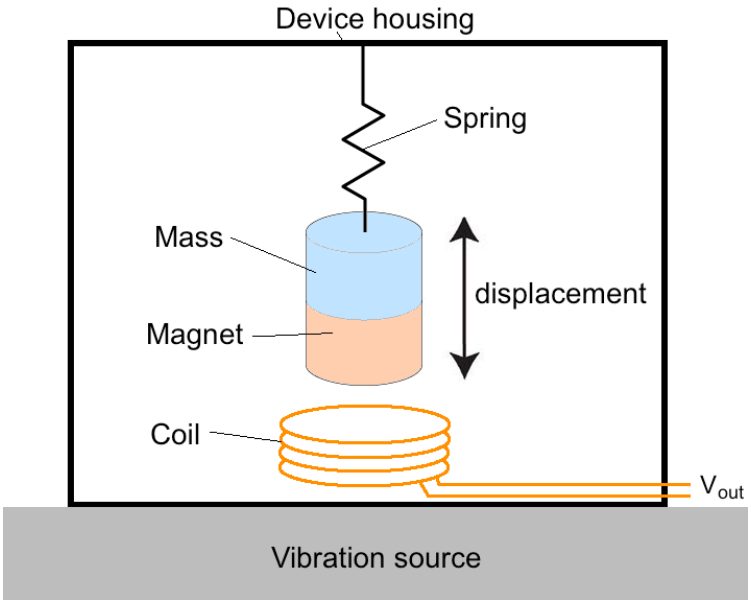



**Figure 2-3:** Typical design of an electromagnetic energy harvesting device

Electromagnetic energy harvesters are currently utilised in both research and commercially, with Perpetuum Ltd. [28] being a British company producing

electromagnetic energy harvesters designed specifically for industrial wireless sensor networks. These energy harvesters are intended to be located on heavy machinery in order to harness the high energy vibrations available from such places.

In research, Jong Cheol and Jae Yeong [29] demonstrated an electromagnetic harvester of volume 600mm$^3$ which produced 102μW from a 53Hz vibration at an acceleration of 0.4g. The voltage produced under these conditions was found to be only 0.14V and in fact Roundy et al. [30] estimate that it is not possible to exceed 0.1V from a 1000mm$^3$ volume utilizing this transduction method. [31],

As with piezoelectric harvesters the power output of electromagnetic energy harvesters is highly dependent on the frequency and amplitude of the vibration being harnessed, with both maximum power and voltage being generated at the resonant frequency of the spring material [29] and dropping away sharply when the frequency is not at this rate. For an ambient source offering variable frequency of vibration the generated voltage may be too low for rectification for long periods of time.

The fatigue life of electromagnetic energy harvesters will depend on the configuration of the device, of the materials utilised and of the applied stresses (frequency and acceleration). The designers of electromagnetic harvesters do not usually describe the fatigue life of the components in their systems. However, for devices which utilise a spring the cycle life may potentially be only of the order of 100,000 cycles (calculated from Shigley [32]) which at 10Hz (as found on a water pipe) would last for less than 3hours. Meanwhile the system described by Bouendeu et al. [33] utilised a cantilever beam constructed of copper and polyimide sheet which, from their own

analysis, should last for only 931 load cycles at a load of 1.156kPa. This device would therefore only be expected to last for 7 seconds at a frequency of 129.6Hz. The useful lifetime of these devices can be extended by damping the oscillation of the magnets within the coils (which will occur naturally due to electrical damping) and also by limiting the amplitude of the motion of the magnets beyond their maximum. The electromagnetic generators available from Perpetuum Ltd. utilize both techniques, however, limiting the amplitude of oscillation also greatly reduces the power that may be generated.

#### 2.2.1.3 Electrostatic systems

First proposed by Meninger et al. in 2001 [34] micro-scale electrostatic energy harvesting systems harness the energy from vibrations to alter the distance between pre-charged capacitor plates separated by a dielectric (or air). So long as the voltage or charge on the plates remains constant then the capacitance value of the device will alter as the distance between the plates changes, and therefore energy will be generated.

One requirement of this type of power source is that the capacitive plates be pre-charged before motion can harvest any electrical energy. This can require a separate power supply to ensure the plates are charged prior to use, but can also be achieved by use of an electret. Liu et al. [35] deposited an electret material onto two base capacitive layers and then allowed a third capacitive plate to move between these two fixed layers, in a modified in-plane overlap layout. The device was vibrated at 50Hz (close to the 44.2Hz resonant frequency of the system) with the 200mm$^3$ electrostatic harvester generating 18nW at 1g of acceleration. From Table 2-1 [36] it

can be seen that the power output of this class of energy harvester may be higher than Liu et al generated, however this may well be at a greater mass, frequency (*F*) or acceleration (*A*) than the 0.01g at 10Hz found on a water pipe.

**Table 2-1:** Table of various electrostatic energy harvesters showing their electrical power outputs (reproduced from [36])

| $P$ ($\mu$W) | $F$ (Hz) | $A$ (m s$^{-2}$) | Mass (g) | Volume (cm$^3$) | Voltage | Power density | Material |
|---|---|---|---|---|---|---|---|
| 58 | 4.76 | 0.5 | 1200 | — | 24 | — | Aluminum/polyester |
| 8 | 2520 | — | — | 75 | — | 8 nW cm$^{-3}$ | Silicon |
| 36 | 6 | 1 | 780 | — | — | — | Aluminum/polyester |
| 3.7 | 30 | 50 | 0.1 | 750 | — | 4.9 nW cm$^{-3}$ | Silicon/pyrex |
| 110 (simulated) | 120 | 2.25 | — | 1000 | — | 0.11 $\mu$W cm$^{-3}$ | Silicon |
| 97 mV | 28 000 | 1395 | — | — | — | — | Aluminum/gold/glass |
| 0.12 | 45 | 0.08 | — | — | — | — | Metal |
| 0.065 | 4200 | 766 | $2 \times 10^{-4}$ | — | 0.4 | — | Gold/silicon |
| 6 | 10 | 3.9 | — | 800 | 200 $V_{p-p}$ | 7.5 nW cm$^{-3}$ | Polymer/glass |
| 80 | 30 | 40 | — | Area = 5.5 cm$^2$ | 220 V | 14.5 $\mu$W cm$^{-2}$ | Glass and silicon |
| 0.3 J/cycle | — | — | 0.5 proof mass | — | 250 V | — | Quartz and silicon |
| 24 | 10 | — | — | Area = 0.56 cm$^2$ | 2.3 kV | 42.9 $\mu$W cm$^{-2}$ | Silicon and quartz |

All types of electrostatic energy harvester are limited in their power generation by either mechanical or electrical damping and this class of energy harvesting device may also require a supplementary power source in order to remain charged. In addition the mechanical properties of electrostatic harvesters may lead to cyclic stress damage over extended periods of operation, which may limit the useful life of this type of system. Additionally, the output voltage and impedance of these devices is very high which results in very low currents with the additional need for voltage regulation. Roundy et al. [30, 37] determined from their micro-scale electrostatic harvester experiments that this form of power generation was not economically practicable at realistic frequencies of excitation in order to generate useful power levels.

Vibration energy harvesters generate an alternating current (AC), though most WSN nodes and sensors required direct current (DC) power. Therefore rectification of the generated current is required in order to provide useful power to a WSN node. Power management electronics reduce the overall efficiency of energy conversion while also increasing both the size and complexity of the harvesting device. The frequency and acceleration (10Hz at 0.01g) of vibrations on a buried water pipe are much lower than are normally used during testing of these classes of device. For example Liu et al. generated 18nW from vibrations of 44.2Hz at 1g, which is significantly less power than is required.

### 2.2.2 Thermal energy harvesting

There are a variety of techniques which are utilised to generate electricity from a thermal difference (such as thermionics, thermotunnelling, and thermophotovoltaics) however thermoelectric systems are by far the most commonly utilised method to harness the available energy from a thermal difference [38]. Thermoelectric harvesters have been created to harvest energy from industrial scale waste heat in the order of killowatts from temperature differences in the hundreds of Kelvin over the last few decades [39]. In recent years this form of energy harvesting technology has also been leveraged in order to attempt to harness useful power for micro power systems such as WSN. Thermoelectric energy harvesters consist of two differently conducting materials exposed to a temperature difference, with electricity then generated via a process known as the Seebeck effect, as shown in Figure 2-4. Thermoelectric energy harvesting is being investigated in academia as well as in the commercial sphere by companies such as Micropelt GmbH [40], Nextreme Thermal Solutions Inc. [41], and Thermo Life® Energy Corp. [42].

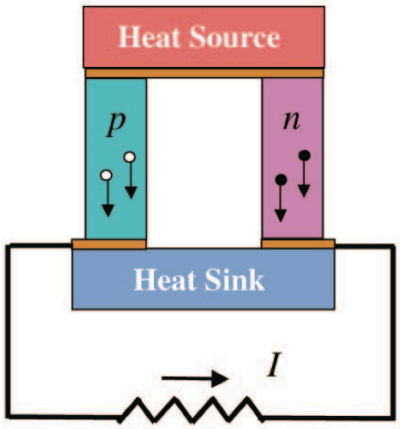



**Figure 2-4:** Diagram of thermocouple utilizing the Seebeck effect (reproduced from [43])

The efficiency ($\eta$) of any thermoelectric harvester is defined by a combination of the material figure of merit ($ZT$) and the Carnot efficiency limit as described in equation **(2-1)** where $T_c$ is the cold temperature and $T_h$ is the hot temperature.

$$\eta = \frac{T_h - T_c}{T_h} \qquad \textbf{(2-1)}$$

Typical local ambient temperature differences are of the order of 1-10K outside industrial applications [44] and for the vicinity of a pipe it was found to be 2K. For a small temperature difference the maximum efficiency is very low, for example at an ambient temperature of 293K a temperature difference of 2K produces a maximum efficiency of 0.7%. In reality thermoelectric devices do not operate near the maximum efficiency and are dependent also on the figure of merit ($ZT$) of the materials in use. Even at a far greater thermal difference it is rare to find conversion efficiencies above 5% even with more modern, novel thermoelectric materials with higher figures of merit [45].

In 1999 Citizen Watch Company of America, Inc. released the Eco-Drive Thermo that utilised a mini thermoelectric energy harvester as a source of power. In the same year Kishi et al. [46] described their experimental construction and testing of such a device (see Figure 2-5) and concluded that the thermal power emitted from a human body in the form of heat could be converted into enough power (1μW) to keep their prototype wristwatch working. However it is not clear at what temperature difference this power was generated which is a critical issue since this determines the energy which is available to harvest. Changes in the ambient temperature will also alter the temperature difference (with the body temperature) which may prevent power from being generated in certain climates. If the ambient and body temperature are the same (for example) then no energy will be available to harvest.

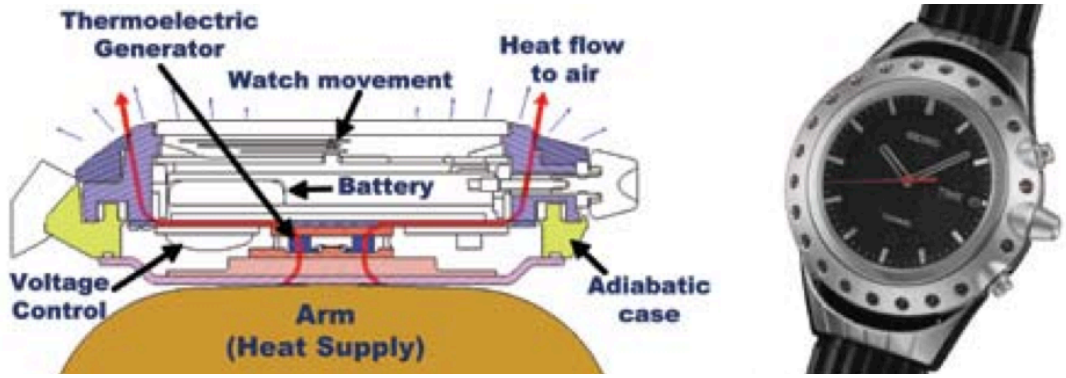



**Figure 2-5:** Thermoelectric watch developed by Kishi et al. (reproduced from [46])

The challenge with generating increased efficiency in thermoelectric systems is to produce a device possessing reduced thermal conductivity while also having increased electrical conductivity. To this end a variety of novel materials and applications of materials are being investigated, however to date those materials which have been generated are expensive, toxic and/or in very short supply [47]. The compound $Bi_2Te_3$ is the most commonly used material for thermoelectric harvesting

[43] and has a ZT of nearly 1 at room temperature [48]. As can be seen from Figure 2-6, which was published by Vining [49], at low temperature differences (such as are likely to exist in buried environments) there is poor efficiency of electrical conversion, even were an improvement in the *ZT* value of the thermoelectric material to be achieved.

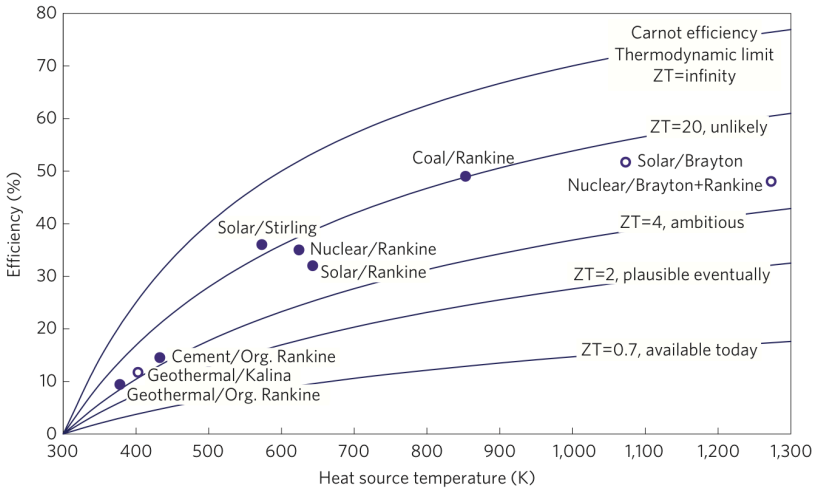



**Figure 2-6:** Efficiency of thermoelectric materials at varying temperature and ZT value (reproduced from [49])

The Seebeck coefficient of a thermoelectric material describes the voltage which can be generated by that material for a given temperature difference, and generally this coefficient lies in the range of 200-300μV/K for frequently used materials. At low thermal differences of the order of 2K (as discovered In the vicinity of a water pipe) many thousands of thermocouples must be connected in series in order to generate a useable voltage, which is challenging to fit within a small space [44] representing a further obstacle to implementing thermoelectric harvesters to power WSN nodes.

### 2.2.3 Fluid flow energy harvesting

In the case of WSN sensor nodes affixed to pipelines it may also be possible to harness energy directly from the kinetic energy of flow of a fluid or gas within the pipe, assuming such a flow is present. The power present within a flow in a pipe is described by Equation (2-2), where $\rho_1$ is the density of the fluid medium, $A_c$ is the cross sectional area of the pipe, and $v$ is the flow rate. However, only a small fraction of the cross-sectional area of the pipe will generally pass over any energy harvesting system, and then only some of that energy will in turn be converted into useful electrical energy.

$$P = \frac{1}{2}\rho_1 A_c v^3 \quad \textbf{(2-2)}$$

As proposed by Taylor et al. [50], it is possible to generate electrical energy from a piezoelectric film held in the flow of a fluid and buffeted by the Karman vortex street produced by a bluff body placed upstream of the energy harvesting device. This energy harvesting system consisted of a 240mmX76mmX150μm PVDF (polyvinylidene difluoride) piezoelectric energy harvester, chosen for its flexibility. Unfortunately the tests conducted on this device only describe reaching 2V of output at a frequency of 50Hz and a flow rate of 0.5ms$^{-1}$, with no mention of power generation being made. Tests by Weinstein et al. [51] on a similar system (as shown in Figure 2-7) in an air flow in a 100mm internal diameter pipe with a 25mm diameter cylindrical bluff body and a bulk PZT piezoelectric harvester produced 100μW of power at a flow rate of 2ms$^{-1}$. The flexible PVDF piezoelectric utilised in the experiment of Taylor et al. [50] has a piezoelectric coefficient ($d_{31}$=20-25pm/V) [52] which is around ten times lower than is found with the bulk PZT ($d_{31}$>190pm/V) and

as such generates far lower electrical power for a given deflection. Meanwhile the bulk PZT used in the experiments of Weinstein et al. [51] did not generate any power at all below flow rates of 1.5ms$^{-1}$ which may well be due to its higher stiffness.

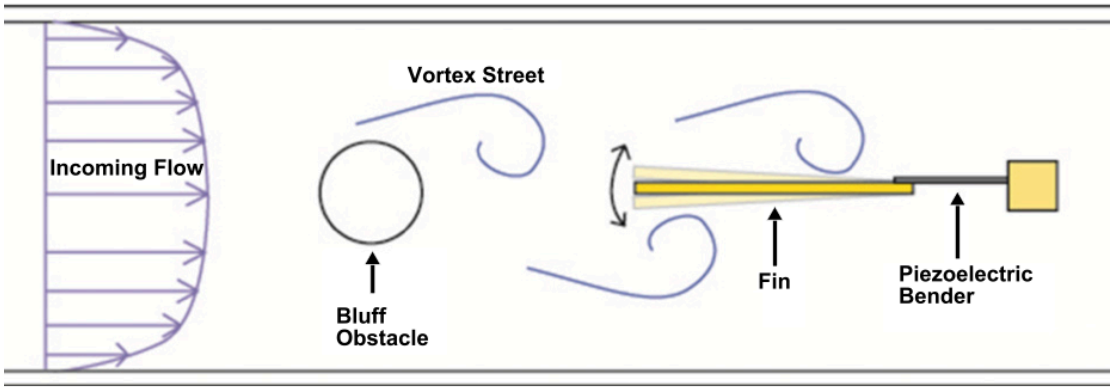



**Figure 2-7:** Layout of fluid flow piezoelectric energy harvester reproduced from [51])

Electromagnetic energy harvesting has also been investigated in order to harness the energy of flow in a fluid. As shown in Figure 2-8, Wang et al. [53] used a trapezoidal bluff body (4.25mm high at the leading edge, 1mm high at the tail edge) in the flow of water through a rectangular channel of dimensions 50mmX15.7mm to generate 1.77μW from a 37,900mm$^3$ volume energy harvester under a flow rate of 1.38ms$^{-1}$, representing a relatively low power density. The tested system would not require the electromagnetic harvester to be directly in the flow of the fluid which is advantageous, however it would require modification of the internal wall of a pipe in order to function.

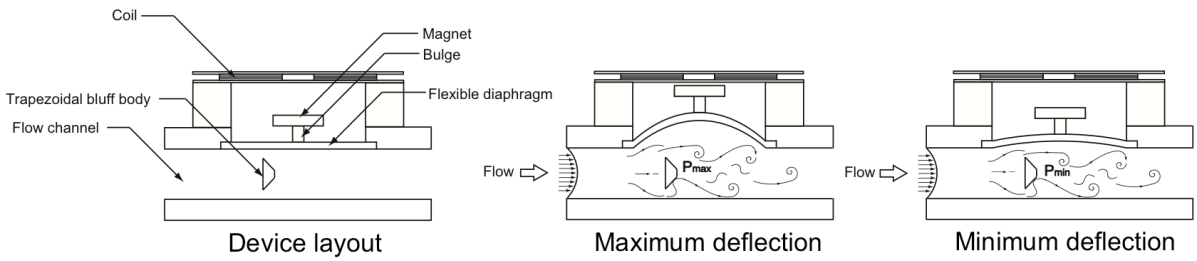



**Figure 2-8:** Design of an electromagnetic fluid flow energy harverster (reproduced from [53])

Small scale conventional turbines (Pelton and propeller, for example) have been investigated as a possible method of generating electrical energy from fluid flow in a pipe, as described by Azevedo and Santos [54]. However Deam et al. [55] discovered that for rotor diameters less than 11mm conventional axial and radial flow turbines become highly inefficient while viscous flow turbines (of the type presented by Tesla [56]) are more useful. Several micro Tesla turbines were created and tested by Krishnan et al. [57] utilising rotors of diameters as small as 13mm, depicted in Figure 2-9. At a water flow rate of $2cm^3/s$ 400μW of power was generated at a conversion efficiency of 36%. However, the rotor was spinning at 1243rpm at which velocity the system would not be reasonably expected to last for many years of continuous use.

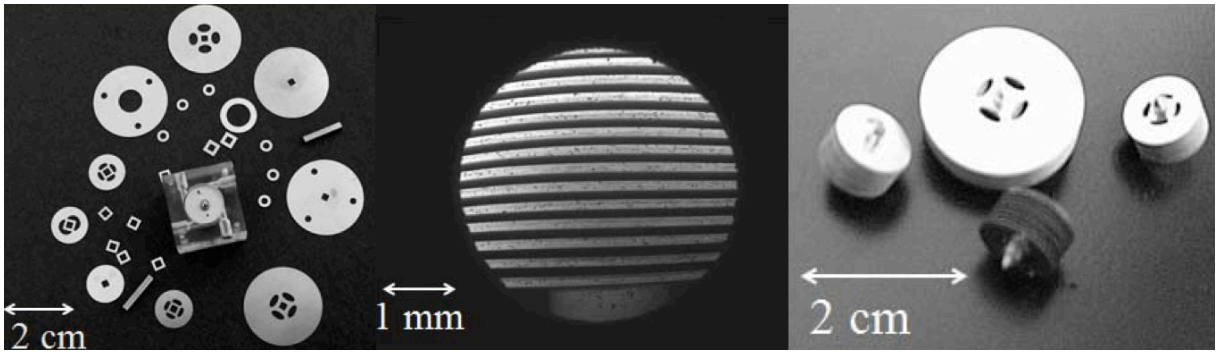



**Figure 2-9:** Components and finished rotors of micro tesla turbines (reproduced from [57])

All designs that harvest energy directly from fluid flow within a pipe are invasive to the pipe to some extent. Energy harvesting from flow using piezoelectric materials or electromechanical harvesting would involve all of the issues reviewed in sections 2.2.1.1 and 2.2.1.2 while also including a bluff body and possibly the harvester in the direct flow of the fluid which may be undesirable. Turbines are capable of generating

high electrical power, but are unlikely to last for an extended period of continuous use.

## 2.3 Non-regenerative power sources

Some power supplies do not rely on their environment to provide a source of fuel, but instead bring their own fuel with them. The most commonly utilised power source, batteries, falls into this category, as do less traditional systems such as micro-turbines, micro-engines, and micro fuel cells. Of further interest are radioisotopic batteries, whose supply of fuel takes the form of a radioisotope.

### 2.3.1 Electrochemical

Electrochemical batteries, usually known simply as batteries, are the most commonly utilised power source for WSN sensor nodes. There are primary and secondary batteries, with the key difference being that secondary batteries are capable of repeated charging cycles, while primary batteries are a use once option. Energy is stored within batteries in the form of negatively charged anions and positively charged cations, which are formed in an electrolyte. In primary batteries these charged particles are generated in separate regions of the battery due to an initial chemical reaction. In secondary batteries the charged particles are forcibly separated from each other (one type to the anode and the other type to the cathode) by means of an applied external electrical charge. After the external charge is removed the anions and cations will tend to remain where they have been moved, though will migrate very slowly towards each other over time, representing the self-discharge of the battery. Primary batteries also suffer from this effect of gradual self-discharge.

The size of electronic devices has decreased over the years but there has not been a comparative reduction in the size of batteries, which has led in many cases to the power source being a number of times larger than the device it is powering [58]. Relatively low energy density is the limiting factor for the scaling of batteries, though advances have been made, especially in the form of lithium-ion batteries (energy density of 570Wh/L), lithium-ion thin-film batteries (energy density of 2mAh/cm$^2$), and zinc air batteries (a primary battery with an energy density of 1350Wh/L) [59]. This issue could potentially be resolved in the future utilizing novel fabrication techniques [60].

Batteries provide a direct and continuous current, however they are not suitable as a power source for an autonomous, long life WSN as their shelf life is only typically in the region of two to three years [61], after which time they will not be able to provide any power to the system. Certain types of battery (such as Lithium-Thionyl-Chloride) are claimed to have a shelf life of 10 year [62], however this claim is only under ideal conditions and does not appear to be supported by any available experimental data.

### 2.3.2 Micro-engines, turbines and fuel cells

A variety of micro-scale versions of traditional power generators have been produced in recent years [63], some of which will be described here. In 2008 Lee et al. [64] utilised deep reactive ion etching to fabricated a micro-turbine with a rotor of diameter 4mm which generated 380mW of power at 35% adiabatic efficiency at a rotational speed of 330,000rpm. This type of power source has also been investigated at the Massachusetts Institute of Technology (MIT) where rotor speeds of 1,700,000rpm have been reached [65] utilising a turbine design shown in Figure 2-10. The turbine

has been reported to generate electrical power of 50W while burning jet fuel at 7g/hr (approximately 10cm$^3$ of jet fuel every hour).

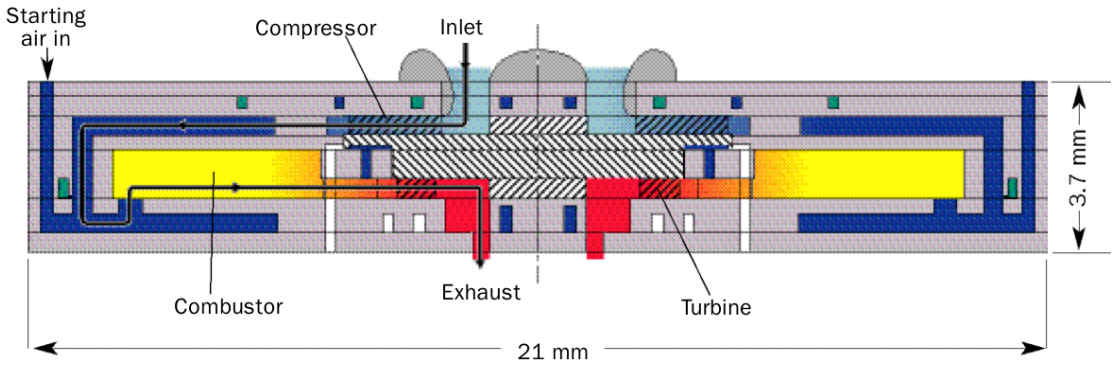



**Figure 2-10:** Design of micro-turbine created at MIT (reproduced from [66])

The micro Wankel engine depicted in Figure 2-11 was designed and fabricated at the University of Birmingham [67], while researchers at the University of Berkley also generated a working prototype [68]. During testing it was found that there were serious issues with this micro-engine, particularly in terms of component sealing and ignition. The University of Minnesota have developed a micro homogenous charge compression ignition (micro-HCCI) engine, which also exhibited serious sealing problems along with erosion of housing materials which severely restricts the useful lifetime of the system [69].

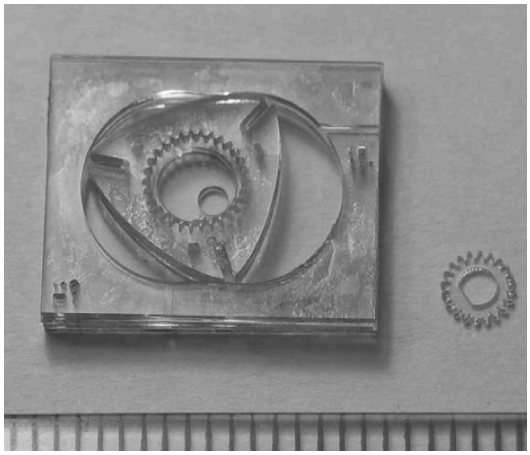


**Figure 2-11:** Micro Wankel engine fabricated at the University of Birmingham (reproduced from [67])

Fuel cells represent another electricity generating system that has been explored as a potential micro power source. Fuel cells operate via an electrochemical process, not from a combustion cycle and can therefore generally operate at much lower temperatures (typically between 20$^{o}$C and 100$^{o}$C) [70]. A further advantage of this class of electrical generator is their resistance to vibrations and lack of moving parts (aside from fluid flow). Yamazaki built a micro fuel cell (shown in Figure 2-12) using a variety of MEMS (microelectromechanical systems) techniques which had a volume of 0.55cm$^{3}$ and generated 37mW of peak power at 0.45V [71]. However fuel cells have a limited operating life, due to chemical degradation and mechanical cracking induced by thermal cycling, The operational lifetime of fuel cells has been estimated at 40,000hrs for a solid oxide fuel cell, which is the equivalent of four and a half years of continuous operation [72]. Starting and stopping the fuel cell degrades its performance [73], while frequent stop/start will lead to cell failure due to developed blockages (such as water drops on the anode side) leading to the carbon in the cell corroding down to $CO_2$ and then outgassing [74].

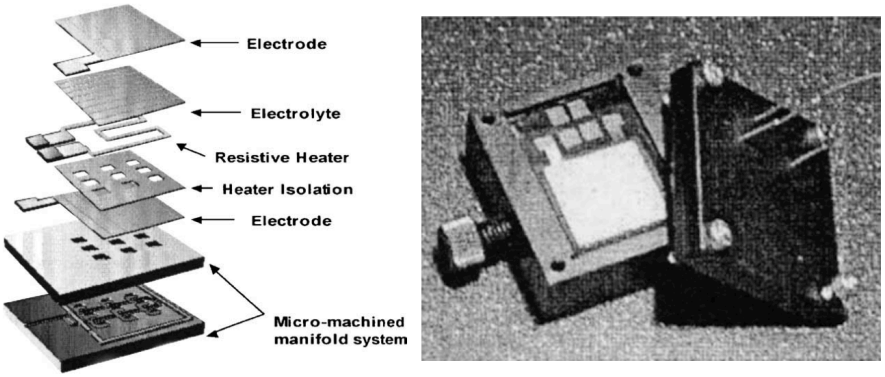



**Figure 2-12:** Micro fuel cell components and housing (reproduced from [71])

A pressing concern for all of these scaled-down systems is the issue of heat loss at such small sizes, and therefore thermal insulation is of great importance. Due to the reduced size of the components, tolerances (which would be acceptable at a macro-scale) are no longer useable, and heat losses from an increased surface to volume ratio are far more significant. Additionally an oxygen source is crucial for many of these generators, which will not be readily available in the environment of some buried WSN nodes.

### 2.3.3 Radioisotopic

Henry Moseley first demonstrated the principle of radioisotopic batteries in 1913 during his experimentations utilising a hollow quartz sphere plated with silver on the inside and filled with radium [75]. This class of battery harnesses the energy radiated through radioisotopic decay of an unstable element and converts that energy into electrical energy through a variety of mechanisms. Radioisotopes typically decay to release; alpha particles which carry a positive charge; beta particles which carry a negative charge and very low mass (similar to an electron); and gamma rays which are not particulate in nature [76].

Radioisotopic batteries generate a continuous supply of (typically low) power and are capable of doing so for a very long time, dependent on the half-life of the radioisotope used in the battery. Nickel-63 ($^{63}$Ni) is often used in this class of battery and has a half-life of 101.2 years [77], so in theory this type of power source may last for more than 100 years. In addition, the energy density of radioisotopic fuel is exceptionally high with Uranium-235 ($^{235}$U) containing $1.5X10^{12}$J/L, which is a million times greater than an electrochemical battery [78].

There are two general categories of radioisotopic battery, thermal and non-thermal types. Thermal types harnessing the thermal energy generated by self-absorbtion of the decay of the radioisotope into itself have been developed and utilised by NASA (the National Air and Space Association, USA) for its deep space missions for the last 50 years [79]. This type of battery generally utilises a thermoelectric converter to generate electricity from the temperature difference between ambient conditions and the surface of the radioisotope, which has commonly been Plutonium-238 ($^{238}$Pu). This class of radioisotopic battery has demonstrated excellent long-life performance, particularly on the Voyager 1 and 2 deep space missions that were launched in 1977 and are still powered by their radioisotopic source over 35 years later as they prepare to be the first man-made objects to enter interstellar space [80]. Providing a source of both heat and power, Figure 2-13 shows the Radioisotope Thermoelectric Generator (RTG) design that NASA has used in many of its space missions. The RTG used in the Ulysses mission launched in 1990 contained 7.8kg of $^{238}$Pu and generated 4400W of thermal power and 289W of electrical power at 28V (at time of launch) [81].

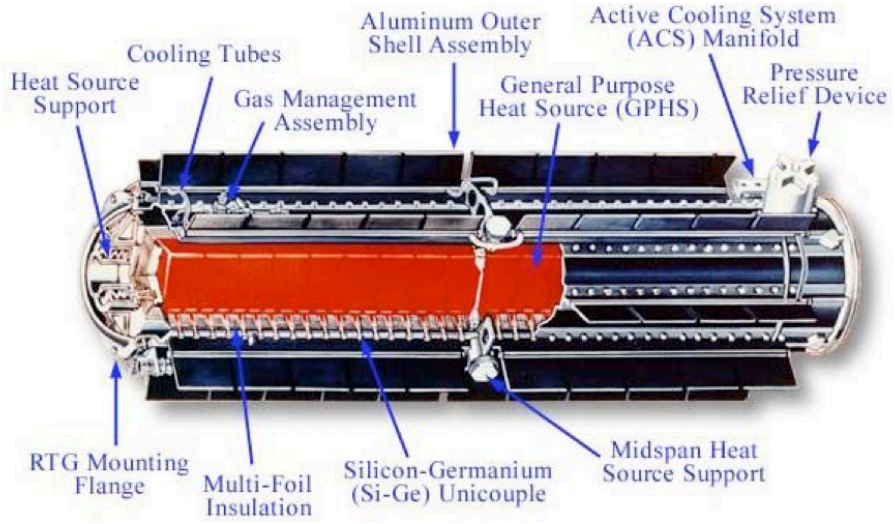



**Figure 2-13:** Cut-away of radioisotope thermoelectric generator used by NASA (reproduced from [81])

Non-thermal types of radioisotopic battery generate electricity by a number of different processes. One such process is demonstrated by the direct conversion radioisotopic battery, which converts the kinetic energy of the decay particles (beta or alpha) into electricity within a semiconductor junction in the same manner that solar energy harvesters do with photons. A schematic of this arrangement is presented in Figure 2-14. The Donald W. Douglas Laboratories, USA, [82] produced a radioisotopic battery using this conversion mechanism which generated 400μW of power at 4V utilising 2.442X10$^{12}$Bq of Promethium-147 ($^{147}$Pm) at an efficiency of 1.7%. $^{147}$Pm has a half-life of 2.63 years and this battery would therefore not be suitable for a 20 year lifetime, however a different radioisotope (such as Tritium) should overcome this problem.

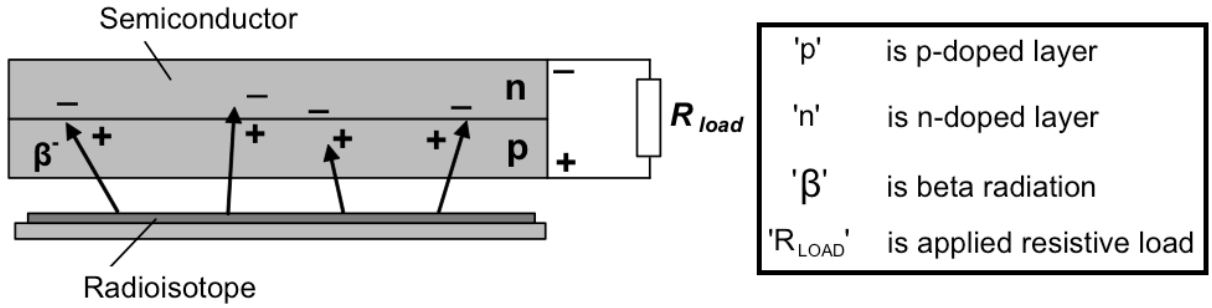



**Figure 2-14:** Layout of a direct conversion radioisotopic battery (reproduced from [83])

The use of radioisotopes in a power source deserves special consideration due to their potentially hazardous characteristics. Some radioisotopes that have found use in radioisotopic batteries are of an extremely hazardous nature (such as $^{238}$Pu) and are therefore possibly not suitable for a power source on earth. However, other radioisotopes may be more suitable. Tritium ($^{3}$H) possesses a low average energy of

decay, with its radiated beta particles not able to penetrate even a layer of dead skin (the range of the beta particles is 0.006mm in water) [84], and should therefore be considered to be safe for use in a buried WSN if contained in the correct manner. In fact tritium is used in commercially available fishing lights and self-powered emergency exit signs in the UK and is covered for such use by current UK legislation [85]. Each radioisotope should therefore be considered on an individual basis to determine whether it is appropriate for use or not, however there are certainly some radioisotopes that may be suitable.

## 2.4 Storage options

Many of the power options discussed here are not capable of providing power directly to a WSN as their power generation is lower than the requirement of the WSN node during reading/transmission mode. There is therefore a need to store the energy generated by these power sources so that the energy can be delivered when required by the WSN node at potentially a far higher power than at which it was generated.

Batteries are the most commonly used storage option in WSN but are not the only option available. Capacitors and supercapacitors (sometimes called ultracapacitors) have found increased use in recent years [86], and possess some significant advantages over batteries. Many supercapacitors are capable of operating for more than 10 years with only a 20% reduction in their capacity (and by limiting the energy stored in the supercapacitor it is possible to extend the useful lifetime beyond 20 years. Batteries, in contrast, will not generally function for more than two or three years (as described earlier) while their capacity to store energy will reduce more quickly over their lifetime than would the capacity of a supercapacitor [87].

One area where batteries hold an advantage over supercapacitors is that their self-discharge current is considerably lower [88]. Additionally batteries have much higher energy density than capacitors or supercapacitors, typically two orders of magnitude higher [38]. However, the energy used to power a WSN node is very low (1μW) and therefore a low energy density should not be problematic in the energy storage system. A disadvantage of batteries relative to capacitors is that they have a much higher internal resistance and therefore do not quickly and efficiently discharge their stored energy at the rate necessary to power a WSN node during transmission. By contrast capacitors have a very high power density and discharge their stored energy with high efficiency.

Capacitors typically use either a liquid electrolyte (aluminium, tantalum, etc.) or a solid electrolyte (ceramic, glass, paper, etc.) and are of varying capacitance and voltage rating. The decision of which capacitor to use depends entirely on the specific application for which it is intended to be used. The energy ($E$) that may be stored in a capacitor is described by Equation (2-3), where $C$ is the capacitance and $V$ is the voltage.

$$E = \frac{1}{2} C V^2 \quad \textbf{(2-3)}$$

Spiral springs represent another potential mechanism which can be used to store energy, where an applied external force gradually winds the spring more and more tightly until the mechanically stored energy is needed and the spring unwinds [89]. A key issue with this storage mechanism is that the generated energy must be converted into mechanical energy (except perhaps in the case of fluid flow energy harvesting) and then later converted back into electrical energy from the stored

mechanical. These conversion processes introduce additional areas of efficiency loss for the system and therefore spiral springs are not suited to act as an energy storage mechanism for many of the power sources discussed in this review. However, it is worth noting that storing mechanical energy in spiral springs based on carbon nanotubes has a modelled energy density which is several orders of magnitude greater than with steel springs and eight times greater than is found in lithium ion batteries [90], and therefore this class of storage device may be worthy of future attention.

## 2.5 Conclusions of power options review

An overview of power sources for buried WSN nodes is presented here with a wide variety of options examined. Table 2-2 shows a summary of the various power source options along with a range of values for their power output, volume and useful lifetime (all values dependent on variables of the power sources themselves).

**Table 2-2:** Summary of power option findings

| | Power | Lifetime | Volume |
|---|---|---|---|
| **Vibration energy harvesting** | 1nW-100nW | 30 mins - 4 years | $1cm^3$ - $100cm^3$ |
| **Thermal energy harvesting** | 10nW-1μW | > 100 years | $0.01cm^3$ - $400cm^3$ |
| **Fluid flow energy harvesting** | 1.77μW-400μW | < 2 years | $10cm^3$ - $100cm^3$ |
| **Electrochemical** | < 10W | 2 years - 3 years | $0.1cm^3$ - $200cm^3$ |
| **Micro-engines, turbines and fuel cells** | 10mW-50W | 10 hours – 4.5 years | $0.55cm^3$ - $100cm^3$ |
| **Radioisotopic** | 1nW-100W | 1 week – 100 years | $0.5cm^3$ - $1000cm^3$ |

The most commonly utilised power source for WSN are electrochemical batteries, however these are unsuited to power an autonomous long-life WSN as their shelf-life was found to be too short and therefore alternative options should be considered.

Through consideration of the characteristics described in Table 2-2 radioisotopic batteries and thermal energy harvesters were identified as a likely candidate for further research due to their long lifetimes. However, the power generated by a thermal energy harvester at the low temperature differences typically found near water pipes is insufficient to provide for the WSN sensor node described in the Introduction.

Based on the review radioisotopic batteries storing their generated charge in capacitors represent the most promising power source to provide useful electricity to a long life, autonomous, buried WSN node. This choice is largely predicated on their ability to be useful for more than 20 years (the shelf life of batteries is far short of this figure, for instance) and the ability of the energy storage option to rapidly discharge all of its stored energy. The wide range of powers, lifetimes, and volumes found with radioisotopic batteries is due to the variety of options which exist within this battery type. The following chapter will, therefore, further examine this class of power source.

# 3 RADIOISOTOPIC BATTERIES

## 3.1 INTRODUCTION

A review of radioisotopic batteries is presented in this chapter following their identification as a suitable power source for buried WSN nodes. The current state of the art in this field of study is presented. Radioisotopic batteries are commonly separated into two categories (thermal and non-thermal) both of which are explored in this chapter. The various battery types that exist within these categories are analysed, with their key characteristics presented and evaluated along with their specific suitability for use as a power source for a WSN node. As part of this review radioisotopes are examined in light of their appropriateness for use in a battery. The health and safety implications of the use of radioisotopes are also examined. Following the above review and analysis conclusions are drawn regarding the most appropriate type of battery to pursue. Appropriate gaps in the literature that invite further investigation are identified, justifying the direction of research presented in the following chapters.

## 3.2 RADIOISOTOPES SUITABLE FOR BATTERIES

Radioactive decay describes a process whereby an atom may change from one (unstable) isotope of an element into another (potentially more stable) isotope of an element through emission of either a decay particle (such as alpha or beta) or electromagnetic radiation (gamma rays). This process is described by the radioactive decay law [91], as shown in Equation (3-1), where $N$ is the number of radioactive

atoms present at a given time, $N_o$ is the number of radioactive atoms initially present, $\lambda$ ($s^{-1}$) is the decay constant, and $t$ (s) is the time over which decay has occurred.

$$N = N_0 . e^{-\lambda t} \quad \textbf{(3-1)}$$

An important criteria of any radioisotope is its activity ($A$) which has units of Curies (Ci) or Becquerels (Bq) (1Ci=3.7X$10^{10}$Bq) and is the multiple of the number of radioactive particles and the decay constant of those particles, as shown in Equation (3-2). One Becquerel is one decay in one second.

$$A = \frac{dN}{dt} = \lambda N \quad \textbf{(3-2)}$$

The lifetime of radioisotopes is commonly described by their half-life ($T_{1/2}$), which is the length of time required for half of the atoms in a given sample of the radioisotope to undergo decay. Equation (3-3) shows the half-life as related to the decay constant ($\lambda$).

$$T_{1/2} = \frac{ln2}{\lambda} \quad \textbf{(3-3)}$$

The specific power ($P_0$) of a radioisotope may be calculated by application of Equation (3-4), where $A_{1Ci}$ is the activity of one Curie of radioactive matter in Becquerels (Bq), $\varepsilon_{avg}$ is the average energy of decay of the radioisotope, and $J$ is the energy in joules of one electron volt (1eV=1.602X$10^{-19}$J).

$$P_0 = A_{1Ci} . \varepsilon_{avg} . J \quad \textbf{(3-4)}$$

Many radioisotopes have been used over the years in battery type power sources, some of which are shown in Table 3-1 [92-94].

**Table 3-1** Key properties of radioisotopes for radioisotopic batteries

| Radioisotope | Half-life, $T_{1/2}$ (years) | Specific Activity (Ci/g) | Average Energy (keV) | Specific Power (μW/Ci) | Emission type |
|---|---|---|---|---|---|
| Tritium ($^{3}H$) | 12.32 | 9798 | 5.7 | 34 | β |
| Sulfur-35 ($^{35}S$) | 87.3 days | 41666 | 49 | 290 | β |
| Nickel-63 ($^{63}Ni$) | 101.2 | 56 | 17.4 | 103 | β |
| Strontium-90 ($^{90}Sr$) | 28.9 | 138 | 195.8 | 1161 | α |
| Promethium-147 ($^{147}Pm$) | 2.62 | 943 | 62 | 367 | α |
| Plutonium-238 ($^{238}Pu$) | 87.7 | 17 | 5499 | 32595 | α, γ |
| Americium-241 ($^{241}Am$) | 432.2 | 3.17 | 5486 | 32518 | α, γ |

Selection of an appropriate radioisotope as a fuel source for a battery depends to a large extent on its intended application. The half-life of the radioisotope used in any battery will be a key determining factor on the useful life of that power source and as such $^{35}S$ may not be suitable to power a long-life WSN node due to halving its power every 87.3 days. $^{147}Pm$ may also suffer in this regard with a half-life of only 2.62 years meaning that a battery planned to last for 10 years should contain at least four times the quantity of the radioisotope at the beginning of life (BOL) in order to still be outputting the required power level at the end of its planned use. Increasing the quantity of radioisotope used will potentially increase the size of any planned battery and also, more importantly, the cost of the device.

Another key metric of any radioisotope under consideration for use in a battery is the average energy of the decay particles. With high energy decay particles there may be a lower quantity of the radioisotope required to produce the necessary power output, however, there may also be an increased requirement for shielding of the device for safety reasons. These conflicting considerations must be balanced against each other when selecting the radioisotope.

## 3.3 HEALTH AND SAFETY

The health and safety of any radioisotope powered battery must be a serious consideration and will also limit the usefulness of several of the radioisotopes presented in Table 3-1. Of the most common forms of radiation the most hazardous to human health is gamma radiation, which may induce cancer if exposure is high enough [95]. $^{238}PuO_2$ generates high energy alpha particles and gamma rays as a consequence of radioisotopic decay. Gamma rays are an issue and require extensive shielding of the radioisotope in order to make the source safe for human use. Assuming adequate shielding has been installed around the radioisotope to protect humans in the direct vicinity of the device then the greatest risk to human health comes from a launch or re-entry failure of the space vehicle carrying the RTG. In the event of an explosive accident in the earth's atmosphere after launch it has been estimated that up to three people might be expected to develop cancer due to radiation exposure [96].

Meanwhile, $^{90}S$ decays to form $^{90}Y$ which emits even higher energy alpha particles and although these may be easily shielded themselves, if they impact on a neutron of certain oxides they may generate a highly energized neutron emission requiring

further extensive shielding. For this reason $^{90}Sr$ is not commonly used in the West in earth based power sources (but was in the USSR).

$^{63}Ni$ and $^{3}H$ emit low energy beta particles which may be completely shielded by even a dead layer of skin [97] and as such should be considered safe for use in terrestrial radioisotopic batteries with minimal shielding. Due to the weak nature of their decay they are not considered a major health or safety concern and their use is allowed by the UK government in such items as self powered exit signs and chemical detectors. These two radioisotopes may still present a health hazard if ingested and therefore should be properly contained in a sealed casing such that access to the radioisotope is not possible unless breakage occurs, in order to prevent this possibility. A further potential hazard of these radioisotopes is the generation of Bremsstrahlung X-rays which occur due to the deceleration of the emitted beta particles in a surrounding medium. These X-rays must be shielded from humans, although Bremsstrahlung is not a major problem with either radioisotope so long as the activity of the radioisotopes present is not excessively high [98].

Meanwhile $^{241}Am$ has found use in commercially available smoke detectors even though it emits gamma radiation along with high energy alpha particles. However the activities of this radioisotope allowed for such a purpose (up to 2.2MBq [99]) are very low and are not suitable to provide a meaningful power source (the total power flux from this activity of the radioisotope, ignoring attenuation, is only 2μW).

## 3.4 THERMAL TYPES OF RADIOISOTOPIC BATTERY

Thermal energy may be generated in the concentrated mass of a radioisotope through self-absorbtion of decay particles (eg. alpha or beta). Decay particles are emitted with kinetic energy by the process known as radioactive decay, whereby an atom may change from one (unstable) isotope of an element into another (potentially more stable) isotope of an element through emission of this decay particle. If the decay particle impacts on another nearby atom then it will bounce off but will lose some of its kinetic energy in the interaction with the loss manifesting itself in the form of thermal energy. The more tightly packed the radioisotope then the more common these interactions between decay particles and neighbouring atoms will be and consequently the level of generated thermal energy will also be higher [100].

Thermal types of radioisotopic battery generate electrical energy by a variety of means from this thermal energy, although by far the most common mechanism is a thermoelectric couple. This, and other mechanisms, will be explored in the following section.

### 3.4.1 RADIOISOTOPIC THERMOELECTRIC GENERATOR

At the height of the cold war space race both the American and then Soviet governments developed radioisotopic power sources based around the principle of thermal harvesting. America developed the Systems Nuclear Auxiliary Power (SNAP) program producing dozens of RTGs that were used in both manned and unmanned missions in space [101]. Figure 3-1 shows the SNAP-27 RTG on the surface of the moon where it was used as a source of power during the Apollo 16 mission in 1972.

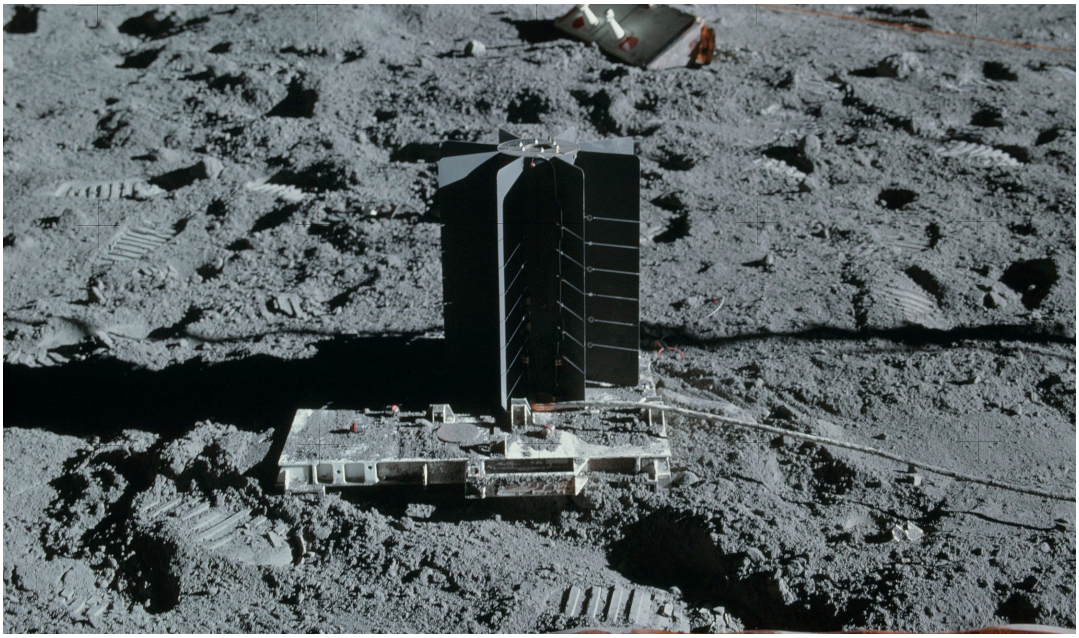


**Figure 3-1:** The SNAP-27 RTG on the surface of the moon as a source of electrical energy during the Apollo 16 mission (reproduced from [102])

To this day the American government (in the form of NASA) continues to make use of this technology as a power source for long life deep space missions. The Mars Curiosity rover (launched 26/11/2011, landed 06/08/2012), that is shown in Figure 3-2 is powered by the Multi-Mission Radioisotopic Thermoelectric Generator (MMRTG) that produces 125W of electrical power at 28V and 2000W of thermal power at the beginning of life (BOL) [103, 104]. These powers are similar to those found with other RTGs that NASA have used over the years. The efficiency of RTG conversion has been modelled to be theoretically limited to less than 10% [105], although real life RTGs often operate at around 6% efficiency [106].

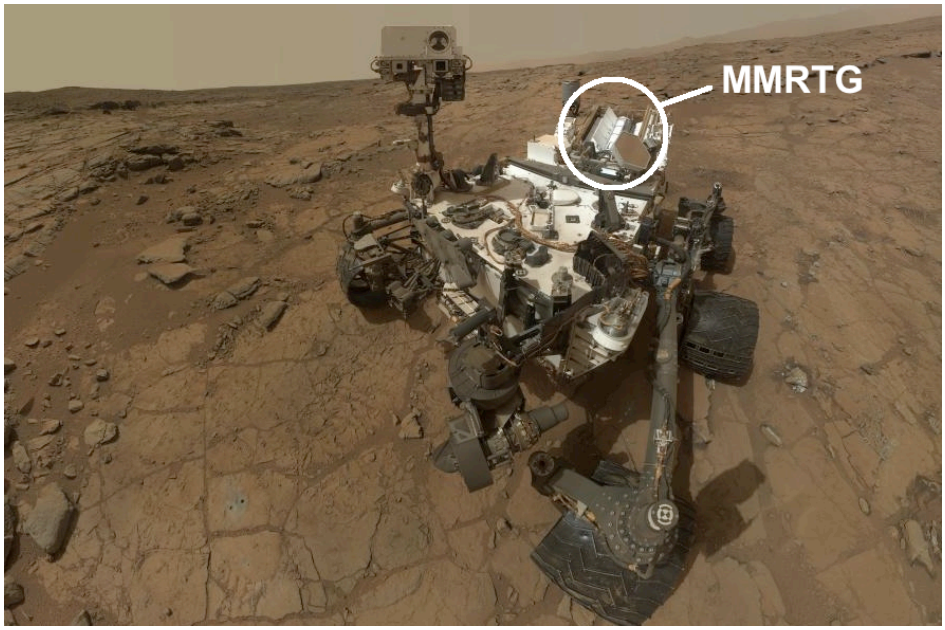



**Figure 3-2:** Mars Curiosity rover self portrait taken on Mars (reproduced from [107])

RTGs generate electricity using the Seebeck effect in a thermoelectric couple. The source of heat is a concentrated mass of radioisotope which self-absorbs most of its own radiated decay energy and thus generates heat. The most commonly utilised radioisotopes for this purpose have been either $^{238}Pu$ or $^{90}Sr$, though $^{210}Po$ has also been used. $^{238}Pu$ is more normally used in its oxide form of $^{238}PuO_2$. Figure 3-3 shows a pellet of $^{238}PuO_2$ (approximately 2cm in height) that was prepared for use in one of NASA's deep space mission RTGs.

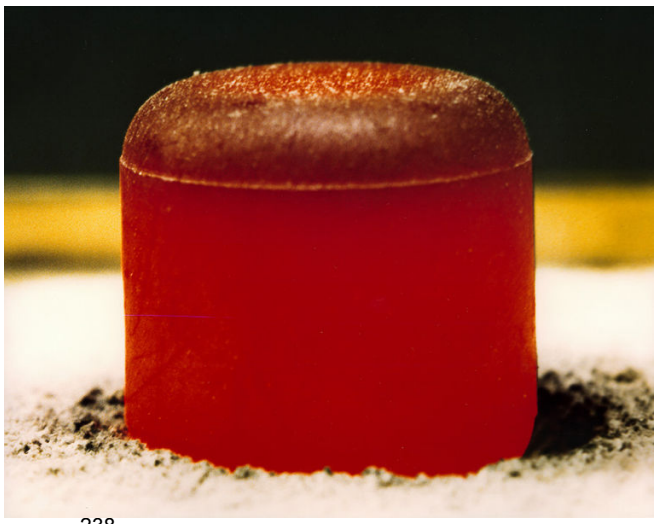


**Figure 3-3:** Pellet of $^{238}PuO_2$ for use in a NASA RTG (reproduced from [80])_

Due in large part to these health concerns, in America RTGs have typically been seen as a power source suited to outer space but in Russia more than a thousand earth based RTGs were constructed and deployed [108]. These RTGs found use as power sources for lighthouses and remote beacons and were planned to last for 10 years, in the case of RHS-90 generating 240W of electrical energy at beginning of life from 1,500TBq of $^{90}$Sr. Many of these RTGs are still deployed in the environment and have been targeted by metal thieves or have corroded significantly presenting a radiological hazard [109].

In Western countries there was a dalliance with terrestrial use RTGs in the 1970s with the manufacture and limited distribution of radioisotope powered cardiac pacemakers. The first such pacemaker (manufactured by Alcatel and Medtronic Corporations) was implanted in a human body in France on 27/04/1970 and used $^{238}$Pu as its source of fuel [110]. The use of radioisotopic pacemakers failed to become commonplace due, in part, to opposition from patients and surgeons concerned at radioactive exposure. A key benefit is the greatly increased lifetime of the power source compared to the alternative lithium battery powered pacemakers, thus requiring far fewer follow-up operations on patients to replace old pacemakers resulting in extended life-expectancy of the patients [111]. However, the RTG based pacemakers were expensive, required tracking for security reasons and the benefits of modern electronics are now seen as outweighing the risks of additional surgery in order to replace old pacemakers. Figure 3-4 shows the casing of a pacemaker manufactured by ARCO in 1974 that produced 300μW of electrical power from approximately 290GBq of $^{238}$Pu [112].




**Figure 3-4:** $^{238}$Pu RTG pacemaker manufactured by ARCO in 1974 (reproduced from [112])

$^{238}$Pu does not exist in nature and was produced by irradiating $^{237}$Np or $^{241}$Am in nuclear reactors but America (and Russia) decommissioned the reactors it used for this purpose in the late 1980s [113] as a part of Glasnost. Since that time NASA has been relying on dwindling American stockpiles of the radioisotope supplemented by the purchased remains of the Russian stockpile. This has led to fears that the supply of $^{238}$Pu is nearly exhausted and these concerns have prompted the consideration of alternative fuels for RTG power sources. The European Space Agency (ESA) alongside National Nuclear Laboratory (NNL, UK) are investigating the use of $^{241}$Am as a potential alternative fuel, although their research is still at an early stage [114]. An additional consideration of this research is a desire to improve the safety of RTGs by using radioisotopes with a lower neutron dose rate, whilst also potentially increasing the useful lifetime of the power source. For example, a 266g pellet of $^{241}AmO_2$ is modelled to have a neutron dose rate one hundred times lower than that from a 188g pellet of $^{238}PuO_2$ [115]. Earlier this year the Department of Energy (USA)

announced plans to begin trials for limited renewed production of $^{238}Pu$ which may help to alleviate the shortage of this isotope [116].

Recently there has been interest in the possibilities of milliwatt power level RTGs for space application. At smaller sizes and quantities of radioisotope the efficiency and power output are reduced relative to larger RTGs (down to around 5.7% and 426mW theoretically [117]), but the concerns over health and safety of this much radioisotope in one place remain. Additionally, scaling thermal systems down to the micro size, which would be required for a WSN node power source, would result in a dramatic increase in the surface area to volume ratio and consequently to heat losses from the power system.

### 3.4.2 ALTERNATIVE THERMAL RADIOISOTOPIC BATTERIES

Other types of thermal radioisotopic batteries exist, although they have found more limited use than have thermoelectric devices. One alternative which has been investigated recently is the advanced Stirling radioisotope generator which was designed and manufactured by Lockheed Martin under contract to the US Department of Energy in 2008 [118]. In this power system the thermal energy generated by the pellets of radioisotope is converted into useful electrical energy by use of a Stirling engine that is shown in Figure 3-5 [119]. The system is undergoing extensive testing at NASA Glenn Research Center (Cleveland, Ohio, USA) [120] with the goal of a conversion efficiency of 40%, which would far exceed the efficiency of RTGs [121].

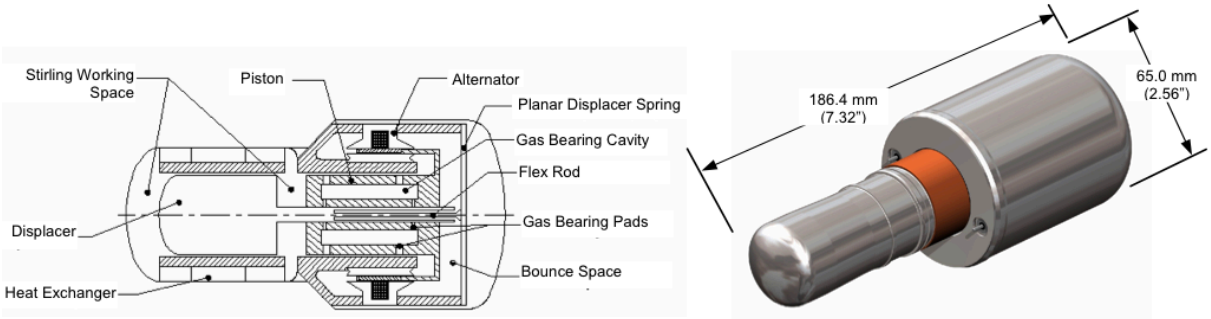



**Figure 3-5:** Schematic of Sunpower 88W advanced Stirling converter for NASA space program (reproduced from [119])

Thermophotovoltaic radioisotopic batteries have lately received much interest from NASA, with contracts awarded to Creare Inc. and Edtek, Inc. to develop efficient power sources which can convert the infrared electromagnetic radiation generated by a radioisotopic source [122]. Lockheed Martin Space Systems Company has produced a system which is ~30% efficient at a temperature of 300K and is described in Figure 3-6. In this system the heat of the radioisotopic source emits electromagnetic radiation that is filtered to only allow infra red wavelength radiation to pass through. This radiation then become incident on a photovoltaic cell which has been optimized for electricity generation from radiation in this part of the spectrum. Much development work is still required with the largest obstacle to be overcome being the degraded photovoltaic cell efficiencies encountered at higher temperatures, which will need to be overcome before anticipated operating temperatures of 500K may be achieved.

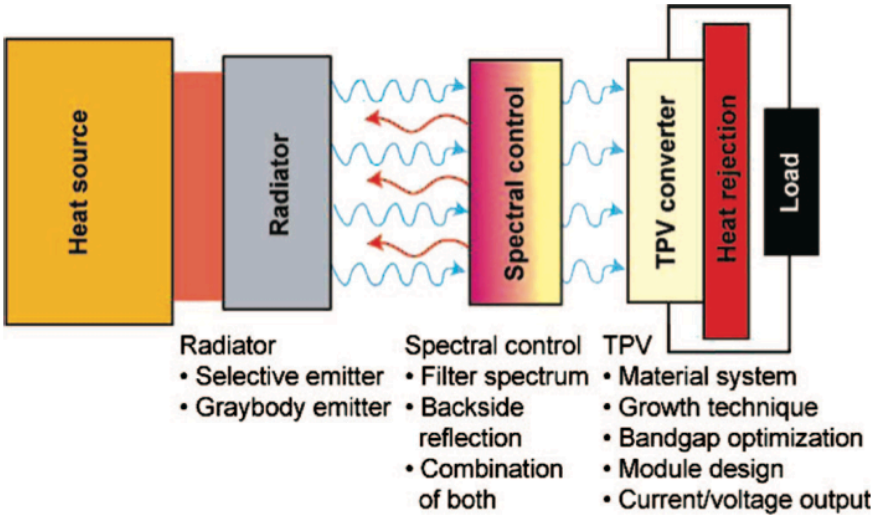



**Figure 3-6:** Process of thermophotovoltaic conversion (reproduced from [123])

Regardless of the promise of improved efficiencies offered by these unconventional thermal batteries the same issues of health and safety and thermal scaling problems remain, suggesting that these types of battery are not well suited to power a WSN node.

## 3.5 NON-THERMAL TYPES OF RADIOISOTOPIC BATTERY

It is possible to convert the energy of radioisotopic decay more directly into electrical energy than through a thermal cycle and there are a number of methods which may be used to accomplish this. The kinetic energy of the decay particle may be converted into electrical energy (such as in a direct conversion type battery) or the charge on decay particles may be collected and turned into useful electrical energy (a direct charge battery). The following section discusses the possible methods of non-thermal radioisotopic energy conversion that exist, along with an appraisal of their suitability to power a WSN node.

### 3.5.1 DIRECT CHARGE

Direct charge radioisotopic batteries (DCRB) are sometimes defined as self-charging capacitors and in their simplest form this is a reasonable description. A radioisotope is coated onto the surface of one of two electrodes facing each other across a controlled distance and the charge on the emitted decay particles (negative for beta decay and positive for alpha decay) is collected directly on the opposite electrode. Figure 3-7 illustrates this principle and also shows the presence of a dielectric between the two electrodes of the battery. The composition of this dielectric is of great importance to the operation of the DCRB since a percentage of the decay particles will be attenuated in air but not be attenuated in a vacuum (for example).

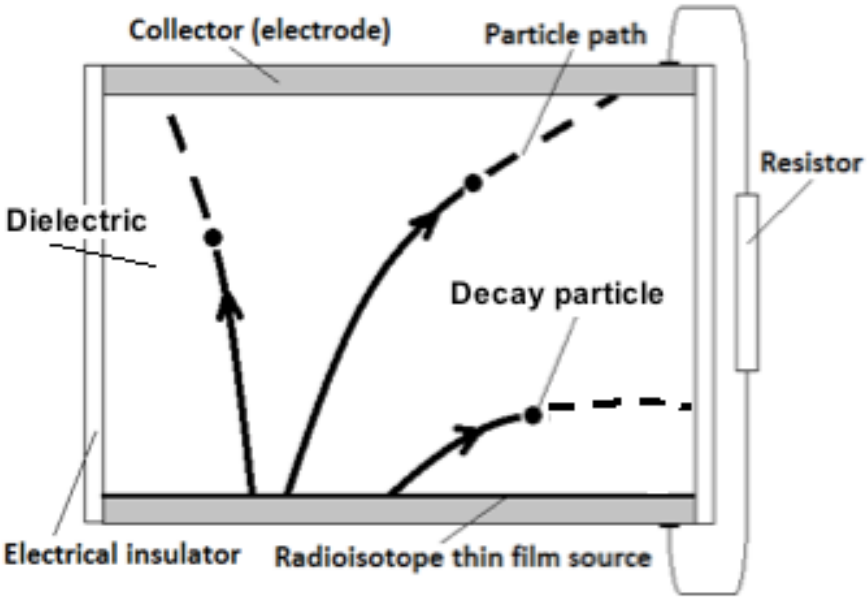



**Figure 3-7:** Schematic of a direct charge radioisotopic battery

Lee et al. (2008) [124] propose a honeycomb structure for DCRBs with thin rods of radioisotope ($^{63}$Ni was considered most suitable) fitted down the middle of each of the hexagonal structures which comprise the honeycomb as can be seen in Figure 3-8. According to their calculations it would be possible to generate a power of

2.3mW at 17.4kV from 5217GBq of $^{63}$Ni in a single cell of this structure with an overall conversion efficiency of 15.8% [124].

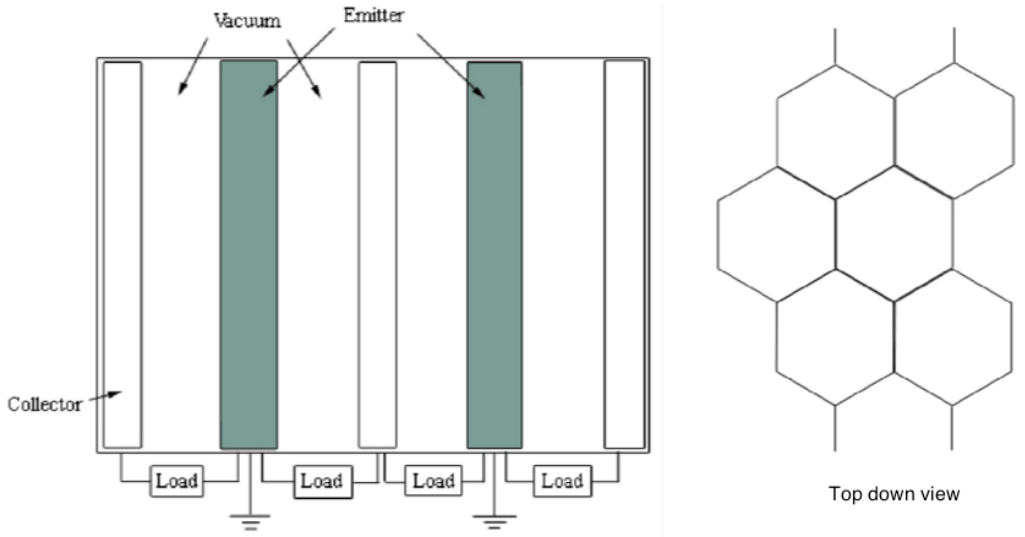



**Figure 3-8:** Honeycomb configuration of proposed direct charge radioisotopic battery (reproduced from [124])

The first radioisotopic battery was a direct charge battery, constructed by Henry Moseley in 1913 and using 0.74GBq of $^{226}$Ra as its radioisotope [75]. This battery generated 380nW at 150kV at an overall conversion efficiency of 0.06% [75]. Since that time many direct charge batteries have been built, using a variety of radioisotopes such as $^{90}$Sr, $^{3}$H, $^{147}$Pm and $^{210}$Po. In 1952 a DCRB was constructed using 9.3GBq of $^{90}$Sr as the radioisotope and having a vacuum dielectric between the electrodes. This battery achieved an overall efficiency of 10.4% and generated 91μW but at a voltage of 365kV [125]. In 1973 Braun et al. tested a DCRB using 180GBq of tritium which produced 480nW at 690V at 0.29% efficiency [126].

Kavetsky et al. experimented with a DCRB in 2009 which used 96GBq of $^{147}$Pm in a 4π structure and generated 140μW at 35kV at overall conversion efficiency of 14% [127]. Yakubova was a contributor to this work and also produced a DCRB using

tritium as its radioisotope that he described in his PhD thesis of 2010 [128]. The tritium based DCRB is shown in Figure 3-9 and contained 4000GBq total activity. An overall efficiency of 5.5% was achieved with this device at a generated power of 200μW at 2.6kV.

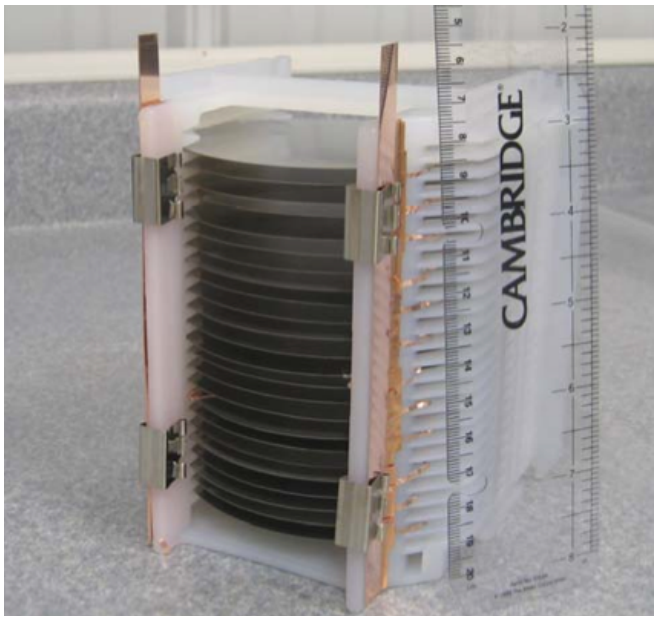



**Figure 3-9:** Direct charge radioisotopic battery containing 24 tritium sources of total 4000GBq activity (reproduced from [128])

A comparison of the direct conversion radioisotopic batteries discussed here is presented in Table 3-2.

**Table 3-2:** Comparison of direct charge radioisotopic battery characteristics

| Radioisotope | Activity (Gbq) | Voltage (V) | Power | Efficiency | Type | Reference | Year |
|---|---|---|---|---|---|---|---|
| | | | | | | | |
| Nickel 63 | 5217 | 17,4kV | 2.3mW | 15.80% | theory | [124] | 2008 |
| Radium 226 | 0.74 | 150kV | 380nW | 0.06% | practical | [75] | 1913 |
| Strontium 90 | 9.3 | 365kV | 91μW | 10.40% | practical | [125] | 1952 |
| Tritium | 180 | 690V | 480nW | 0.29% | practical | [126] | 1973 |
| Promethium 147 | 96 | 35kV | 140μW | 14.00% | practical | [127] | 2009 |
| Tritium | 4000 | 2.6kV | 200μW | 5.50% | practical | [128] | 2010 |

It seems clear from reviewing the experimental record that high conversion efficiencies with DCRBs may only be obtained at high output voltages. The high voltages (often in the range of kV) present a significant problem in the usefulness of this class of radioisotopic battery. Most electronics operate at or below 3.3V and therefore the output of this type of battery would require voltage conversion down to this value. Even though there are several methods to achieve voltage conversion (known as step down when the voltage is reduced) none is suitable to such high input voltages. Voltage rectifiers effectively burn all of the voltage above the desired level, which would result in a huge waste with such a high input voltage and hence a dramatic reduction in overall efficiency. Buck converters can operate at efficiencies as high as 90%, however, in this class of converter a 50V input voltage is considered high and their efficiencies drop off considerably at lower currents. At the ultra low currents achieved by DCRBs buck converters will not output any usable power (the LM5019 from Texas Instruments Incorporated is capable of accepting an input as high as 100V but has an operating current of 1.9mA at this voltage) [129]. Meanwhile DC-DC converters are capable of converting voltages as high as 1000V though they are expensive and have quiescent currents of 20μA or more (which is the current consumed by the device itself when connected to the source of power).

### 3.5.2 MECHANICAL AND DIRECT CHARGE

An alternative approach to DCRBs has been taken by Lal et al. (2005) [97] who have developed a hybrid power source utilizing a DCRB attached to an oscillating cantilever with a piezoelectric plate overlaid along its length as shown in Figure 3-10.

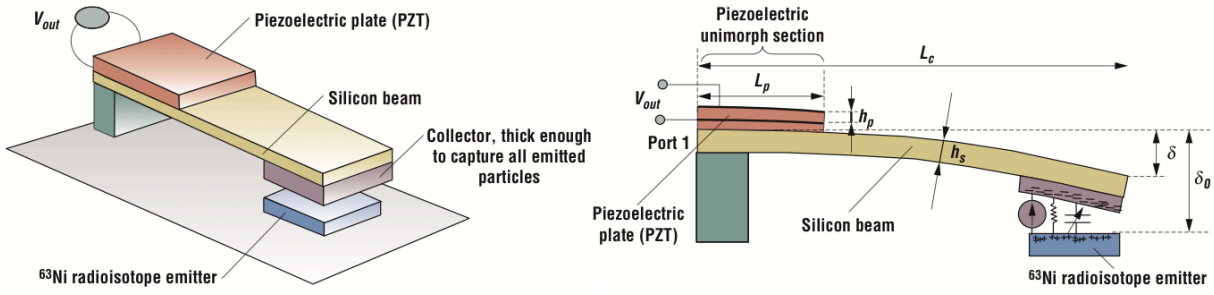



**Figure 3-10:** Oscillating cantilever based direct charge radioisotopic battery (reproduced from [97])

The DCRB aspect of this power source operates in the same manner as described previously but the collector electrode is attached to a cantilever beam which is drawn towards the radioisotopic source over time due to attracting charges accumulated on the two components. Eventually the radioisotopic source and the collecting electrode become close enough for a discharge to occur between them and the cantilever springs back and oscillates generating current in the overlaid piezoelectric plate. This process then begins again, and is illustrated in **Figure 3-11**.

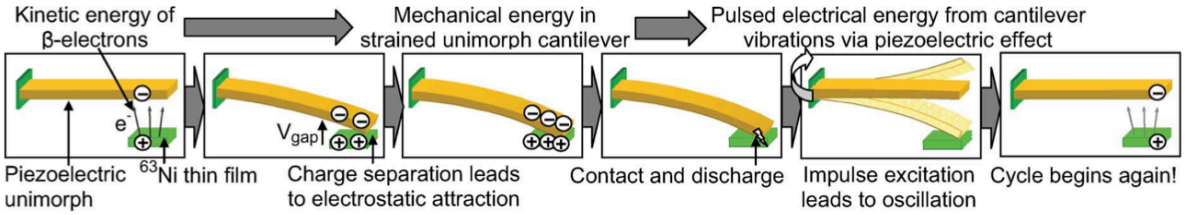



**Figure 3-11:** Energy cycle of the oscillating direct charge radioisotopic battery (reproduced from [130])

Using a 0.333GBq thin-film of $^{63}$Ni a continuous DCRB power output of 10-*22nW* was generated along with 750μW generated in pulses from the piezoelectric plate at a duty cycle of 0.07%. Combining the power output of the DCRB with the pulsed power output of the piezoelectric plate gives a total energy conversion efficiency of 5.1% [131]. However the power generated by the DCRB aspect of this device is produced at up to 7kV while the power generated in the piezoelectric plate is at less than 2V

after rectification. The issue of voltage step-down for the DCRB generated power remains a serious concern along with potential problems regarding the useful lifetime of a device in which the contacts to the piezoelectric plate will be continuously cycled every 20 minutes.

### 3.5.3 DIRECT CONVERSION

Direct conversion batteries function by converting the kinetic energy of radioactive decay particles into electrical energy within a semi-conductor or p-n junction (sometimes known as a photovoltaic (PV) cell) as shown in Figure 3-12.

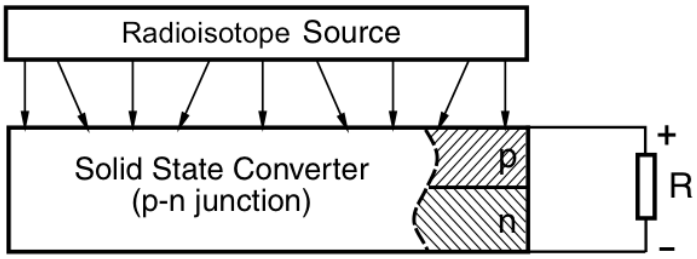



**Figure 3-12:** Schematic of direct conversion radioisotopic battery (reproduced from [132])

Unlike the photovoltaic effect where each photon may generate at most one electron-hole pair in the depletion region of the p-n junction [133], in direct conversion batteries the decay particles may generate many thousands of electron-hole pairs each, dependent on the starting energy of the particle and on the depth of the junction. The phenomenon of electron-hole generation in direct collection batteries is illustrated in Figure 3-13.

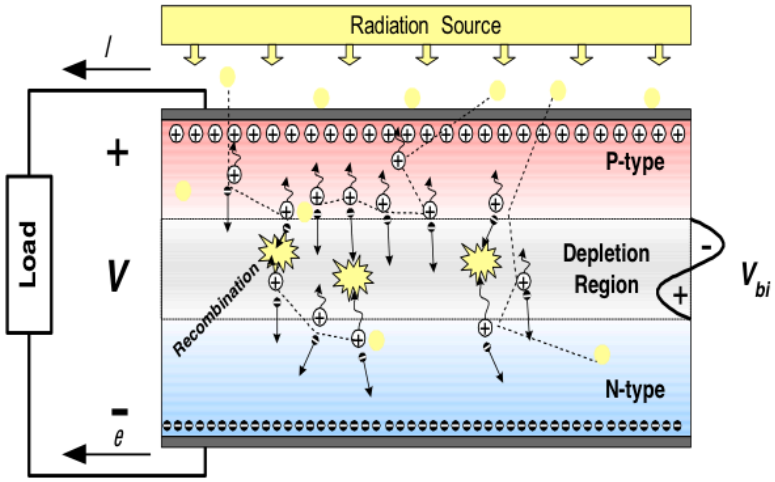



**Figure 3-13:** Operating principle of a direct conversion radioisotopic battery (reproduced from [134])

The number of electron-holes which may be generated by each incident decay particle may be calculated by dividing the average energy of the decay particle by the energy required to form an electron-hole pair in the depletion region. The energy required to form an electron-hole pair ($E_{eh}$) varies depending on the bandgap of the p-n junction and may be approximated in silicon by Equation (3-5) [135] where $E_g$ is the bandgap of the p-n junction in eV.

$$E_{eh} = 2.15.E_g + 1.21 \quad \textbf{(3-5)}$$

The interaction between decay particles and a p-n junction has been modelled using Monte Carlo programs in order to better understand this type of device [136]. Tang et al. (2012) modelled the interaction of $^{63}$Ni with an Si p-n junction and found that a 4.94% conversion efficiency was theoretically possible [137].

Also known as betavoltaics or electron-voltaics the principle of direct conversion batteries was first experimentally explored at the RCA Laboratories, USA (now part of SRI International, California, USA) in the 1950s [138]. In 1954 Rappaport (working

at RCA Laboratories) constructed and tested a direct conversion battery using 1.85GBq of $^{90}Sr$ and a silicon p-n junction. 800nW of electrical power was measured to have been generated at peak power giving an overall efficiency of 0.4% according to Rappaport (which has been misquoted in a number of other papers as 0.2%). Rappaport states in his paper that $^{90}Sr$ (along with its daughter product $^{90}Y$, which also emits beta particles with a half-life of 60hrs) has an average energy of decay of 0.7MeV which is incorrect. In fact the average energy of decay of $^{90}Sr$ is 0.195MeV and of $^{90}Y$ is 0.935MeV [92]. Using these values for the average energy gives an overall efficiency for his experiment of 0.24%.

In 1964 Flicker et al. [139] constructed and tested a direct conversion battery using 251.6GBq of $^{147}Pm$ emitting into a silicon p-n junction which produced 9.1μW at 0.2V and 0.77% overall conversion efficiency. A diagram of this power source is shown in Figure 3-14.

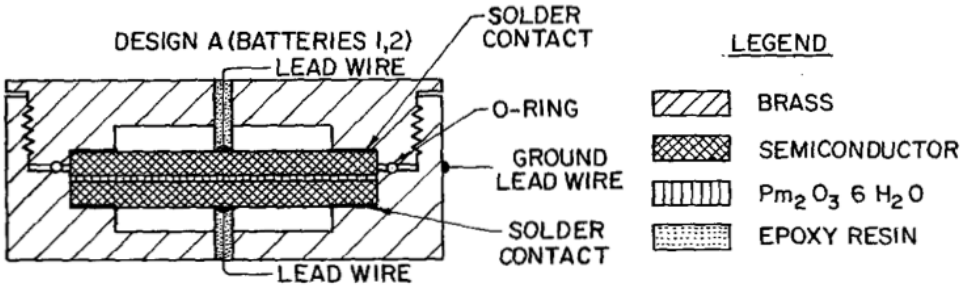



**Figure 3-14:** Pm indirect conversion battery design from 1964 (reproduced from [139])

The Donald W. Douglas Laboratories, USA conducted extensive testing of direct conversion batteries between 1968 and 1974 led by Olsen [140]. They successfully commercialized their batteries for a brief time, representing the only (to date) commercially available (non-thermal) radioisotopic batteries. These batteries, known

as “Betacel”, were used in more than 100 pacemakers which were fitted into patients. The Betacel-400 (shown in Figure 3-15) contained 2442GBq of $^{147}Pm$ and generated 400μW at 4V at beginning of life with a 1.7% conversion efficiency [140]. The development of lithium batteries at around this time led pacemaker manufacturers to abandon the Betacel in favour of the non-radioisotopic power sources.

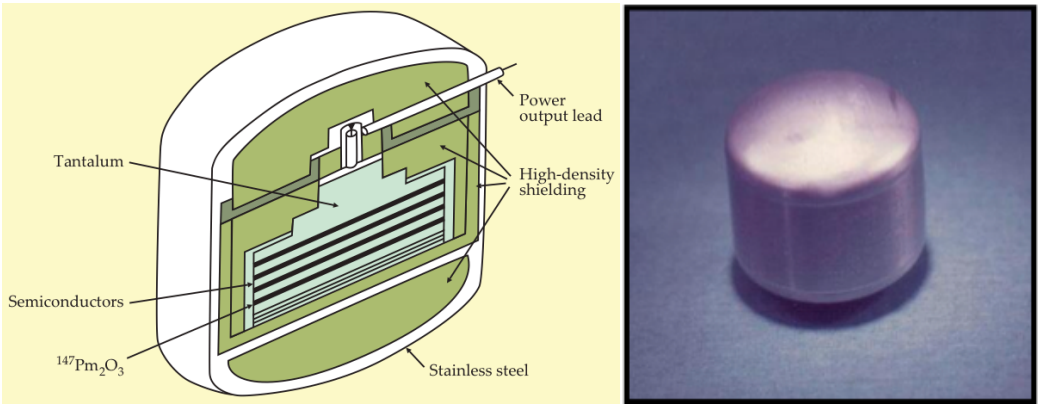



**Figure 3-15:** The Betacel-400 battery used in pacemakers during the 1970s (reproduced from [141, 142])

Many direct conversion batteries have been constructed, most using $^{147}Pm$ [139], $^{63}Ni$ [143], or $^{3}H$ [144] as the radioisotope. A variety of p-n junctions have been experimentally matched to these sources, including Si [145], a-Si [146], GaN [147], SiC [148] and AlGaAs [149]. The efficiencies of these batteries have not tended to exceed 2% except on rare occasions. In 2000 Deus pumped $^{3}H$ gas at a pressure of 90,000Pa into a canister with an amorphous silicon (a-Si) p-n junction inside of it and achieved an initial conversion efficiency of 1.2% at 0.3V [1]. An AlGaAs p-n junction was exposed in the same manner and achieved an initial conversion efficiency of 2.3% at 0.35V. In both cases the experiment was conducted over a 46 day period during which the p-n junctions were continuously exposed to the pressurized $^{3}H$ gas. After 46 days the efficiency of the a-Si p-n junction had fallen to 0.07% while the

AlGaAs p-n junction was producing electrical energy at a conversion efficiency of 0.71%. These dramatic decreases in performance of the p-n junctions are due to radiation damage to the junction and are a major drawback of this design.

A number of companies have been formed recently (mostly start-ups from Universities) which claim to sell direct conversion radioisotopic batteries, although it is not clear that these devices are in fact for sale. City Labs, inc. [150] (Florida, USA) have a license to sell their $^{3}H$ based betavoltaic battery within the USA and according to some reports [151, 152] have begun to do so at the of time of writing, 2013 (nominally for around US$1000 per unit [153]). One such battery is the P100 NanoTritium$^{TM}$ device shown in Figure 3-16 and uses 8.3GBq of $^{3}H$ to generate 75nW at beginning of life (at 0.7V) dropping to 24.3nW after 20 years [154]. Widetronix Inc., Ithika, New York (linked to Cornell University, USA) is another company which claims to be selling direct conversion radioisotopic batteries. Two such types of batteries are described on their website, one using $^{3}H$ and the other $^{63}Ni$ [155]. The batteries are described as generating between 10nW and 1μW using a SiC p-n junction, although it is unknown at what activities of radioisotopes these electrical powers are obtained.




**Figure 3-16:** NanoTritium$^{TM}$ P100 battery sold by City Labs, inc. (reproduced from [156])

A comparison of the direct conversion radioisotopic batteries discussed here is presented in Table 3-3.

**Table 3-3:** Comparison of direct conversion radioisotopic battery characteristics

| PV cell | Radioisotope | Activity (GBq) | Voltage (V) | Power | Efficiency | Type | Reference |
|---|---|---|---|---|---|---|---|
| | | | | | | | |
| **Silicon** | Nickel 63 | - | 0.23V | 99.85nW | 4.94% | theory | [137] |
| **Silicon** | Strontium 90 | 1.85 | - | 800nW | 0.24% | practical | [138] |
| **Silicon** | Promethium 147 | 251.6 | 0.2V | 9.1uW | 0.77% | practical | [139] |
| **Silicon** | Promethium 147 | 2442 | 4V | 400µW | 1.70% | practical | [140] |
| **a-Si** | Tritium | - | 0.3V | 129nW | 1.20% | practical | [1] |
| **AlGaAs** | Tritium | - | 0.35V | 77.8nW | 2.30% | practical | [1] |
| **SiC** | Phosphorous 33 | 8.5 | 1.6V | 580nW | 4.50% | practical | [148] |

The generated efficiencies of this class of battery are lower than the efficiencies found with direct charge batteries, however in this type of battery the voltages at which the maximum powers are generated are in a more useful range. The use of PV cells based on AlGaAs and SiC has resulted in increased efficiencies. The development of various commercial ventures with this class of battery suggests that there is renewed promise in this field. However, the key drawback of radiation damage to the p-n junction through long-term exposure to the radioisotope remains a limiting factor on the effective lifetime of this type of device. The damage observed by Deus was generated by Beta decay particles from $^{3}H$, which are the weakest and least damaging decay particles available. In order to generate increased power outputs more powerful radioisotopes have been utilized and these will damage the p-n junction even more rapidly, particularly if the decay particles are alphas. In order to attempt to mitigate this effect some researchers have attempted to use radiation

hard p-n junctions such as GaN, although even with this construction the useful lifetime of the battery was shown to have been reduced by a factor of 5 [157].

### 3.5.4 INDIRECT CONVERSION

Indirect conversion radioisotopic batteries function in much the same manner as direct conversion radioisotopic batteries described in Section 3.5.3, with the difference that a scintillating medium is introduced between the radioisotope and the photovoltaic converter. The scintillator (often a phosphor layer) generates photons when bombarded by sufficiently energetic particles (such as the particles of decay) and this light is then converted into electricity within the photovoltaic cell. In this manner the photovoltaic cell is protected from radiation damage, although the phosphor will itself degrade over time through exposure to the radioisotope at a slower rate, which will be discussed in more detail in Section 5.4.

A number of different configurations have been proposed for this type of battery as demonstrated in Figure 3-17 which are in the form of; Figure 3-17(a) a mixture of radioisotope and phosphor between photovoltaic cells [158]; Figure 3-17(b) sealed glass spheres coated internally with a thin layer of phosphor and filled with radioisotopic gas and all positioned on a photovoltaic cell [159]; Figure 3-17(c) sealed glass tubes filled with tritium gas and internally coated with a thin layer of a phosphor and all situated between two photovoltaic cells [160]; and Figure 3-17(d) photovoltaic cells surrounding an aerogel containing both a radioisotope and a phosphor [158].

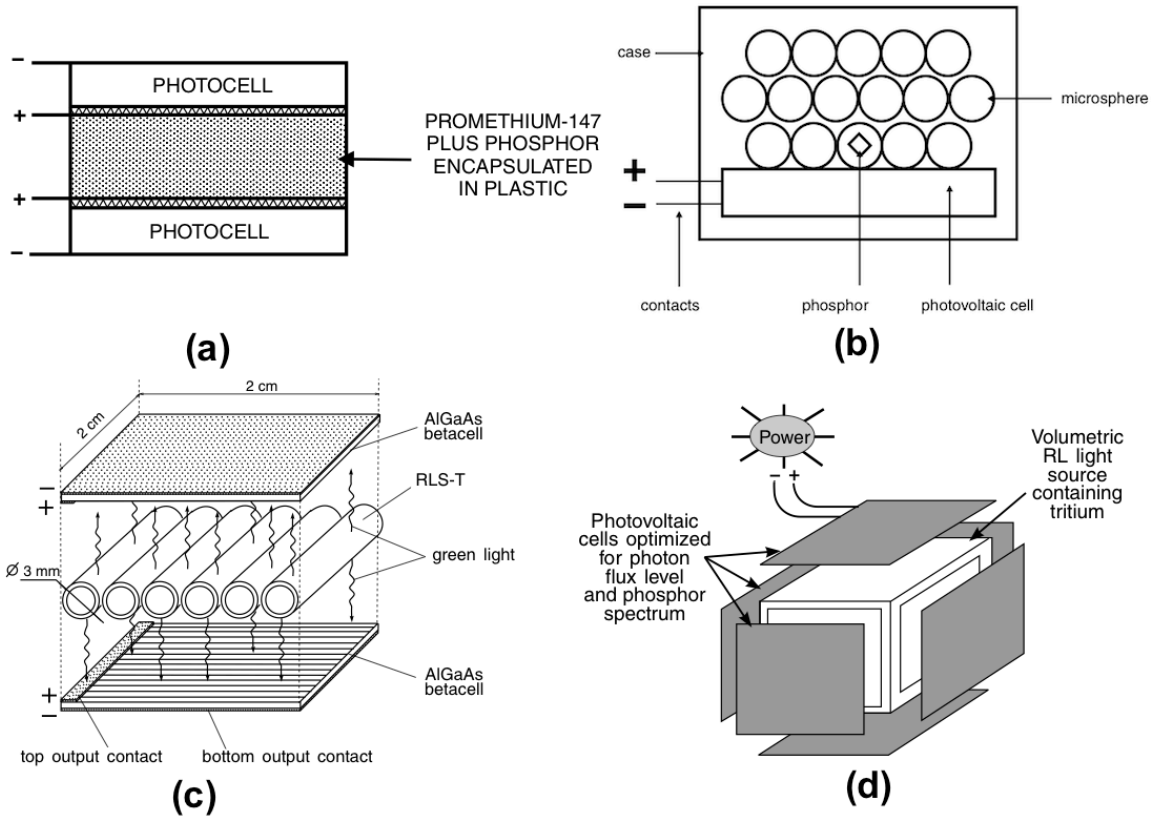



**Figure 3-17:** Four configurations of indirect conversion radioisotopic battery, (a) PV cells surrounding a polymer containing phosphor and radioisotope, (b) spheres on a PV cell, (c) sandwich formation, (d) aerogel surrounded by PV cells (reproduced from [158-160])

A number of practical batteries based on some of the configurations in Figure 3-17 have been constructed with experimental investigation of their characteristics reported in the literature which will now be discussed.

In 1957 the Walter Kidde Nuclear Laboratories and Elgin National Watch company (both USA) jointly developed what has become known as the Elgin-Kidde battery [161], shown in Figure 3-18. This nuclear battery utilised a $^{147}$Pm source of *166.5GBq* to excite a Cadmium sulphide phosphor with which it is mixed, and then a silicon photovoltaic cell to convert the generated light into electricity at a maximum power of *20μW*. This battery was never commercialised due to a combination of the low half-

life of the $^{147}Pm$ source (2.62 years) and of the far higher power demands of electrical components at that time.

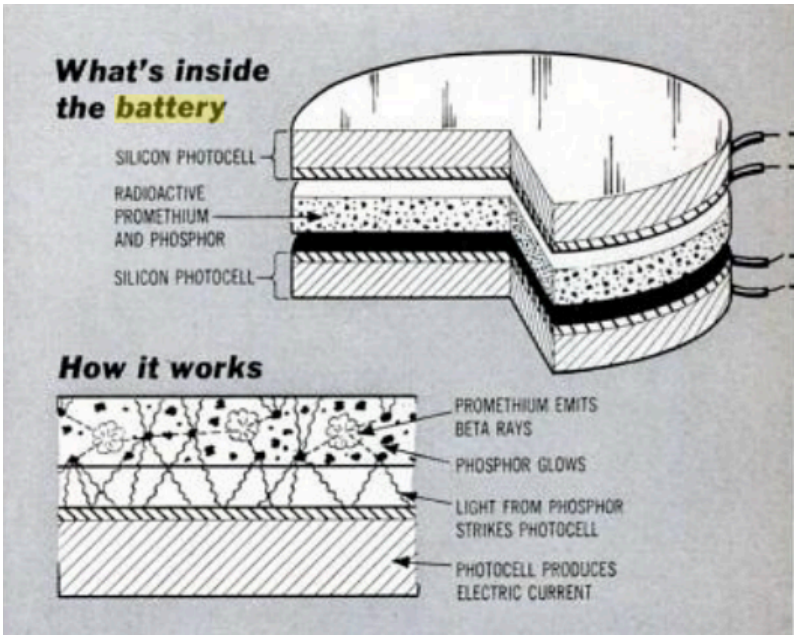



**Figure 3-18:** Elgin-Kidde indirect conversion radioisotopic battery schematic (reproduced from [161])

Deus (2000) used an amorphous silicon photovoltaic device converting the light generated by $^{3}H$ decay incident on a ZnS phosphor coated on a glass sheet and produced a peak power of 2.57nW (at 0.2393V and 10.74nA) [1]. 24.2GBq of tritium was used in this experiment and the phosphor coated glass sheet had an area of 65mmX18mm while the a-Si photovoltaic to which this glass sheet was aligned only had an area of 80mm$^2$. Clearly this disparity in surface areas calls into question the precise power flux of light which was incident on the photovoltaic cell, although it was claimed that the green light emitted carried a luminescence intensity of 66mcd/m$^2$ and that the overall efficiency of the device was only 0.17%.

Another experiment conducted in 2000 used two green gaseous tritium light sources (GTLSs – see Section 3.6) of dimension 5mmØX8mm each, set against two

$Al_{0.32}Ga_{0.68}As$ photovoltaic cells with a surface area of 50mm$^2$ each and generated a peak power of 74nW [149]. The voltage at which this peak power was generated is not known, though the $V_{OC}$ was only 0.78V which must be higher than the operating voltage and it would therefore be necessary to either use a voltage step up or to combine a number of these devices in series in order to generate a useable voltage.

Sychov et al. (2007) experimented using a solid mass of $^{238}Pu$ as the radioisotope, which generated highly energetic alpha particles as a product of its decay [162]. Using $Al_xGa_{1-x}As$/GaAs photovoltaic cells of surface area 25mmX60mm, glass slides coated with phosphor (ZnS) were placed against 11.1GBq of $^{238}Pu$. A thin reflective layer of aluminium (Al) or gold (Au) was inserted between the radioisotope and the phosphor screen, resulting in increased electrical power generation in the photovoltaic due to reflected light from the phosphor layer becoming incident on the photovoltaic cell (measured power results are presented in Figure 3-19). In this way an electrical output of 10μW peak power at 0.75V was produced at a low 0.11% overall conversion efficiency. The peak power of this battery is high, although at a relatively low voltage and a low efficiency.

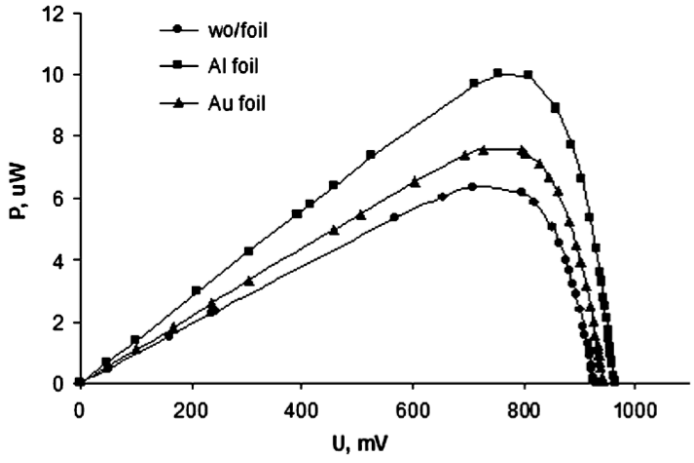



**Figure 3-19:** Alpha powered indirect conversion battery power curves relative to voltage (U) with and without (wo) reflective foils. (reproduced from [162])

The $^{238}$Pu alpha particle indirect conversion batteries were demonstrated to provide sufficient power to run a calculator. The higher energies and masses (relative to beta decay) of the alpha particles induced accelerated damage to the phosphor and after only 17 days the radioluminescent intensity from the most radiation hard phosphor was found to be 19% lower than initially measured. For this reason alpha emitters are not suitable for long lifetime indirect conversion batteries.

Andreev (2002) experimented using GTLSs of green (most common wavelength 510nm) and yellow (most common wavelength 570nm) illuminating AlGaAs photovoltaic cells [163]. The current and voltage of the photovoltaic cells under illumination were measured and formed into current/voltage (I-V) curves with power/voltage (P-V) curves extrapolated from this data. Six batteries were constructed and tested in this manner with the results of the most powerful test displayed in Figure 3-20 where the peak power generated was found to be 234nW at 1.2V. The photovoltaic cells used in this battery had a surface area of 692mm$^2$ and an activity of 48.84GBq of tritium was estimated to be in the 8 GTLSs (of dimensions 30mm length by 3mm diameter). This battery operated at an overall conversion efficiency of 0.525% which is far higher than the efficiencies described here by other experimental investigations.

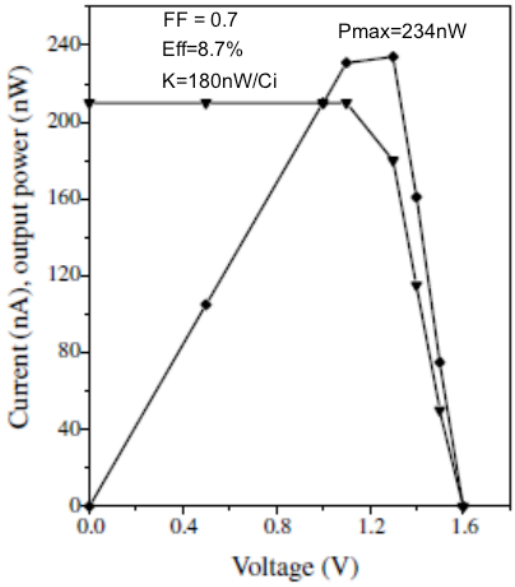



**Figure 3-20:** Current/voltage and power/voltage curves measured for AlGaAs photovoltaic cells illuminated by green GTLSs of total activity 48.84GBq (reproduced from [163])

Indirect conversion radioisotopic batteries have been theoretically modelled in a number of configurations. The University of Florida has used the Monte Carlo method in a Monte Carlo Nuclear Program (MCNP) to model the performance of this class of battery [164]. The model utilised a 0.5μm thick solid layer of $^{63}$Ni surrounded on both surfaces with a ZnS based phosphor and surrounded by monocrystalline silicon photovoltaic cells or AlAs photovoltaic cells as illustrated in Figure 3-21. Utilising silicon photovoltaic cells a conversion efficiency of 1.53% was calculated while for AlAs photovoltaic cells the conversion efficiency was modelled to be 2.98%. The modelled battery was estimated to generate 0.92nW at the beginning of life. Experiments into the radiation hardness of monocrystalline silicon photovoltaic cells suggested that after the equivalent of 12 months of radiation exposure (at the intensity and activity of the $^{63}$Ni source) the photovoltaic power performance had only degraded by 1.2%.

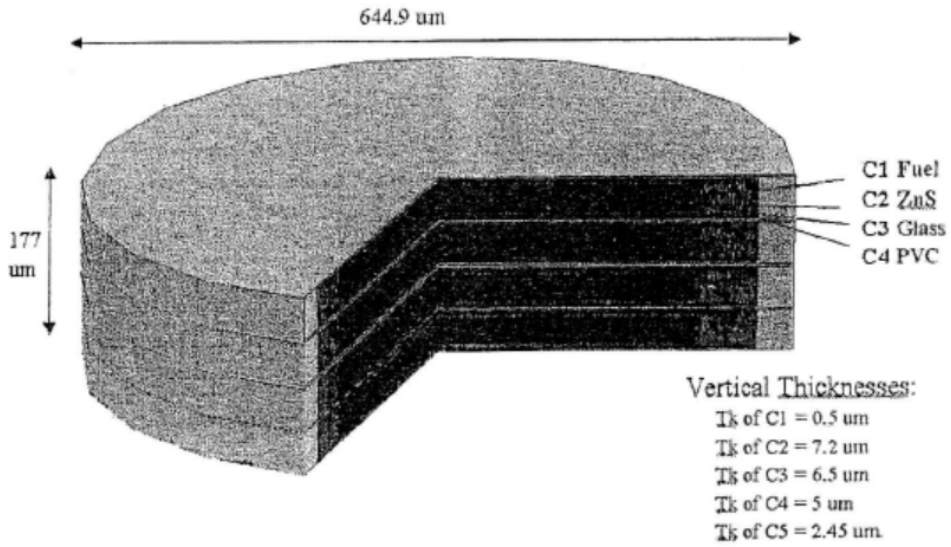



**Figure 3-21:** An indirect conversion radioisotopic battery theoretically modelled using MCNP (reproduced from [164])

Two Aerogel-phosphor composition batteries using a-Si and AlGaAs photovoltaic cells were modelled by Walko et al. in 1990 [132] where the starting assumptions were that the aerogel was saturated with 100% pure tritium gas, that the phosphor did not decay due to radiation damage and that the electrical conversion efficiency of the aSi photovoltaic cells was 12.5% and 22% for the AlGaAs photovoltaic cells. Using these starting assumptions and activities of tritium of *214,600GBq* (with a-Si photovoltaics) and 118,400GBq (with AlGaAs photovoltaics) electrical powers of 2mW were estimated at overall conversion efficiencies of 1% and 1.8% respectively. The radiated light intensity from the saturated aerogel-phosphor was estimated to be 22.8μW/cm$^2$ at the beginning of life, compared with the maximum radiated light intensity from a GTLS of only 2.3μW/cm$^2$.

Aerogel-phosphor configuration radioisotopic batteries present an impressive option as a power source from the theoretical analysis of Walko et al. [132]. However, the high power of 2mW was estimated with a very high concentration of tritium and furthermore the radiated light intensity of this system is highly unstable. According to

Renschler et al. the light intensity reduces after 250 days to only 10% of its starting value [165], which would reduce the radiated light intensity to the same range as that generated by a GTLS. The accelerated nature of the reduction in light intensity suggests that this configuration of indirect radioisotopic battery may not be suited to providing a long life source of power.

A comparison of the various battery designs described here for ICRBs is shown in Table 3-4.

**Table 3-4:** Comparison of indirect conversion radioisotopic battery characteristics

| Battery type | PV cell | Radioisotope | Activity (GBq) | Voltage (V) | Power | Efficiency | Type | Reference |
|---|---|---|---|---|---|---|---|---|
| | | | | | | | | |
| AeroGel | a-Si | Tritium | 214,600 | - | 2mW | 1.00% | theory | [158] |
| AeroGel | AlGaAs | Tritium | 118,400 | - | 2mW | 1.80% | theory | [158] |
| Thin film | m-Si | Nickel 63 | - | - | 0.92nW | 1.53% | theory | [164] |
| Polymer | Si | Promethium 147 | 166.5 | - | 20µW | - | practical | [161] |
| GTLS | a-Si | Tritium | 24.2 | 0.24V | 2.57nW | 0.17% | practical | [1] |
| GTLS | AlGaAs | Tritium | 8.2 | >0.78V | 74nW | 0.98% | practical | [149] |
| Thin film | AlGaAs/GaAs | Plutonium 238 | 11.1 | 0.75V | 10µW | 0.11% | practical | [162] |
| GTLS | AlGaAs | Tritium | 48.84 | 1.2V | 234nW | 0.53% | practical | [163] |

Practically achieved efficiencies of ICRBs range between 0.1% and 1% with the construction type of the battery, the radioisotope used and the PV cell used all contributing to the variance in efficiency of the devices. The overall efficiency of practical indirect conversion batteries generally does not exceed 0.5% (except in one reported case), which is around half the efficiency of direct conversion batteries and is a consequence of introducing an additional energy transformation stage. Although the initial efficiency may be lower, the long term stability of this type of device is far greater than direct conversion batteries due to shielding the p-n junction from radiation damage with the phosphor layer. The phosphor does suffer radiation

damage itself but this reduces the useful lifetime of the battery by a factor of 2 instead of at least a factor of 5 as shown with direct radiation damage of the p-n junction.

## 3.6 GASEOUS TRITIUM LIGHT SOURCES

Gaseous tritium light sources are a self-powered light source which uses the kinetic energy from beta particle decay from $^{3}H$ gas as a long life fuel. GTLSs are sold in the UK as a component part of some emergency exit signs [166], as fishing lights, in watches and in gun sights (as shown in Figure 3-22).

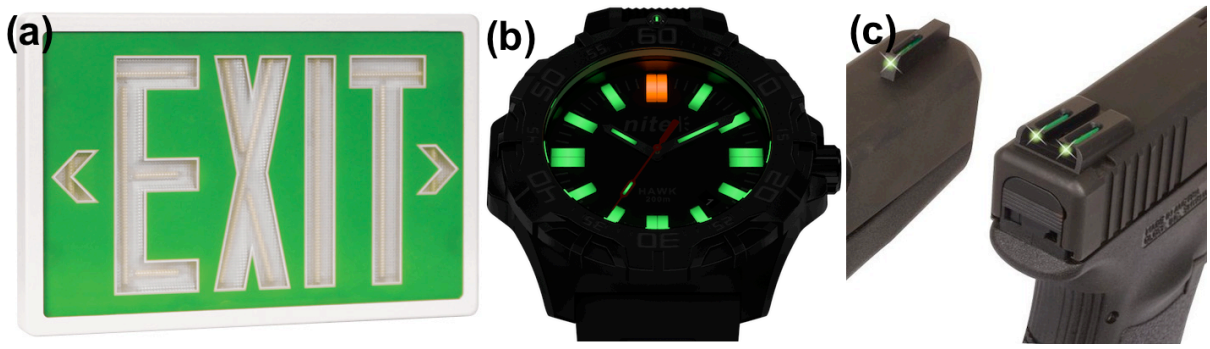



**Figure 3-22:** Examples of commercial GTLS usage: (a) a self-luminous exit sign, (b) a “glow in the dark” watch and (c) gun sights (reproduced from [167-169])

GTLSs are manufactured in a wide variety of shapes and sizes as shown in Figure 3-23 (dependent only on the ability to form the glass container) and radiate light in a range of colours which are achieved through the use of different phosphors on the GTLS inner surface.

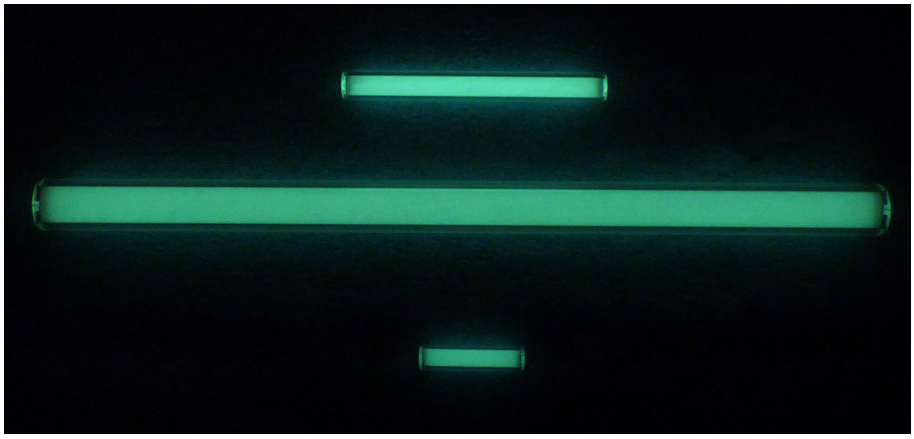


**Figure 3-23:** GTLSs radiating light predominantly in the green spectrum of various sizes

A GTLS is typically composed of a borosilicate glass tube which is coated on its inner surface with a phosphor and filled with pressurized $^{3}H$ gas before having both ends sealed shut with a $CO_2$ laser. The pressure of gas in the glass tube does typically not exceed 250,000Pa [170]. Phosphors are scintillators which generate photons when excited by energetic bombardment from particles such as alphas and betas. GTLSs give off very low intensity light but will continue to do so (at a reducing rate) for more than 20 years.

Radioisotope usage in the UK is covered by the Environmental Protection, England and Wales: The Environmental Permitting (England and Wales) (Amendment) Regulations 2011 (No. 2043), in which gaseous $^{3}H$ in sealed containers is restricted by Part 7 “Radioactive substances activity exemptions” Section 1, General – Interpretation [171]. According to these regulations a device containing sealed containers of gaseous $^{3}H$ may contain up to 80GBq of $^{3}H$ in each container for a total in the entire device not to exceed 1000GBq of $^{3}H$. GTLSs have been manufactured and sold to the general public for many decades now (radioluminescent lights for more than 50 years) with a very good safety record. While breakages of these

devices do occur and members of the public are then exposed to $^{3}H$ gas the consequences of this exposure have not to date been serious [172].

## 3.7 CHOICE OF RADIOISOTOPIC BATTERY TYPE

Thermal cycle radioisotopic batteries are not suitable for micro-systems due to the issue of thermal sealing which leads to increased relative energy losses at that scale. In addition, this class of battery requires a concentrated mass of a radioisotope which may present both health and security issues and as such is not suitable for use in a terrestrial use battery.

Of the non-thermal radioisotopic batteries the direct charge type are the most efficient although at very high generated voltages (>10kV). These elevated voltages present a serious challenge to their use as a power source and have prevented their application up to now. Until a method of efficiently and cheaply converting such high voltages down to 3.3V is developed then this class of battery will likely remain a curiosity.

Direct charge batteries based on a cantilever and utilising a piezoelectric generator are a very innovative idea and offer the possibility of even higher efficiencies than have been achieved with straight direct charge devices. Unfortunately, this type of device still presents the issues of very high generated voltage alongside the potential problems associated with moving parts in any system. While the cantilever itself may be constructed from a single crystal of silicon and as such have a nearly infinite cycle life the contacts attached to the piezoelectric generator will be cycled and will limit the useful lifetime of the overall device.

Batteries using the direct conversion principle have achieved limited commercialisation to date. This suggests that the principle may be worth pursuing as a power source, although there is a serious issue with the lifetime of these devices. The damage caused to the PV cell in these batteries due to direct exposure to the radioisotope significantly reduces their useful lifetime. Using radiation hard PV cell has reduced the speed at which the damage occurs, though the lifetime of the battery is still reduced.

The class of battery known as indirect conversion has the lowest overall practically achieved efficiency of the non-thermal types of radioisotopic battery. However, it does not generate unusably high voltages and does not suffer from radiation damage of the p-n junction. Damage does occur to the phosphor through exposure to a radioisotope, but at a far slower rate than the damage that occurs in direct conversion batteries. For this reason, the efficiency of the indirect conversion type of battery will reduce far less swiftly than that of the direct conversion battery and therefore the average efficiency of the device over its lifetime will be far higher. According to Steinfelds et al. [164] this class of battery should theoretically be able to reach 3% efficiency. Since there has been relatively little research conducted into this class of battery it may be that there are efficiency gains yet to be made in this class of device.

Following this review of potential radioisotopic power sources, it was decided to pursue research into indirect conversion radioisotopic batteries further. $^{3}H$ has been identified as the most suitable radioisotope to use due to its reasonable half-life and the low energy of its beta decay. The $^{3}H$ used will be contained in the form of

gaseous tritium light sources (GTLSs) due to the regulatory framework already existing for these devices in the UK and their inherent safety and stability. The areas of particular interest which have been identified where potential gains may be achieved are in the use of different PV cells to those used by Andreev (2002) [163] and the use of alternate reflective materials to surround the device.

## 3.8 THEORETICAL MODELLING OF INDIRECT CONVERSION RADIOISOTOPIC BATTERIES

Indirect conversion radioisotopic batteries have received minimual research interest, with most researchers providing little or no theoretical modelling of their devices. Andreev et al. [149] and Deus [1], for example, did not provide any theoretical analysis at all. Sychov et al. [162] provide a simple analysis of the absorption of alpha particle radiation in a phosphor layer, as shown in Equation (3-6), where $R_x$ is the range of the particle, $A_x$ is the averaged atomic weight of the phosphor, $E_0$ is the initial energy of the alpha particle and $\rho_x$ is the density of the phosphor. From this equation a basic calculation was formed of the percentage of alpha particle energy absorbed in the phosphor and hence the optimum thickness of the phosphor layer.

$$R_x = \frac{10^{-4}\sqrt{A_x E_0^3}}{\rho_x} \quad \textbf{(3-6)}$$

Walko et al. [158] considered the power flux at the surface of a gas of tritium radioisotope and modelled this using an electron/photon transport computer program called TIGER-P. Results of this modelling are shown in Figure 3-24 where it can be seen that increasing the volume of the gas does not result in a linear increase in the

surface power flux of the tritium (due to self-absorption of the tritium beta particles). In this figure the line with squares corresponds to pure tritium at 1atm, the line with crosses to 50% tritium 50% helium at 1.5atm and the line with diamonds to 25% tritium 75% helium at 1.75atm. The equations this model was constructed on are not known. All other aspects of the ICRB were taken as assumptions rather than being modelled, with phosphor conversion efficiency assumed to be 25%, 100% of the light generated incident on the photovoltaic cells and photovoltaic conversion efficiency assumed to be 35% all of which seem optimistic.

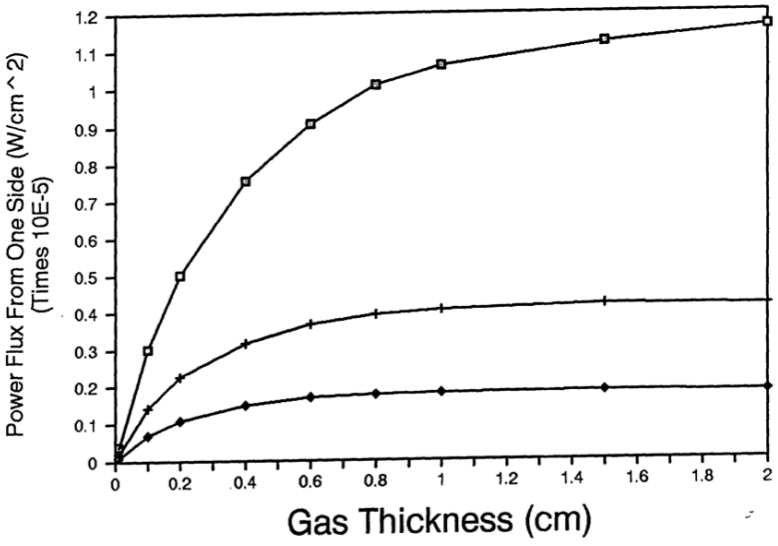



**Figure 3-24:** Computer predicted surface power flux of tritium against gas thickness (reproduced from [158])

The most detailed investigation of the theory behind IRCB operation was conducted by Kavetsky et al. [160] who have modelled the beta particle emission from a radioisotope and have considered the efficiency of photon generation in a phosphor layer. However, even these researchers did not produce a complete model of the processes occurring within an ICRB.

In order to accurately model the overall efficiency of an ICRB it is necessary to consider each stage of energy conversion and transport within the device separately and then combine the results for a complete answer. The energy stages occurring within an ICRB are illustrated in Figure 3-25 and consist of the kinetic energy of radioisotopic decay, generation of light energy in the phosphor, transport of the light within the device, conversion of light into electricity in photovoltaic cells and storage of electrical energy in a capacitor.

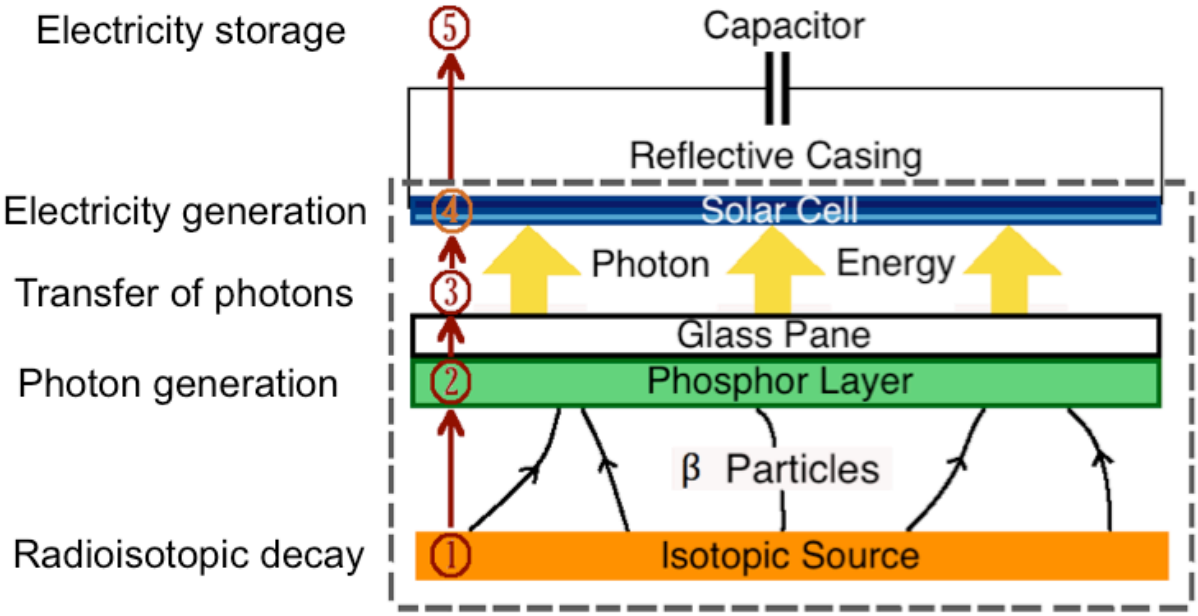



**Figure 3-25:** Energy pathways in an indirect conversion radioisotopic battery

### 3.8.1 First stage: Kinetic energy of radioisotopic decay

The process of radioactive decay generates a beta particle at random within the tritium radioisotope. Decay occurs due to the radioisotope transforming from an unstable isotope into another (potentially more stable) isotope, and in the process emitting energy in the form of a particle or wave. In the case of tritium the decay produces a helium atom, an electron (a beta particle) and a neutrino, as shown in Equation (3-7) where $e$ is an electron and $\overline{\nu_e}$ is an electron antineutrino.

$$^{3}_{1}H \rightarrow {}^{3}_{2}He + e + \overline{\nu}_e \quad \textbf{(3-7)}$$

The helium atom is stable, and the neutrino is neutral and will be ignored from here onwards. The beta particle is negatively charged and carries a kinetic energy that is randomly generated within the range described by Figure 3-26 [173]. The average value of this kinetic energy is $5.7keV$ [174].

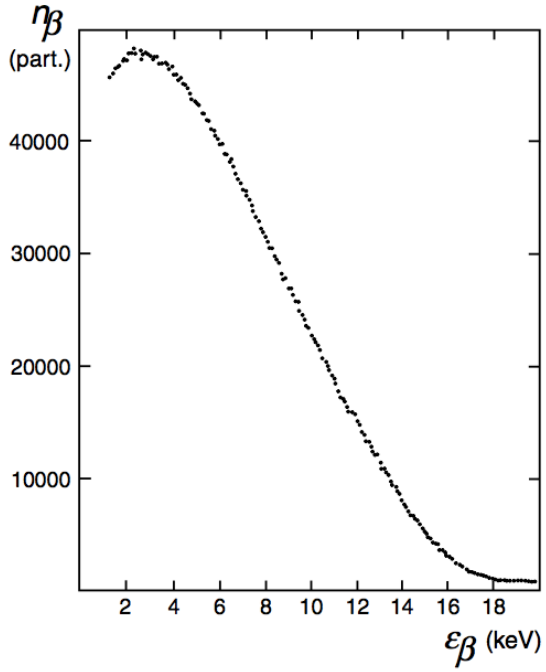



**Figure 3-26:** Energy spectrum of tritium beta decay particles (reproduced from [173])

There are a number of methods which might be employed in order to form a working approximation of this process, such as application of the Spencer-Fano equation; use of partial continuous slowing down approximation (PCSDA); the use of Monte Carlo N-Particle (MCNP) code; and application of the point beta source dose function (PBSDF). The PBSDF, as modelled by Bower et al. [175] is shown in Equations (3-8) and (3-9) where $r_p$ is a distance along the path $\rho$, $b$ is the density of the beta emitter,

$\varphi(r_p)$ is the dose function of the beta emitter, $\varepsilon_{av}$ is the average energy of decay of the emitter (in *keV*), $dP_\beta$ is the power of beta flux, $dS_L$ is unit surface area along the length and $dS_E$ on the end of the cylinder, $D_C$ is the diameter of the cylinder, $R_C$ is the radius of the cylinder, while $L$ is its length, $A_m$ is the specific activity of the beta emitter and $dv$ is an elemental volume of the beta emitter.

$$\frac{dP_\beta}{dS_L} = \frac{3.7X10^{10}.b.A_m}{4\pi}\int_0^{2\pi}\int_0^{\frac{\pi}{2}} cos\theta sin\theta \int_0^{C_1}\left[\varepsilon_{av} - \int_0^{\rho.b} 4\pi r^2.\varphi(r_p)dr_p\right] d\rho d\theta d\emptyset \quad \textbf{(3-8)}$$

where $C_1 = min\left(\frac{L}{2sin\theta cos\emptyset}, \frac{D_C cos\theta}{sin^2\theta sin^2\emptyset + cos^2\theta}\right)$

$$\frac{dP_\beta}{dS_E} = \frac{3.7X10^{10}.b.A_m}{4\pi}\int_0^{\frac{\pi}{2}} cos\theta sin\theta \int_0^{C_2}\left[\varepsilon_{av} - \int_0^{\rho.b} 4\pi {r_p}^2.\varphi(r_p)dr_p\right] d\rho d\theta \quad \textbf{(3-9)}$$

where $C_2 = \frac{L}{cos\theta}$ if $0 \le \theta \le arccos\left(\frac{L}{\sqrt{R_C^2+L^2}}\right)$ or $C_2 = \frac{R_c}{sin\theta}$ if $arccos\left(\frac{L}{\sqrt{R_C^2+L^2}}\right) < \theta \le \frac{\pi}{2}$

The dose function of the beta emitter ($\varphi(r_p)$) describes the variable energy loss along path $\rho$ as a beta particle moves from its point of emission to the surface of the beta emitter. The dose function may be approximated by a number of forms, however the most suitable for tritium gas is shown in Equation (3-10) [176], where $W_0$ is the stopping power of the beta particle emitting material in *keVcm²/mg*, and $v'$ is the absorption coefficient in *cm²/mg*.

$$\varphi(r_p) = \frac{1}{\pi \boldsymbol{r_p^2}}\left[0.25W_0 e^{-10r_p.v'} + 0.75W_0 e^{-2r_p.v'} + (\varepsilon_{av}.v' - 0.4W_0).r_p v' e^{-r_p.v'}\right] \quad \textbf{(3-10)}$$

The density ($b$) of the radioisotopic gas may be calculated through the application of Equation (3-11), where $M_3$ is the molecular mass of the radioisotope, $p$ is the

pressure of the gas (in atmospheres), $k'$ is a correction factor (0.6), and $T$ is the absolute temperature of the gas.

$$b = \frac{1.6\times10^{-5}.M_3.760.p.k'}{T} \quad \textbf{(3-11)}$$

### 3.8.2 Second stage: Conversion into light energy

Phosphors are a class of materials that convert the energy of incident photons or of radiation (such as beta particles) into emitted photons, through processes called photoluminescence and radioluminescence respectively. Taking the form of crystal lattices, phosphors are composed of a wide variety of materials, and each emit photons over a relatively narrow range of wavelengths (thus seeming to generate green light, or red light, etc.) as illustrated in Figure (3-27) [177].

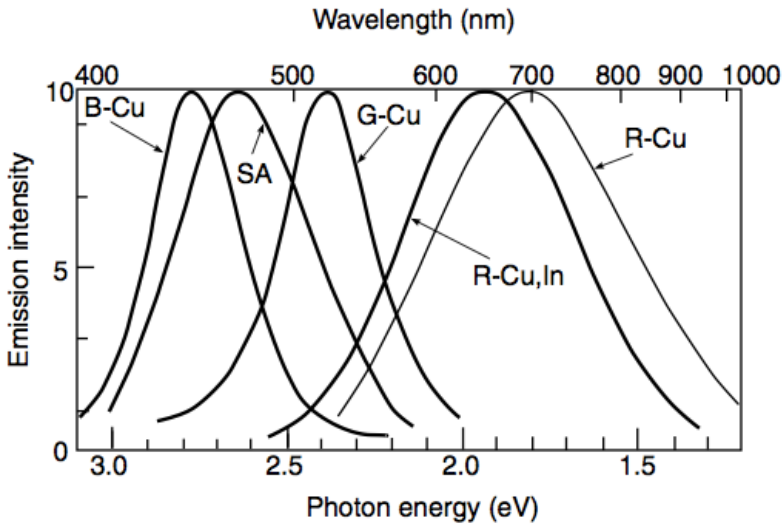



**Figure 3-27:** Emission spectra of ZnS phosphors containing different percentages of activator Cu (reproduced from [177])

The efficiency with which phosphors generate photons from received energy are quantities which have been studied and measured over many years. The Phosphor

Handbook [178] lists the efficiencies of many commonly utilized phosphors, which are presented in Table 3-5 along with data from several other sources [179-183].

**Table 3-5:** Properties of selected phosphors [178-183]

| Phosphor | Photon energy, $h\nu$ $(eV)$ | Calculated efficiency, $\eta_{pc}$ (%) | Experimental efficiency, $\eta_{pe}$ (%) |
|---|---|---|---|
| **ZnS:Ag** | 2.75 | 22.0 | 20.4 |
| **ZnS:Cu** | 2.30 | 19.0 | 17.5 |
| **$Y_3Al_5O_{12}:Tb^{3+}$** | 2.30 | 6.0 | 9.0 |
| **$Y_2O_3:Eu^{3+}$** | 2.00 | 6.5 | 7.5 |
| **$YVO_4:Eu^{3+}$** | 2.00 | 6.5 | 6.0 |
| **$La_2O_2S:Eu^{3+}$** | 2.00 | 10.5 | 6.0 |

### 3.8.3 Third stage: Transport of light energy into photovoltaic cell

The percentage of light reflected at a given angle ($R_\theta$) through a boundary from a material with one refractive index ($n_1$) to a material with a different refractive index ($n_2$) may be calculated by application of the Fresnel Equations [184] as shown in Equation (3-12).

$$R_\theta = \left( \frac{n_1 cos\theta - n_2 \sqrt{1 - \left(\frac{n_1}{n_2} sin\theta\right)^2}}{n_1 cos\theta + n_2 \sqrt{1 - \left(\frac{n_1}{n_2} sin\theta\right)^2}} \right)^2 + \left( \frac{n_1 \sqrt{1 - \left(\frac{n_1}{n_2} sin\theta\right)^2} - n_2 cos\theta}{n_1 \sqrt{1 - \left(\frac{n_1}{n_2} sin\theta\right)^2} + n_2 cos\theta} \right)^2 \quad \textbf{(3-12)}$$

At a critical angle ($\theta_c$), which may be calculated through application of Equation (3-13) light will be totally reflected.

$$\theta_c = arcsin\left(\frac{n_2}{n_1}\right) \quad \textbf{(3-13)}$$

Some ICRBs have a complex internal geometry, which should be taken into account when modelling light losses. Ray tracing software was considered for this task but was found wanting in the aspect of 3D modelling of light within complex geometries and the resultant angles of incidence of that light with the inner surfaces of the geometry for all possible angles [185, 186]. Many ray tracing packages are intended for computer game production or image manipulation and therefore provide a graphical result rather than a numerical result to their processing [187]. In addition it is not clear what algorithms are being calculated in some of these packages [188]. In some instances the Fresnel equations are not being solved but instead only a process of ray casting takes place, where the path of a ray is calculated to occur until it reaches an object, at which point it ceases to travel [189]. An alternative method of modelling will be explored.

### 3.8.4 Fourth stage: Conversion of light into electricity in the photovoltaic cell

Energy in the form of light is converted into electrical energy within a p-n junction of a photovoltaic (PV) cell by the formation of electron-hole pairs in the junction. Each photon of light incident on the junction is assumed to be capable of generating a single electron-hole pair, so long as the photon carries sufficient energy to remove the electron from the atom it was orbiting [190].

The performance of a photovoltaic cell may be modelled by forming an approximation of the processes occurring within the device that result in the conversion of light into electrical energy. One commonly utilized equivalent circuit of a photovoltaic cell is presented in Figure 3-28, and is known as a single diode double resistor model.

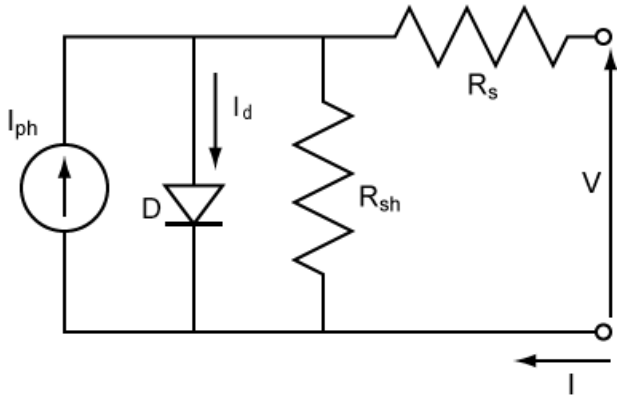



**Figure 3-28:** Equivalent circuit diagram for a photovoltaic cell (reproduced from [191])

The efficiency of conversion of photons into electrical energy can be calculated by considering the current flowing through the circuit depicted in . The series resistor ($R_s$) models resistance at the contact/semiconductor boundary and at the outer surface of the semiconductor. The shunt resistor ($R_{sh}$) models the conductance pathways within the photovoltaic cell (due to imperfections in the structure) or along the edges of the cell. In a perfectly operating device the series resistance would be negligible and the shunt resistance extremely large. The diode ($D$) represents the dark condition reverse flow of current (recombination) and current diffusion within the p-n junction.

Equation (3-14) [192] describes the current flow within a photovoltaic cell. where $I_o$ is the reverse saturation current, $q$ is the elementary charge ($1.602X10^{-19}C$), $V$ is the voltage across the diode, $n$ is a diode ideality factor, $k$ is the Boltzmann Constant ($1.380X10^{-23}J/K$), $T$ is absolute temperature (in $K$), $I$ represents the generated current, $I_{ph}$ is the generated photocurrent, $I_d$ is the current across the diode while $I_{sh}$ is the current across the shunt resistance.

$$I = I_{ph} - I_o\left[e^{\left(\frac{q(V+IR_S)}{nkT}\right)} - 1\right] - \frac{V + IR_s}{R_{SH}} \quad \textbf{(3-14)}$$

The efficiency of a PV cell ($\eta_{pv}$) may be calculated by application of Equation (3-15), where $FF$ is the fill factor of the PV cell and $P_{in}$ is the power of light incident upon the cell.

$$\eta_{pv} = \frac{V_{oc}.I_{sc}.FF}{P_{in}} \quad \textbf{(3-15)}$$

The fill factor of a PV cell is a ratio between the voltage ($V_{mp}$) and current ($I_{mp}$) at the maximum power point relative to the open circuit voltage and short circuit current as described in Equation (3-16).

$$FF = \frac{I_{mp}.V_{mp}}{I_{sc}.V_{oc}} \quad \textbf{(3-16)}$$

If the circuit's series resistance is lower than $10\Omega/cm^2$ then the short circuit current ($I_{SC}$) may be used as the photocurrent ($I_{ph}$). The short circuit current density of the photovoltaic cell ($J_{SC}(\lambda)$) can be compared to the photon flux incident upon it by considering the quantum efficiency ($QE(\lambda)$) of the photovoltaic cell. Equation (3-17) (adapted from [193, 194]) describes this relationship, where $\phi(\lambda)$ is the photon flux density at wavelength $\lambda$.

$$J_{SC}(\lambda) = QE(\lambda).q.\phi(\lambda) \quad \textbf{(3-17)}$$

The photon flux density incident on the photovoltaic cell may be represented in the form of Equation (3-18) [195], where $N_p$ is the number of incident photons, $A_{pv}$ is the surface area of the photovoltaic cell and $t$ is the time of measurement.

$$\phi(\lambda) = \frac{N_p}{A_{pv}.t} \quad \textbf{(3-18)}$$

### 3.8.5 Fifth stage: Storage of electrical energy in a capacitor

A capacitor may be described by the equivalent model [196] presented in Figure 3-29, where *ESR* is the equivalent series resistance, $R_p$ is the parallel resistance (also known as insulation resistance), and *C* is the capacitance. Because charging occurs using Direct Current (DC) the inductance of the capacitor may be ignored. Capacitance and equivalent series resistance are values which may be obtained from the datasheet of a capacitor, but parallel resistance must be calculated.

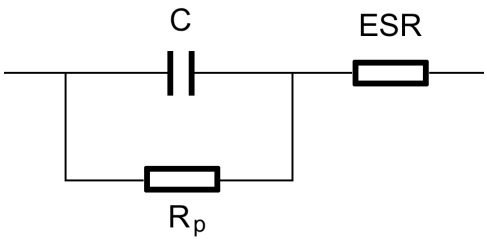



**Figure 3-29:** Equivalent model of a capacitor

The voltage ($V$) of a capacitor that has discharged from starting voltage ($V_0$) over time ($t$) as described by Equation (3-19), where $C$ is the capacitance and $R_a$ is the resistance of the applied load.

$$V = V_0 e^{\frac{-t}{R_a.C}} \quad \textbf{(3-19)}$$

The general formula for energy stored in a capacitor is described by Equation (3-20) [197].

$$E = \frac{1}{2} C.V^2 \quad \textbf{(3-20)}$$

For a power source planned to operate for 20-years or more the operational lifetime of the components is of great importance. Manufacturers of capacitors test their products under certain specific conditions and then provide formulae that may be used to determine the operational life of their capacitors under a much broader range

of operating conditions. Equation (3-21) shows a formula for determining the operating life of capacitors ($L_{op}$), formulated by Cornell Dubilier Electronics Inc. (CDE) [198], where $M_v$ is a voltage based multiplier, $L_b$ is the operating life at full rated voltage and temperature (as measured by CDE), $T_m$ is the maximum allowable internal operating temperature of the capacitor, and $T_a$ is the actual internal operating temperature.

$$L_{op} = M_v . L_b . 2^{(T_m - T_a)/10} \quad \textbf{(3-21)}$$

## 3.9 Conclusions of the literature review

Indirect conversion radioisotopic batteries using a capacitor as an electrical storage device have been identified as the power source to take forward for further investigation. The previous methods of theoretical modelling of this type of power source have been analysed and found wanting. Therefore, it was decided to separate the processes occurring in the power source and model each stage individually, before recombining the results for an over-all model. Available theoretical models of each of the stages in the power source were presented and discussed as to their appropriateness for use.

# 4 INDIRECT CONVERSION RADIOISOTOPIC BATTERY

## 4.1 Introduction

Having selected indirect conversion radioisotopic batteries (ICRB) utilizing GTLSs to investigate further it was necessary to conduct a preliminary investigation of the most effective configurations of this power source. This chapter details the configurations attempted along with a review of the findings of this early experimentation.

## 4.2 Potential configurations

Due to availability and high standards of manufacture it was decided to use pre-made PV cells and GTLSs in the manufacture of the ICRBs. Using these components there were a variety of potential arrangement of GTLSs and PV cells identified as shown in Figure 4-1, where the golden coloured sheets are reflective materials, the blue rectangular bases are PV cells and the green cylinders are GTLSs.

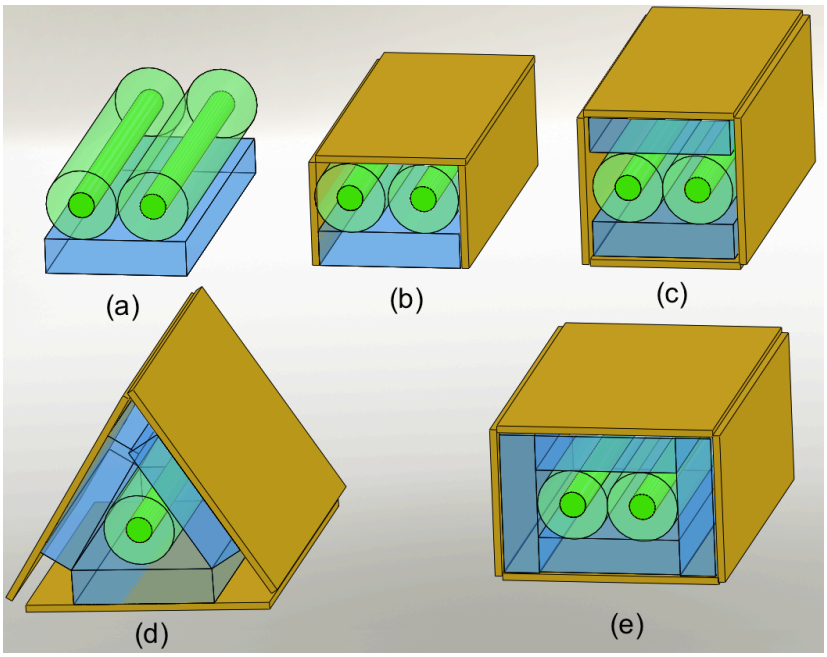



**Figure 4-1:** Potential configurations of ICRBs with two GTLSs and (a) one PV cell without reflective material, (b) one PV cell with reflective material, (c) two PV cells, (d) three PV cells, and (e) four PV cells

GTLSs were not arrayed in stacks in these configurations in an effort to minimise the amount of light lost to self-absorbtion between GTLSs themselves.

## 4.3 Initial experimentation

Batteries were constructed of each potential configuration using a-Si PV cells measuring 55mmX4.5mm and 1.1mm thick and two GTLSs 25mm long and 3mm diameter radiating light in the green spectrum. The GTLSs were calculated (using data from the manufacturer, shown in Appendix A) to contain 17.0GBq of $^{3}$H at beginning of life giving a total of 34.0GBq of $^{3}$H present. The reflective material used was Mylar sheeting, which was wrapped around the batteries. The constructed batteries were placed in a sealed box designed to eliminate any ambient light which might invalidate the results. The batteries were then connected to a 1μF 50V aluminium electrolytic capacitor and the voltage in the capacitor was measured at timed intervals. The difference in voltage ($dv$) was then applied to Equation (4-1) (where $C$ is the capacitance) to determine the power ($P$) required to induce the voltage change in the capacitor over the given time interval ($t$). The test layout and methodology is described in greater detail in Section 4.9.1.1.

$$P = \frac{\frac{1}{2} C dv^2}{t} \quad \textbf{(4-1)}$$

The results of the testing of the single PV cell without reflective foil are presented in Figure 4-2, which shows measured voltages set against the time taken for the voltages to accrue in the connected 1μF 50V capacitor. The voltage may be said to increase in the capacitor at a nearly linear rate to begin with before decreasing and then plateauing to a steady voltage. The final voltage of the capacitor is directly

related to the open circuit voltage of the connected PV cell under the illumination level of the GTLSs.

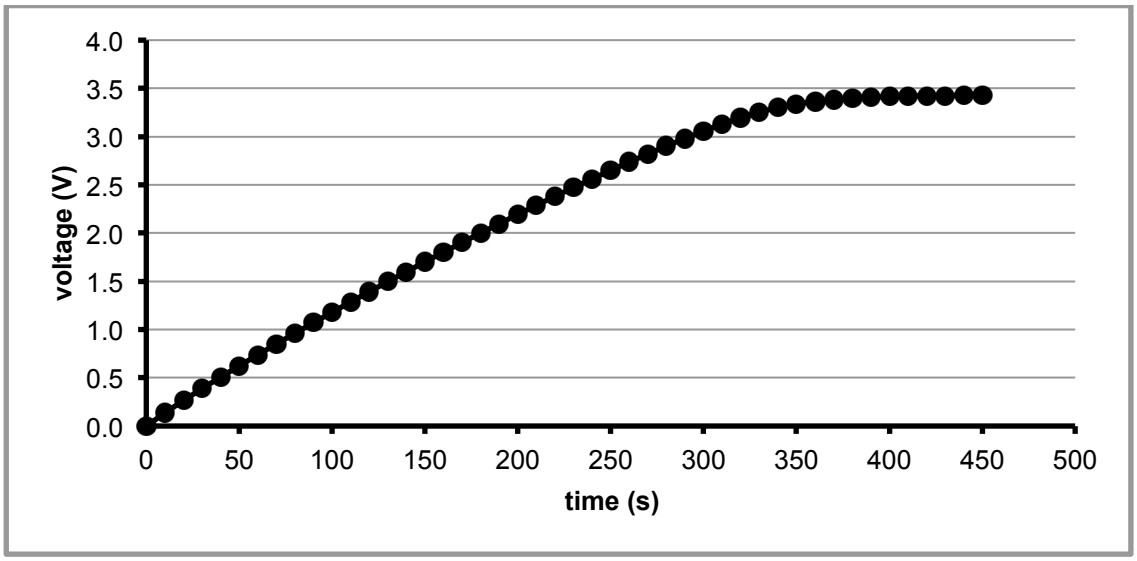



**Figure 4-2:** Test results of single PV cell without reflective foil showing voltage in the connected 1μF 50V aluminium electrolytic capacitor changing over time

Through application of Equation (4-1) to these test results it is possible to generate Figure 4-3, which shows the power required to charge the capacitor as measured over the time periods of measurement. The power required to generate charge in the capacitor is measured at a peak of 23nW in this configuration.

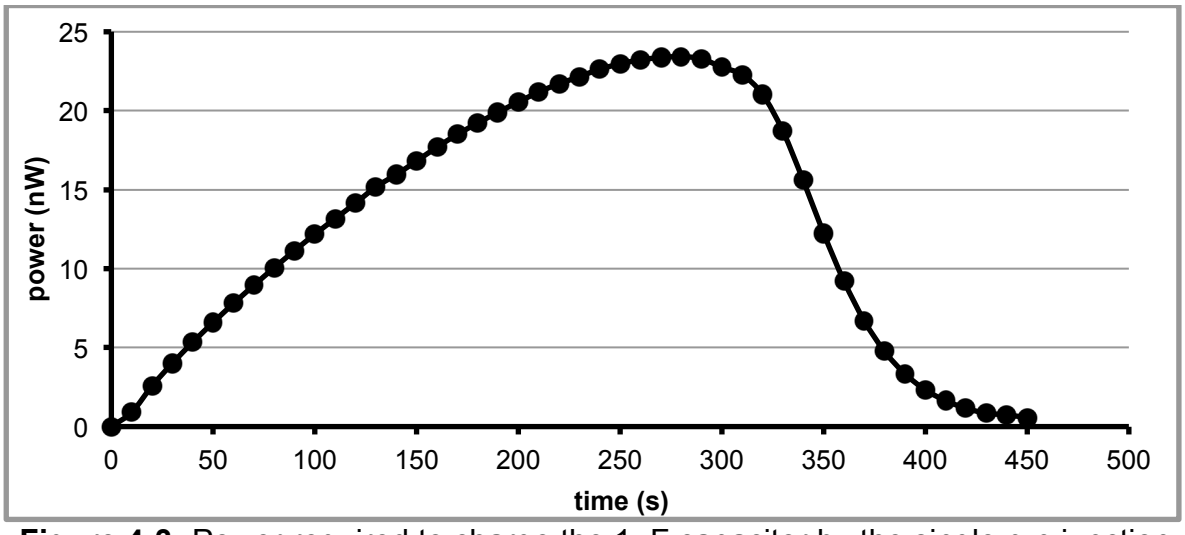



**Figure 4-3:** Power required to charge the 1μF capacitor by the single p-n junction without reflective foil set against time

It is important to note that the power generated by the ICRB is nearly constant and is not being measured directly in these tests. Only a percentage (unknown at this stage) of the power from the ICRB is used to charge a capacitor even at peak (with the rest being lost to heat), though this percentage efficiency of charging should be very similar for the same capacitor regardless of the configuration of ICRB used.

The batteries with two and three PV cells were tested with the junctions connected in both series and in parallel configurations though the battery with four PV cells was only tested in parallel configuration due to earlier test results indicating that this arrangement was not beneficial. The reflective foil used was composed of Mylar. Results for the series configuration of PV cells is shown in Figure 4-4 with power plotted against voltage generated. The most powerful configuration in this comparison is clearly using two PV cells, giving 75.1nW at 6V.

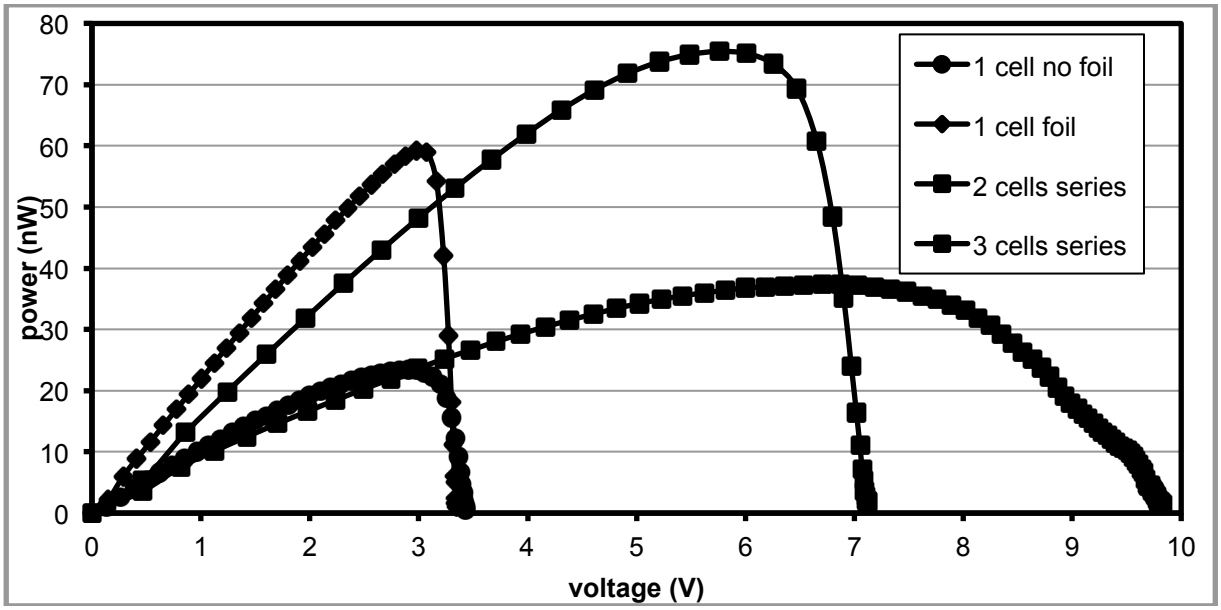



**Figure 4-4:** Comparison of initial battery results with p-v junctions connected in series

The PV cells were also connected in parallel in each of the battery configurations with the results presented in Figure 4-5. From comparison of these layouts it is clear that the most power was generated from two PV cells in parallel, giving 118.8nW at 3.08V. Not only is this a higher power than was generated when the two PV cells were in series but the voltage at which this power was generated is also far more useful to powering electronic applications.

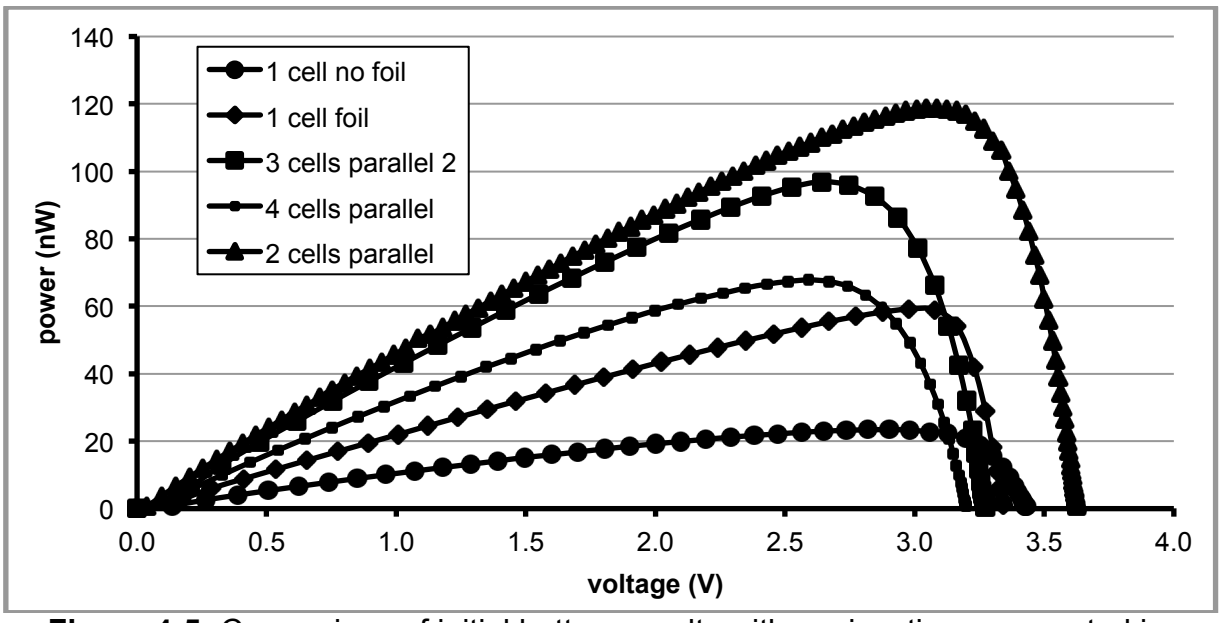



**Figure 4-5:** Comparison of initial battery results with p-v junctions connected in parallel

Aside from the overall power produced the efficiency and power density of the batteries are also key metrics. Efficiency may be determined by comparing the power flux from the radioisotope with the generated electrical power, while power density is a comparison of the total volume of each battery with the electrical power it is determined to have generated.

The maximum power flux generated by the radioisotope ($P_r$) in the GTLSs may be calculated by application of Equation (3-4), where $A$ is the activity of radioisotope

present in Becquerels, $\varepsilon_{avg}$ is the average energy of decay of the radioisotope (5.7keV for $^{3}H$) and $J$ is the energy in joules of one electron volt ($1eV=1.602X10^{-19}J$).

$$P_r = A.\varepsilon_{avg}.J \quad \textbf{(4-2)}$$

For the two GTLSs used in these initial tests, assuming the activity is the same as at beginning of life, the total power flux present may be calculated through application of Equation (3-4) to be 31.046μW. Applying this power to the peak power found to have been generated by the ICRB configurations provides the efficiency of that design. Similarly by determining the volume of the ICRB configurations and dividing the peak power by this value the power density of the various configurations may be calculated. This data is presented in Table 4-1, where it is clear that the most efficient battery (and the most powerful) was the design featuring two PV cells connected in parallel. This ICRB configuration also had the highest power density.

**Table 4-1:** Peak power, efficiency and power density of initial ICRB designs

| Battery configuration | Volume (cm3) | Peak power (nW) | Efficiency (%) | Power density (nW/cm3) |
|---|---|---|---|---|
| 1 cell no foil | 1.027 | 23.43 | 0.075 | 22.81 |
| 1 cell with foil | 1.065 | 59.18 | 0.191 | 55.57 |
| 2 cells series | 1.355 | 75.08 | 0.242 | 55.41 |
| 2 cells parallel | 1.355 | 118.76 | 0.383 | 87.65 |
| 3 cells series | 1.486 | 37.39 | 0.120 | 25.16 |
| 3 cells parallel | 1.486 | 96.89 | 0.312 | 65.20 |
| 4 cells parallel | 1.941 | 67.81 | 0.218 | 34.94 |

Of the various configurations investigated in this initial investigation it was found that joining the PV cells in parallel generated a higher peak power than did joining the cells in series. The current generated by the ICRBs is extremely low (~20nA) and the leakage current of the capacitor (representing loss in the capacitor) may become significant against this low charging current at a relatively early time (before much

charge has been stored in the capacitor). By connecting the PV cells in parallel the currents of the cells are added together and therefore the current is not as low and not as susceptible to this issue.

A comparison of the results obtained using one PV cell with and without a reflective surround shows the importance of this aspect of ICRB design in attempting to reflect as high a proportion of the emitted light from each GTLS onto the PV cells present. The power generated increased by a factor of 2.5 which may in part be explained by the particular design of the IRCB in question. With only one PV cell present the light emitted from the far side of the GTLS is not incident on any PV cells in this design without a reflective surround. Meanwhile the GTLSs do not cover the entire surface area of the PV cell (only 60% is covered) and there is therefore much uncovered space on the surface of the PV cell for reflected light to be incident upon.

GTLSs provide illuminance of around 0.3Lux to 3Lux which is similar to moonlight as visible at the earth's surface but PV cells are not designed for operation at these extremely low light levels. The aSi PV cells used in this testing are designed for operation in low light levels encountered indoors and are rated at 200Lx. Therefore the illumination of the PV cells may be 100 times lower than the level for which they have been optimally designed. By increasing the number of PV cells while maintaining the same number of GTLSs there is a greater chance that light will be incident on a PV cell and therefore generate electrical power, however the surface area over which the light is incident is also increased and therefore the illuminance is decreased. Comparison of the parallel configurations of one, two, three and four PV cells demonstrates this decrease in illuminance becoming significant relative to the

increased likelihood of light incidence. Two PV cells generate increased electrical power than one PV cell, but three cells produce less power, and four cells even less power.

## 4.4 Selected design

The selected design uses two PV cells “sandwiched” around GTLSs as illustrated in Figure 4-6. The number and dimensions of GTLSs along with the type of PV cells and reflective material surrounding the device (not shown in Figure 4-6) will be investigated further.

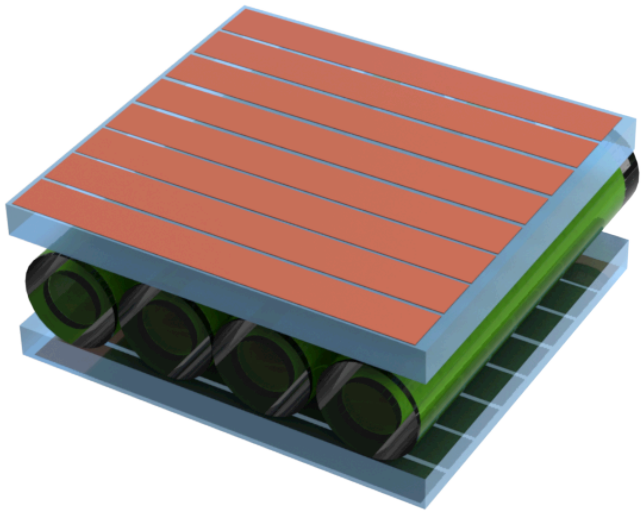


**Figure 4-6:** Selected layout of indirect conversion radioisotopic battery (without reflective cover)

## 4.5 Areas of investigation

A number of features of the ICRB were identified as deserving of more detailed study. A variety of PV cells, of different type, shape and size were to be matched with a variety of GTLSs of different shapes and sizes. Changing the medium between the GTLSs and PV cells was also to be experimentally investigated along with varying the reflective material surrounding the entire device. Additionally, the capacitor type

and size most suitable for use with an ICRB as part of the power source was to be explored. Batteries would have to be constructed and tested in order to examine each of these design characteristics.

## 4.6 Challenges

Specific areas of the design presented issues which needed to be considered and overcome. The most obvious issue lay with the limited repeatability of the manufacturing of the battery. The initial ICRBs held their components in place through use of the reflective material (Mylar® - Biaxially-oriented polyethylene terephthalate) which was wrapped around the PV cells and GTLSs. The limitation of this design was that the orientation and location of the PV cells to GTLSs could not be guaranteed to any great degree and this was reflected in variable results of power output from batteries nominally of the same design, as shown in Figure 4-7. The GTLSs in Battery 1 in these tests were discovered to have moved relative to the PV cells which accounts for the lower power generated. This level of deviation was, however, unusual and the variation was generally of a much lower order.

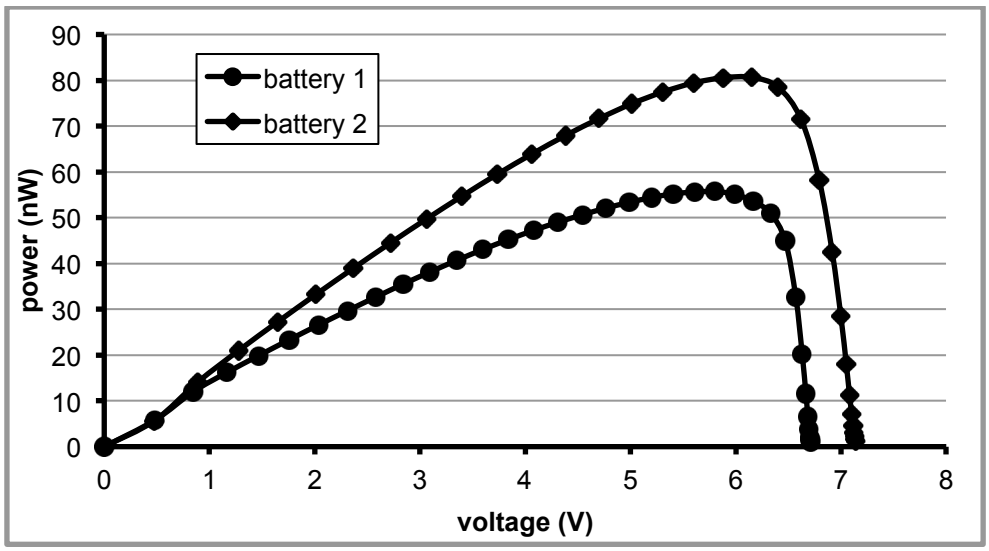



**Figure 4-7:** Results of two batteries constructed using two PV cells and two GTLSs

It was therefore determined that a casing to hold the PV cells and GTLSs in exactly the required positions should be designed and manufactured in order to overcome this issue. The casing should be strong enough to provide some protection to the PV cells (which are constructed in large part from glass and are therefore fragile and susceptible to being easily damaged) and rigid enough to maintain the relative location of the PV cells and GTLSs to each other throughout each experiment even if the battery was reconstituted at a much later date.

The decision to use a hard casing around the ICRB design presented issues of its own regarding the implementation of a reflective screen around the battery. A variety of reflective materials were identified as worthy of further experimentation in this regard, and each material would then have to be contained within the casing. Each type of reflective material would have to be applied in the most appropriate manner to ensure that the maximum percentage of light was prevented from leaking from the ICRBs produced.

Some of the reflective materials under consideration are electrically conductive, which presented a further challenge. The contacts on the PV cells needed to be electrically isolated from the conductive reflective materials which would otherwise provide a short circuit within the battery design. The contacts for each PV cell type had to be considered individually as the location of the contacts differed depending on PV cell type.

Examination of the medium between the GTLSs and PV cells involved introducing a fluid into the ICRB which brought a number of associated problems. A key concern

with this area of testing was to ensure that any fluid introduced would not leak out over time, as this would alter the performance of the device over time. It was therefore necessary to ensure that the casing designed for containment of the ICRB for these tests was watertight. Introduction of a fluid medium into the ICRB also carried the risk of further short circuit between contacts of the PV cells if they were not adequately insulated.

## 4.7 Casing designs

Two general designs of casing were selected as most suitable for containing the ICRBs during testing. The first design, shown in Figure 4-8, was a clamshell configuration and was appropriate for all experimental tests except those that involved the introduction of a fluid medium into the device. Leakage would (and did) occur if this design was used in that manner. The open nature of this design made it most suitable to the application of reflective materials in a variety of techniques and for easy battery construction.

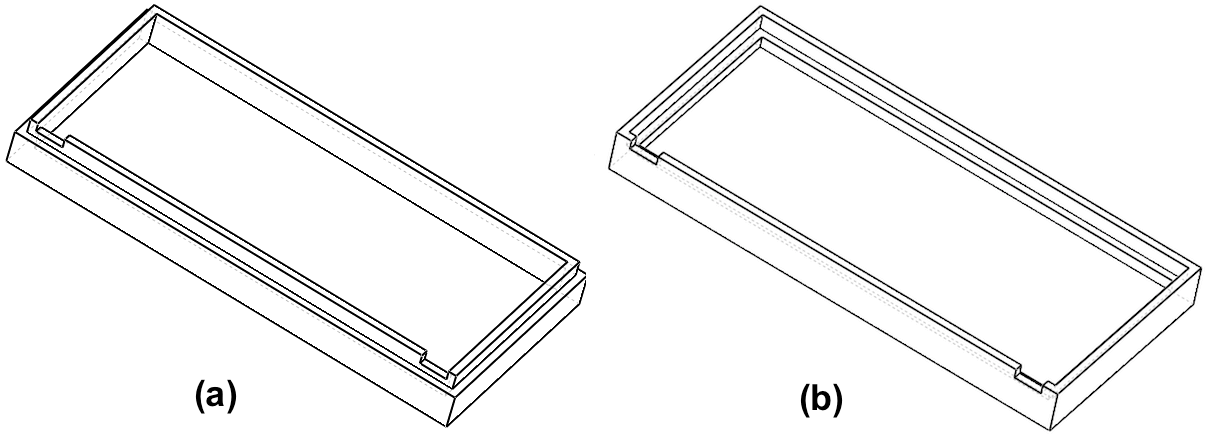



**Figure 4-8:** Casing design in Solidworks® [199] showing (a) base and (b) top

The second design of casing was a trough with a lid, which was best able to contain any fluid introduced into the battery, and is shown in Figure 4-9. Due to the depth of

the trough in this design this was not suitable for some reflective materials to be applied.

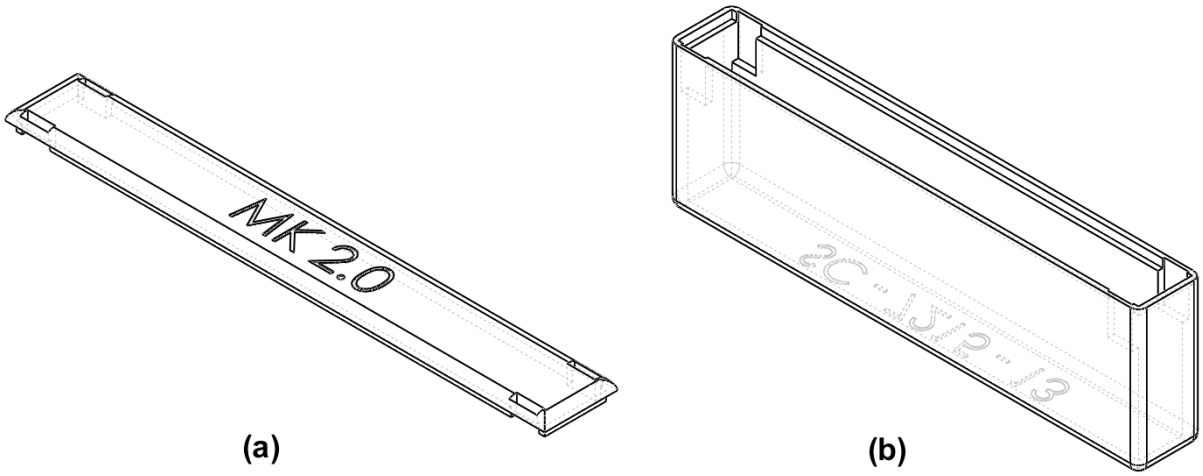



**Figure 4-9:** Casing design in Solidworks® [199] showing (a) lid and (b) trough

## 4.8 Fabrication

Having arrived at final designs suitable for experimental investigation of the characteristics described in Section 4.5 the ICRBs were manufactured.

### 4.8.1 Gaseous tritium light sources

As described in Section 4.2, gaseous tritium light sources were used in the construction of the ICRBs. Silicon PV cells are most commonly used to convert light from across the visible spectrum (white light) into electricity and therefore green light (lying midway through the visible spectrum) was chosen as the wavelength of light to use for testing. Another characteristic of GTLSs under consideration was the effect of size on intensity of emission and on the efficiency of the produced ICRBs, and therefore GTLSs of different sizes were selected to be used. A selection of the GTLSs which were used are shown in Figure 4-10. The characteristics of the GTLSs

selected for use in the ICRBs were investigated and their values are given in Chapter 6.

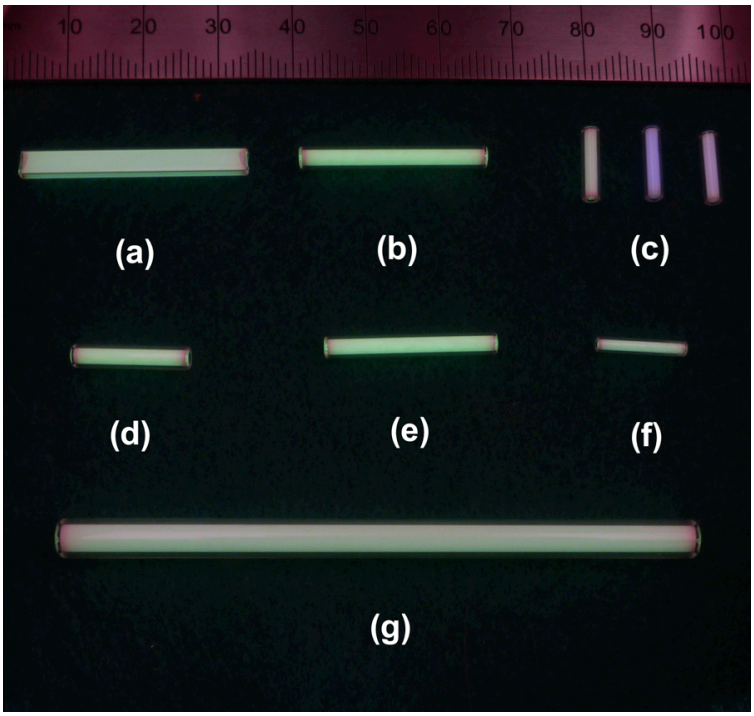



**Figure 4-10:** Selection of (green unless stated otherwise) GTLSs used in ICRB construction showing (a) 30mmX4mmX2mm, (b) 25mmX3mmØ, (c) green, blue and white 10mmX2.5mmØ, (d) 15mmX3mmØ, (e) 22.5mmX3mmØ, (f) 12mmX2mmØ, (g) 80mmX5mmØ

### 4.8.2 Photovoltaic cells

A variety of silicon PV cells were investigated for use in ICRBs, ranging in size and composition and including monocrystalline, polycrystalline and amorphous types of cells. A selection of these PV cells is presented in Figure 4-11. The key characteristic of these PV cells that was investigated was their performance at the ultra low light levels generated by GTLSs with the results of this experimentation presented in Section 6.2.4.2.

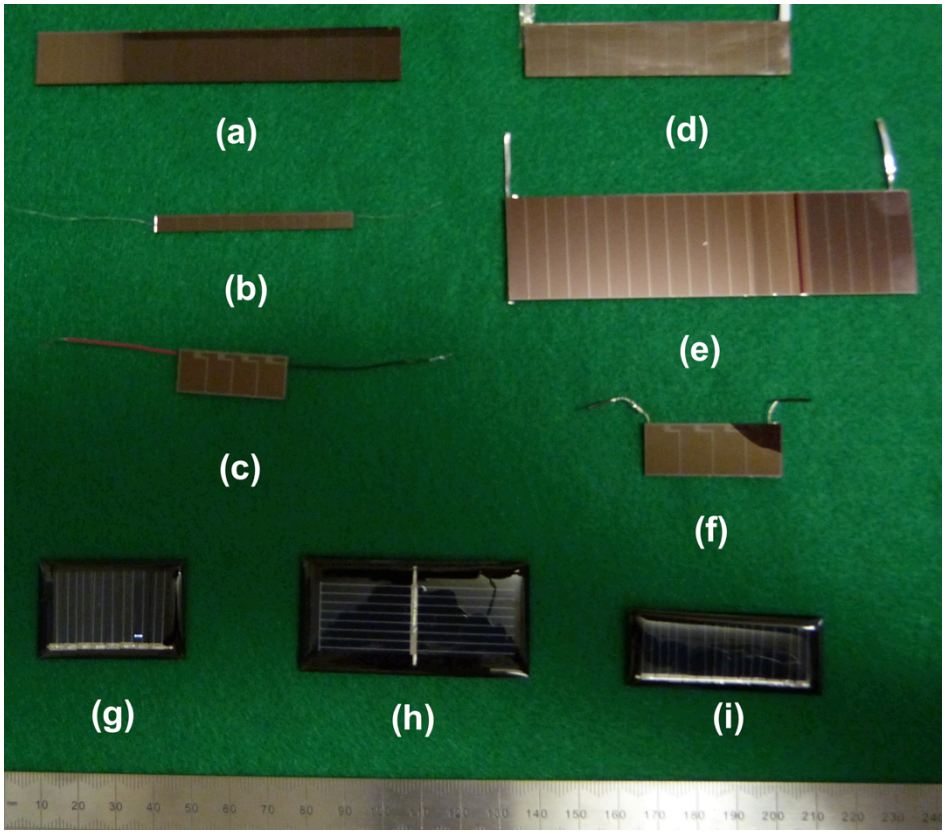



**Figure 4-11:** PV cells used in ICRB construction showing (a) 103.0mmX15.5mm a-Si, (b) 54.5mmX4.5mm a-Si, (c) 29.6mmX11.7mm a-Si, (d) 72.3mmX15.0mm a-Si, (e) 107.7mmX28.0mm a-Si, (f) 34.9mmX13.8mm a-Si, (g) 39.8mmX26.0mm m-Si, (h) 59.9mmX30.0mm m-Si, (i) 49.8mmX19.9mm p-Si

### 4.8.3 Contacts

An important aspect of ICRB construction was the creation and isolation of contacts to the positive and negative terminals of the PV cells. Each type of PV cell had terminals of a different type and location, making a universal design solution impossible. One solution was to solder a wire to the terminals on the back of the PV cells and then feed the wire out of the casing surrounding the ICRB. An alternate solution was to produce modified casings capable of accepting removable clip contacts, as shown in Figure 4-12.

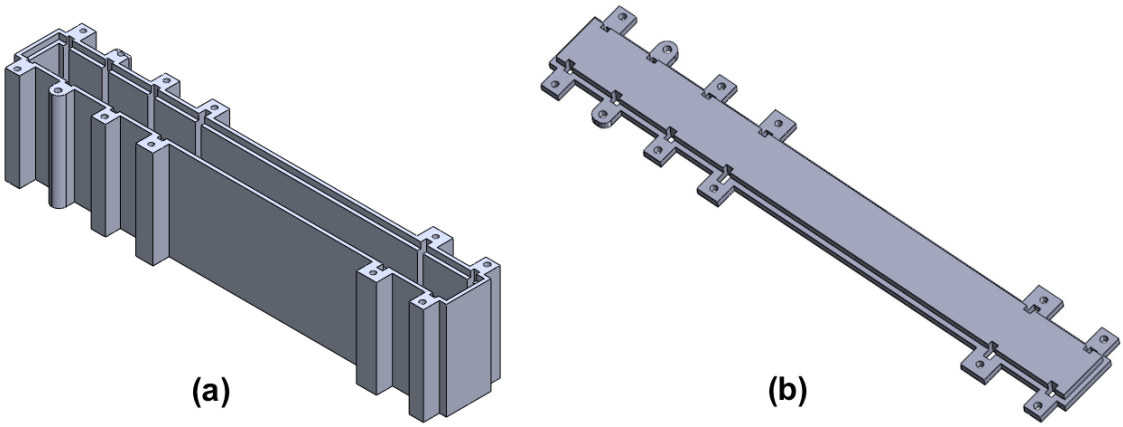



**Figure 4-12:** Modified casing design for removable contacts showing (a) trough, (b) lid

Clips were then generated from sprung steel, with only their leading surface exposed from insulation, as shown in Figure 4-13(a), which could then be slotted into the top of the ICRB casing as shown in Figure 4-13(b). When the clips were pushed into place the spring of the clip pushed one side of it into contact with the free terminal on the back of the PV cell, therefore creating a low resistance electrical connection.

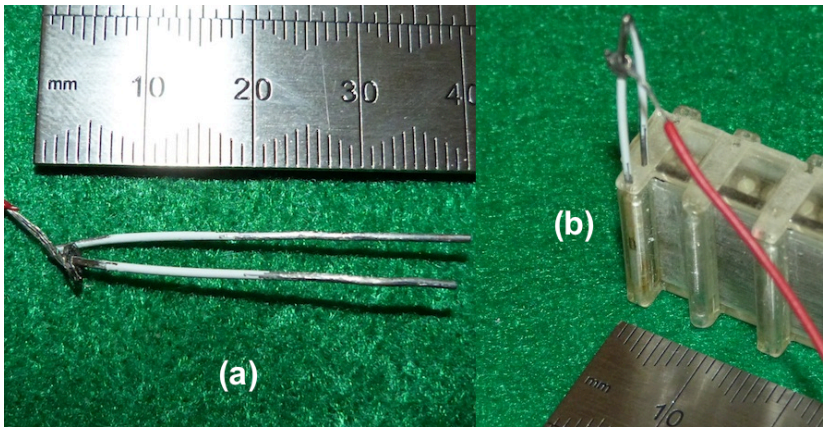



**Figure 4-13:** Removable contacts, showing (a) clip contact, (b) clip contact attached to ICRB

Due to the electric conductivity of some reflective coatings the contacts required insulation before they were suitable for use in the ICRBs. One solution to this problem was to coat the entire terminal and contact area with an epoxy resin, preventing any potential contact with the inner casing wall. An alternate solution was

to spray a lacquer, composed of a solution of acrylic copolymer and plasticizer in xylene (designed for electrically isolating printed circuit boards), onto the terminals and contacts. However, this later solution proved unsuitable when using an index-matching fluid in the ICRB as the fluid dissolved the lacquer and the contacts then short circuited with the casing wall reflective material.

### 4.8.4 Casings

The casings to contain the ICRBs were manufactured from designs presented in Section 4.7 using an Objet Eden250$^{TM}$ 3D printer [200] using a material called FullCure©720 [201] which is an acrylic based photopolymer resin. The resin was deposited in layers 16μm deep at the locations specified in the 3D design. These layers were then exposed to ultra-violet light for a second which cured them, before a new layer was deposited on top and the process began again. Where the finished design called for a space instead of the resin to be deposited a support material (FullCure©705) was laid down in its place. This support material may then have the acrylic resin (FullCure©720) deposited on top of it if that is then required by the design. The FullCure©705 was later removed from the finished casing model with a high power water jet. A selection of the casings produced in this manner is shown in Figure 4-14.

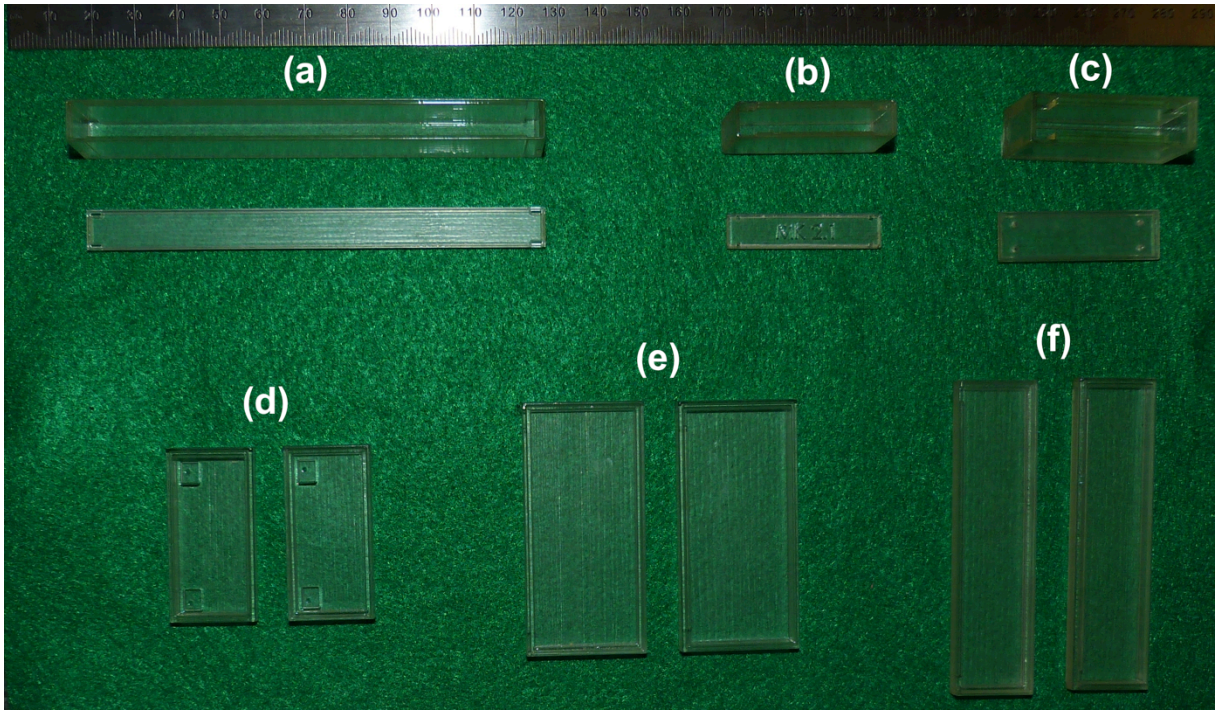



**Figure 4-14:** Selection of casings manufactured to contain the ICRBs showing (a) trough and lid for 103.0mmX15.5mm a-Si PV cells, (b) trough and lid for 29.6mmX11.7mm a-Si PV cells, (c) trough and lid for 34.9mmX13.8mm a-Si PV cells, (d) top and base for 34.9mmX13.8mm a-Si PV cells, (e) top and base for 59.9mmX30.0mm mono-Si PV cells, (f) top and base for 72.3mmX15.0mm a-Si PV cells

### 4.8.5 Coatings

The inside of the casings were coated with various reflective materials and the effects on ICRB power generation experimentally determined. Reflectance may be described as a percentage of the incident electromagnetic radiation at a given wavelength which is reflected back by a material instead of being absorbed. The materials selected to line the inside of the casings were chosen due to their reflective index within the relevant portion of the visible spectrum. The GTLSs used in this experimentation emitted a light apparently green to the human eye, however this was not the only part of the electromagnetic spectrum in which they emitted radiation and it was therefore important to choose reflective materials capable of high reflectance across the entire visible spectrum (390nm to 700nm [202]) and possibly further.

The reflectance of some common materials, aluminium (Al), silver (Ag) and gold (Au) at suitable wavelengths is shown in Figure 4-15. Of these materials it is clear that aluminium is the most suitable for reflectance across the entire visible spectrum, though silver has a greater peak reflectance. Aluminium has a largely stable reflectance across the visible spectrum being 92.1% reflective at 300nm and 89.8% reflective at 700nm [203]. Silver displays an unusual property of almost total transmission (ultra low reflectance) at 310nm but reaches a peak of 98.2% reflectance at 700nm [204]. The reflectance of gold varies greatly across the visible spectrum from a low of 34.6% (at 300nm) to a peak of 96.3% (at 700nm) [203].

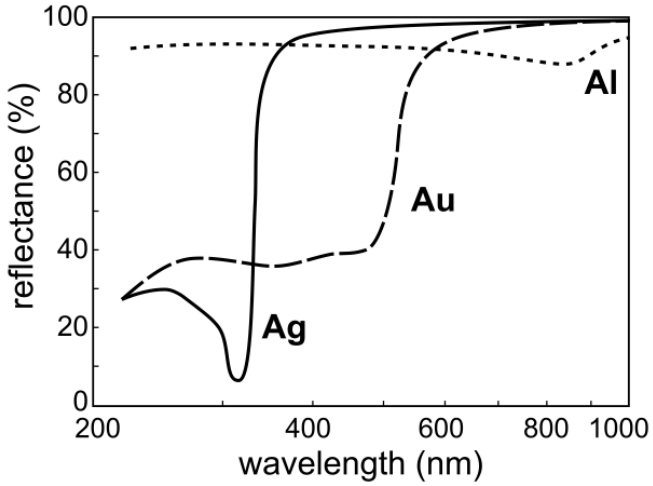



**Figure 4-15:** Reflectance of aluminium (Al), gold (Au) and silver (Ag) from 200nm to 5000nm (reproduced from [205])

The reflectance of $BaSO_4$ (barium sulfate) across the visible spectrum and beyond is shown in Figure 4-16. $BaSO_4$ provides reflectance of between 96% and 98% across the visible spectrum, although this is dependent on the thickness of the $BaSO_4$ layer, with 0.5mm being ideal and the reflectance percentage decreasing as the layer of $BaSO_4$ falls below this optimal thickness [206].

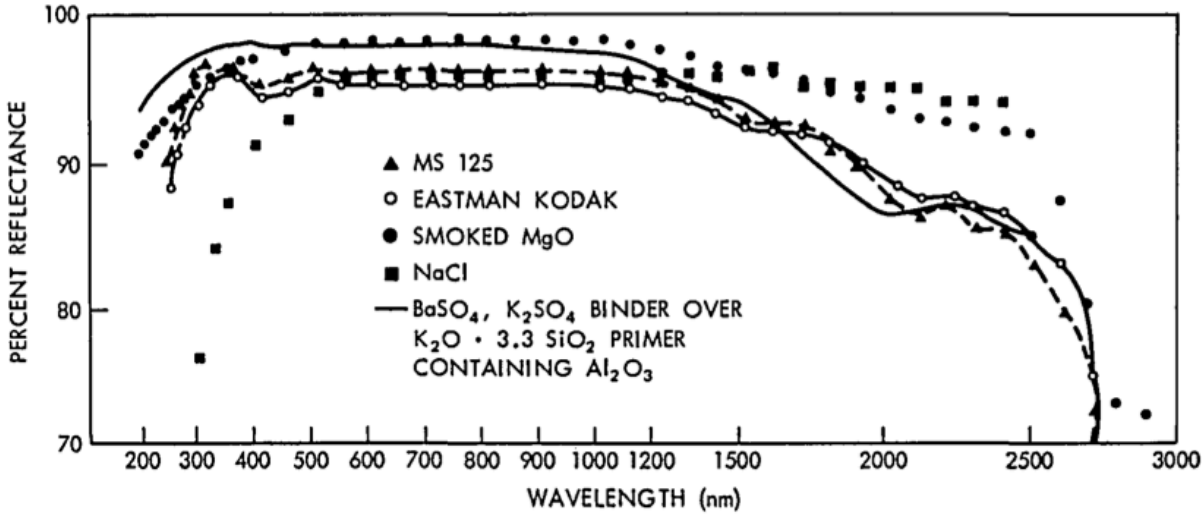



**Figure 4-16:** Reflectance of $BaSO_4$ and other substances from 200nm to 2700nm (reproduced from [207])

Operating temperature affects the reflectance of materials and therefore it should be noted that the above values were obtained at ambient (around 25°C) temperatures. Similarly the angle of incidence of the electromagnetic radiation on the material affects the reflectance as illustrated for aluminium in Figure 4-17, where the effect has been exacerbated by a protective coating of disilicon trioxide ($S_2O_3$) on the surface of the aluminium.

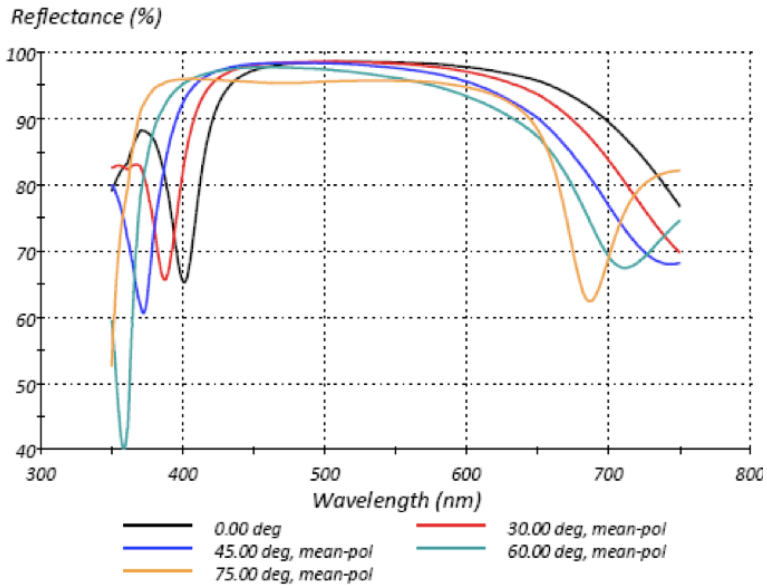



**Figure 4-17:** Effect of angle of incidence on reflectance of coated aluminium (reproduced from [208])

From analysis of these reflectance curves it was decided to compare the effect of gold and $BaSO_4$ as reflective materials. $BaSO_4$ was chosen because of its high level of reflectance across the visible spectrum while gold was selected as a comparative material due to its lesser reflectance, which should therefore provide a contrast to the effect of $BaSO_4$ reflectance. The gold layer was deposited by sputter coating while the $BaSO_4$ was sprayed on with an air gun. Both methods required the deposition of multiple layers until sufficient material had been lined to the inside of the casings. Casings coated internally with gold and $BaSO_4$ are shown in Figure 4-18.

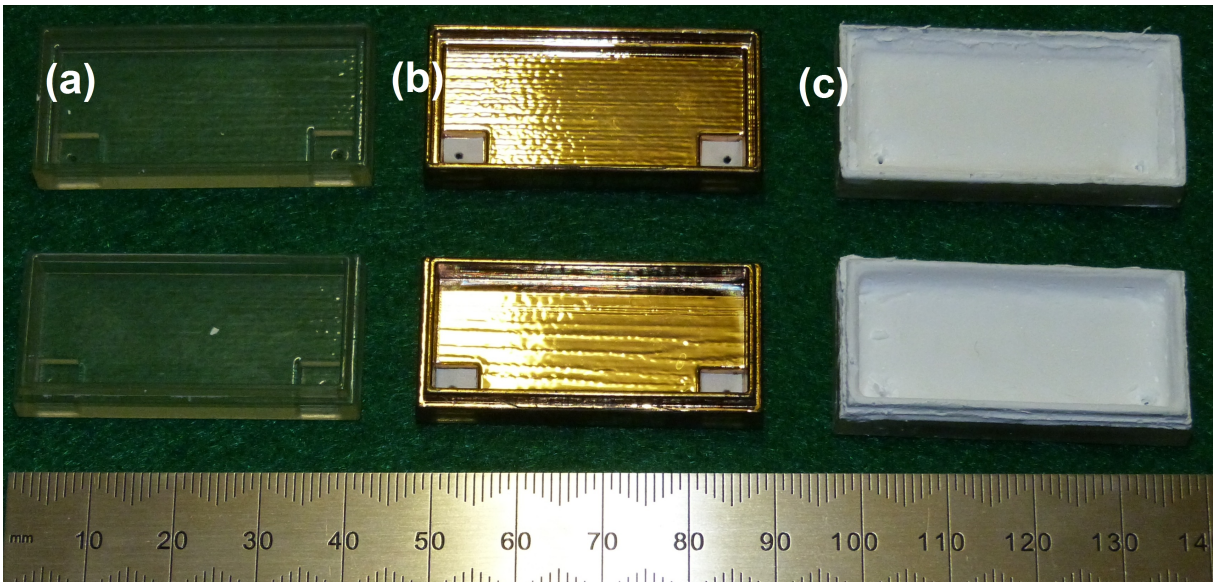



**Figure 4-18:** Casings coated with reflective material, (a) no coating, (b) gold (c) $BaSO_4$

### 4.8.6 Capacitors

A wide variety of capacitor types and sizes exist and it was therefore necessary to investigate which capacitors were most suitable for use with the ICRB as a power supply system. A selection of the capacitors experimentally investigated is shown in Figure 4-19 and includes capacitors with electrolytes based on aluminium, niobium oxide, tantalum and ceramics. In addition capacitors are rated by their capacitance

(in farads – F) and by the maximum voltage to which they may be charged. The impact of both characteristics was investigated during testing to determine their effect on the operation of the power supply system.

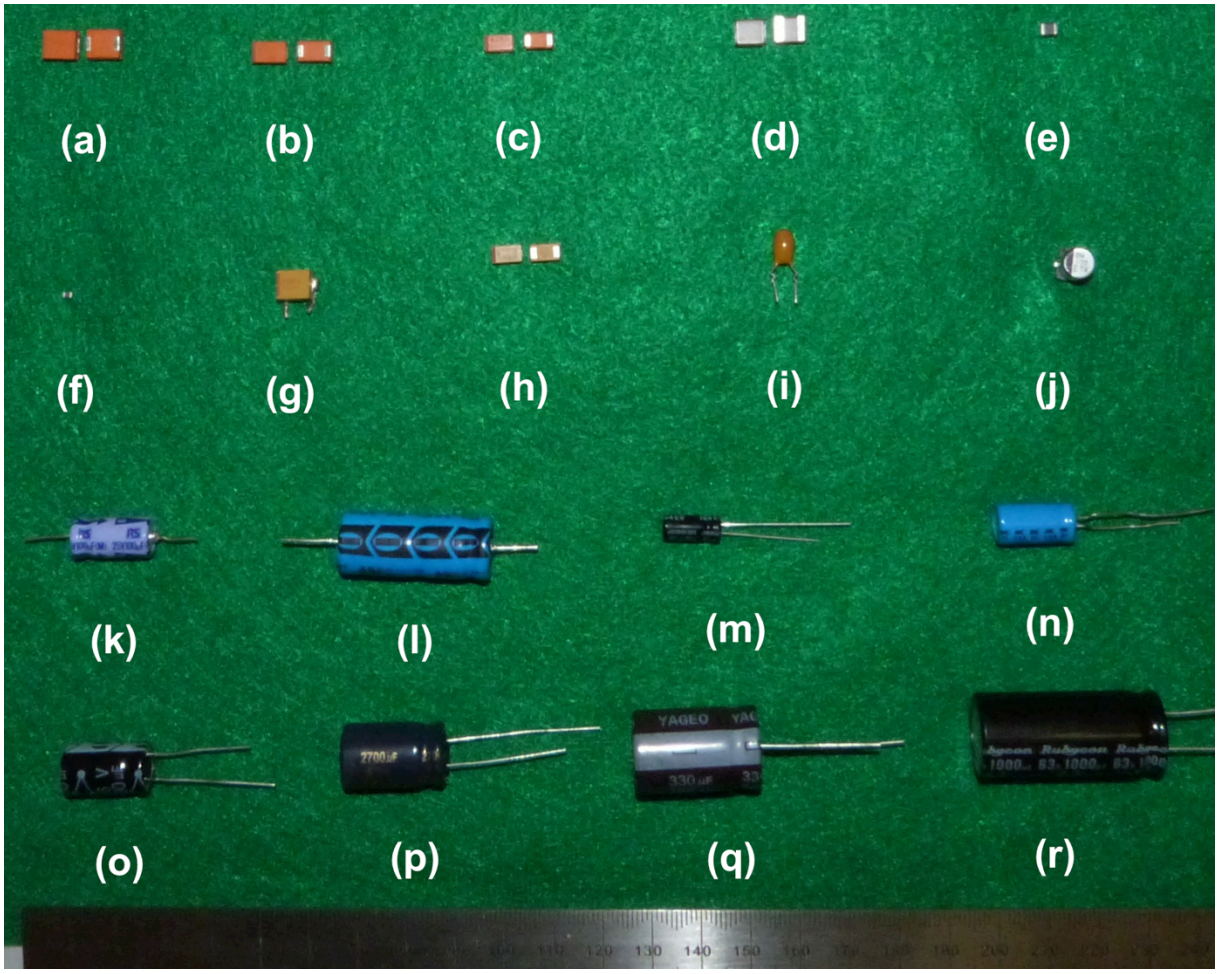



**Figure 4-19:** Selection of the capacitors used during testing showing (a) front and rear view of AVX niobium oxide 10V 100µF, (b) front and rear view of AVX niobium oxide 10V 47µF, (c) front and rear view of AVX niobium oxide 6.3V 47µF, (d) front and rear view of TDK ceramic 16V 47µF, (e) Taiyo Yuden ceramic 16V 47µF, (f) Taiyo Yuden ceramic 6.3V 10µF, (g) AVX tantalum 6.3V 1000µF, (h) front and rear view of Kemet tantalum 16V 100µF, (i) Radio Spares tantalum 16V 22µF, (j) Rubycon 'button' aluminium electrolytic 25V 100µF, (k) Radio Spares radial aluminium electrolytic 25V 100µF, (l) Vishay radial aluminium electrolytic 25V 1000µF, (m) Jamicon aluminium electrolytic 25V 47µF, (n) Vishay aluminium electrolytic 10V 470µF, (o) Multicomp aluminium electrolytic 16V 1000µF, (p) aluminium electrolytic 6.3V 2700µF, (q) aluminium electrolytic 25V 1000µF, (r) Rubycon aluminium electrolytic 63V 1000µF

A key factor of capacitors is their leakage losses and these were experimentally investigated at a range of voltages which was accomplished by charging the capacitors with a DC voltage to a pre-determined voltage, disconnecting the capacitors from all circuitry, and then measuring the stored voltage over time. The drop in voltage was due to this leakage loss and could therefore be determined.

### 4.8.7 Dielectric between the PV cells and the GTLSs

The medium between the GTLSs and PV cells was designated as a further aspect of ICRB design worthy of further investigation. To this end ICRBs were produced utilizing casings similar to the design shown in  and were filled with fluids attempting to match the refractive index of the borosilicate glass surrounding the GTLSs and cover the PV cells. In this manner it was intended to reduce the effect of reflection and refraction within the ICRB and potentially increase the efficiency of the device. Experiments were run with and without the index matching fluid and the results compared. These results are presented and discussed in Section 6.2.3.4.

## 4.9 Testing

The ICRBs were tested in order to ascertain their power output. Additionally, the PV cells were tested at various levels of illuminance in order to better characterize them and to assist the development of the theoretical model. The spectral intensities of the GTLSs were also measured in order to corroborate their theoretical modelling.

### 4.9.1 Testing of battery power into capacitor

The power of the ICRBs was measured indirectly by charging a capacitor and measuring over time the change in its voltage. The capacitor is part of the power

source system and should therefore be measured along with the ICRBs. In addition, direct measurement of the power generated by the ICRBs is problematic due to the very low currents (tens of nanoamps) which they produce. It was therefore decided to measure the increasing voltage in the connected capacitor by taking voltage readings at timed intervals which reveals the power forcing charge into the storage device by application of Equation (4-1)from Section 4.3.

Initially the changing voltage in the capacitor was measured using a multimeter, however it was found that this was an inadequate system. Measurement of this voltage by multimeter was not useful even to measure the increasing voltage in a capacitor (particularly of a low capacitance) as the impedance of this device was not high enough (only 1MΩ) to avoid some of the current under measurement from being drawn through the multimeter circuitry, therefore skewing the results. Therefore an alternative method of measurement was developed, as described in Section 4.9.1.1.

#### 4.9.1.1 Automated indirect measurement of power into capacitor

It was decided to produce a system capable of reporting in real-time the results of the testing in an easy to understand graphical format. To this end a data acquisition (DAQ) device called a LabJack U6-PRO [209] was used to take readings during tests. The charging capacitor was connected to the DAQ using switching circuitry on a breadboard as shown in . The LabJack U6-PRO is capable of measuring inputs of -10V to 10V but was adapted to measure between 0V and 20V. The resolution of readings was 18 bit which provided a measurement resolution of 0.076mV over a 20V range. The DAQ has an impedance of 1GΩ which greatly exceeded the impedance of a multimeter (at only 1MΩ). A test circuit for use with the DAQ was

designed and formed on a breadboard. The circuit diagram for this test regime is shown in Figure 4-20.

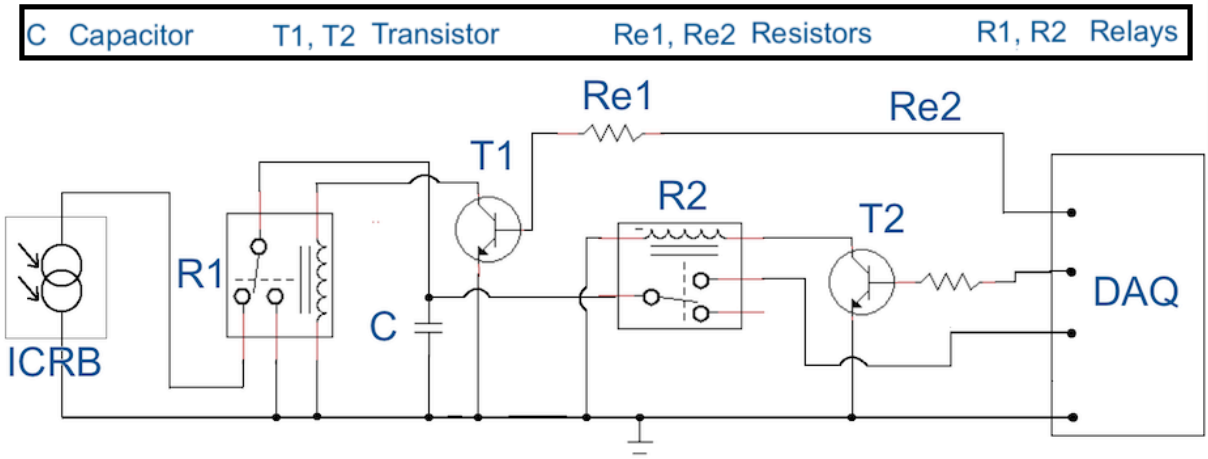



**Figure 4-20:** Test circuit for indirect conversion radioisotopic battery testing using an Arduino

The LabJack U6-PRO was connected to a computer via a USB cable and was controlled by a program called LabVIEW [210], which also controlled the test circuitry shown in Figure 4-21.

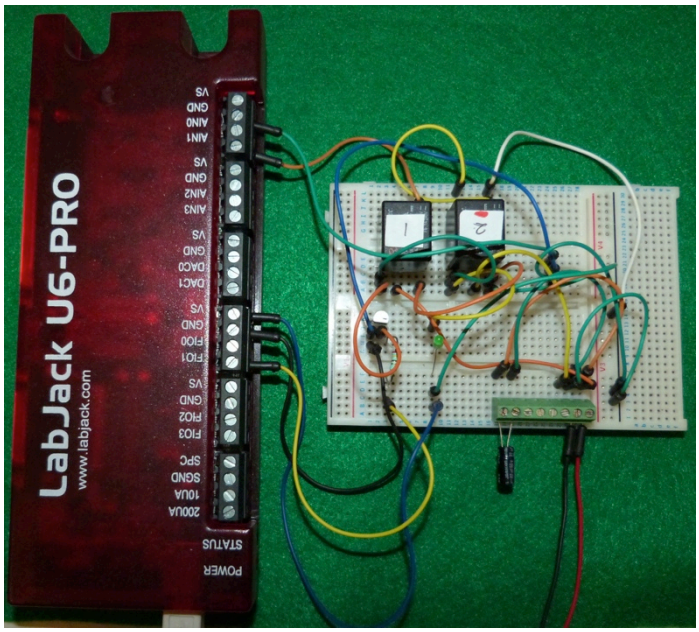



**Figure 4-21:** LabJack U6-PRO automated test-bed for measurement of voltage in capacitors

The LabVIEW program designed to control the test circuitry and take measurements with the DAQ also collated the generated results into graphs of voltage against time and power against time, which were displayed in a graphical user interface (GUI) in real-time, as shown in Figure 4-22. Using this GUI it was possible to stipulate the length of time between each sample, the time each sample should take (both in milli-seconds) and the capacitance of the attached capacitor (in Farads). The GUI was capable of showing readings for two capacitors simultaneously and displaying voltage vs time curves and power vs time curves of the generated data. The block diagram code controlling the experimentation is presented in Appendix C.2.3.

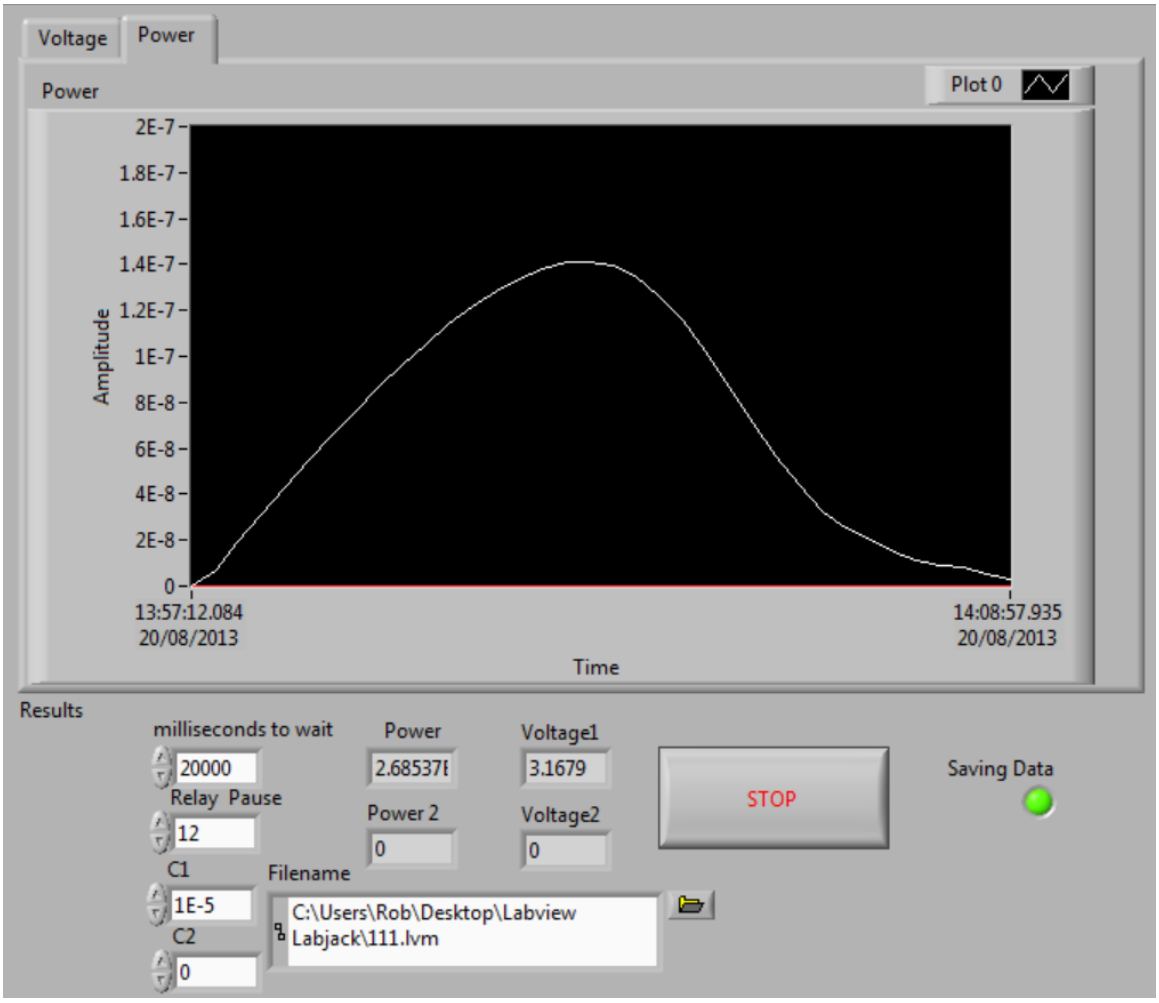



**Figure 4-22:** Graphical user interface of automated measurements run through LabVIEW [210]

Control experiments were conducted to ensure that the capacitors under test were not being charged through the very system measuring them. A 1000μF 25V aluminium electrolytic capacitor was charged by connection to an ICRB (in the test box) and was measured by the automated method described above. The same capacitor was then charged by the same ICRB but was not connected to the automated test equipment. After the time taken to run the automated test the voltage in the capacitor was measured with a multimeter. In this instance use of a multimeter for measurement was acceptable as the capacitance was suitably high and therefore the draw on the charge stored within was insignificant for the one-off reading (requiring only a second). The final voltage in the capacitor measured after each type of testing was then compared. The difference in these two voltages was minimal (of the order of 0.4%) suggesting that the automated system of measurement was robust for testing the changing voltage in capacitors.

#### 4.9.1.2 Isolation of the battery

It was important to ensure that ambient electromagnetic radiation (both in the visible spectrum and infra red) was not incident on the ICRB while testing as this might have generated additional current in the PV cells of the ICRB. For this reason it was necessary to properly isolate the ICRB in a well sealed and dark environment. To this end the ICRB was placed in a box, constructed of aluminium and lined with both plywood and rubber, during testing. Contacts to the ICRB passed through a well-sealed hole in the side of the box and connected to the test platform. An image of this test environment is provided in Figure 4-23.



**Figure 4-23:** Darkened environment for the testing of ICRBs

### 4.9.1.3 Control experiment

The efficiency of isolation of the ICRB in its test environment was measured by running control experiments. These experiments consisted of placing ICRBs without their GTLSs in the test box and measuring the voltage change in the capacitor over time in the manner described in Section 4.9.1.1. Results of this testing using 54.5mmX4.5mm a-Si PV cells connected to a 1μF 50V aluminium electrolytic capacitor are shown in Figure 4-24. Power is clearly generated into the capacitor even within the testing environment, suggesting further investigation was necessary.

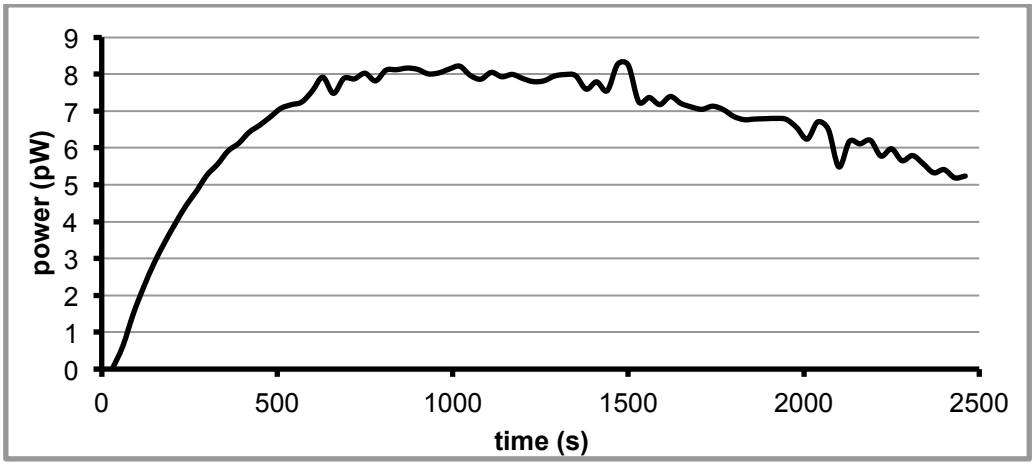



**Figure 4-24:** Results of control experiment on ICRB without GTLSs in the test environment

Capacitors suffer from a phenomenon called dielectric absorption, also known as ‘soak’, whereby a discharged capacitor will seem to soak up charge again even if not connected to a power source. This phenomenon occurs because the dipole created in the capacitor takes time to fully depolarize during discharge [211]. Unless the capacitor is discharged for an extended period of time across a suitable resistance then residual charge will remain in the system which will manifest itself as a charge at the electrodes of the capacitor. The power calculated to be entering the capacitor during this testing is greatest at the beginning of testing suggesting that ‘soak’ may be partly a factor in the charging of the capacitor.

Figure 4-25 was produced by Pease [212] and shows the voltage in a 1μF mylar capacitor over time having been charged and then discharged. The time of discharge clearly has a significant impact on the rate to which dielectric absorption (soak) will then occur.

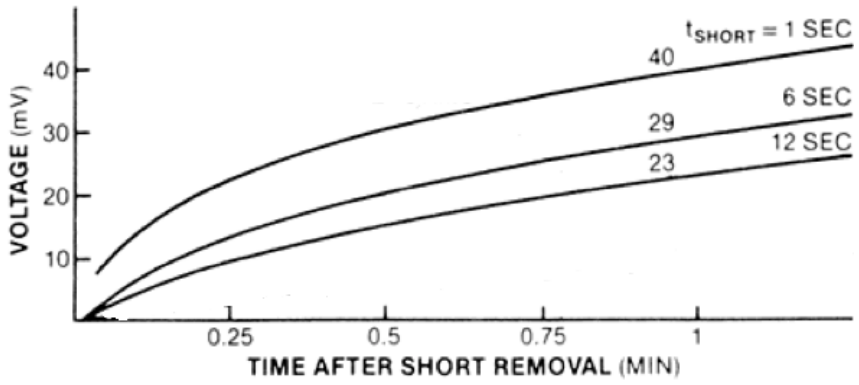



**Figure 4-25:** Voltage measurements against time of discharged capacitors showing dielectric absorption measured by Pease (reproduced from [212])

It was decided to conduct a similar experiment using the 1uF aluminium electrolytic capacitor utilized in the control experiment to study the effect of soak in this capacitor. The capacitor was shorted for 10 seconds before measurement began.

The results of this experimentation are presented in Figure 4-26 in the form of voltage increase in the capacitor over time and follow a nearly linear path (not quite a straight line). There is a clear similarity of shape to the dielectric absorption presented by Pease in the lowest curve of  for a capacitor shorted for 12 seconds before measurement began. Less curvature is seen in Figure 4-26 than in Figure 4-25 because the experiment was conducted over a longer period of time.

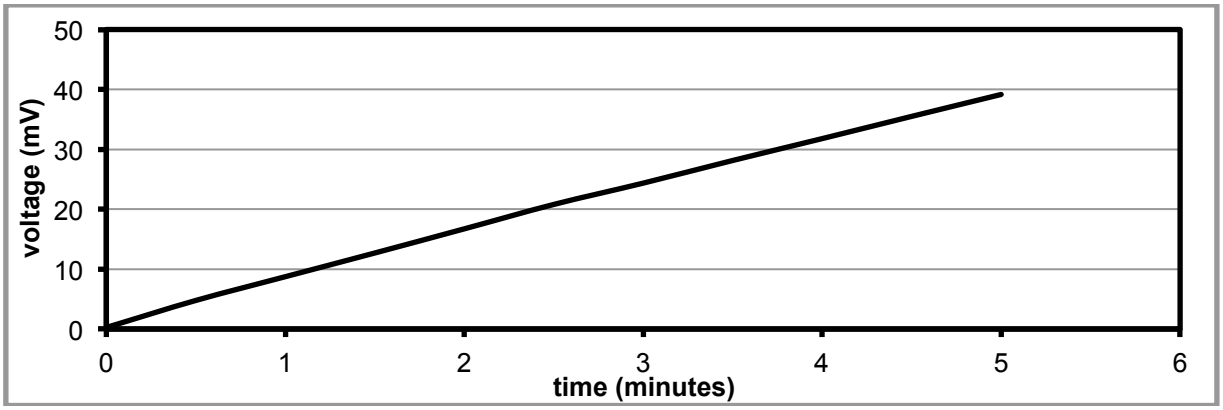



**Figure 4-26:** Measured dielectric absorption in a 1μF aluminium electrolytic capacitor

The voltage rise is more gradual than in the case of the mylar capacitor which Pease investigated which was charged to 10V over one minute, while the aluminium electrolytic capacitor was charged to only 1V in a few seconds. Generally the dielectric absorption of aluminium electrolytic capacitors is quite high (as high as 10% of initial value) [213] and is higher than for mylar capacitors.

A comparison of the voltage rise in the 1μF capacitor control experiment with the voltage rise in the capacitor observed during the soakage experiment is shown in Figure 4-27. From this comparison it appears that the voltage rises more rapidly in the capacitor when it is not connected to the PV cells contained in the test box. This suggests that, even though it is possible that some ambient electromagnetic radiation

may be incident on the PV cells in the test box, the intensity of this radiation is of a very low value. Furthermore the PV cells themselves contain a low series resistance (largely at the terminals) and it is believed that this resistance, when connected to the capacitor, accounts for the lessened rise in voltage during the period of soakage as shown in Figure 4-27. It can therefore be suggested that a capacitor connected to an external load (such as the PV cells) experiences less soak than a capacitor on its own.

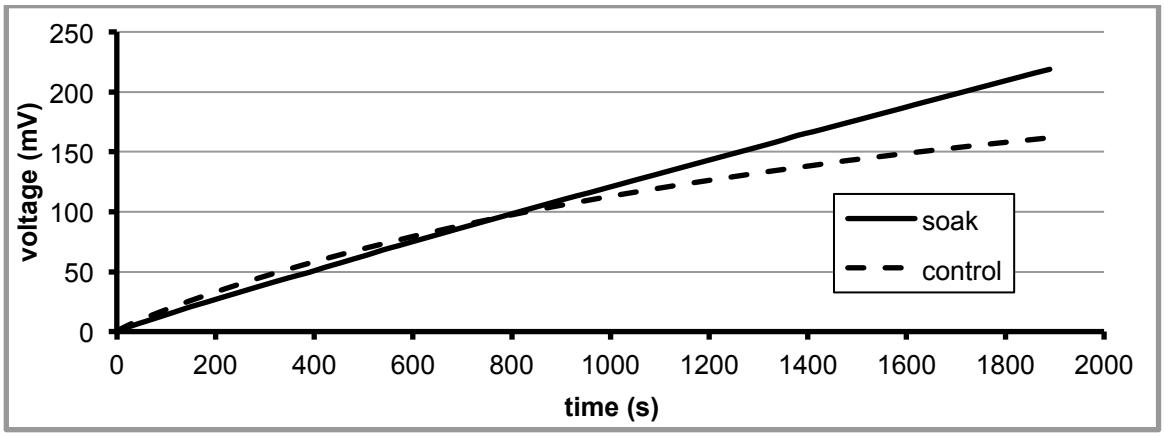



**Figure 4-27:** Measured voltage rise in capacitor during control test and soakage test

It was therefore determined that some of the power calculated to have driven charge into the capacitor during the control test was the result of dielectric absorption and a small portion may be due to ambient electromagnetic radiation incident on the PV cells. The power generated in the capacitor during the control testing had a peak of less than 9pW which was more than 1000 times lower than the power measured during testing of the ICRBs and can therefore be considered as insignificant. For these reasons it was concluded that the test environment was suitably shielded from electromagnetic radiation to ensure accurate and usable test results. However, the effect of dielectric absorption would have to be considered and removed from test results in order to ensure they were accurate.

### 4.9.2 Measurement of the PV cells current and power output

PV cells are commonly characterised by the short circuit current, open circuit voltage and maximum power which they can generate. These values, however, are dependent on the spectral intensity to which the PV cells are subjected. Because the light intensity provided by the GTLSs is considerably lower than is usual for most PV cells (either indoors or outdoors) the components require characterisation at these exact conditions. The values of interest may be determined from an I-V curve read from the PV cell under examination. In order to generate this I-V curve the voltage and current must be determined for the PV cell at a wide range of values of external load to which it should be connected.

Figure 4-28 presents a circuit diagram illustrating how I-V curves were obtained for the PV cells under examination. Two voltage measurements were taken (at points 'A' and 'B' in Figure 4-28) by use of the data acquisition device known as LabJack U6-PRO. The LabJack U6-PRO [209] contains instrumentation amplifier inputs which buffers the test circuit and allows the voltages associated with such ultra low currents generated in the PV cells to be read directly without distortion by the test circuitry.

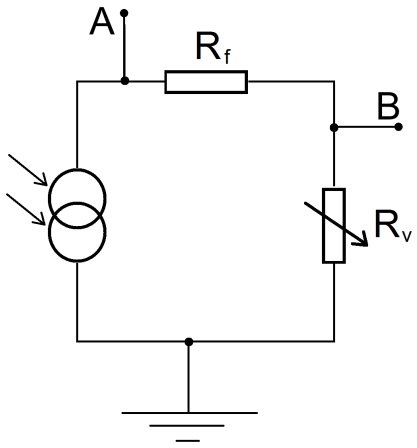



**Figure 4-28:** Test circuit in order to generate IV curves of the PV cells at various light intensities

The voltage drop between ‘A’ and ‘B’ may be easily calculated. The resistance ($R_f$) is a fixed known value, while the resistance ($R_v$) is variable and is incrementally increased as the experiment progresses. Increasing the resistance of the circuit alters the voltage generated by the PV cell. Meanwhile the resistance ($R_f$) being known allows the current across this component (and hence through the entire circuit, by Kirchoff’s current law) to be calculated, by application of Equation (4-3). In this way an I-V curve for the PV cell under test could be generated. This variable resistance also mimics the behaviour of a capacitor under charge which increases in resistance as charge accumulates in it.

$$V = I.R \tag{4-3}$$

The PV cells were characterised in this manner at three different illumination values, outdoors in direct sunlight (~100,000lux), indoors under office lighting (~200lux) and under illumination from only the GTLSs (~3.8lux). Light illuminance for indoors and outdoors was read using a light meter. A comparison of the results of this illumination and the I-V curves which were generated would provide an insight into the behaviour of the different types of PV cells at various intensities of illumination. Results from this experimentation are presented in Section 6.2.4.2 and Appendix D.1.

### 4.9.3 Testing of GTLS spectral intensity

The light emitted by the GTLSs was measured In order to better understand the spectral variance in intensity of light and the overall illumination provided by the GTLSs. This characterization was undertaken at the National Physics Laboratory (UK) using array based spectral radiometers and a luminance meter. A darkened environment was used for this testing and to ensure accurate measurements a

background reading was taken and deducted from all subsequent readings. Results of this testing are presented and discussed in Section 6.2.3.1.

### 4.9.4 Burial and duration testing

The performance of the ICRB was also evaluated under buried conditions on a water company test site (Lake House, Severn Trent Water [214]) 8 miles north of Leicester, UK. The primary purpose of this experimentation was to investigate the effect of burial on the battery and hence further classify its suitability as a power source for WSN nodes in remote and/or harsh environments. In addition, the operation of the battery was monitored over time in order to determine the variation of the power output over an extended period of time.

The environment under the ground is not conducive to long-life operation of electronics and therefore the ICRB was suitably contained within a waterproof enclosure designated to meet the IP65 standard. A rubber ‘o-ring’ between the lid and the main body of the enclosure ensured that moisture was unable to enter the box. Contacts for the ICRB were allowed through a hole drilled in the side of the enclosure, after which the hole and contacts were sealed with epoxy glue. In order to ensure moisture did not come in contact with the ICRB the enclosure was then filled with a transparent ‘potting’ material composed of polyurethane. The preparation of potting materials entails the mixing of two or more constituent compounds (typically consisting of a resin and a hardener) which then set to form a solid substance. The reaction between these compounds can be endothermal or exothermal, both of which would result in the presence of heat surrounding the PV cells and GTLSs which was unwelcome. The specific potting material was chosen due to its relatively low

exothermic generation of heat (<90$^{o}$C) [215] during curing and its transparent nature which allowed on-going visual inspection of the battery and the safety markings made on it.

The installation of devices containing radioisotopes on third-party premises requires the notification of the UK Health and Safety Executive (HSE), which was undertaken at a time sufficiently in advance of the installation. The installed device was labelled in accordance with UK legislation, which requires markings on the device to indicate the number of GTLSs present; the total activity of radioisotope present, the word “radioactive”; the symbol for radioactivity; and the symbol for Tritium (T). In addition the external enclosure to the ICRB was labelled with radioactive warning tape. The ICRB in its enclosure (missing its lid) is shown in Figure 4-29, which ably illustrates the transparency of the potting material used.

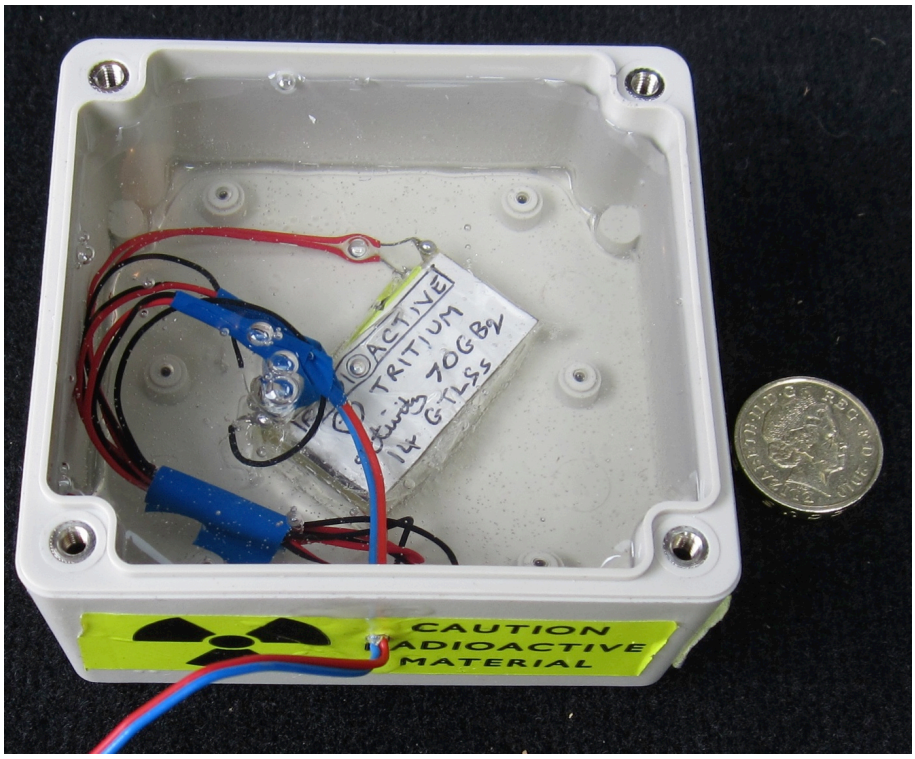



**Figure 4-29:** ICRB prepared for burial in ground, showing potting material and radioactive markings on the protective casing

The ICRB was buried at a depth of 90cm in soil of 19% gravimetric moisture content (at the time of installation) as illustrated in Figure 4-30. The battery enclosure was affixed to the buried water pipe (of diameter 100mm) by means of a Jubilee® clip [216] and two plastic cable ties.

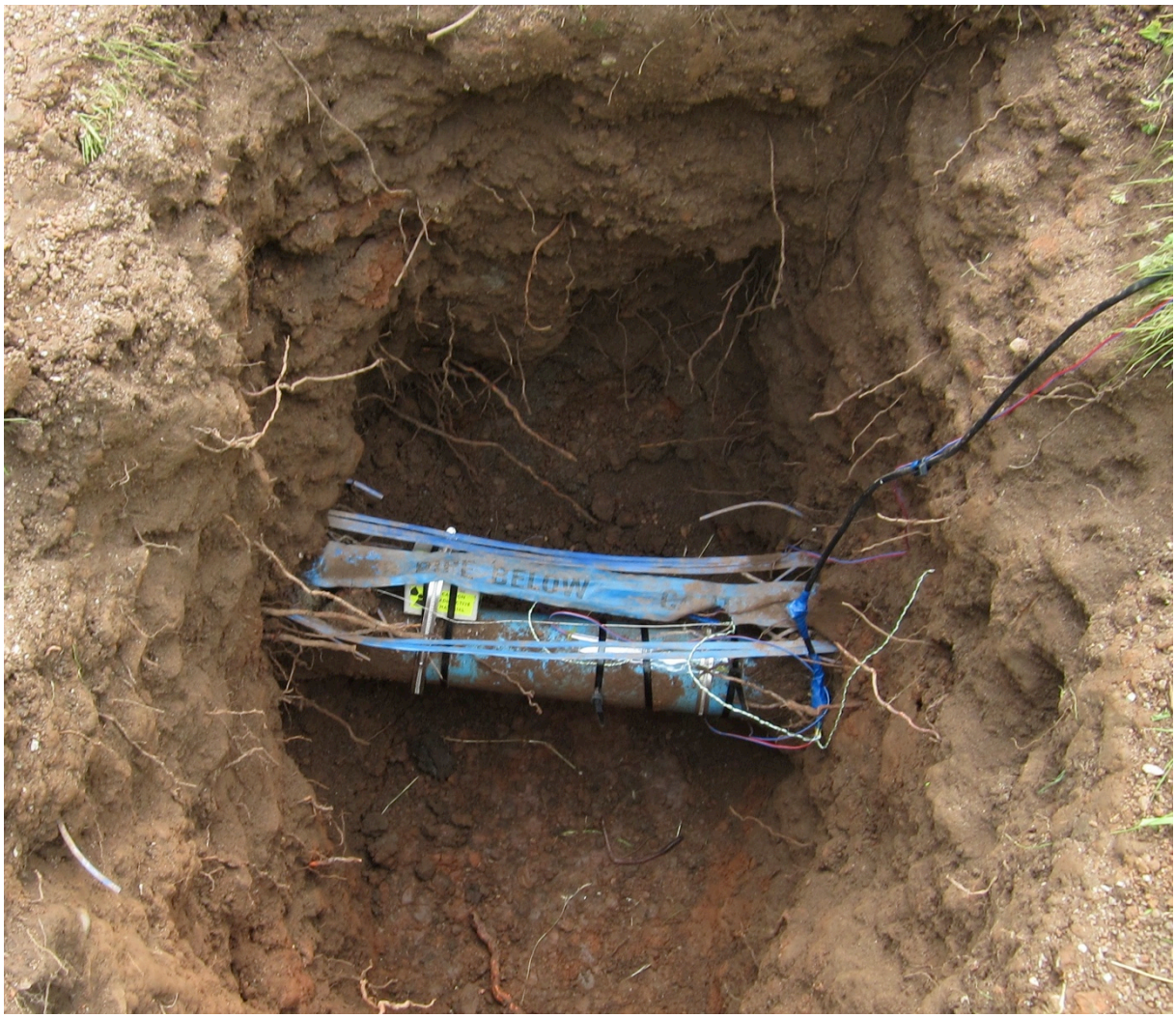


**Figure 4-30:** ICRB burried at a depth of 90cm in soil and fixed to a water pipe

The battery was connected to a sensor node (above ground) able to read the voltage of the device and transmitted the reading wirelessly to a mother-node with a data logger The voltage readings were stored in this data logger over time before transmitting them to a storage place in the cloud where the data could then be

accessed remotely via the internet. The sensor node used a 10 bit (1024 steps) ADC to compare the incoming voltage from the ICRB against a steady reference voltage of 5V giving a measurement resolution of 4.88mV. The ADC is accurate to ±0.05% according to the components's datasheet. Further images of the burial are shown in Appendix C.3.

## 4.10 Conclusions

Aspects of the indirect conversion radioisotopic battery and capacitor power system worthy of further practical investigation were identified following initial testing. A wide variety of ICRB component parts were investigated as to their effect on the performance of the overall power source. Casings to house the ICRB components were designed in Solidworks [199] and manufactured using a 3D printer.

Testing of the ICRB and capacitors evolved into increasingly accurate automated testing regimes. A secure test environment to ensure ambient electromagnetic radiation was not incident on the PV cells of the ICRBs was developed and successfully tested to ensure its robustness for purpose. Testing of capacitors revealed a characteristic known as dielectric absorption, which would have to be considered when evaluating the results of ICRB testing.

The performance of the PV cells was investigated at a variety of illuminance levels, in order to generate I-V curves. In addition an ICRB was buried on a working water pipe in order to determine the suitability of this power source for extended buried use. The results of all of the testing described in this chapter are given and commented upon in Chapter 6.

# 5 THEORY OF ENERGY CONVERSION IN AN ICRB

## 5.1 Introduction

It is useful to build up a theoretical understanding of the processes occurring within the radioisotopic battery and also of how altering specific parameters of the battery (such as GTLS dimensions) will affect the electrical output and efficiency of the device. This chapter will provide a model of the entire radioisotopic battery system by investigating the passage of energy within the system. The aim of this chapter is to produce a model capable of estimating the effect on overall efficiency of the battery of altering key parameters within the battery system.

## 5.2 Model of energy conversion and transport in battery

Overall efficiency of the energy system ($\eta_{total}$) can be calculated from Equation (5-1), where $P_{out}$ is the generated electrical power and $P_i$ is the power of isotopic decay.

$$\eta_{total} = \frac{P_{out}}{P_i} \quad \textbf{(5-1)}$$

Overall efficiency may also be expressed in a different way, as shown in Equation (5-2), where $\eta_\beta$ is the efficiency of beta particles leaving the Tritium gas source, $\eta_p$ is the efficiency of photon generation and emission in the phosphor layer, $\eta_t$ is the efficiency of photon transport between emission from the phosphor layer and incidence upon the photovoltaic (PV) cell, $\eta_{pv}$ is the efficiency of conversion of photons into electrical energy inside the photovoltaic cell, and $\eta_c$ is the efficiency of charging of the capacitor.

$$\eta_{total} = \eta_{\beta} \times \eta_{p} \times \eta_{t} \times \eta_{pv} \times \eta_{c} \quad \textbf{(5-2)}$$

Each of the efficiencies utilized in Equation (5-2) relates to the stages of energy transformation and transmission described in Figure 3-25.

By dividing the battery in this manner it is possible to describe these processes individually whilst also discussing the theory used to build up a worthwhile theoretical model of the same stage. The complete theoretical model, much like the battery itself, is therefore simply a combination of all of its constituent parts. The system is treated as an energy transfer and transformation device with each stage (1 through 5) examined and modelled in the following sections of this chapter.

## 5.3 First stage: Kinetic energy of radioisotopic decay

The first stage of the radioisotopic indirect conversion battery entails the generation of beta particles by radioisotopic decay of the tritium gas cloud at the centre of the GTLSs. The key criteria determining the flux at this location are; the activity of the tritium; the density of the gas; the average energy of decay of the tritium; and the volume of the tritium gas.

### 5.3.1 Description of the process

Tritium, in a gaseous form, generates multiple decays every second, with the number of decays determined by the age of the radioisotope and the number of tritium atoms present. If an emitted beta particle collides with a tritium atom then some of the kinetic energy it was emitted with will be lost. Each further collision will further reduce the energy of the beta particle until the energy may be entirely attenuated. The more

closely packed the atoms of tritium are (at higher pressure in a gas) the more likely it is that collisions will occur. For the purpose of this model it is necessary to calculate the energy per time per unit area (power flux) at the surface of the gas cloud of tritium atoms, taking into account the energy lost due to attenuation within the cloud.

### 5.3.2 Model of the process

The point beta source does function as described in Section 3.8.1 is used to model the beta flux power at the surface of the tritium, through application of Equations (3-9) and (3-10). A series of suggested values for the variables in Equations (3-8), (3-9) and (3-10) is presented in

**Table 5-1** [175, 176].

**Table 5-1:** List of variables and suggested values for tritium for the point beta source equations [175, 176]

| Parameter | Specific activity (*Ci/g*) | Molecular mass (*g*) | Average tritium decay energy (*keV*) | Absorption coefficient ($cm^2/mg$) | Stopping power of the medium ($keV.cm^3/mg$) |
|---|---|---|---|---|---|
| **Abbreviation** | $A_m$ | $M_3$ | $\varepsilon_{av}$ | $v'$ | $W_0$ |
| **Value** | 9700 | 6 | 5.7 | 15 | 56.6 |

The total beta power flux ($P_\beta$) from a GTLS of given geometry may be calculated by multiplying the surface area by the flux per unit area as shown in Equation (5-3).

$$P_\beta = (\pi . D_C . L)\frac{dP_\beta}{dS_L} + (2\pi R_c^2)\frac{dP_\beta}{dS_E} \quad \textbf{(5-3)}$$

The power that could potentially be generated by the same volume of tritium gas as in the above equations (if there were to be no losses of energy due to self-

absorbtion) ($tP_\beta$) may be arrived at by Equation (5-4), where $J$ is the conversion factor from electron volts into Joules ($1eV=1.602X10^{-19}J$).

$$\boldsymbol{tP_\beta = 3.7X10^{10}.A_m.b.L.\pi.R_C^2.\varepsilon_{av}.J} \quad \textbf{(5-4)}$$

Therefore the efficiency of the beta power flux from the tritium gas ($\eta_\beta$) may be calculated through application of Equation (5-5).

$$\boldsymbol{\eta_\beta = P_\beta / tP_\beta} \quad \textbf{(5-5)}$$

Utilising the mathematical modelling software MATLAB® (Mathworks, Inc.), the code for which is shown in Appendix B.1, the power flux and efficiency of beta power flux have been calculated. Various lengths and diameters of GTLSs along with different gas pressures were considered during these calculations. Figure 5-1 shows a graph generated by application of Equation (3-9) for the beta flux (relative to the saturation level of beta flux) of a 100% pure tritium gas inside a cylindrical formation of radius 0.85cm and length 1cm (with the geometry chosen to match an earlier use of these equations).

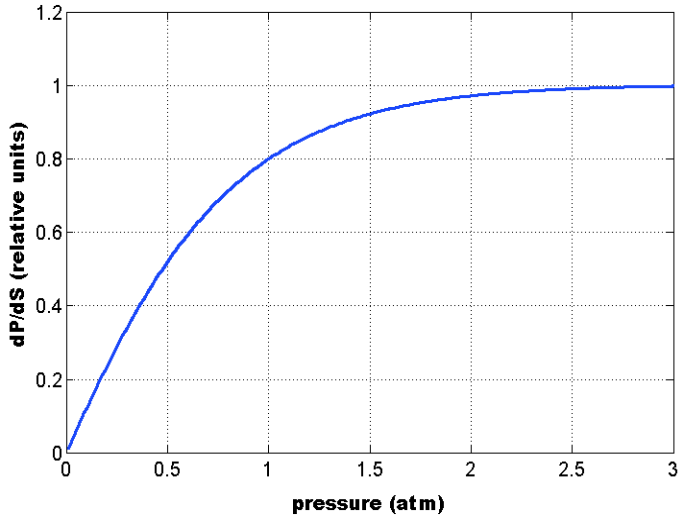



**Figure 5-1:** Beta power flux at the surface of a cylinder of radius 0.85cm and length 1cm with increasing pressure

From Figure 5-1 it can be seen that increasing the pressure of the tritium gas does not correspond to a linear increase in the surface power flux of beta radiation. The surface beta flux power reaches a saturation point above which any increase in tritium gas pressure will no longer result in gains. This is due to the attenuation of beta particle energies by tritium molecules. As the pressure of the gas increases the number of beta particles emitted at any given time will be similarly increased, however, the tritium molecules are also more densely packed next to each other. There is therefore an increased likelihood of emitted beta particles hitting nearby tritium molecules and losing some of their kinetic energy. Eventually any additional beta particles being generated will lose all of their kinetic energy in impacts with tritium molecules before reaching the surface of the gas. In this way saturation may be said to have occurred.

## 5.4 Second stage: Conversion into light energy

In the second stage of energy transformation within the indirect conversion radioisotopic battery, beta radiation from the first stage is incident on a phosphor layer, generating photons (light) in the process. The process of photon generation is described in this section, with a discussion of the effect of their prolonged exposure to radiation. The efficiency of the phosphor (as taken from empirical tables) may be applied directly to the overall calculation for the efficiency of the radioisotopic battery. There is no need to separately model this aspect of the battery operation as these are known values.

### 5.4.1 Description of process

The phosphor commonly used in green light emitting GTLSs is ZnS:Cu, where the Zinc Sulphide (ZnS) is the metallic compound and copper (Cu) is the activator (sometimes with Aluminium as a co-activator

The spectral radiance of a green GTLS (using ZnS:Cu) as manufactured by mb-microtec AG and used in this research is shown in Figure 5-2 and posesses a peak spectral emission at 531nm

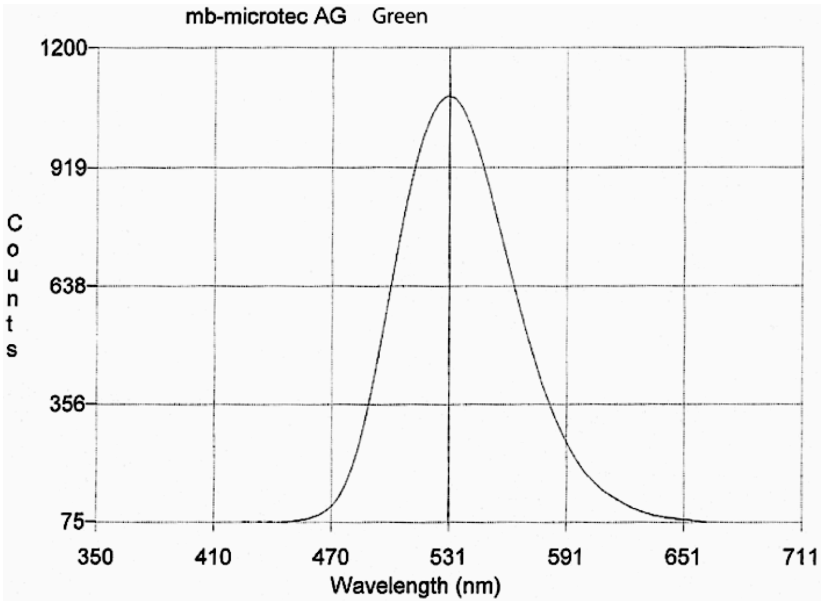



**Figure 5-2:** The spectral radiance of a green light emitting GTLS (reproduced from [217])

Phosphors in the form of a crystal lattice are damaged by the bombardment from radioactive decay products. The extent of this damage is related to the type of phosphor, the type of radioactive decay, the energy and activity of the radioisotope, and the duration of exposure. As can be seen from Figure 5-3 [218, 219] GTLSs coated internally with ZnS have been measured/predicted to decrease in illumination intensity by a factor of four over a time period when the tritium activity within them

has decreased by only a factor of two. This suggests that the ZnS layer has halved its efficiency of photon generation over the corresponding period, due to radiation damage of the ZnS layer.

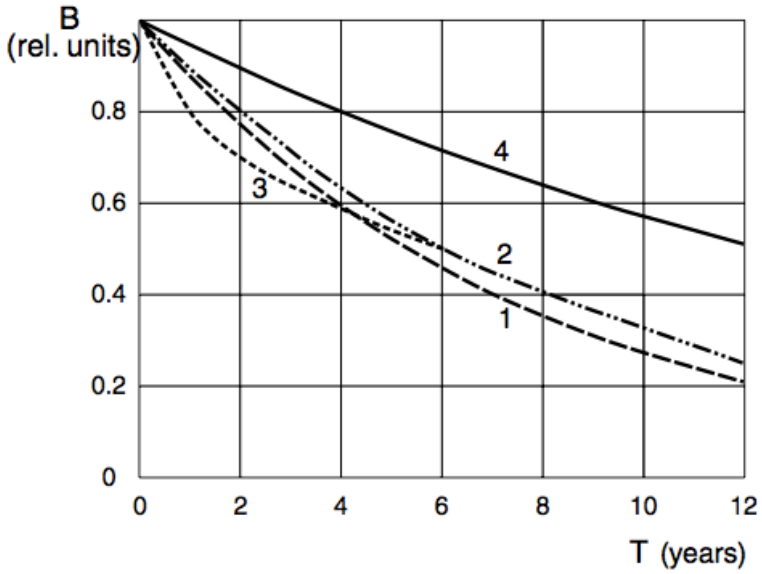



**Figure 5-3:** Decrease in brightness of GTLSs over time (1,2,3) and decrease in tritium power (4) (reproduced from [218, 219])

Damage to the phosphor layer may comprise phosphor atoms being displaced from the crystal lattice, or of impurities being generated in the lattice. In the case of ZnS exposed to low energy beta radiation degradation occurs mainly due to the generation of a Zn layer on the inner surface of the phosphor layer [220]. Examination of GTLSs many years after initial construction has shown that this layer of metallic zinc thickens over time, reducing the power flux of beta particles capable of reaching the phosphor layer and reducing the brightness of the phosphor illumination. It has been found that thermal annealing of the phosphor layer prior to exposure to radiation may reduce the damage inflicted by radioactive bombardment [221].

## 5.5 Third stage: Transport of light energy into photovoltaic cell

The light emitted by the phosphor layer (and modelled in the previous stage) must first travel to the surface of the p-n junction in the PV cell before it may be transformed into electrical energy. This transmission of light may seem trivial at first, however much of the energy contained in the light can be lost during this stage unless the method of transmission has been correctly considered. This section will concern itself with energy losses incurred through the transmission of light from the glass/phosphor boundary inside an individual GTLS right up to the surface of the p-n junction. The key aspects affecting photonics (reflection, refraction, and absorbtion) will all be considered and described. Absorbtion of light within the glass surround of the GTLSs or in the protective glass layer atop the p-n junction will be ignored due to the high transparency of these materials to light and their relative thinness, resulting in extremely low levels of absorbtion occurring in these regions. Key areas where absorbtion of light (and hence energy loss) within the battery system may be reasonably expected to occur are into the casing surround of the battery and back into the phosphor layer of the GTLSs. The model will therefore attempt to determine percentages of emitted light which are incident on these areas along with the losses which might be reasonably expected to occur as a result. The modelling of this stage of energy transfer will be separated into three sections: light leaving a single GTLS; the photonics of multiple GTLSs in close proximity to each other; and light interacting with the casing and becoming incident on the PV cell.

The method used to model the transport of light within the ICRB will involve separating the geometry into perpendicular component planes and then multiplying

the results together. This concept is shown in Figure 5-4 where the effect of vector AB is formed by combining the effects of the vectors AC and AD.

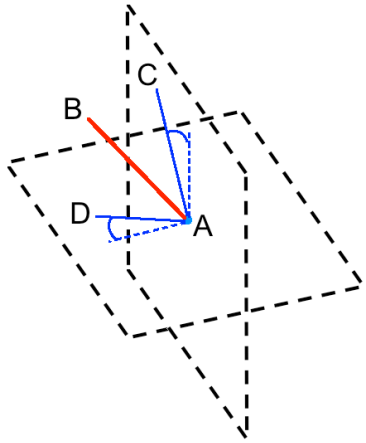



**Figure 5-4:** Method of combining vectors in the transport of light within the ICRB

In this example light is modelled to have been generated at point A and is then incident on a surface (for example the glass/air boundary) at point B. The vector AB is never explicitly modelled with the vectors AC and AD being formed instead and their combination giving an approximation for the effect of AB. This methodology does not give an entirely accurate value for the amount of light transmitted from a given geometry, as the angle of incidence with a surface at point B will not be the same as either the angle of incidence of point C or point D. The losses of light modelled in this manner will be an underestimation for some angles and an overestimation for other angles but will average out to a rough approximation of reality.

The interaction of light within the geometry of the ICRB is further explained by Figure 5-5, where light originating from point ‘O’ is incident on the plane ‘D’ at point ‘A’. Plane ‘D’ lies in the x=-6 line and is parallel to the x and z axis as seen in the figure. In this example plane ‘D’ represents the transition point between two materials

having different refractive indexes (going from glass to air). For the purposes of this example glass will be said to have refractive index 1.5 and air a refractive index of 1. Light incident on the plane 'D' may pass into the plane, be reflected back, or be partially transmitted and partially reflected. The percentage of light transmitted is the quantity which is of interest to this model and may be generated by use of the Fresnel equations which will be introduced later.

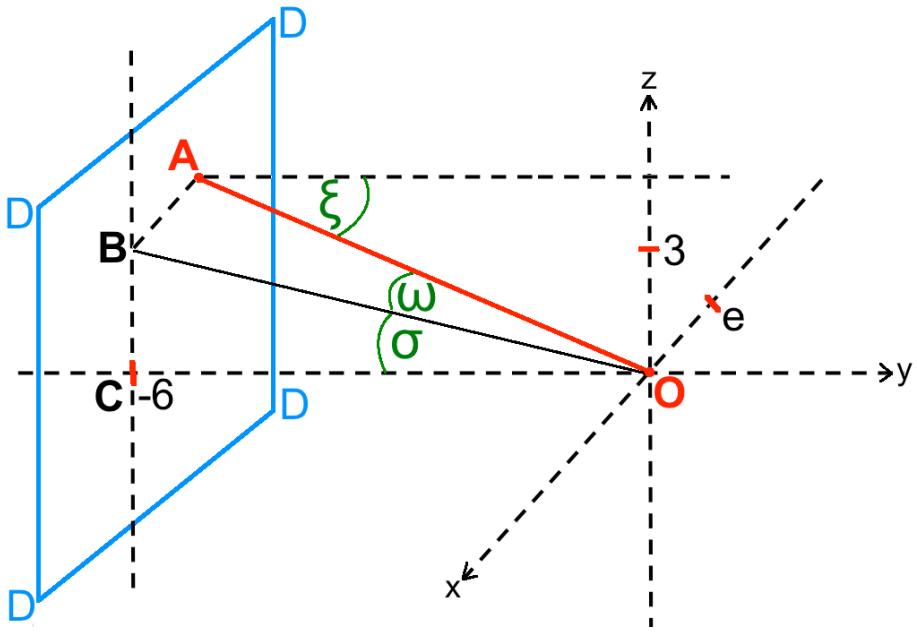



**Figure 5-5:** The percentage of light transmitted as calculated from actual path of the light or a combination of the component parts of the path of light

In Figure 5-5 point 'A' is at y=-6, z=3 and x=e where e is a variable. Perfect modelling of the incidence of light on the plane 'D' requires creating a normal to the plane at point 'A' and then finding the angle ξ between these two vectors. Application of the Fresnel equations to the angle ξ then reveals the percentage of light (if any) that is transmitted. The model that has been used in this research separates the path of light into two constituent parts, shown here as OCB, which generates angle σ, and OBA, which generates angle ω. These two angles are then applied to the Fresnel

equations and the resultant transmissions of light are multiplied together in order to generate an approximation of the light transmitted by the incidence of OA with plane ‘D’. The suitability of this theory may be tested by calculating the transmission of light in this geometry, at various angles and by the two methods, and then comparing the results.

From Figure 5-5 it is possible to describe ‘B’ with the coordinates (e, -6, 3), while ‘O’ is at the origin. A normal from the plane ‘D’ at any point ‘B’ will have the vector form (6j). The angle ξ between the vector AO and the normal from plane ‘D’ at point ‘A’ can then be calculated using the dot product of these two lines (as described later in this chapter). Meanwhile, angle σ can be calculated by taking the inverse tangent of CO and CB, and angle ω can be found by taking the inverse tangent of BA and BO. The generated angles are then applied to the Fresnel equations to produce the percentage of light transmitted into plane ‘D’.

Taking point ‘B’ at coordinates (-2, -6, 3) angle ξ can be calculated to be $31.00^{o}$ which will result in a loss of 5.88% of light incident on plane ‘D’ according to the Fresnel equations. Meanwhile, angle σ is found to be $26.56^{o}$ giving a loss of 4.74% of light and angle ω is $16.60^{o}$ giving a loss of 4.07%. Multiplying the percentage of transmitted light for angle σ and angle ω gives an overall loss of 8.62% for this geometry using the methodology of separating the light vector into its constituent parts. This is an overestimation of the amount of light lost in this geometric configuration.

Moving point ‘B’ to coordinates (-3, -6, 3) produces a new angle ξ, which is calculated to be 35.26$^{o}$, and would produce a 8.91% loss of light at plane ‘D’. Angle σ remains 26.56$^{o}$, which produces a 4.74% loss of light and angle ω changes to 24.10$^{o}$, which produces a 4.44% loss of light. Multiplication of the transmitted percentage of light for angles σ and ω in this new configuration results in 8.97% overall loss of light, which is very similar to the loss of light calculated from the actual path of the light (angle ξ).

Moving point ‘B’ once more to coordinates (-4, -6, 3) produces another angle ξ, which is 39.81$^{o}$, and produces a 22.91% loss of light at plane ‘D’. Angle σ remains 26.56$^{o}$ giving a 4.74% loss of light while the new angle ω is 30.81$^{o}$, which gives a 5.80% loss of light. Combining the losses of light from these two angles gives a 10.27% overall loss of light, which is an underestimation of the amount of light lost in this geometric configuration.

From these three positions of point ‘B’ it can be said that at times the model used in this research overestimates the amount of light lost, at times underestimates the amount of light lost, and sometimes provides a very close estimates of the light loss. Overall the instances of overestimation and underestimation should, to a large extent, balance each other out. The model used in this research provides results which overall slightly underestimates the transmission of light.

The chosen methodology is a reasonable approximation of the transmission and reflection of light within the ICRB structure and is, if anything, an underestimation of the amount of light transmitted. It is believed that the methodology chosen to model the transport of light in this section is of use for comparing the effects of altering the

geometry and materials of the ICRB. Empirical measurements of the light emitted from the GTLSs will test the validity of this supposition.

### 5.5.1 Transmission of light from a single GTLS

In this section the efficiency of the transmission of light from the phosphor/glass boundary and through the glass/air boundary on the outside of the GTLS will be considered. The light will be assumed to be of one wavelength (which is a reasonable assumption for the GTLSs as discussed in Section 5.4.1) and therefore fixed values of refractive indices may be utilized for each of the mediums. A further starting assumption is that the emission of light will be considered to be in all directions from any given point with even intensity. Light will be assumed to have left the phosphor layer at this stage and the following modelling will consider the path of light after it has just entered the glass surrounding this phosphor layer (i.e. at the phosphor/glass boundary), as illustrated in Figure 5-6.

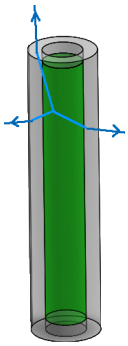


**Figure 5-6:** Emission of light from a GTLS

The geometry of the phosphor/glass layer where light emission occurs is best described as a cylinder with closed ends. In order to facilitate a clearer picture of the path of light in this area the model will be divided into smaller segments, Section X and Sections Y1 and Y2, as illustrated in Figure 5-7. The transmission of light from

these sections will then be considered individually before a unified model of transmission of light from an individual GTLS may be constructed.

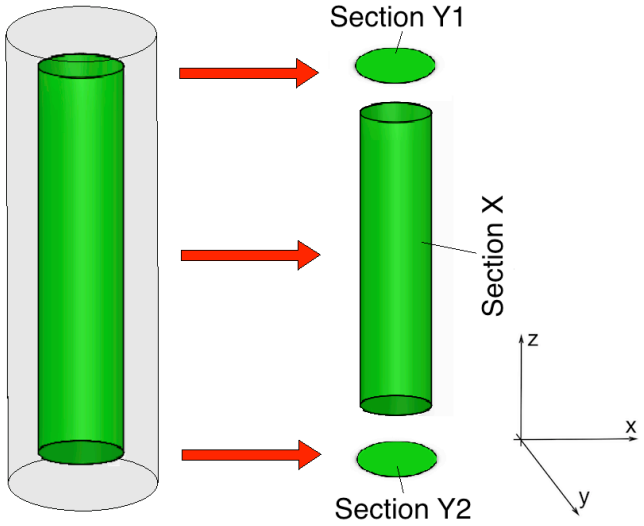



**Figure 5-7:** Glass/Phosphor boundary displayed graphically and segmented into constituent parts

### 5.5.1.1 Light emitted from the open ended cylinder

Considering first the transmission of light from Section X in Figure 5-7 it is beneficial to initially study the 'x-z' plane of potential light emission. An infinitely small ($\delta\beta$) segment of the cylinder is considered as illustrated in Figure 5-8, and light emissions over the length of this segment are calculated. This model is useful due to the infinite symmetry of a circle about its origin, meaning that all segments through the cylinder are similar to each other and that therefore only one such segment must be considered. In addition, due to symmetry it is only necessary to consider $0 \leq \theta \leq \frac{\pi}{2}$, where $\theta$ is the angle of light emission from a normal to the phosphor/glass boundary.

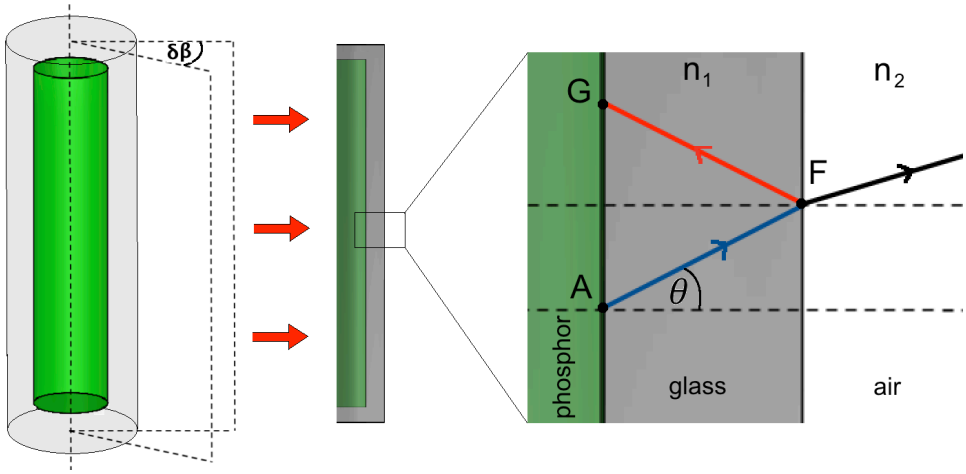



**Figure 5-8:** Infinitely small angle (δβ) segment of Section X and demonstration of emission, transmission and reflection of light

Emission of light from point 'A' will result in transmission through the glass/air boundary at point 'F' (as illustrated in Figure 5-8) so long as angle $\theta$ does not exceed the critical angle ($\theta_c$), which may be calculated through application of Equation (5-6) (where $n_1$ is the refractive index of the material the light is transmitted from and $n_2$ is the refractive index of the material the light is transmitted into).

$$\theta_c = arcsin\left(\frac{n_2}{n_1}\right) \tag{5-6}$$

The percentage of light transmitted ($T_\theta$) and reflected ($R_\theta$) is calculated for each angle $0 \leq \theta \leq \frac{\pi}{2}$ at this point by application of the Fresnel equations [184] as shown integrated between these limits in Equation (5-7), where $T_\theta = 1 - R_\theta$.

$$R_\theta = \frac{2}{\pi}\int_0^{\frac{\pi}{2}}\left[\left(\frac{n_1 cos\theta - n_2\sqrt{1-\left(\frac{n_1}{n_2}sin\theta\right)^2}}{n_1 cos\theta + n_2\sqrt{1-\left(\frac{n_1}{n_2}sin\theta\right)^2}}\right)^2 + \left(\frac{n_1\sqrt{1-\left(\frac{n_1}{n_2}sin\theta\right)^2} - n_2 cos\theta}{n_1\sqrt{1-\left(\frac{n_1}{n_2}sin\theta\right)^2} + n_2 cos\theta}\right)^2\right]d\theta \tag{5-7}$$

The transmission of light in the x-z plane of this geometry is further illustrated by Figure 5-9 (a) (b) (c), where *A, B* and *C* are points of light emission, *O* to X the height

of the phosphor layer, l the external height of the GTLS cylinder, ti the thickness of glass at the top and bottom of the GTLS, d the thickness of glass on the sides of the GTLS and z the distance from the emission to the base of the section.

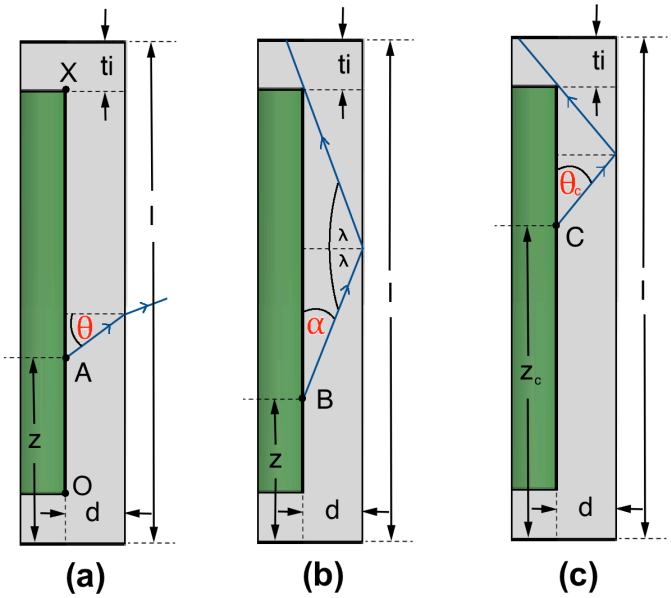



**Figure 5-9:** 'x-z' plane of Section X showing (a) transmission through the side, (b) reflection and transmission through the end, and (c) point of maximum reflective transmission

Equation (5-7) can be resolved between points 'O' and 'X' in order to form a solution for the total percentage of light transmitted through the side ($T_{sX}$) of Section X.

$$T_{sX} = \frac{1}{l-2ti}\int_{ti}^{l-ti}\frac{2}{\pi}\int_{0}^{\frac{\pi}{2}}(1-R_{\theta})d\theta\, dz \qquad \textbf{(5-8)}$$

Light may also be emitted from the end of Section X (as shown in Figure 5-9 (b)) from point 'B' both directly and also due to reflection from the side glass/air boundary. As is illustrated in Figure 5-9 (c) this emission will occur until point 'C' where the angle of incidence on the end glass/air boundary will be $\theta_c$. This transmission of light from the end of Section X is described by Equation (5-9) with the derivation shown in Appendix B.2.1.

$$ti \le z < z_c \qquad T_{e1} = \frac{1}{(z_c - ti)} \int_t^{z_c} \frac{1}{(\kappa)} \int_{\left(\frac{\pi}{2} - \kappa\right)}^{\frac{\pi}{2}} (1 - R_{A\kappa}) d\kappa dz$$

$$z_c \le z \le (l - ti) \qquad T_{e2} = \frac{1}{(l - ti - z_c)} \int_{z_c}^{(l-ti)} \frac{1}{\theta_c} \int_{\left(\frac{\pi}{2} - \theta_c\right)}^{\frac{\pi}{2}} \left(1 - R_{A\theta_c}\right) d\theta dz \qquad \textbf{(5-9)}$$

$$\text{where } z_c = \left(l - ti - \frac{2d}{tan\theta_c}\right) \text{ and } \kappa = tan^{-1}\left(\frac{2d}{l - ti - z}\right)$$

The overall percentage of light transmitted into air through the ends ($T_{eX}$) of Section X can then be calculated as shown in Equation (5-10).

$$T_{eX} = \frac{T_{e1}(z_c - ti) + T_{e2}(l - ti - z_c)}{(l - 2ti)} \qquad \textbf{(5-10)}$$

When added together Equations (5-8) and (5-10) will provide the average percentage transmission of light from Section X when it has become incident on the glass/air boundary for the first time. However, it is also necessary to consider what happens to the light if it reflects from the glass/air boundary at point ‘F’ in Figure 5-8. This light will then be incident on the phosphor/glass boundary at point ‘G’ where a percentage of this light will be transmitted into the phosphor and will be absorbed while the remaining percentage will be reflected back towards the glass/air boundary. This light will now be subject to Equation (5-8) or (5-10) again for its second transmission at the glass/air boundary. Reflection at point ‘C’ on the glass/phosphor boundary is modelled by application of the Fresnel equations this time utilizing the refractive indices of phosphor and glass as the mediums through which the light travels. Reflections and transmissions may proceed in this manner until all light has been transmitted or has been absorbed into the phosphor. A general formula for transmission at a single point and for a single angle ($T_\infty$) is presented in Equation

(5-11), using the total light reflected from the phosphor/glass boundary ($R_{PE}$) and the total light reflected from the glass/air boundary ($R_{AE}$) at the end of Section X.

$$T_{\infty} = \sum_{n=0}^{\infty} R_{AE}^{n} R_{PE}^{n} (1 - R_{AE}) \tag{5-11}$$

In practice the percentage of light left after the first reflection against the glass/phosphor boundary is negligible and therefore Equation (5-12) is a more useful expression of the light transmitted through the end of Section X ($T_{EX}$). In Equation (5-12) $R_{P\alpha}$ is the result from Equation (5-7) using the refractive indices at the phosphor/glass boundary and replacing $\theta$ with $\kappa$ (from Equation (5-9)).

$$T_{EX} = \frac{1}{(l - 2ti)} \left[ \int_{ti}^{z_c} \frac{1}{\alpha} \int_{\left(\frac{\pi}{2} - \alpha\right)}^{\frac{\pi}{2}} \left( (1 - R_{A\alpha}) \left( 1 + (R_{P\alpha})(R_{A\alpha}) \right) \right) d\alpha dz + \int_{z_c}^{(l-ti)} \frac{1}{\theta_c} \int_{\left(\frac{\pi}{2} - \theta_c\right)}^{\frac{\pi}{2}} \left( (1 - R_{A\alpha}) \left( 1 + (R_{P\alpha})(R_{A\alpha}) \right) \right) d\theta dz \right] \tag{5-12}$$

Light transmitted through the side of Section X ($T_{SX}$) must be treated in a similar fashion, and therefore Equation (5-8) is reconstructed into the form of Equation (5-13) in order to include the effect of a secondary transmission through the glass/air boundary.

$$T_{SX} = \frac{1}{l - 2ti} \int_{ti}^{l-ti} \frac{2}{\pi} \int_{0}^{\frac{\pi}{2}} \left( (1 - R_{A\theta}) \left( 1 + (R_{P\theta})(R_{A\theta}) \right) \right) d\theta \, dz \tag{5-13}$$

It is also necessary to consider the transmission of light in the 'x-y' axis, which may be simplified by considering an infinitely thin slice ($\delta z$) of Section X as pictured in Figure 5-10, where *E* is the point of light emission, $\theta$ is the angle of emission, $\alpha$ is the

angle of incidence, $r_i$ is the radius of the phosphor layer circle, and $r_o$ is the radius of the glass circle.

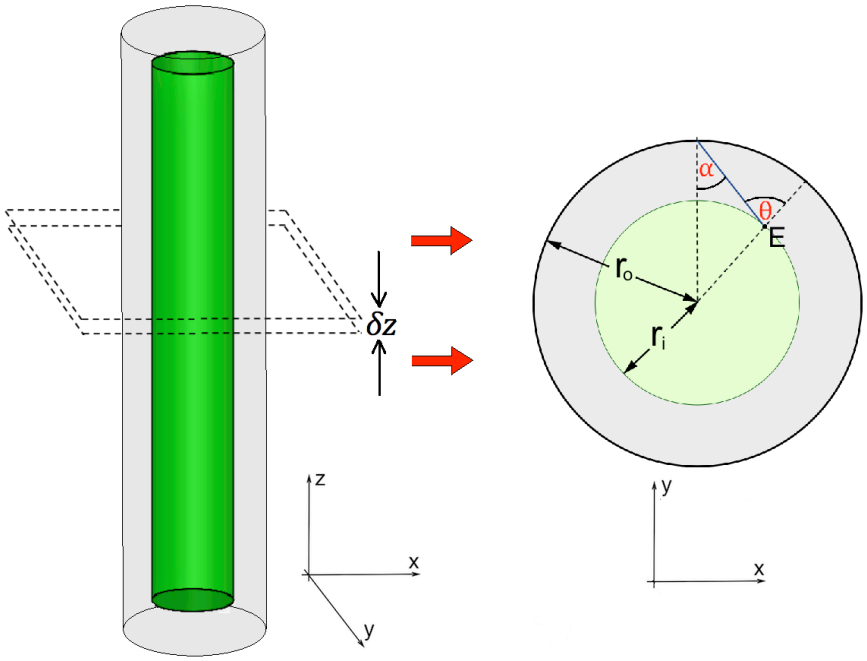



**Figure 5-10:** Schematic of light emission in the 'x' and 'y' directions of Section X

Transmissions in this plane will be the same as in the plane of any other slice taken at any point along the 'z' axis of Section X. Due to the infinite symmetry of circles it is only necessary to calculate the average transmission of light for a single point 'E' on the glass/phosphor boundary. In this configuration the glass/phosphor and glass/air boundaries are not parallel to each other but are instead concentric circles. Therefore the angle of light emission on the glass/phosphor boundary will not be the same as the angle of incidence of that light on the glass/air boundary, except when $\theta=0$. The relationship between the angle of emission ($\theta$) and the angle of incidence ($\alpha$) is described by Equation (5-14), which was formed through application of the sine rule.

$$\alpha = sin^{-1}\left(\frac{r_i}{r_o} sin(\pi - \theta)\right) \qquad \textbf{(5-14)}$$

An interesting consequence of Equation (5-14) is that the maximum angle of incidence in this plane may be lower than the critical angle for the medium change at the glass/air boundary, depending on the ratio of the inner and outer radii of the glass tube. In this configuration of concentric circles there is therefore potentially a greatly reduced loss of light to internal reflection at the glass/air boundary.

Any light reflecting from the glass/air boundary will be incident again on the glass/phosphor boundary at the same angle as of initial emission. This is true for any angle of emission, and light emitted from the glass/phosphor layer will always be re-incident on the glass/phosphor layer after a single reflection.

Calculating the average percentage of light transmitted for any angle of emitted light $0 \leq \theta \leq \frac{\pi}{2}$ requires application of the Fresnel equations as before, however instead of utilizing the angle of emission ($\Theta$), the angle of incidence ($\alpha$) as described in Equation (5-14) should be used. The average percentage of light transmitted in this plane of Section X ($T_{xX}$) is therefore described by Equation (5-15), where the Fresnel equations for incidence with the glass/air boundary ($R_{A\alpha}$) use angle $\alpha$ and the Fresnel equations for incidence with the glass/phosphor boundary ($R_{P\theta}$) use angle $\theta$.

$$T_{xX} = \frac{2}{\pi}\int_0^{\frac{\pi}{2}}[(1 - R_{A\alpha}) + R_{A\alpha}R_{P\theta}(1 - R_{A\alpha})]d\theta \qquad \textbf{(5-15)}$$

The total percentage of light emitted from the open-ended cylinder ($T_{TX}$) may therefore be described by Equation (5-16).

$$T_{TX} = T_{xX}(T_{EX} + T_{SX}) \qquad \textbf{(5-16)}$$

### 5.5.1.2 Light emitted from the flat discs

The remaining surface area of the glass/phosphor boundary can be modelled as a flat disc as displayed in Figure 5-11.

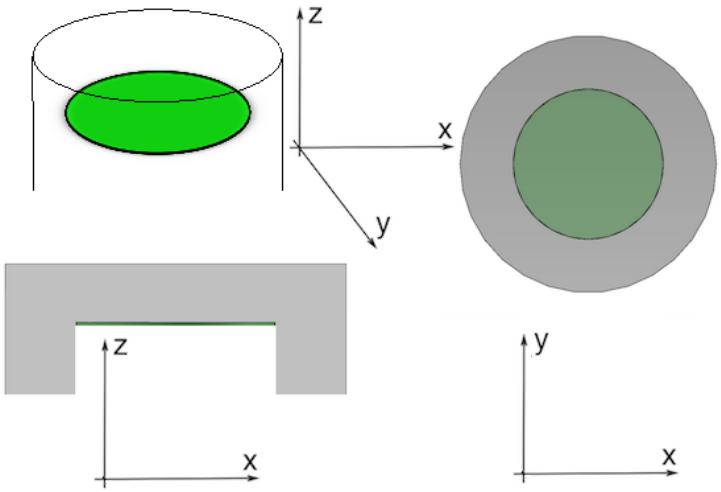
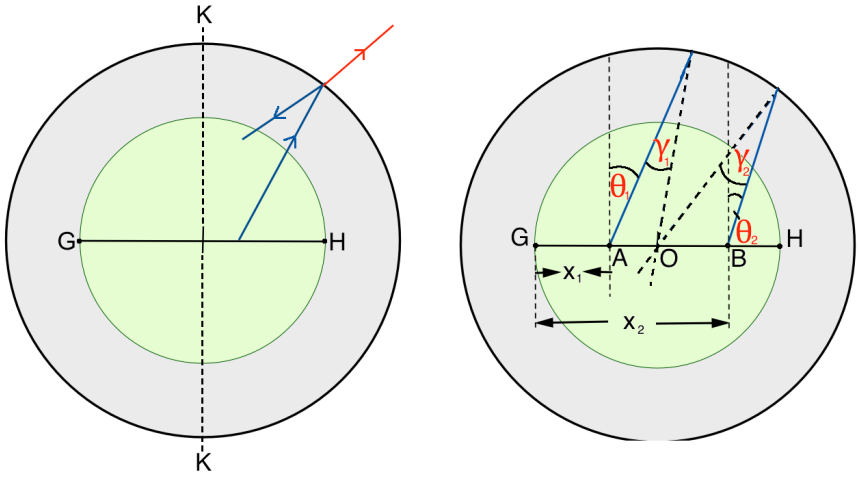



**Figure 5-11:** Representation of the ends (Section Y) of the GTLS

Taking the top down view (x-y plane) first, the disc of the glass/phosphor boundary can be considered as being composed of an infinite number of infinitesimally thin concentric and adjacent circles. Taking a point 'F' on one of these circles reveals that light will be emitted in the same percentage as for any other point on that particular circle. This is true for all of the concentric circles and therefore a simplified model of this geometry can be presented in Figure 5-12(a) where the line 'G' to 'H' is representative of all points on the disc. It is now necessary to calculate the average light transmission which will occur for every angle and from all points along the 'G-H' line. However, due to the symmetry of the circle about the K-K line it is only necessary to consider angles $0 \leq \theta \leq \frac{\pi}{2}$.




**(a)** **(b)**

**Figure 5-12:** Simplified model of the 'x-y' plane of Section Y (a) a single ray of light emission from 'G-H' line, (b) relative angles of emission and reflection in the plane

In Figure 5-12(b) point 'A' exists on the G-H line between 'G' and 'O' (where 'O' is the origin of the two circles) at a distance $x_1$ from 'G', and point 'B' exists on the G-H line between 'O' and 'H' at a distance $x_2$ from 'G'. Light emitted from point 'A' with angle $\theta_1$ and point 'B' with angle $\theta_2$ from the G-H line shown in Figure 5-12(b) will have angles of incidence $\gamma_1$ and $\gamma_2$ with the glass/air boundary. These angles of incidence may be calculated by application of Equation (5-17).

$$0 \leq x \leq r_i \qquad \gamma_1 = sin^{-1}\left[\left(\frac{r_i - x}{r_o}\right) cos\theta\right]$$

$$r_i < x \leq 2r_i \qquad \gamma_2 = sin^{-1}\left[\left(\frac{x - r_i}{r_o}\right) cos\theta\right] \qquad \textbf{(5-17)}$$

After a first reflection from the glass/air boundary the angle of incidence with the glass/phosphor boundary may be considered to be the same as the initial angle of emission ($\theta$) as shown in Figure 5-13.

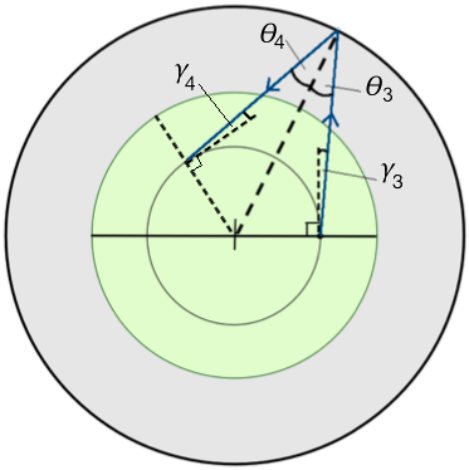



**Figure 5-13:** Angles of transmission and incidence from the 'x-y' plane of Section Y

The total average percentage of light transmitted in the x-y plane of Section Y ($T_{xyY}$) can therefore be calculated by application of the Fresnel equations for incidence with the glass/air boundary using angles $\gamma_1$ and $\gamma_2$ (Equation (5-7) adapted to form $R_{a1}$ and $R_{a2}$) and the Fresnel equations for incidence with the glass/phosphor boundary using angle $\theta$ (Equation (5-7) adapted to $R_p$) as described in Equation (5-18).

$$T_{xyY} = \frac{2}{\pi r_i}\int_0^{r_i}\int_0^{\frac{\pi}{2}}\left[(1-R_{a1})+R_{a1}R_p(1-R_{a1})\right]d\theta dx + \frac{2}{\pi r_i}\int_{r_i}^{2r_i}\int_0^{\frac{\pi}{2}}\left[(1-R_{a2})+R_{a2}R_p(1-R_{a2})\right]d\theta dx \quad \textbf{(5-18)}$$

where $\gamma_1 = sin^{-1}\left[\left(\frac{r_i - x}{r_o}\right)cos\theta\right]$ is substituted for $\Theta$ in $R_{a1}$

and $\gamma_2 = sin^{-1}\left[\left(\frac{x - r_i}{r_o}\right)cos\theta\right]$ is substituted for $\Theta$ in $R_{a2}$

The x-z plane of Section Y must also be considered, as demonstrated graphically in Figure 5-14.

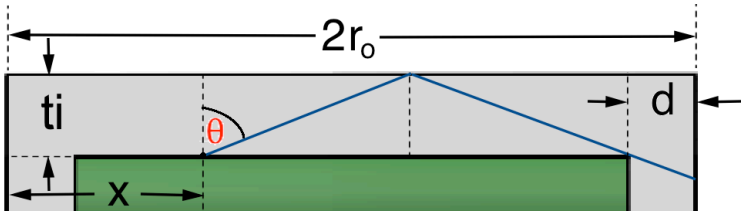



**Figure 5-14:** Light transmission from the 'x-z' plane of Section Y

As can be seen from Figure 5-14 the passage of light from this geometry is similar to that from the x-z plane of Section X shown in Figure 5-9. Therefore it is possible to form expressions for the transmission in the x-z plane of this geometry through the end ($T_{EY}$) (Equation (5-19)) and through the side ($T_{SY}$) (Equation (5-20)), by substituting some of the geometrical component values ($2r_o$ for $l$, $ti$ for $d$, and $d$ for $ti$) into Equations (5-12) and (5-13). In Equation (5-20) $R_{A\tau}$ is Equation (5-7) with $\theta$ replaced by $\tau$ and $R_{P\tau}$ is Equation (5-7) using the indices for the phosphor/glass border and replacing $\theta$ with $\tau$.

$$T_{EY} = \frac{1}{2r_o - 2d}\int_d^{2r_o-d}\frac{2}{\pi}\int_0^{\frac{\pi}{2}}\Big((1-R_A)\big(1+(R_P)(R_A)\big)\Big)\,d\theta\,dx \qquad \textbf{(5-19)}$$

$$T_{SY} = \frac{1}{(2r_o-2d)}\left[\int_d^{x_c}\frac{1}{(\tau)}\int_{\left(\frac{\pi}{2}-\tau\right)}^{\frac{\pi}{2}}\Big((1-R_{A\tau})\big(1+(R_{P\tau})(R_{A\tau})\big)\Big)\,d\alpha dx + \int_{x_c}^{(2r_o-d)}\frac{1}{\theta_c}\int_{\left(\frac{\pi}{2}-\theta_c\right)}^{\frac{\pi}{2}}\Big((1-R_{A\tau})\big(1+(R_{P\tau})(R_{A\tau})\big)\Big)\,d\theta dx\right] \qquad \textbf{(5-20)}$$

where $x_c = \left(2r_o - d - \frac{2ti}{tan\theta_c}\right)$ and $\tau = tan^{-1}\left(\frac{2ti}{2r_o-d-x}\right)$

The total light transmitted from Section Y ($T_{TY}$) is therefore the sum of Equations (5-19) and (5-20) all multiplied by Equation (5-18), as shown in Equation (5-21).

$$T_{TY} = T_{xyY}(T_{SY} + T_{EY}) \qquad \textbf{(5-21)}$$

### 5.5.1.3 Total percentage transmission of light from a single GTLS

The total percentage transmission of light from the GTLS ($T_{gtls}$) is related to the overall surface area of the glass/phosphor boundary ($A_s$), which is described in Equation (5-22).

$$A_s = 2\pi r_i(l - 2ti) + 2\pi r_i^2 \quad \textbf{(5-22)}$$

The overall efficiency of transmission of light may now be calculated by utilizing the discovered efficiencies of transmission of light for Section X and Section Y (which must be considered twice, once for each end, as presented in Equation (5-23).

$$T_{gtls} = \frac{2\pi r_i^2[T_{TY}] + 2\pi r_i(l - 2ti)[T_{TX}]}{2\pi r_i(l - 2ti) + 2\pi r_i^2} \quad \textbf{(5-23)}$$

### 5.5.1.4 Percentage of light transmitted from the end or side of GTLS

It is important to know not only how much light is emitted from the GTLS but also where that light is transmitted and at what intensity. This information will be utilized later in the overall model and must therefore be calculated here first. The percentages of light transmitted can be easily found by separating the direction of light transmission early in the calculations. Light emitted from the side of the GTLS includes light transmitted directly through the sides of Section X and light transmitted from the ends of Section Y as shown in Figure 5-15.

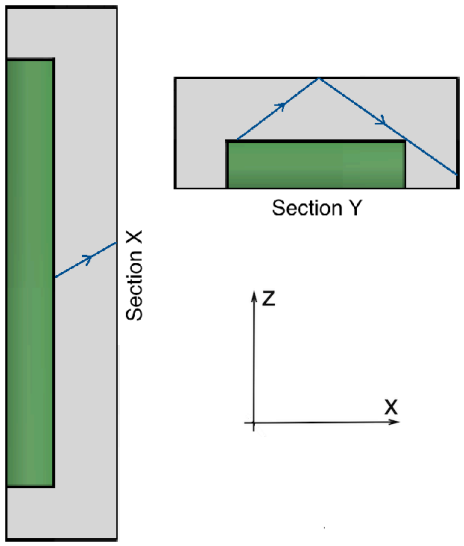



**Figure 5-15:** Light transmitted through the side of the GTLS

The surface area over which transmission of light occurs for each section is now considered. These values of surface area are then applied to the values found in Equations (5-13) (5-15) (5-18) and (5-20), forming a new Equation (5-24) for the overall percentage of light transmitted through the side of the GTLS.

$$T_{sides} = \frac{2\pi r_i^2 \left[T_{xyY}(T_{SY})\right] + 2\pi r_i (l - 2ti)[T_{xX}(T_{SX})]}{2\pi r_i (l - 2ti) + 2\pi r_i^2} \quad \textbf{(5-24)}$$

Light emitted from the ends of the GTLS includes light transmitted through the ends of Section X and light transmitted from the top of Section Y as displayed in Figure 5-16.

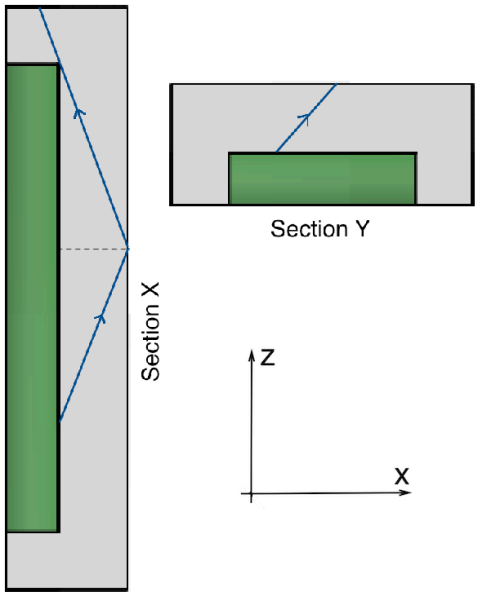



**Figure 5-16:** Light transmitted through the end of the GTLS

Again the surface areas over which transmission of light occurs is considered and these values of surface area are then applied to the values found in Equations (5-12) (5-15) (5-18) and (5-19) forming a new Equation (5-25) for the overall percentage of light transmitted through the ends of the GTLS.

$$T_{ends} = \frac{2\pi r_i^2 \left[T_{xyY}(T_{EY})\right] + 2\pi r_i (l - 2ti)[T_{xX}(T_{EX})]}{2\pi r_i (l - 2ti) + 2\pi r_i^2} \quad \textbf{(5-25)}$$

### 5.5.1.5 Model of light transmitted from a single GTLS

The light transmitted from a single GTLS has been modelled using commercially available software known as Simulink® which is a block diagram graphical interface running on top of MATLAB® [222]. Simulink® is characterized by mathematical block diagrams where some blocks may themselves contain entire block diagrams. Simulink® can therefore be said to contain layers of block diagrams each of which interact with the others and will generate an output from an input when the program is "run". In Addition a Microsoft Excel model was constructed in order to provide verification of the output of the Simulink® model.

An example of block diagrams existing within a single block is provided in **Figure 5-17**, where the block on the left represents one of the Fresnel equations (Equation (5-7)) and the block diagram on the right is the mathematical structure which was created to sit below this block to solve the first Fresnel equation for any values which might be input to it.

The top layer of the Simulink® model created to model the transmission of light from a single GTLS is displayed in Figure 5-18, where the inputs are shown on the left of the program and the outputs on the right. The yellow dialogue box on the left of the image contains the generated value for the overall percentage of light transmitted from a single GTLS. Additional block diagrams from the Simulink® model along with a description of their use are presented in Appendix B.2.2.

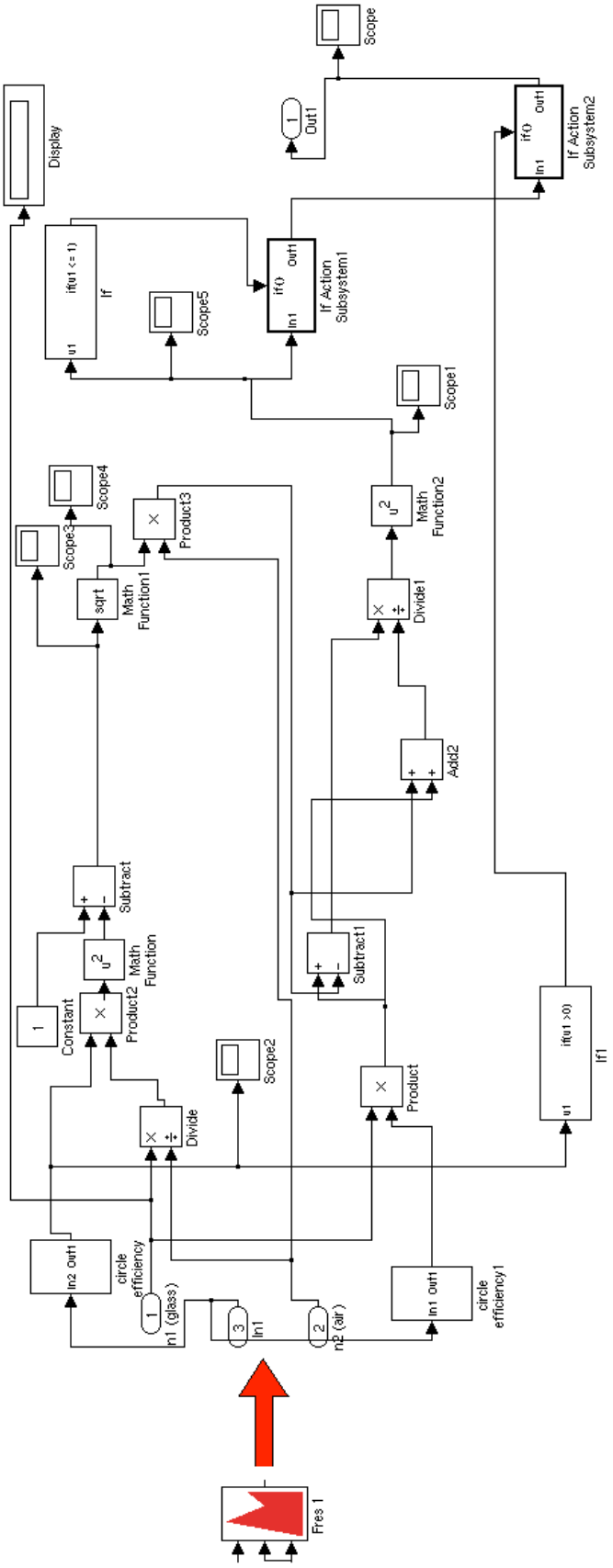



**Figure 5-17:** Simulink® block and block diagram of the first Fresnel equation

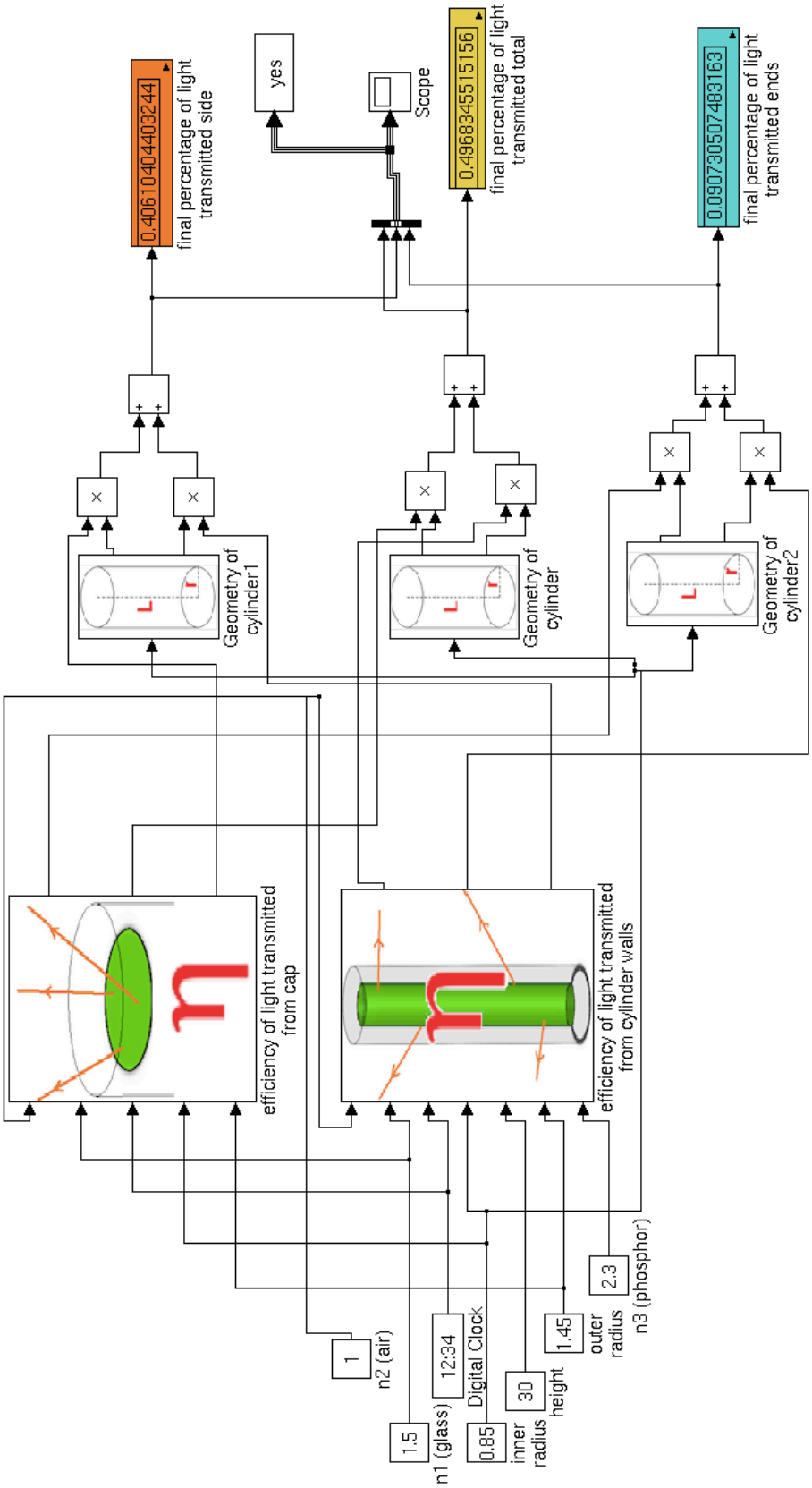



**Figure 5-18:** Master block diagram for Simulink® model of light transmitted from a GTLS

### 5.5.1.6 Total light transmission from a single GTLS

Any light considered to be “lost” in this geometry has in fact become re-incident on the phosphor layer within the GTLS. These photons of light will now generate new photons in the phosphor layer via photoluminescence, and the emission cycle will begin again. Therefore the total percentage of light emitted from a single GTLS may be calculated by applying Equation (5-26), where $\eta_{pc}$ is the efficiency of photon generation in the phosphor layer, taken from Section 3.8.2, and $T_{GTLS}$ may be calculated from Equation (5-23).

$$T_{GTLS} = \sum_{\infty}^{n=0} T_{gtls}\left(\eta_{pc}\left(1 - T_{gtls}\right)\right)^{n} \quad \textbf{(5-26)}$$

## 5.5.2 Efficiency of light emitted from adjacent GTLSs

In Section 5.5.1 the efficiency of light emitted from a single GTLS was considered, however in most battery configurations considered in this research multiple GTLSs are in use at any one time. Generally these GTLSs are positioned parallel and directly adjacent to each other as illustrated in Figure 5-19.

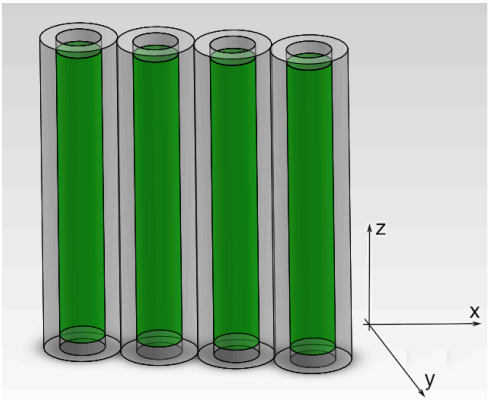



**Figure 5-19:** View of multiple GLTSs positioning

Light emitted by one GTLS may be transmitted into one of the adjacent GTLSs, representing a reduction in transmission of overall light. The exact percentage of light actually transmitted in this type of configuration of GTLSs will be calculated in this section.

### 5.5.2.1 Transmission losses in the x-y plane between 2 GTLSs

As before it is useful to break the geometry down into two complementary planes of investigation. The first plane, the x-y plane, is shown in Figure 5-20 and is generated by taking an infinitely thin slice ($\delta z$) across the two GTLSs. Any slice taken along the height of the GTLSs and parallel to the x-y plane will be similar to itself.

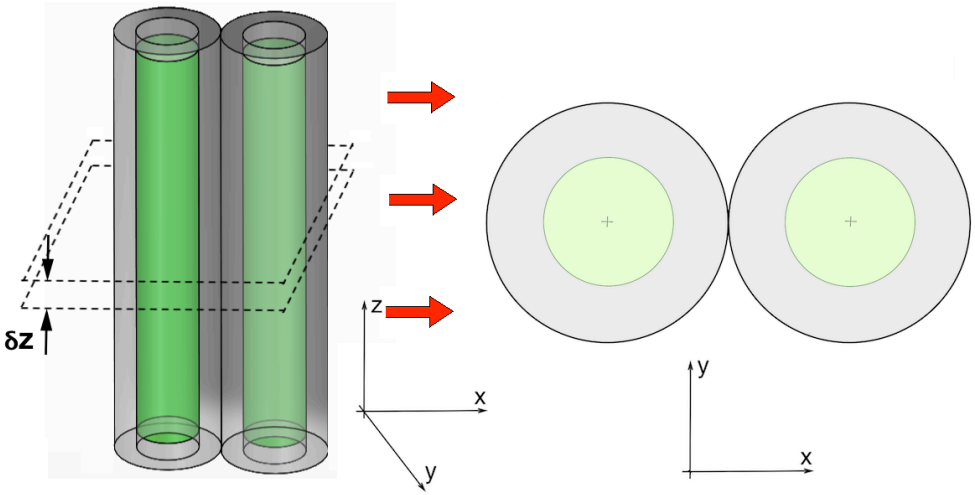



**Figure 5-20:** Transmission of light in the x-y plane of multiple GTLSs

Figure 5-21 shows light emitted from a point 'A' on GTLS1 on the phosphor/glass boundary at an angle $\theta$ to the origin of GTLS1. Light is assumed to be emitted from GTLS1 in the range $0 \leq \theta \leq \frac{\pi}{2}$ with equal intensity in all directions, and is incident from point A on GTLS2 with the angles $\alpha_1, \alpha_2, \beta_1$ *and* $\beta_2$, and not incident in angles $\gamma$ and $\mu$ (such that $\gamma + \beta_1 + \alpha_1 + \alpha_2 + \beta_2 + \mu = \pi$). This is true for any point 'A' along the phosphor glass boundary of GTLS1.

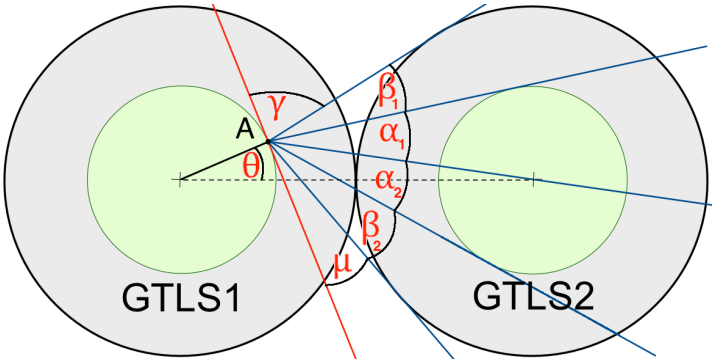



**Figure 5-21:** Light from GTLS1 incident on GTLS2 in the x-y plane

The driving assumption for calculations in this plane will be that any light incident on the phosphor/glass boundary of GTLS2 in Figure 5-21 (designated as angles $\alpha_1$ and $\alpha_2$) will be considered as lost. In addition a certain percentage of light incident on GTLS2 in the glass region (designated $\beta_1$ and $\beta_2$) will also be lost entirely to total internal reflection, while some will be transmitted. Finally, the reflection of light incident on GTLS2 from GTLS1 will be calculated in the $\beta_1$ and $\beta_2$ regions since light incident in these regions represents a high probability of reflecting back beyond GTLS1 and therefore not being subject to a secondary incidence (and hence additional loss) against a GTLS. Due to the symmetry of circles it is only necessary to consider $0 \leq \theta \leq \frac{\pi}{2}$.

Angle $\alpha_1$ may be calculated by considering the geometry described in Figure 5-22, from which it is clear that angular regions $\alpha_1$ and $\alpha_2$ are equal to each other.

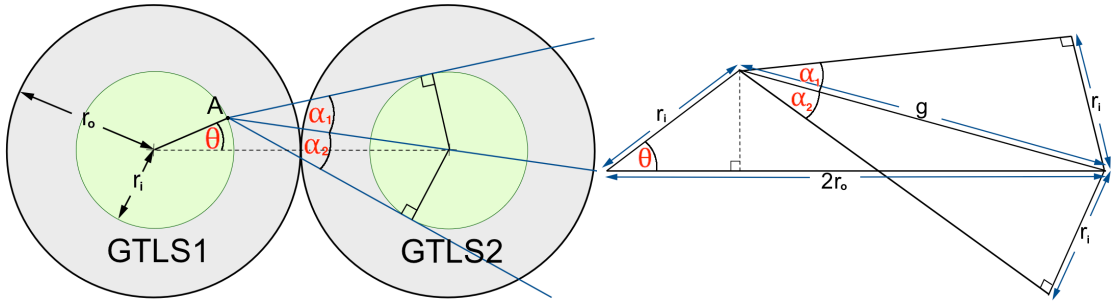



**Figure 5-22:** Geometry of angle $\alpha$ for light emitted from GTLS1 and incident on GTLS2 in the x-y plane

The relationship between the geometrical constants and angles $\theta$ and $\alpha_1$ is presented in Equation (5-27).

$$\alpha_1 = \alpha_2 = sin^{-1}\left(\frac{r_i}{g}\right) \quad \text{where} \quad g = \sqrt{(r_i sin\theta)^2 + (2r_o - r_i cos\theta)^2} \tag{5-27}$$

Consideration of Figure 5-23 shows that $\beta_1$ and $\beta_2$ have the same value, which can be calculated through a similar process as has been shown for $\alpha_1$ and $\alpha_2$.

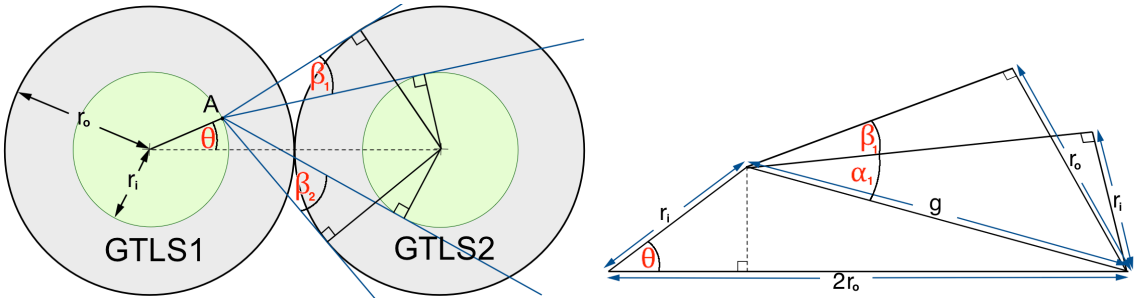



**Figure 5-23:** Geometry of angle $\beta$ for light emitted from GTLS1 and incident on GTLS2 in the x-y plane

A formula for angles $\beta_1$ and $\beta_2$ is presented in Equation (5-28).

$$\beta_1 = \beta_2 = sin^{-1}\left(\frac{r_o}{g}\right) - sin^{-1}\left(\frac{r_i}{g}\right) \quad \text{where} \quad g = \sqrt{(r_i sin\theta)^2 + (2r_o - r_i cos\theta)^2} \tag{5-28}$$

Within the region designated by angle $\beta_1$ there is another region covered by angle $\Omega$ as displayed in Figure 5-24. The light within this region is incident on GTLS2 but will not all be lost, with the percentage of light transmitted through GTLS2 also requiring calculation. The percentage of angle $\beta_1$ that is covered by angle $\Omega$ is dependent on $\theta_c$ for the glass of GTLS2 and the surrounding medium (often air).

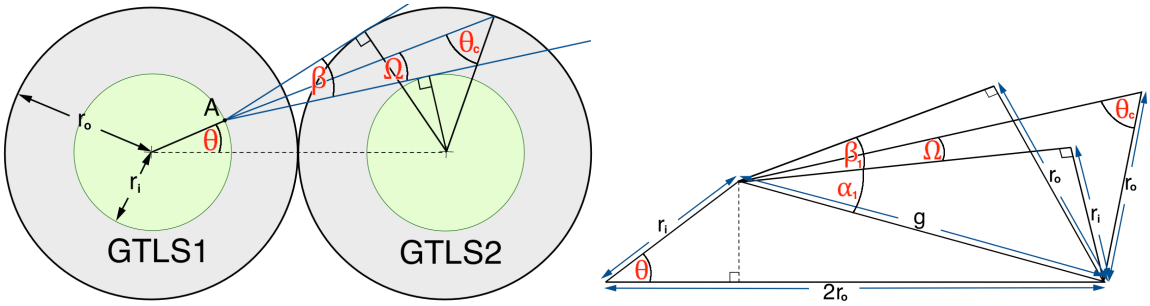



**Figure 5-24:** Light emitted from GTLS1 and transmitted through GTLS2 in the x-y plane

The range of angle $\Omega$ can be calculated by utilizing Equation (5-29).

$$\Omega = sin^{-1}\left(\frac{r_o sin\theta_c}{g}\right) - sin^{-1}\left(\frac{r_i}{g}\right) \quad \text{where} \quad g = \sqrt{(r_i sin\theta)^2 + (2r_o - r_i cos\theta)^2} \tag{5-29}$$

Reflection of light from the glass/air boundary of GTLS2 of light emitted from GTLS1 is illustrated in Figure 5-25. Reflection of light from GTLS2 is ignored in the $\alpha$ regions due to the reflected angle of the light resulting in secondary incidence on GTLS1 (and therefore loss) in the majority of instances. This represents a simplification of the model but the difference in overall transmission between this solution and the optimal solution is assumed to be minimal. It is, however, necessary to calculate the percentage of light which, when emitted from GTLS1, is then reflected from the air/glass boundary (at points 'C' and 'D') on GTLS2 in the $\beta$ regions of incidence.

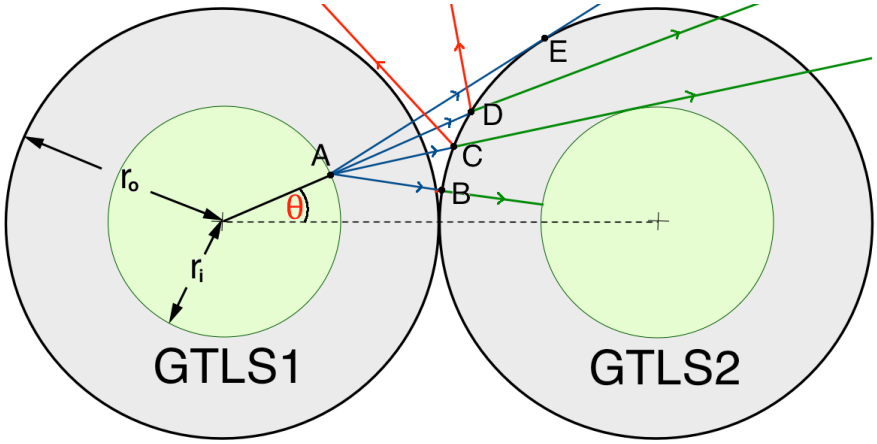



**Figure 5-25:** Reflection of light emitted from GTLS1 against GTLS2

From Figure 5-26, when the angle of light emitted from point A exceeds angle $\alpha_1$ by amount $\delta$, the angle of incidence of the light with GTLS2 will be defined by angle $\gamma_3$.

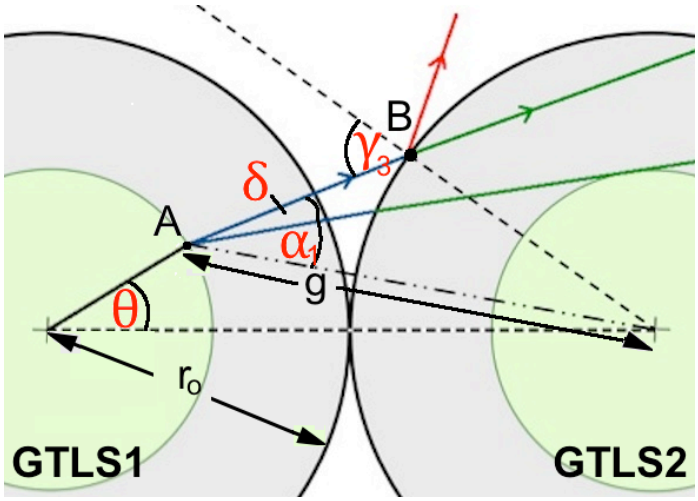



**Figure 5-26:** Calculating the angle of reflectance of light emitted from GTLS1 and incident on GTLS2

Angle $\gamma_3$ may be formulated by application of Equation (5-30).

$$\gamma_3 = sin^{-1}\left(\frac{g.sin(\alpha+\delta)}{r_o}\right) \quad \textbf{(5-30)}$$

By applying the Fresnel equations (Equation (5-7)) utilizing angle $\gamma_3$ in place of $\theta$ the percentage of light reflected at point B in Figure 5-26 may be calculated as $R_B$. Total reflective gains within the $\beta_1$ region ($\beta_g$) for $0 \leq \theta \leq \frac{\pi}{2}$ may then be calculated by application of Equation (5-31), where $R_C$ is the Fresnel equations using angle $\theta$.

$$\beta_g = \frac{2}{\pi}\int_0^{\frac{\pi}{2}} \frac{1}{\pi(\beta-\beta_c)} \int_{\beta_c}^{\beta} (1-R_B)\,d\delta\,d\theta + \frac{2}{\pi}\int_0^{\frac{\pi}{2}} \frac{1}{\pi(\beta_c)} \int_0^{\beta_c} (1-R_B)(R_C+R_C^2)\,d\delta\,d\theta \quad \textbf{(5-31)}$$

### 5.5.2.2 Incomplete regions of light incidence between GTLSs

As angle $\theta$ within GTLS1 increases a point will be reached where light emitted from the point 'B' on the phosphor/glass boundary of GTLS1 will no longer encompass all of GTLS2, as shown in Figure 5-27.

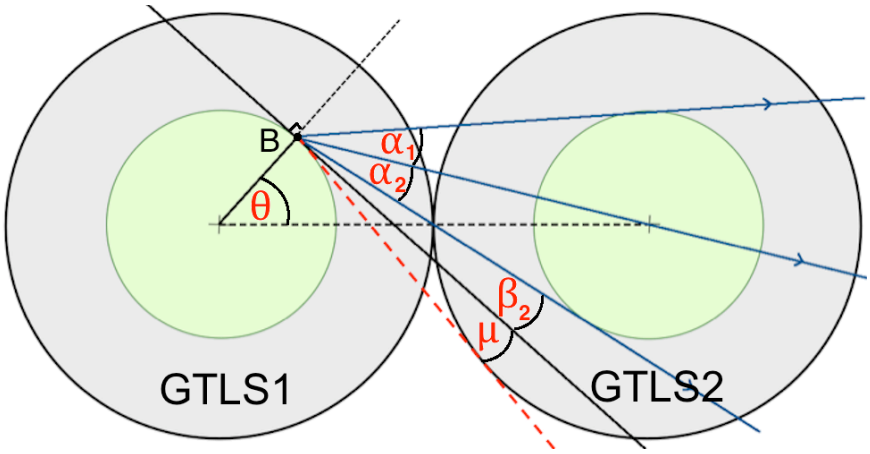



**Figure 5-27:** Angle for which light from GTLS1 is not incident on GTLS2

Light from a point 'B' on the phosphor/glass boundary of GTLS1 may only be transmitted in a spread of angles whose outer limits are defined as a tangent to the circle of the phosphor/glass boundary at point 'B'. In the example presented in Figure 5-27 the region designated as $\beta_2$ is no longer a complete segment. At this point angle $\mu$ (from Figure 5-21 and Figure 5-27) has attained a negative value. As angle $\theta$ increases, $\alpha_1$ and $\alpha_2$ will be similarly effected until finally at $\theta = \frac{\pi}{2}$ only light in the $\beta_1$ region will be incident on GTLS2 from GTLS1. In order to determine the exact amount of each angular region ($\alpha_1$, $\alpha_2$, $\beta_1$, and $\beta_2$), which must be calculated for any given angle of $\theta$, it is necessary to determine the value of angle $\mu$. As angle $\theta$ increases then angle $\mu$ will become negative and will represent the proportion of GTLS2 that does not have light incident upon it from GTLS1 at the given starting point. Angle $\mu$ can be calculated by applying Equation (5-32).

$$\mu = \frac{\pi}{2} - \theta - sin^{-1}\left(\frac{r_i sin\theta}{g}\right) - sin^{-1}\left(\frac{r_o}{g}\right) \quad \textbf{(5-32)}$$

There are specific angles of $\theta$ at which angle $\mu$ will begin to encroach on each of the previously described regions (angles $\alpha_2$, $\beta_1$ and $\beta_2$), which will therefore no longer represent complete angles where loss into GTLS2 may occur, as shown in Figure 5-28.

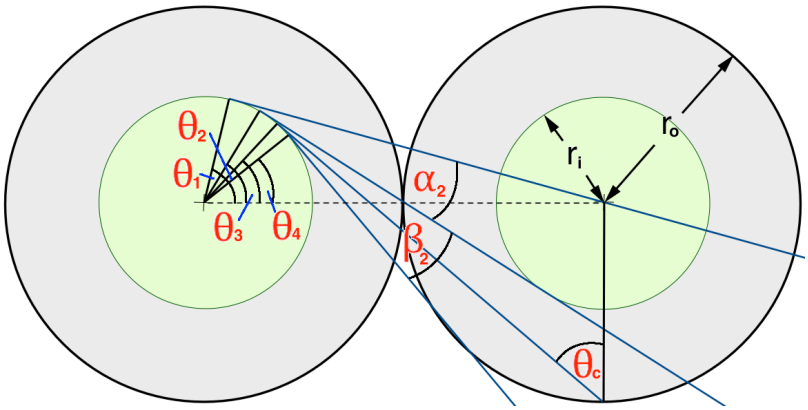



**Figure 5-28:** Limits of angle $\mu$ for light incident on GTLS2 from GTLS1 in the x-y plane

These values of $\theta$ may be calculated from a given geometry of GTLSs by applying Equations (5-33).

$$\theta_1 = cos^{-1}\left(\frac{r_i}{2r_o}\right) \quad \theta_2 = cos^{-1}\left(\frac{r_i}{r_o}\right) \quad \theta_3 = cos^{-1}\left(\frac{(r_o sin\theta_c + r_i)}{2r_o}\right)$$
$$\theta_4 = cos^{-1}\left(\frac{r_o + r_i}{2r_o}\right) \quad \textbf{(5-33)}$$

### 5.5.2.3 Overall formulae for the transmission of light between GTLSs in the x-y plane

For any given angular region ($\alpha_1$, $\alpha_2$, $\beta_1$, and $\beta_2$) of incident light on GTLS2 losses are comprised of two constituent parts: the entirety of that region (as stated in Equations **(5-27)** and **(5-28)**); less the partial region of non-incidence as defined by angle $\mu$ which is related to the specific value of $\theta$ (Equation **(5-32)**). Reflection from the

glass/air boundary of GTLS2 (as expressed in Equation **(5-31)**) must also be taken into account. Drawing together all of these elements a series of formulae for light losses in each angular region in the x-y plane for light emitted from GTLS1 and incident on GTLS2 is presented in Equations (5-34a) to (5-34e).

$\beta_2 \rightarrow \beta_c,$

$$L_{\beta 2c} = \frac{1}{\theta_4}\int_0^{\theta_4} \frac{1}{\pi(\beta_2-\beta_c)} \int_{\beta_c}^{\beta_2} (1-R_B) d\delta d\theta + \frac{1}{(\theta_3-\theta_4)} \int_{\theta_4}^{\theta_3} \frac{1}{\pi(\beta_2+\mu)} \int_0^{(\beta_2+\mu)} (1-R_B) d\delta d\theta \quad \textbf{(5-34a)}$$

$\beta_c \rightarrow \alpha_2,$

$$L_{\beta 2} = \frac{1}{\theta_3}\int_0^{\theta_3} \frac{1}{\pi(\beta_c)} \int_0^{\beta_c} (1-R_B)(R_C+R_C^2) d\delta d\theta + \frac{1}{(\theta_2-\theta_3)} \int_{\theta_3}^{\theta_2} \frac{1}{\pi(\beta_2+\mu)} \int_0^{(\beta_2+\mu)} (1-R_B)(R_C+R_C^2) d\delta d\theta \quad \textbf{(5-34b)}$$

$\alpha_2 \rightarrow \alpha_1,$

$$L_{\alpha 2} = \frac{1}{\theta_2}\int_0^{\theta_2} \frac{1}{\pi(\alpha_2)} \int_0^{\alpha_2} d\delta d\theta + \frac{1}{(\theta_1-\theta_2)} \int_{\theta_2}^{\theta_1} \frac{1}{\pi(\alpha+\beta+\mu)} \int_0^{(\alpha+\beta+\mu)} d\delta d\theta \quad \textbf{(5-34c)}$$

$\alpha_1 \rightarrow \beta_1,$

$$L_{\alpha 1} = \frac{1}{\theta_1}\int_0^{\theta_1} \frac{1}{\pi(\alpha_2)} \int_0^{\alpha_1} d\delta d\theta + \frac{1}{\left(\frac{\pi}{2}-\theta_1\right)} \int_{\theta_1}^{\frac{\pi}{2}} \frac{1}{\pi(2\alpha+\beta+\mu)} \int_0^{(2\alpha+\beta+\mu)} d\delta d\theta \quad \textbf{(5-34d)}$$

$\beta_1,$

$$L_{\beta 1} = \frac{2}{\pi}\int_0^{\frac{\pi}{2}} \frac{1}{\pi(\beta_c)} \int_0^{\beta_c} (1-R_B)(R_C+R_C^2) d\delta d\theta + \frac{2}{\pi}\int_0^{\frac{\pi}{2}} \frac{1}{\pi(\beta_1-\beta_c)} \int_{\beta_c}^{\beta_1} (1-R_B) d\delta d\theta \quad \textbf{(5-34e)}$$

Total light losses in the x-y plane between two GTLSs ($L_{y2}$) may therefore be calculated through application of Equation (5-35).

$$L_{y2} = L_{\beta 2c} + L_{\beta 2} + L_{\alpha 2} + L_{\alpha 1} + L_{\beta 1} \quad \textbf{(5-35)}$$

### 5.5.2.4 When GTLS1 is located between two other GTLSs

When GTLS1 is situated between two other GTLSs as shown in Figure 5-29 light emitted from GTLS1 will also begin to become incident on GTLS3 in addition to GTLS2.

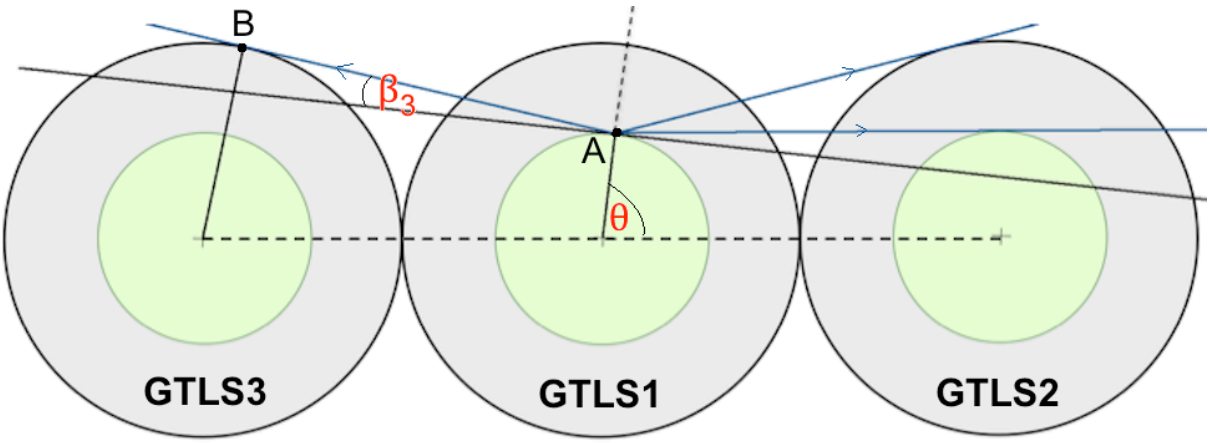



**Figure 5-29:** GTLS1 located between two other GTLSs with light incident on both

The angular region of incidence ($\beta_3$) represents a new source of light loss within the system. As can be seen from Figure 5-30 losses within this region are again separated into two sub-regions as with the other $\beta_1$ and $\beta_2$ regions, with the region separated at the angle of $\beta_c$ where incidence of light at point C with the glass/air boundary of GTLS3 equals the critical angle ($\theta_c$) for those media.

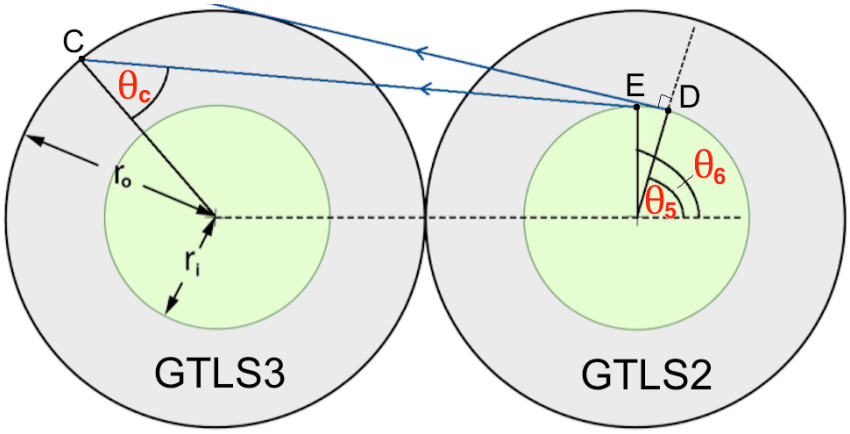



**Figure 5-30:** Calculation of limits for light emitted from GTLS1 into GTLS3

The limits of these sub-regions (angles $\theta_5$ and $\theta_6$) from points D and E are illustrated in Figure 5-31 (a) and (b) which describe the geometry of these limits.

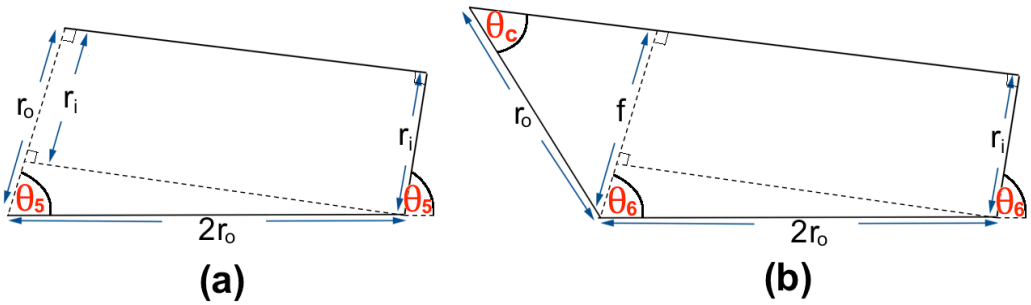



**Figure 5-31:** Geometrical consideration of angles (a) $\theta_5$ and (b) $\theta_6$

Angles $\theta_5$ and $\theta_6$ may then be calculated by application of Equation (5-36).

$$\theta_5 = cos^{-1}\left(\frac{(r_o - r_i)}{2r_o}\right) \qquad \theta_6 = cos^{-1}\left(\frac{(r_o sin\theta_c - r_i)}{2r_o}\right) \tag{5-36}$$

Total losses of light emitted from GTLS1 into GTLS3 ($L_{y3}$) may therefore be calculated by application of Equation (5-37), where $R_B$ represents the Fresnel equations (Equation (5-7)) with angle $\gamma_3$ (Equation (5-30)) substituted for $\theta$.

$$L_{y3} = \frac{1}{(\theta_6 - \theta_5)} \int_{\theta_5}^{\theta_6} \frac{1}{\pi(2\alpha - \mu)} \int_0^{(2\alpha-\mu)} (1 - R_B) d\delta d\theta + \frac{1}{\left(\frac{\pi}{2} - \theta_6\right)} \int_{\theta_6}^{\frac{\pi}{2}} \frac{1}{\pi(\beta - \beta_c)} \int_{\beta_c}^{\beta} (1 - R_B)(R_C + R_C^2) d\delta d\theta + \frac{1}{\left(\frac{\pi}{2} - \theta_6\right)} \int_{\theta_6}^{\frac{\pi}{2}} \frac{1}{\pi(2\alpha - \mu)} \int_0^{(2\alpha-\mu)} (1 - R_B)(R_C + R_C^2) d\delta d\theta \quad \textbf{(5-37)}$$

### 5.5.2.5 Transmission losses in the x-z planes of two adjacent GTLSs

It is also necessary to consider the transmission losses that occur in the x-z planes of two adjacent GTLSs. The x-z plane (P1), shown in Figure 5-32, is generated by taking an infinitely thin slice through the line of origin of the two GTLSs under consideration.

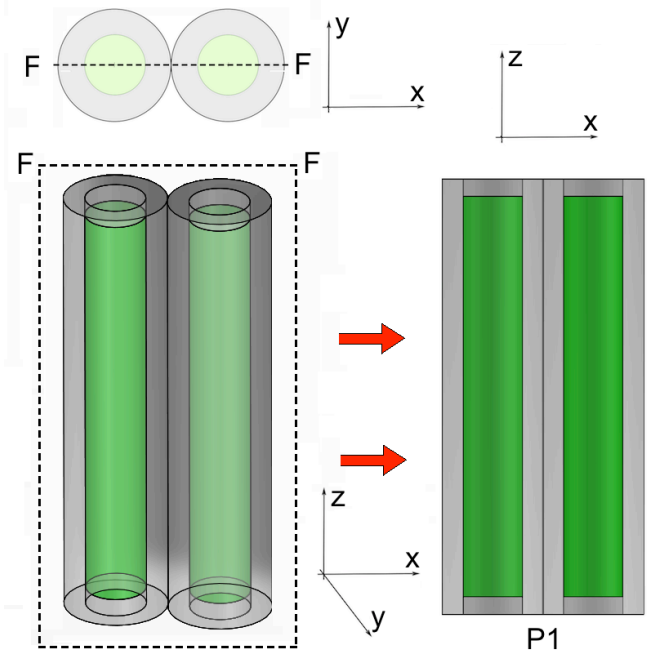



**Figure 5-32:** Transmission of light in the x-z plane of multiple GTLSs through the origins

A slice through the two GTLSs taken at a different location (F-F) as shown in Figure 5-33 reveals a far different geometry in a new x-z plane (P2). The P1 plane represents the 'worst case scenario' regarding light losses in this geometry since any light transmission from GTLS1 around GTLS2 has the smallest angle to travel in.

Meanwhile a plane which just brushed the tangent to the inner circles would provide the best case and light transmitted from GTLS1 would have a much increased potential angle for travel around GTLS2.

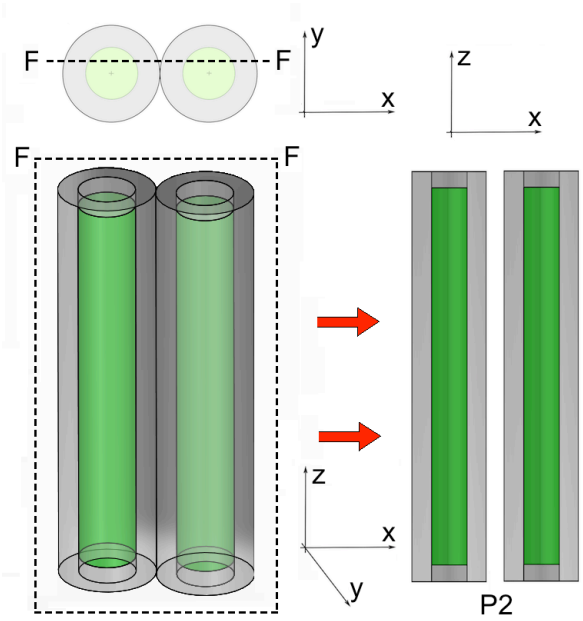



**Figure 5-33:** Transmission of light in the x-z plane of multiple GTLSs at a distance y1 from the origin

Figure 5-34 shows an x-z plane through the two GTLSs taken at an offset of y1 from their origins, where y1 is half of the inner radius of the phosphor cylinder. Calculating the losses of transmitted light in this geometry will provide a reasonable approximation for the average losses of light in all possible x-z planes through the two GTLSs because the x-z geometry formed is the average of all possible planes.

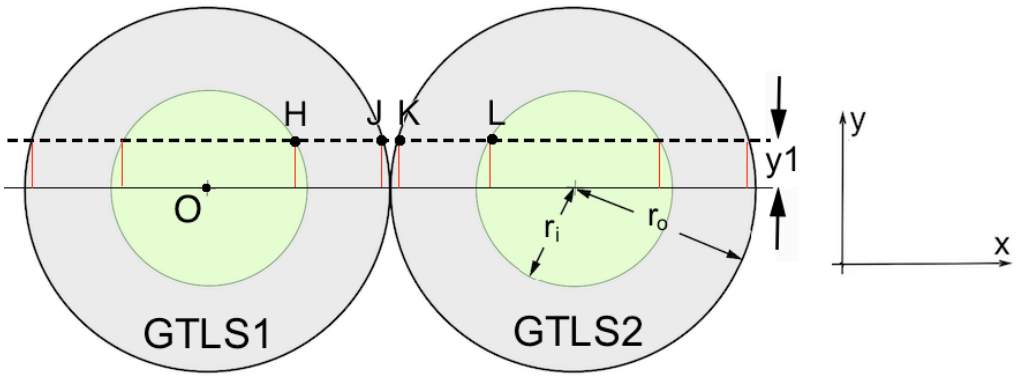



**Figure 5-34:** x-z plane location through two GTLSs offset from the line of origin by 'y1'

The relative dimensions of the glass and phosphor layers found in the x-z plane generated as an approximate average are described in Figure 5-34 as points H, J, K and L. Taking point O at the origin of GTLS1 as having x-y components of (0,0) it is possible to calculate the locations of the other points through application of the equation for a circle, Equation (5-38).

$$x^2 + y^2 = r^2 \tag{5-38}$$

The 'x-axis' components of OH, HJ, JK, and KL may be calculated through application of Equation (5-39) and also by realising that in this instance $y_1=r_i/2$, as described previously.

$$OH = \frac{\sqrt{3}}{2} r_i \qquad HJ = \sqrt{r_o^2 - \frac{r_i^2}{4}} - \frac{\sqrt{3}}{2} r_i$$
$$JK = 2r_o - 2\sqrt{r_o^2 - \frac{r_i^2}{4}} \qquad KL = \sqrt{r_o^2 - \frac{r_i^2}{4}} - \frac{\sqrt{3}}{2} r_i \tag{5-39}$$

These values may now be used to determine the geometry through which light transmission from GTLS1 will be calculated to pass around GTLS2. As shown in Figure 5-35 (a) light emitted from a point 'M' on the outer surface of GTLS1 (the J-J line) will only be transmitted into GTLS2 (line K-K) at angles below the critical angle ($\theta_c$) (this time with the refractive indices of glass and air reversed from Equation (5-7)). For light emitted from point 'M' at angles above $\theta_c$ the light will reflect from GTLS2 (and also from GTLS1 if it is re-incident upon it) and will be transmitted out from the array.

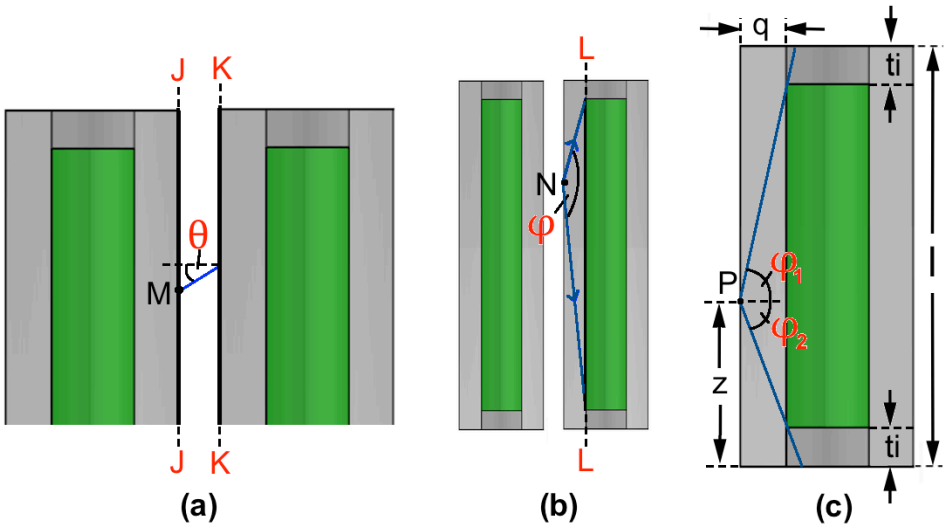



**Figure 5-35:** Representation of light losses in the x-z plane between two GTLSs (a) light incident on GTLS2 from GTLS1, (b) path of light around GTLS2, (c) dimensioned path of light around GLTS2

For a transition from air to glass there is no critical angle, though it is possible that the medium surrounding the GTLSs may be altered and that the refractive index of the 'air' ($n_1$) may then exceed that of the glass layer ($n_2$). Under these conditions there would be a critical angle and the percentage of light transmitted into GTLS2 ($L_{z1}$) should be calculated based on this value, as expressed in Equation (5-40). For $n_1<n_2$ it is assumed that all light incident on the K-K line will pass into GTLS2 and Equation (5-40) may be ignored.

$$L_{z1} = \frac{\frac{\pi}{2}}{arcsin\left(\frac{n_2}{n_1}\right)} \qquad \textbf{(5-40)}$$

From Figure 5-35 (b) light transmitted just through the surface of GTLS2 (line K-K) at a point 'N' will be refracted by its passage through the air/boundary at this point and will then be transmitted in a new range of angles. Light transmitted from point 'N' may be incident on the phosphor layer of GTLS2 through a range of angle $\varphi$. Any light transmitted from the K-K line and not determined to be incident on the phosphor layer

of GTLS2 (the L-L line) will be considered to be transmitted from the array of GTLSs, while light incident on the phosphor layer represents loss in this x-z plane. Due to symmetry of the x-z plane (as shown in Figure 5-35 (b)) it is again only necessary to consider $0<\varphi<\pi/2$. By using the geometries described in Figure 5-35 (c) it is possible to calculate the percentage of light transmitted from point 'P' into the phosphor layer, denoted by angles $\varphi_1$ and $\varphi_2$. In this geometry $q$ is the distance between the K-K and L-L lines of Figure 5-35 and is calculated in Equation (5-39) where it was designated as KL. The percentage of light transmitted (and therefore lost) from point 'P' into GTLS2 ($L_{z2}$) is therefore expressed in Equation (5-41).

$$L_{z2} = \frac{1}{l}\left[\int_0^{l-t}\left(\frac{l-t-z}{q}\right)dz + \int_t^{l}\left(\frac{z-t}{q}\right)dz\right] \quad \textbf{(5-41)}$$

The total percentage of light which will be transmitted from GTLS1 into GTLS2 in the x-z plane ($L_{zt}$) is therefore a multiple of the percentage of light transmitted from GTLS1 onto GTLS2 and then of the percentage of light transmitted into GTLS2 which is then incident on that light source's phosphor layer. This total percentage can be calculated by application of Equation (5-42).

$$L_{zt} = L_{z1} \times L_{z2} \quad \textbf{(5-42)}$$

### 5.5.2.6 General formula for an array of parallel and adjacent GTLSs

When the GTLSs are arrayed in a similar style to Figure 5-36 some GTLSs will be on the ends and some will be in the centre of the array.

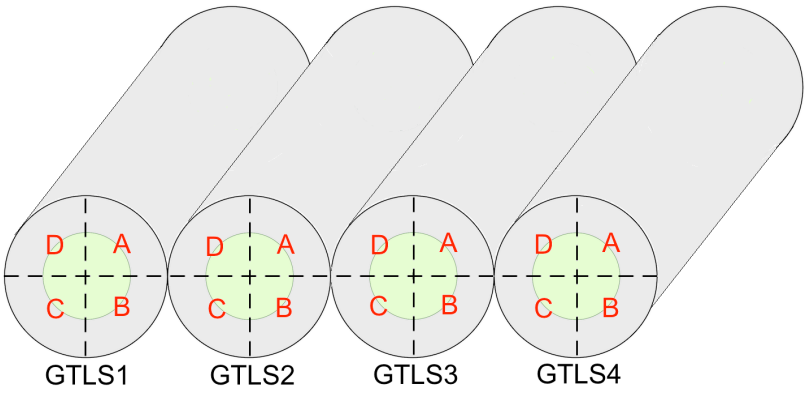



**Figure 5-36:** Side view of an array of GTLSs showing quadrants for each

For a GTLS situated in the middle of the array (such as GTLS2) the losses of light emitted from all four quadrants (A, B, C and D from Figure 5-36) will be the same ($L_1$) as shown in Equation (5-43).

$$L_1 = L_{zt}\left(L_{y2} + L_{y3}\right) \tag{5-43}$$

For GTLS4, located on the end of the array, the losses will not occur in quadrants A and B, and the losses in quadrants C and D ($L_2$) will not include $L_{y3}$ (Equation (5-37)) and may be described by Equation (5-44).

$$L_2 = \frac{1}{2}\left(L_{zt}.L_{y2}\right) \tag{5-44}$$

Therefore for an array of GTLSs of number '$g$' the general formula for the transmission of light from the array ($T_A$) considering losses in both the x-y plane and the x-z plane may be expressed in the form of Equation (5-45).

$$T_A = (g-2)(1-L_1) + (1-L_2) \tag{5-45}$$

### 5.5.2.7 Model of transmission losses between adjacent GTLSs

The losses within this geometry have been determined by construction of suitable MATLAB® scripts, presented in Appendix B.2.3, to model the equations described in

this section. Results from the application of these MATLAB® scripts are presented and discussed in Section 6.2.3.

### 5.5.3 Light reflected from the casing to the solar cell surface

This section will describe the path of light after it has left the GTLSs and its interaction with the casing and ultimately the surface of the solar cells. There are two key areas where light generated in the GTLSs interact with the battery casing: on the ends of the GTLSs and on the sides of the GTLSs at the end of the array, as shown in Figure 5-37. It is necessary to consider the two regions separately and discover mathematical descriptions of their behaviour. It will be assumed that the casing is perfectly diffuse and that therefore any light incident upon it will then reflect at a random angle.

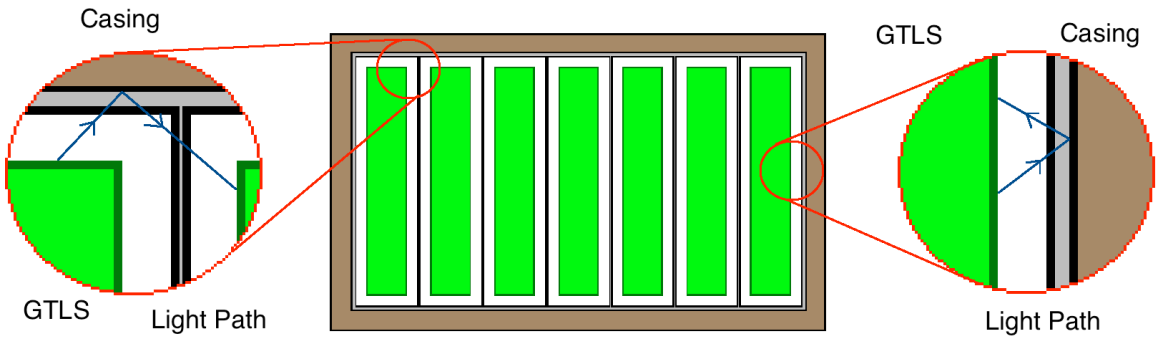



**Figure 5-37:** Top down view of reflection of light against casing inside radioisotopic battery

#### 5.5.3.1 Region 1: Reflection of light emitted from the sides of the end GTLSs with the end of the casing

As can be seen from Figure 5-38 the geometry is symmetrical about the X-X line, and therefore only light from region ‘A’ needs be considered. Losses in this region consist of light reflecting from the casing back into the GTLS and also light which is absorbed

upon incidence with the casing. For this reason the reflectivity of the casing is a crucial factor in this calculation.

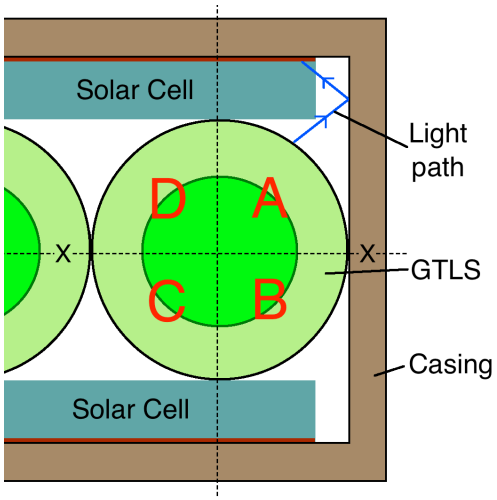



**Figure 5-38:** Side view of reflections in region 1 of battery

The light incident on the solar cell surface due to reflection from the casing is a function of the amount of light incident on the casing from the GTLS and the amount of light from any point on the casing that would reflect back to the surface of the solar cell. It is important to separate these two problems.

The percentage of light incident on the casing from the GTLS can be calculated by considering a point 'E' on the glass/air boundary of the GTLS, as shown in Figure 5-39, and determining the angular range of light ($\beta$) which is incident on the casing.

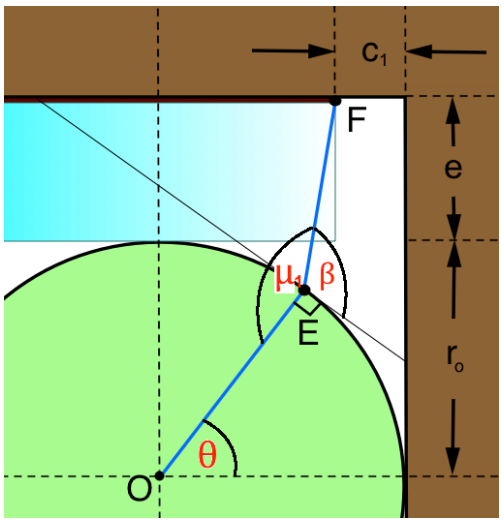



**Figure 5-39:** Light incident on casing from surface of GTLS at point 'E' in region 1

The most effective method for determining the relevant angles within this geometry is by the use of vectors. Taking 'O' as the origin of the GTLS and at position (*0,0*), the angular range $\beta$ may be determined by consideration of OE and FE (where 'F' is the end of the solar cell) as vectors and then finding the angle formed between them. The general solution for the unit vectors of OE and FE are given by Equation (5-46). Point 'E' is located at ($r_o cos\theta$, $r_o sin\theta$), while point 'F' is located at ($[r_o\text{-}c_1]$, $[r_o+e]$), where $c_1$ is the gap between the side of the GTLS and the side of the PV cell, and $e$ is the thickness of the solar cell.

$$\therefore \underset{OE}{\rightarrow} = (\mathrm{r_o cos\theta})\mathbf{i} + (\mathrm{r_o sin\theta})\mathbf{j} \quad \underset{FE}{\rightarrow} = (\mathrm{r_o cos\theta + c_1 - r_o})\mathbf{i} + (\mathrm{r_o sin\theta - e - r_o})\mathbf{j} \qquad \textbf{(5-46)}$$

$$\left(0 \leq \theta \leq {}^{\pi}/_{2}\right)$$

The angle between $\underset{OE}{\rightarrow}$ and $\underset{FE}{\rightarrow}$ is designated as angle '$\mu_1$', which can be calculated by use of the dot product [223] of these two vectors as shown in Equation (5-47).

$$\mu_1 = cos^{-1}\left\{\frac{\overrightarrow{OE}.\overrightarrow{FE}}{\left\|\overrightarrow{OE}\right\|\left\|\overrightarrow{FE}\right\|}\right\} \qquad \textbf{(5-47)}$$

Using the values from Equation (5-46) in Equation (5-47) allows the formation of Equation (5-48).

$$\mu_1 = cos^{-1}\left\{\frac{[(\mathrm{r_o cos\theta})(\mathrm{r_o cos\theta - r_o + c_1})] + [(\mathrm{r_o sin\theta})(\mathrm{r_o sin\theta - r_o - d})]}{\mathrm{r_o}\sqrt{(\mathrm{r_o cos\theta - r_o + c_1})^2 + (\mathrm{r_o sin\theta - r_o - d})^2}}\right\} \qquad \textbf{(5-48)}$$

The angular range of light incident on the casing ($\beta$) can then be calculated from $\mu_1$ according to two regions of $\theta$ where the separating limit is the value of $\theta$ when $\underset{OE}{\rightarrow}$ and $\underset{FE}{\rightarrow}$ are in a straight line. Therefore the total percentage of light emitted from the GTLS

in quadrant A and incident on the casing ($L_{c1}$) may be calculated by solving Equation (5-49).

$$L_{c1} = \frac{1}{\pi(\theta_L)} \int_0^{\theta_L} \left(\frac{3\pi}{2} - \mu_1\right) d\theta + \frac{1}{\pi\left(\frac{\pi}{2} - \theta_L\right)} \int_{\theta_L}^{\frac{\pi}{2}} \left(\mu_1 - \frac{\pi}{2}\right) d\theta \qquad \textbf{(5-49)}$$

$$\text{where } \theta_L = tan^{-1}\left(\frac{r_o+e}{r_o-c_1}\right)$$

### 5.5.3.2 Region 1: Light incident on the PV surface from the casing

By considering the casing surface as perfectly diffuse it is not necessary to consider the angle of incidence on the casing when considering where the light will reflect from this surface. Figure 5-40 provides a graphical representation of the reflection of light from the inner surface of the casing at a point 'H' onto the solar cell with an angular range $\Omega_1$, which is limited by the location of the GTLS at a point 'G'.

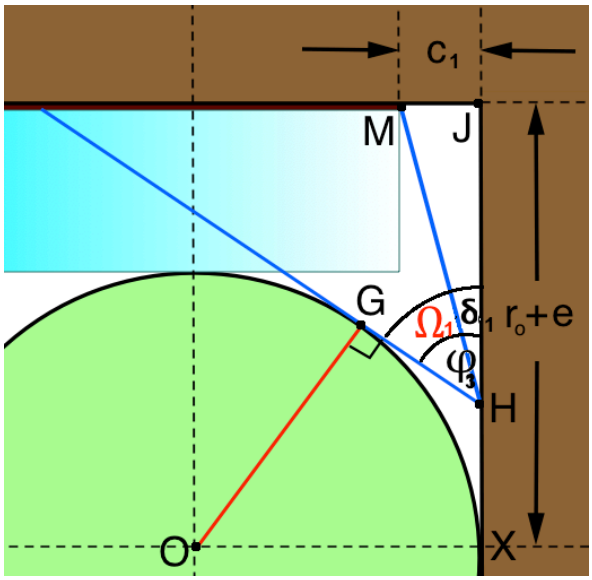



**Figure 5-40:** Light reflecting from the inner surface of the casing onto the solar cell

Point 'O' is again defined as the origin (*0,0*) of the GTLS with point 'G' at ($x_1$, $y_1$), 'H' at ($r_o$, $y$) and 'J' at ($r_o$, $[r_o+e]$). Vector $\underset{HG}{\rightarrow}$ is always a tangent to the GTLS and therefore

the angle between $\underset{HG}{\rightarrow}$ and $\underset{OG}{\rightarrow}$ must always be $\frac{\pi}{2}$. Therefore it is possible to calculate the values of $x_1$ and $y_1$ for point 'G' in terms of $r_o$ and $y$ as shown in Equation (5-50) which is derived in Appendix B.2.4.

$$y_1 = \frac{2yr_o^2}{(y^2+r_o)^2} \qquad x_1 = \sqrt{r_o^2 - \left(\frac{2yr_o^2}{(y^2+r_o)^2}\right)^2} \tag{5-50}$$

From this information it is possible to form an equation describing the angle $\varphi_3$ as shown in Equation (5-51).

$$\varphi_3 = cos^{-1}\left\{\frac{(\mathrm{y}-\mathrm{y}_1)(\mathrm{y}-\mathrm{r_o}-\mathrm{e})}{(\mathrm{y}-\mathrm{r_o}-\mathrm{e})\sqrt{(r_o-x_1)^2+(y-y_1)^2}}\right\} \tag{5-51}$$

Angle $\Omega_1$ is equal to angle $\varphi_3$ less angle $\delta_1$, where angle $\delta_1$ is defined in Equation (5-52).

$$\delta_1 = \tan^{-1}\left(\frac{\mathrm{c}_1}{\mathrm{r_o}+\mathrm{e}-\mathrm{y}}\right) \tag{5-52}$$

It is therefore possible to generate a formula describing the average percentage of light incident on the solar cell surface from the casing from all points between 'X' and 'J'. This general formula is presented in Equation (5-53).

$$L_{S1} = \frac{1}{\pi r_o}\int_0^{r_o}(\varphi_3 - \delta_1)dy + \frac{1}{\pi e}\int_{r_o}^{r_o+e}\left(\frac{\pi}{2} - \delta_1\right)dy \tag{5-53}$$

The total percentage of light from the GTLS that is reflected onto the solar cell surface can now be calculated. This value is dependent on the reflectivity ($R_{ca}$) of the casing inner surface and is expressed in Equation (5-54), which incorporates Equations (5-49) and (5-53).

$$L_T = R_{ca}.L_{S1}.L_{C1} \quad \textbf{(5-54)}$$

### 5.5.3.3 Region 2: Reflection of light emitted from the ends of the GTLSs with the side of the casing

This section describes the interaction of light leaving the ends of the GTLSs and reflecting with the casing as shown in Figure 5-41. Again it is useful to separate this problem into two parts: light from the GTLS to the casing; and light from the casing to the solar cell surface. Once again the casing surface is considered as perfectly diffuse as a working approximation of reality.

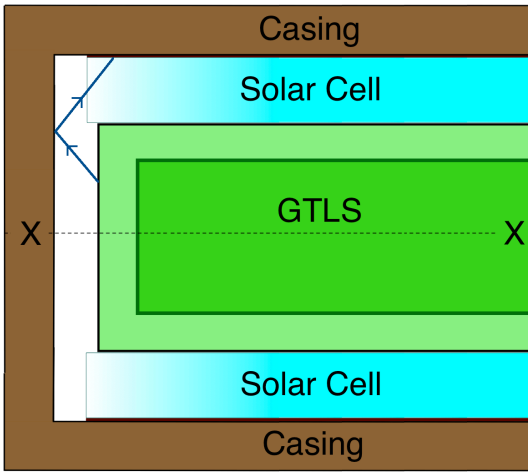



**Figure 5-41:** Side view of the reflection of light in region 2 of the battery

Considering first the light which is incident on the casing from the GTLS leads to a simplified view of the model as presented in Figure 5-42. Light is transmitted from the GTLS at point 'A' and is incident on the casing over the angular range $\alpha_6$ which is the equivalent to $\pi$ less angles $\beta_6$ and $\beta_7$.

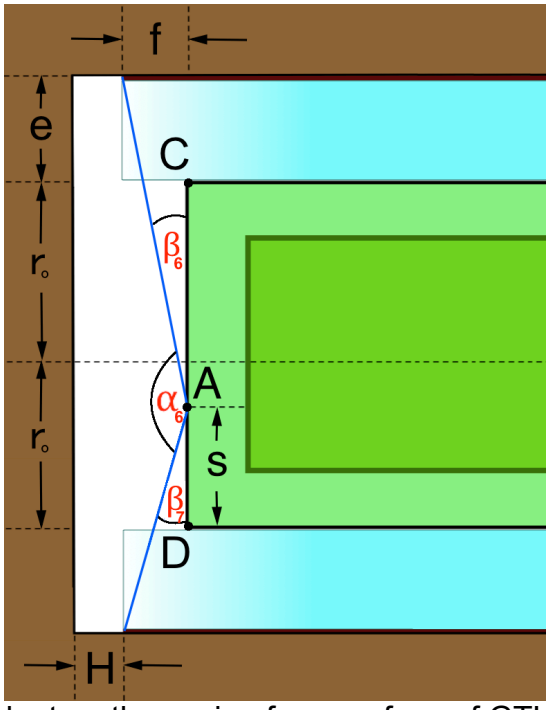



**Figure 5-42:** Light incident on the casing from surface of GTLS at point 'A' in region 2

Angles $\beta_6$ and $\beta_7$ may be calculated by applying Equation (5-55), where $s$ is an arbitrary distance between points 'A' and 'D', the gap between the end of the solar cell and GTLS is denoted by distance $f$ and the gap between the end of the solar cell and the end of the casing is denoted by distance $H$.

$$\beta_6 = tan^{-1}\left(\frac{f}{2r_o+e-s}\right) \qquad \beta_7 = tan^{-1}\left(\frac{f}{s+e}\right) \tag{5-55}$$

By resolving for all points on the end of the GTLS between 'C' and 'D' it is possible to form an expression for the total percentage of light emitted from the GTLS which is incident on the casing. This expression is shown in Equation (5-56).

$$L_{c2} = \frac{1}{2r_o\pi}\int_e^{2r_o+e}\left[\pi - tan^{-1}\left(\frac{f}{s+e}\right) - tan^{-1}\left(\frac{f}{2r_o+e-s}\right)\right]ds \tag{5-56}$$

### 5.5.3.4 Region 2: Light incident on the PV surface from the casing

The percentage of light reflecting from the casing that is then incident on the solar cell must also be calculated. Any light that is incident on the GTLS will be treated as a loss due to the minimal amount of light which would be emitted from a secondary reflection onto the casing. A graphical representation of this problem is presented in Figure 5-43, where point 'B' is the point of reflection on the casing.

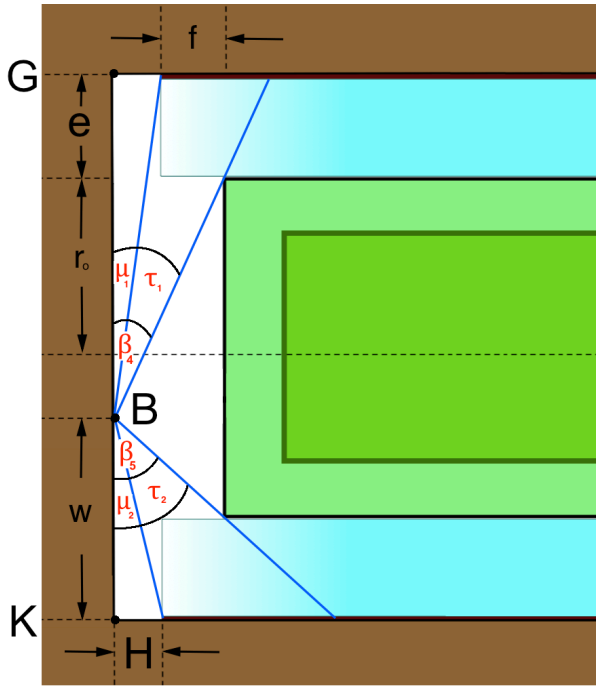



**Figure 5-43:** Light reflecting from the inner surface of the casing onto the solar cell in region 2

Light reflecting from point 'B' will only be incident on the solar cell within the regions denoted as $\beta_4$ and $\beta_5$ in Figure 5-43 which may be calculated from Equation (5-57).

$$\beta_4 = tan^{-1}\left(\frac{H+f}{2r_o+e-w}\right) \qquad \beta_5 = tan^{-1}\left(\frac{H+f}{w-e}\right) \tag{5-57}$$

By resolving for all points along the inside of the end of the casing (point 'G' to point 'K') the total percentage of light directly incident on the solar cell from a single reflection from the casing may be calculated as expressed in Equation (5-58).

$$L_{s2} = \frac{1}{\pi d}\int_0^e \left(\frac{\pi}{2} + \beta_5\right) dw + \frac{1}{2r_o\pi}\int_e^{2r_o+e} (\beta_4 + \beta_5) dw + \frac{1}{\pi e}\int_{2r_o+e}^{2r_o+2e} \left(\beta_4 + \frac{\pi}{2}\right) dw \quad \textbf{(5-58)}$$

The overall percentage of light emitted by the GTLS that is reflected onto the solar cell surface may now be found by application of Equation (5-59), which utilizes Equations (5-56) and (5-58) and the previously described reflectivity ($R_{ca}$) of the casing.

$$L_{T2} = R_{ca}.L_{c2}.L_{s2} \quad \textbf{(5-59)}$$

#### 5.5.3.5 Model of light reflected from the casing to the PV surface

Equations (5-54) and (5-59) have been modelled by generating a MATLAB® script, which is shown in Appendix B.2.5. Results from this modelling are presented in Section 6.2.3.3.

## 5.6 Fourth stage: Conversion of light into electricity in the photovoltaic cell

The photovoltaic cell (also known as a solar cell, or PV cell) converts incident light into electrical energy within a p-n junction. The PV cells used in this research utilized silicon in three main configurations, mono-crystalline silicon, poly-crystalline silicon, and amorphous silicon. In this section the mechanism of conversion from light to electrical energy will be considered and a model of efficiency of this conversion will be presented.

### 5.6.1 Calculated photocurrent in a photovoltaic cell

It is necessary to relate the light incident on the photovoltaic cell with the generation of photocurrent in the device. By substituting Equation (3-18) and into Equation (3-

17) it is possible to generate an expression for the generated short circuit current density within the photovoltaic cell based on measured or known properties. The surface area of the photovoltaic cell may be removed from this expression in order to provide an expression for the generated short circuit current as described below in Equation (5-60).

$$I_{SC}(\lambda) = \frac{q.N_p.QE(\lambda)}{t} \quad \textbf{(5-60)}$$

In this way Equation (5-60) may be used as the link between the energy of incident photons and the current initially generated in the photovoltaic cell. If, however, the series resistance is higher than $10\Omega/cm^2$ then the short circuit current will be lower than the photocurrent with the difference being lost in heat generated in the resistance. Under this condition it is not acceptable to use $I_{SC}$ and $I_{ph}$ interchangeably.

### 5.6.1.1 Modelling the efficiency of a photovoltaic cell

Assuming all other values are known then Equation may be solved via an iterative process for all values $0<I<I_{SC}$. One such method of iterative solution uses what is known as the Newton-Raphson method [224] as expressed in Equation (5-61), where $x_{n+1}$ is the new answer, $x_n$ is the previous answer, $f(x_n)$ is a function of $x$ and $f'(x_n)$ is the derivative of the function of $x$. By this method it is possible to produce convergence to a suitably accurate answer after only a few steps of application.

$$x_{n+1} = x_n - \frac{f(x_n)}{f'(x_n)} \quad \textbf{(5-61)}$$

The input values necessary to solve Equation, however, must be determined experimentally for each specific photovoltaic cell and for the applicable intensity and

range of illumination. A model of a photovoltaic cell has been developed using MATLAB® based in part on the script developed by González-Longatt [225]. The MATLAB® model developed for this stage of energy transformation in the radioisotopic battery is presented in Appendix B.3 An example of such an I-V curve is presented in Figure 5-44.

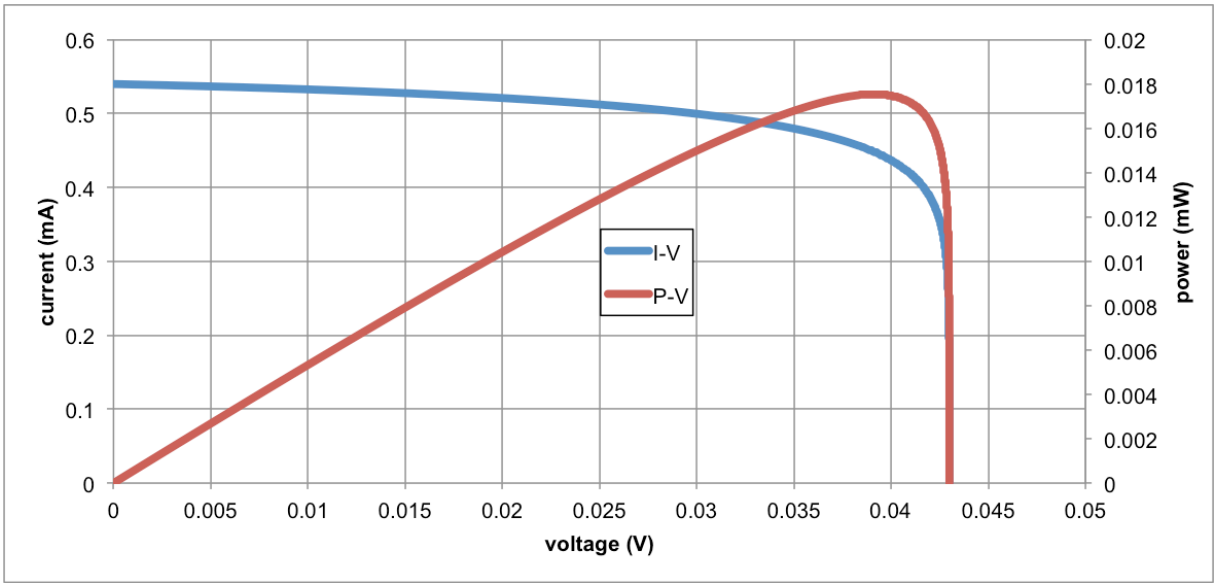



**Figure 5-44:** I-V curve generated from a MATLAB® model for a mono-crystalline PV cell exposed to direct sunlight (1sun)

The generated power at any point on the I-V curve may be simply calculated by multiplying the voltage and current together. From these calculations it is therefore possible to discover the maximum power point (and hence maximum efficiency) of the photovoltaic cell under the given input conditions.

## 5.7 Fifth stage: Storage of electrical energy in a capacitor

Following electricity generation within the p-n junction, there is now a necessity for storage of this electrical energy in a capacitor. A wide variety of capacitors exist, many of which require differences in the manner in which they are modelled. However, it has been decided for the purposes of this section to focus on aluminium

electrolytic capacitors due to their discovery during laboratory experimentation as the most efficient at charging when connected to an ICRB.

### 5.7.1 Efficiency of charging a capacitor

During charging, the current entering a capacitor is opposed by the equivalent series resistance (ESR) of the capacitor, which is of a far lower value than the parallel resistance. The process of charging results in energy loss ($E_R$) due to the ESR, which may be calculated through application of Equation (5-62), where $J$ is the current, $R$ is the resistance, and $dt$ is an elemental time.

$$E_R = \int J^2.R.dt \tag{5-62}$$

Photovoltaic cells are a constant current source [226], meaning that the current ($J$) is a constant and therefore Equation (5-62) solves to form Equation (5-63).

$$E_R = J^2.R.t = C.V.J.R \tag{5-63}$$

By assuming that the loss of energy due to charging in this fashion is a percentage ($x$) of the applied energy it is possible to form equation (5-64).

$$C.V.J.R = x.\left(\frac{1}{2}C.V^2\right) \rightarrow J = \frac{x.V}{2R} \tag{5-64}$$

From this it follows that the time of charging required to ensure that a percentage ($x$) of the applied energy is lost during charging may be obtained through application of Equation (5-65).

$$t = \frac{C.V}{J} = \frac{2}{x}R.C \tag{5-65}$$

Rearranging Equation (5-65) allows the formation of Equation (5-66) which describes a desired percentage loss of energy during charging as a function of time, resistance and capacitance.

$$x = \frac{2}{t} R.C \tag{5-66}$$

It therefore follows that increasing the time of charging also reduces the losses experienced during charging, and that therefore the lowest current possible should be used to efficiently charge a capacitor. Equation (5-67) represents a simple approximation of the relation between capacitance and parallel resistance ($R_p$) [213] taken from Cornel Dubilier..

$$R_p = \frac{100}{C} \tag{5-67}$$

Applying Equation (5-67) to Equation (5-67) in the form of MATLAB® code (shown in Appendix B.4) to a 47µF capacitor models the efficiency of charging the capacitor to its peak voltage dependent on the charging time. The results generated are presented in a graph of efficiency versus time and are shown in Figure 5-45.

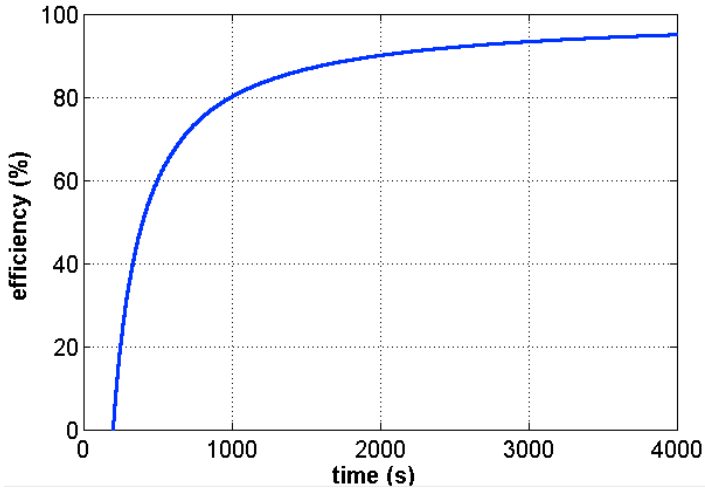



**Figure 5-45:** Modelled efficiency of charging a 47µF capacitor from a constant current source dependent on the time of charging

A PV cell behaves as a constant current source, charging the capacitor attached to it, until the voltage in the capacitor begins to approach the voltage generated in the PV cell. The combination of these two factors ensures that, as the voltage in the capacitor approaches the voltage generated in the PV cell, the current flow will tail off, until it reaches zero and no more charge is stored in the capacitor.

Three currents flow within a capacitor connected to a power supply, as described by Equation (5-68), where $J$ represents the total current, $J_{store}$ is the current which results in stored charge in the capacitor, $J_{abs}$ is the absorbtion current in the capacitor dielectric, and $J_{leak}$ is the leakage current in the capacitor. $J_{abs}$ is the current absorbed into the dielectric shortly after a capacitor has been discharged (usually within the first 5 seconds), and is also known as “soak”. For charging over longer time periods this current is insignificant and may be ignored, though the change in Voltage due to this effect must be removed from any readings taken later as the capacitor charges. Therefore only the leakage current and the stored current need be considered when modelling the charging of the capacitor in this manner.

$$J = J_{store} + J_{leak} + J_{abs} \quad \textbf{(5-68)}$$

## 5.7.2 Leakage loss of the capacitor

The leakage current in a capacitor is defined in manufacturers’ datasheets, however the value or formula given is often the maximum possible leakage current which may well not be the true value at a given voltage. The reason a high value is given is to enable an easier choice of capacitor for applications where a leakage within the capacitor may prove crucial to the operation of the overall system. As an example a

*47μF 25V* aluminium electrolytic capacitor from Rubycon Corporation (ZL series) is said to have a leakage current as described in Equation (5-69), where $C$ is capacitance and $V$ is voltage.

$$3\mu A \; or \; 0.01C.V \; whichever \; is \; higher \quad \textbf{(5-69)}$$

The formula given in Equation (5-69) provides a useful approximation of the leakage current, and by application of Ohm's law [227] the parallel resistance of the capacitor may also be calculated from this equation. This is only an approximation, since the parallel resistance is not a constant and will in fact decrease as the stored voltage increases. However, for the purposes of these calculations, the value of parallel resistance calculated as described is an acceptable estimate.

The value of applied resistance ($R_a$) which models the leakage loss of a capacitor is the sum of all of the resistances which are in effect on that component. For a capacitor connected to a charging p-n junction the resistance of the p-n junction must be considered alongside the parallel resistance of the capacitor, the resistance of the casing of the capacitor, and even the resistance of the air. The applied resistance in these circumstances is therefore much greater than the parallel resistance of the capacitor on its own.

By measuring the changing voltage of a capacitor which has been charged and then disconnected from a power supply it is possible to generate a plot of the discharge of said capacitor. By reversing Equation (3-19) it is then possible to develop a plot for the change of parallel resistance during the discharge of the capacitor. Curve fitting to this plot then generates a general formula for this resistance for this specific

capacitor. A MATLAB® script simulating the leakage power using this methodology is presented in Appendix B.4 with a plot based on a 47μF 25V aluminium electrolytic capacitor discharging shown in Figure 5-46.

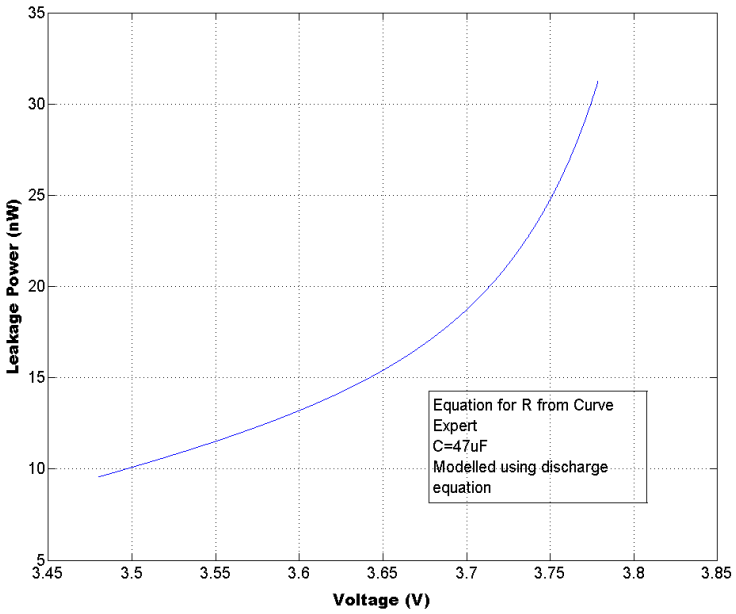



**Figure 5-46:** Leakage power from capacitor discharging as plotted from MATLAB® script

### 5.7.3 Calculated operational lifetime of a capacitor

Using the lifetime formula provided by Cornell Dubilier Electronics Inc. (Equation3-21) it is possible to calculate the theoretical lifetimes of aluminium electrolytic capacitors. Values for $T_m$ and $L_b$ from are provided by the manufacturer, while the value of $T_a$ may be generated by equation (5-70) where $T_{amb}$ is the ambient temperature, $P_{chg}$ is the power of charging ($I.V^2$), and $K_c$ is the thermal resistance (in $^oC/W$) which may be found in charts provided by the manufacturer. The value of $M_v$ may be determined by application of equation (5-71), where $V_a$ is the voltage applied to the capacitor, and $V_r$ is the voltage to which the capacitor is rated.

$$T_a = T_{amb} + K_c . P_{chg} \quad \textbf{(5-70)}$$

$$M_v = 4.3 - 3.3\left(\frac{V_a}{V_r}\right) \quad \textbf{(5-71)}$$

For a radial lead, *300/301* capacitor with *JS2* style case (*25mmX22mmϕ*), CDE rate the thermal resistance to be *23.33°C/W*, $L_b$ is *4000hrs*, and $T_m$ is *85°C* [228]. If the capacitor charges to 5V peak and provides power to the WSN sensor node at an average rate of 1μW then the calculated lifetime of the capacitor would be 150 years.

## 5.8 Complete Model

A complete theoretical model of the radioisotopic battery has been presented in this chapter. The overall efficiency of the battery may be obtained by combining the efficiency equations for each stage, as described earlier in Equation (5-2). Similarly the power output may be calculated by combining the power generation or transfer within each stage. It is possible to use this model to predict the effect on battery performance of altering parameters such as GTLS quantity, arrangement, and dimensions; reflectivity of the casing; radioisotope gas pressure; phosphor type; PV cell type; and the type of capacitor in use. Results obtained by running these models with a variety of parameters are presented in Chapter 6.

# 6 ICRB PRACTICAL AND THEORETICAL COMPARISON

## 6.1 Introduction

The results of laboratory and field experimentation and theoretical modelling are presented and discussed in this chapter. The ICRBs are described in two manners; by their efficiency and by the power they produce. Each stage of ICRB energy conversion or transport (see Chapter 5) is addressed in turn and then combined into a complete description of the power source. The results of buried testing of an ICRB are given and commented on along with the suitability of the ICRB as a power source for a WSN sensor node. Conclusions regarding the key factors affecting ICRB operation are reached and suggestions are made for improvements which could be made to this class of power source.

## 6.2 Efficiency

The efficiency of ICRBs is described by separate consideration of all of their constituent parts: emission of radioactive particles; generation of photons; transport of photons to the PV cells; generation of electricity in the PV cells and storage of electricity in capacitors. The results of each constituent efficiency are then combined to generate an overall efficiency for ICRBs.

### 6.2.1 Efficiency of radioactive flux

The relationship between gas pressure and surface beta flux power is illustrated in Figure 6-1. Here the dashed green line represents the increase in beta flux power at the surface of a cylindrical volume of gas if attenuation does not occur and is therefore a straight line. The effect of attenuation on the surface beta flux power can

be seen in the red dotted line, which is similar to the graph displayed in Figure 3-24. As the pressure increases so the effect of attenuation within the gas becomes more significant until, at around 2 atmospheres pressure in this example, saturation occurs and the beta flux power at the surface of the gas no longer increases. The solid blue line is the efficiency of beta flux within the gas in reaching the surface of the gas. Starting from 100% this efficiency rapidly decreases as the pressure increases.

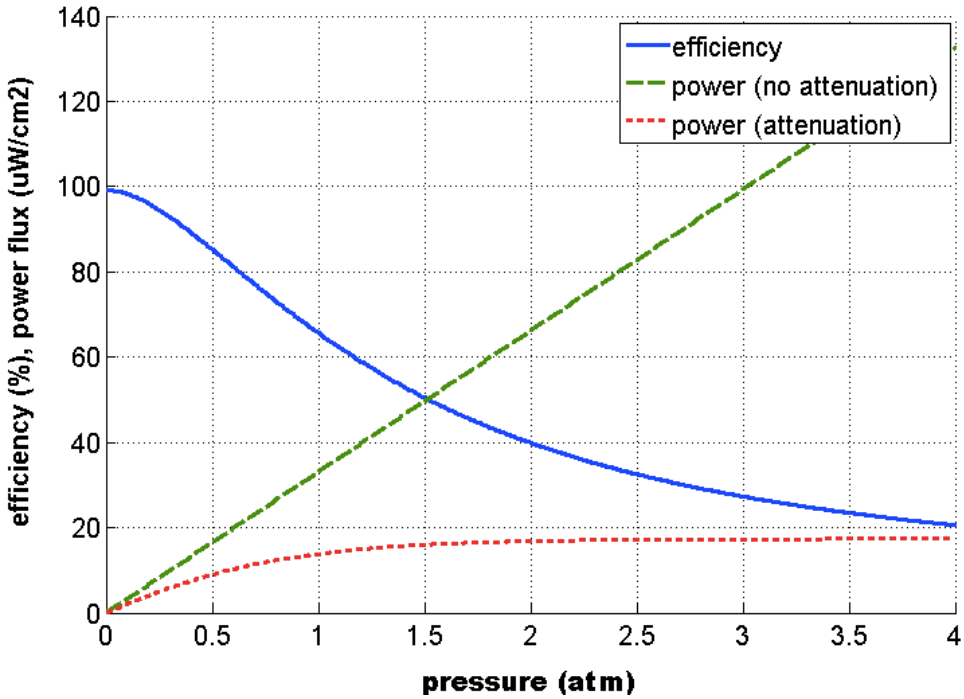



**Figure 6-1:** Efficiency of power flux at the surface of a cylinder of radius 0.85cm and length 1cm related to change in tritium pressure

The effect of altering the diameter of the attenuation cylinder of gas on the beta flux power at its surface is presented in Figure 6-2. This curve follows a similar shape to that seen by increasing the pressure within the cylinder of tritium gas; as the diameter increases so does the beta flux power on the surface. However, the relationship is not linear and eventually reaches a saturation point, due again to attenuation of the beta particles released by the increased presence of tritium in a given volume. For any given pressure (and hence density of tritium molecules) of

tritium gas there is an attenuation length beyond which all energy from a beta particle decay will be self-absorbed in the gas before reaching the surface. Any increase in diameter beyond this attenuation length will not result in any increase in the surface beta flux power and therefore saturation can be said to have occurred.

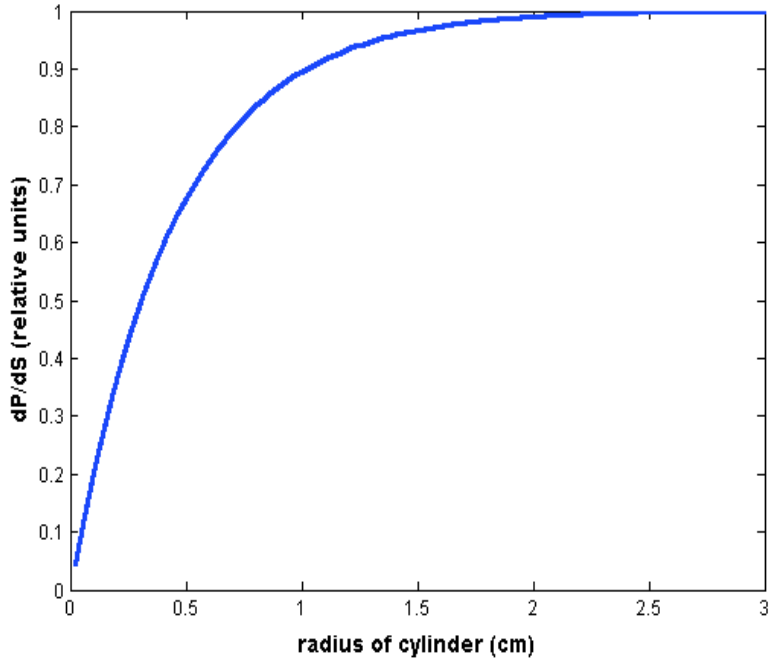



**Figure 6-2:** Modelled change with increase of radius of beta flux power (relative units) on the surface of a cylinder of length 1cm with a pressure of 2 atmospheres

The surface beta flux power of the internal cylinder of a 15mmX3mmØ GTLS used during laboratory experimentation was modelled using this MATLAB® code. According to the manufacturer of these light sources the pressure of gas within the GTLSs is 1.013 atm at room temperature, giving a modelled efficiency of the beta flux to the surface of the tritium contained in the GTLSs of this geometry of approximately 82%.

Table 6-1 shows a list of calculated values (using the equations described in Section 5.3.2) of beta flux power at the inner surface of the phosphor layer in the GTLSs which were used during laboratory experimentation in the manufacture of ICRBs. The

activities of tritium contained in these GTLSs were given by the manufacturer and are valid at the time of manufacture. The surface area was calculated for the inner surface of the phosphor layer not the outer surface of the GTLSs while the efficiencies of beta flux were taken to be 82% in all cases.

**Table 6-1:** Calculated values of surface beta flux power for the geometries of the key GTLSs used during laboratory testing

| External length (cm) | External diameter (cm) | Surface area (cm2) | Activity (GBq) | Total power (uW) | Beta flux power (uW/cm2) |
|---|---|---|---|---|---|
| | | | | | |
| **2.50** | 0.17 | 1.33 | 17.0 | 15.5 | 9.32 |
| **2.25** | 0.17 | 1.20 | 15.0 | 13.7 | 9.14 |
| **1.50** | 0.17 | 0.80 | 5.3 | 4.8 | 4.85 |

From the theoretical modelling it is reasonable to assume an efficiency of approximately 82% for the emission of beta particle energy from within a gas of tritium to its surface with the pressures and dimensions (3mmØ) of the GTLSs used during this study.

### 6.2.2 Efficiency of photon generation in phosphors

The efficiency of photon generation within a phosphor layer was taken from the Phosphor Handbook [229]. The phosphor used in the GTLSs in this study is ZnS:Cu (from the manufacturer) and has a 17.5% conversion efficiency from incident energy into photons.

Using an efficiency of 17.5% in combination with the power flux of 9.32μW/cm$^2$ modelled in Section 6.2.1 for 25mmX3mmØ GTLSs gives a surface light flux of 1.63μW/cm$^2$. The power of light generated per unit area is a key input to the modelling of PV cell efficiencies and will be used later in this chapter in just this way.

### 6.2.3 Efficiency of light transport within an ICRB

The modelling of light transport from GTLSs depends to some extent on the geometry of the GTLSs themselves. Several different types of GTLS were used during laboratory experimentation and these light sources were measured under a microscope in order to determine their exact dimensions, as shown in Figure 6-3. These measurements were confirmed by using digital vernier callipers.

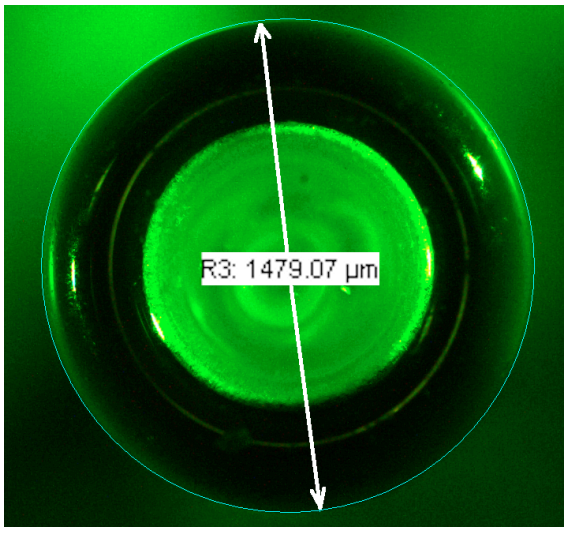



**Figure 6-3:** End on image of a 25mmX3mmØ GTLS taken under X25 magnification and showing the outer radius measurement (R3)

Even within GTLSs nominally of the same size there was a variance in their dimensions, as shown by the tolerance in Table 6-2. Interestingly, these measurements did not agree with the stated dimensions from the manufacturer who claimed that the glass wall thickness of the GTLSs are 0.45mm, whereas the measured wall thickness ($r_o$-$r_i$) was found to be 0.65mm. The dimensions relevant to the GTLSs used during laboratory experimentation and theoretical modelling are given in Table 6-2.

**Table 6-2:** Measured dimensions of selected GTLSs

| GTLS type | Length | Outer radius | Inner radius |
|---|---|---|---|
| | | | |
| 25mmX3mmØ | 24.980±0.07mm | 1.495±0.015mm | 0.866±0.08mm |
| 15mmX3mmØ | 14.993±0.04mm | 1.497±0.008mm | 0.861±0.07mm |
| 22.5mmX3mmØ | 22.498±0.09mm | 1.496±0.011mm | 0.865±0.07mm |

These values are taken forward and used in the next aspect of theoretical modelling which was the amount of light leaving a single GTLS. If incorrect values were used for this modelling then the calculated efficiencies of this stage of the ICRB would be inaccurate.

### 6.2.3.1 Light leaving a single GTLS

For light transmitted from a GTLS in the x-y plane of Figure 5-10 the angle of light incident on the glass/surroundings interface (point F) may be calculated by using Equation (5-14).

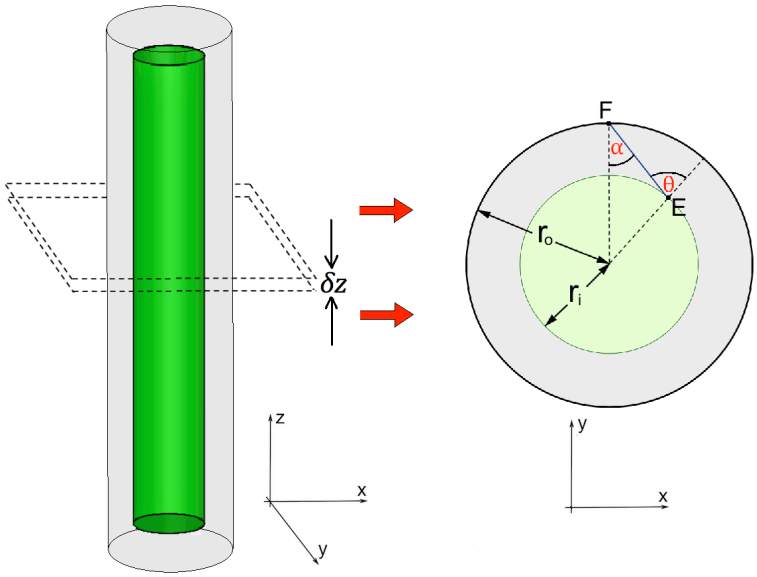



**Figure 5-10:** Light emission from the x-y plane of a GTLS

$$\alpha = sin^{-1}\left(\frac{r_i}{r_o} sin(\pi - \theta)\right) \quad \textbf{(5-14)}$$

Depending on the relative refractive indices of the glass of the GTLS and the medium surrounding the GTLS, the incident angle of light on the glass/surroundings may never reach the critical angle. This also depends on the ratio of the inner and outer radii of the GTLS. Therefore, choosing the correct ratio of radii will result in more efficient transmission of light from the GTLS. For example, an inner radius of 0.85mm and an outer radius of 1.5mm produces a maximum incident angle (alpha) of 34.5°, which is far less than the critical angle of 42° for light traveling from glass of refractive index 1.5 into air (refractive index 1).

The efficiency of light leaving the side of a 25mmX3mmØ GTLS as modelled by the Simulink model was found to be 54.2%. Combined with the previously calculated light flux (from Section 6.2.2) of 1.63μW/cm$^2$, this gives a light flux at the outer surface of the glass/air boundary of the side of the GTLS of 0.71μW/cm$^2$. This light flux was verified through physical testing of the actual GTLSs used during laboratory experimentation. Light leaving a single GTLS was measured using an array based spectral radiometer at the National Physics Laboratory (UK). This was accomplished by using a macro lens that focused a small field of view onto the central aspect of an individual GTLS, as illustrated in Figure 6-4.

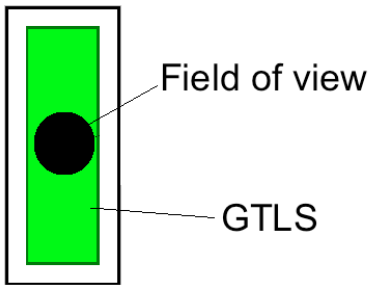



**Figure 6-4:** Impression of the field of view on a single GTLS generated with a macro lens for spectroscopy testing

Using this methodology the spectral distribution of radiant flux was measured for a range of sizes and colours of GTLSs. The spectral distribution of radiant flux of a 25mmX3mmØ green GTLS is shown in Figure 6-5. The peak radiant flux was measured to occur at 530nm which is very close to the 531nm peak provided by the manufacturer (mb-microtec AG [217]) and shown in Figure 5-2. The distribution of radiant flux shown by the shape of the curve is also in broad agreement with the information provided by the manufacturer.

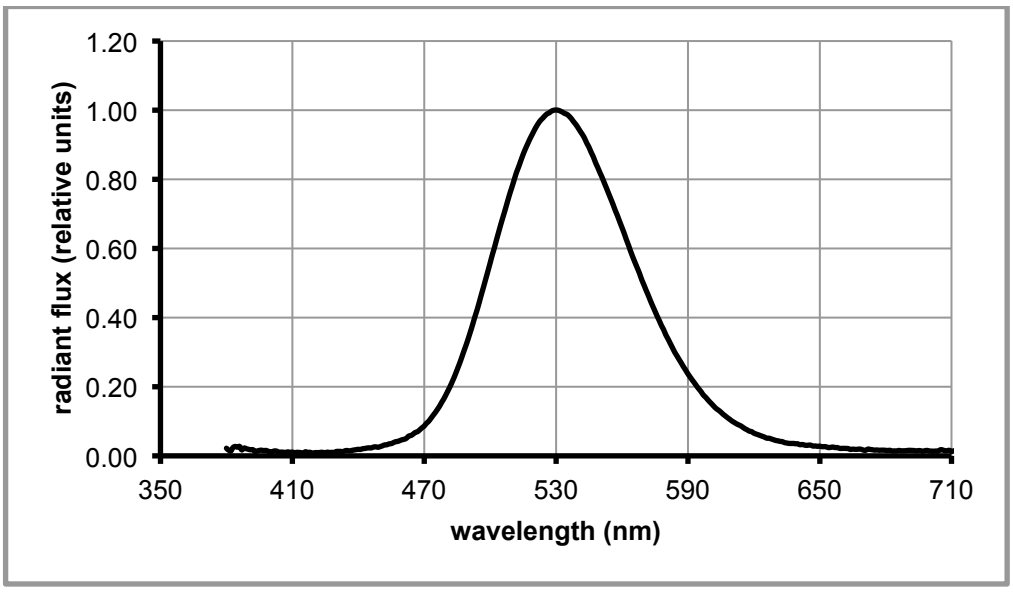



**Figure 6-5:** Measured spectral distribution of radiant flux for a 25mmX3mmØ green GTLS

The radiant emittance of a 25mmX3mmØ GTLS was measured at The National Physics Laboratory using a Minolta CS1000 spectroradiometer. The light flux was found to be 0.685μW/cm$^2$ in these laboratory experiments, showing very good agreement with the 0.710μW/cm$^2$ predicted by the theoretical model (a 3.5% overestimation by the model). The model was based on a GTLS at beginning of life (BOL) while the laboratory measurements were taken from a GTLS just under a year old, in which the activity of tritium present will have decreased. Adjusting the

modelled light flux by the exponential decay after a year results in a new value of 0.751μW/cm$^2$, which is a 5.5% underestimation by the model.

### 6.2.3.2 Light lost from GTLSs into adjacent GTLSs in an array

Using the equations presented in Section 5.5.2, a MATLAB® model (Appendix B.2.3) was developed to simulate the loss of light from one GTLS if it is adjacent to another GTLS of similar dimensions. The model was applied to GTLSs of inner radius 0.866mm and outer radius 1.495mm (for the 25mmX3mmØ GTLSs) as measured and shown in Table 6-2. The output from the model is shown in Figure 6-6 where the dotted red curves represent the changing percentage of light loss as the angle $\theta$ increases, the short blue solid lines are the averaged loss of light in each of the regions of $\theta$, and the green solid line across the entire range is the overall average percentage loss of light from the GTLS into an adjacent GTLS. GTLSs of these dimensions are calculated to lose 30.18% of their transmitted light into adjacent GTLSs.

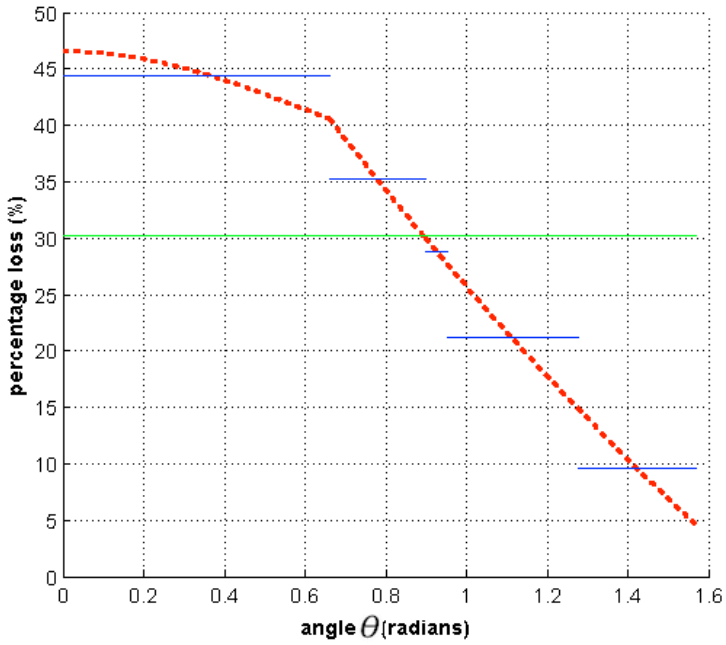



**Figure 6-6:** Calculated losses from a 3mmØ GTLS into an adjacent GTLS of the same size

By changing the value of the inner radius whilst keeping the outer radius fixed at 1.5mm it is possible to see the effect of altering one aspect of the GTLS geometry on its efficiency of light emission in an array, as shown in Figure 6-7.

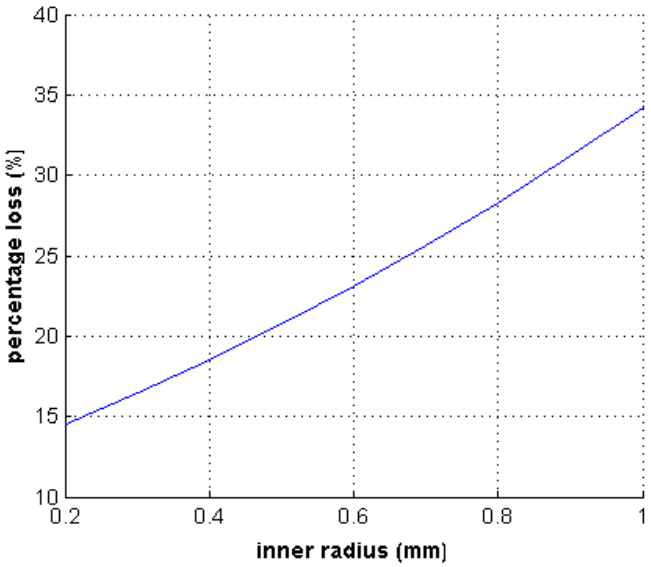



**Figure 6-7:** Percentage loss of light from a GTLS into adjacent GTLSs as a function of changing inner radius with a fixed outer radius of 1.5mm

Therefore, by decreasing the inner radius of the GTLS relative to the outer radius it is possible to increase the amount of light transmitted in an array. Reducing the inner radius of the GTLS also reduces the volume of $^{3}H$ that may be stored in the light source and therefore reduces the power density of the device.

The radiant light flux from a single GTLS and from an array of 12 GTLSs was measured at the National Physics Laboratory using an array based spectral radiometer. The field of view used for measurement was altered by changing the distance between the GTLSs and the radiometer and by changing the radiometer's lens. In order to measure the radiance and luminance of an individual GTLS the field of view was kept as small as practically possible and within the geometric bounds of the GTLS. To measure the same properties of an array of GTLSs the field of view

was increased in size and spread across multiple GTLSs whilst staying within the confines of the entire array. Both methodologies are illustrated in Figure 6-8.

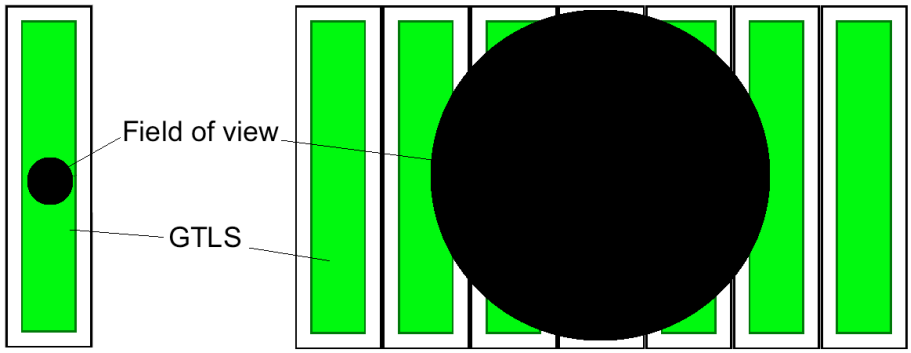



**Figure 6-8:** Field of view during measurements of individual GTLS and a GTLS array radiance and luminance

The spectral radiance results for the two experiments are presented together in Figure 6-9, where it is clear that, at all wavelengths, the measurement of the individual GTLS provided a higher radiance than did the array of GTLSs. The array of 15mmX3mmØ GTLSs produced a radiance of approximately 21.5% lower than from a single GTLS of the same size and age.

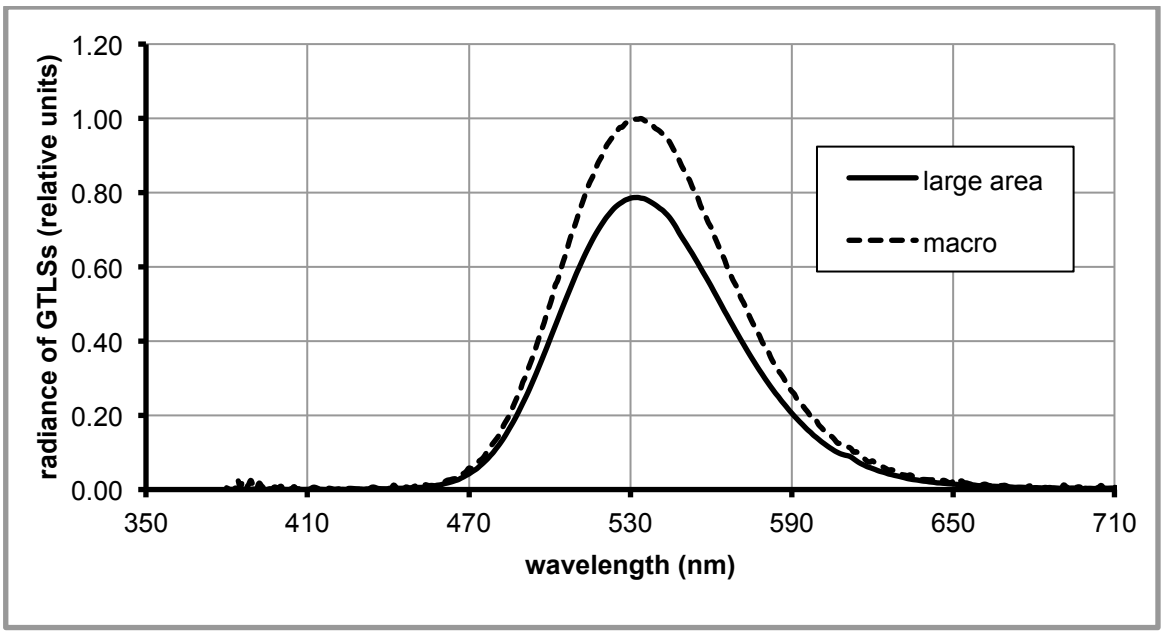



**Figure 6-9:** Measured spectral radiance results for a single 15mmX3mmØ GTLS and an array of 15mmX3mmØ GTLSs

The inner radius of this type of GTLS is 0.861mm (as per Table 6-2) and therefore from reading the graph shown in Figure 6-7 the loss of light would be expected to be of approximately 30%. While this is greater than the 21.5% discovered experimentally it is of the same order of magnitude. The luminance measured in the same manner was found to be 1.324cd/$m^2$ from a single GTLS and 1.051cd/$m^2$ for an array of GTLSs. This, similarly, equates to a 20.7% reduction in the brightness of the GTLS array compared to a single GTLS and is similar to the ratio of the radiance measurements. The suggestion must be that the theoretical model is too simplistic and (as was previously assumed in Section 5.5) is an underestimation of the amount of light emitted from an array of GTLSs. At this percentage loss the radiant emittance of 0.685μW/$cm^2$ from a single GTLS would be 0.55μW/$cm^2$ in an array for 3mmØ GTLSs.

### 6.2.3.3 Effect of reflective surrounding

Using the theory and associated equations developed in Section 5.5.3 a theoretical model was generated with MATLAB® code as shown in Appendix B.2.5. Applying this model to an ICRB configuration comprising of twelve 15mmX3mmØ GTLSs and two 34.9mmX13.8mm a-Si PV cells produced interesting results. An assumption was made that the light was transmitted from the GTLSs evenly in all directions and from all points of their surface. It was found that the percentage of light transmitted from the GTLSs that might be reflected onto the PV cells by a reflective material on the casing was only 2.36%. Of this value 1.06% was reflection of light transmitted from the ends of the GTLSs and 1.30% was the reflection of light transmitted from the sides of the 2 GTLSs on the ends of the configuration.

Reducing the number of GTLSs in an array increases the percentage of total light which may be reflected, as shown in Figure 6-10, while increasing the number of GTLSs eventually results in a percentage value of reflectance equal to just above the amount of light reflected from the ends of the GTLSs.

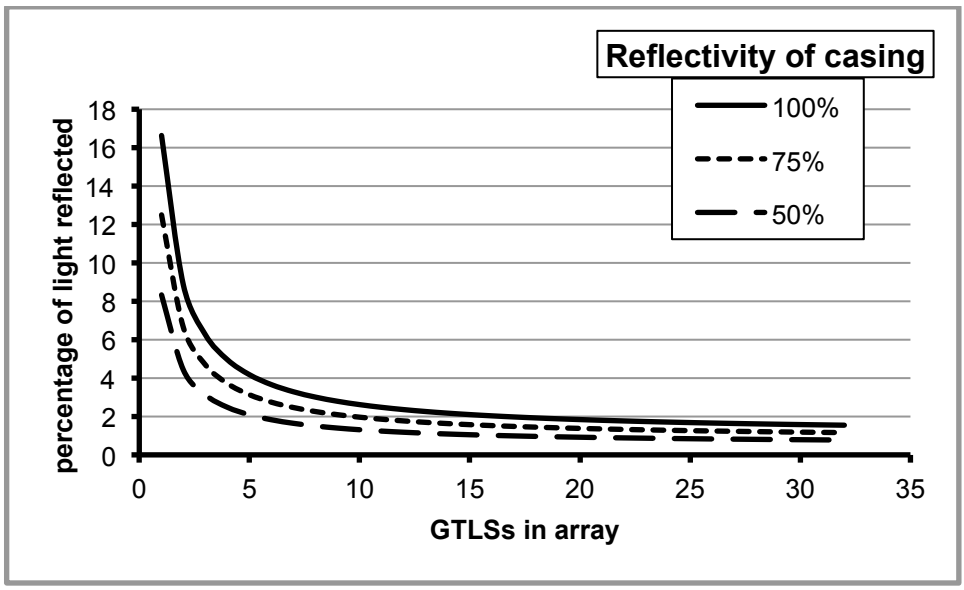



**Figure 6-10:** Effect of reflective material surrounding the ICRB dependent on the number of GTLSs in the ICRB array

Reducing the reflectivity of the surrounding material results in less light reflecting back to the PV cells and the effect on the total percentage of light reflected relative to the number of GTLSs in the array is also displayed in Figure 6-10. For ICRBs with very few GTLSs the effect of the reflective material significantly affects the level of light incident on the PV cells (as much as a 16% increase in light intensity), but for arrays featuring many GTLSs the impact of the reflective material relative to the intensity of light incident on the PV cells is insignificant. Using GTLSs of 25mm length instead, results in an even lower maximum percentage of reflected light of just 2.01% (reduced from 2.35% for 15mm long GTLSs).

The effect of different reflective materials was then investigated in laboratory experimentation with the results compared with the theoretical modelling presented above. Twelve 15mmX3mmØ GTLSs and two a-Si PV cells of dimension 34.9mmX13.8mm were enclosed in casings coated with nothing (clear), gold and barium sulphate, as shown in Figure 6-11.

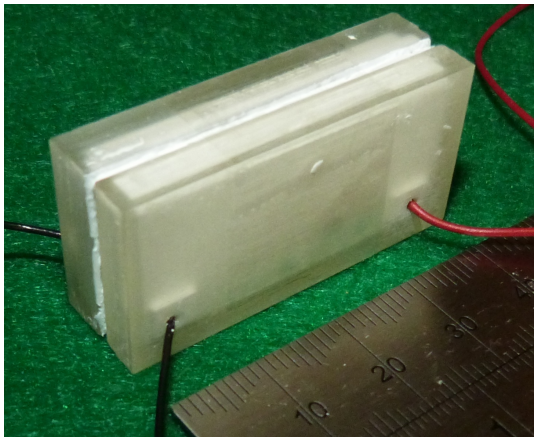


**Figure 6-11:** Indirect conversion radioisotopic battery with barium sulphate as a reflective coating

The PV cells were connected in series (producing an increased voltage) and testing was conducted by the methodology described in Section 4.9.2. These procedures were repeated for all three types of reflective material encasing the ICRB, with each battery rebuilt and retested to confirm the results. The power versus voltage results generated in this manner are presented in Figure 6-12.

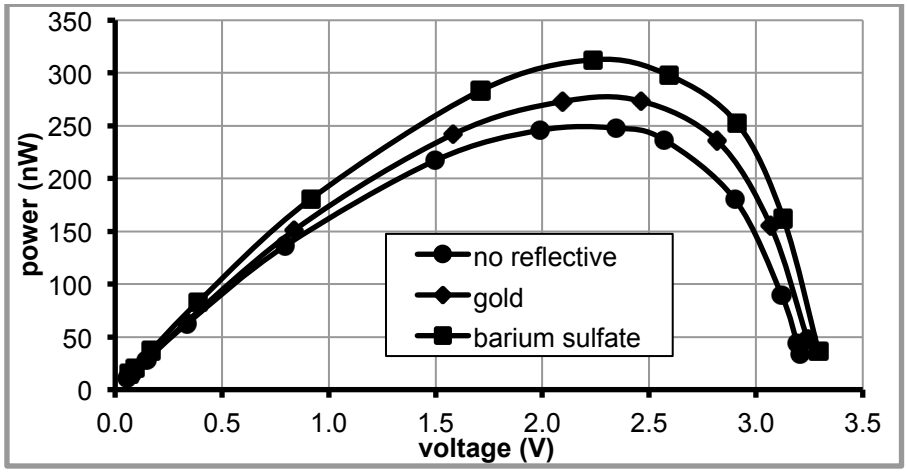



**Figure 6-12:** Power against voltage of three ICRBs using different reflective materials

The battery using barium sulphate as a reflective medium generated 26% more power than did the battery with no reflective coating. Meanwhile the battery with a gold reflective layer produced only 10% more power than the battery with no reflective coating. These results were unexpected and were not predicted by the theoretical model that suggested a maximum of 2.3% increase in power from the presence of a reflective material. The reasons for the difference between the theoretically predicted increase in power and the experimental results may be explained due to deficiencies in the theoretical model. Firstly, the geometry of the battery which was modelled (shown in Figure 6-13(a)) is different to that which was experimentally tested (shown in Figure 6-13(b)) with the ends of the GTLSs protruding 0.5mm beyond the outer edges of the PV cells at the top and bottom and 0.6mm over the edge at the two sides of the PV cells.

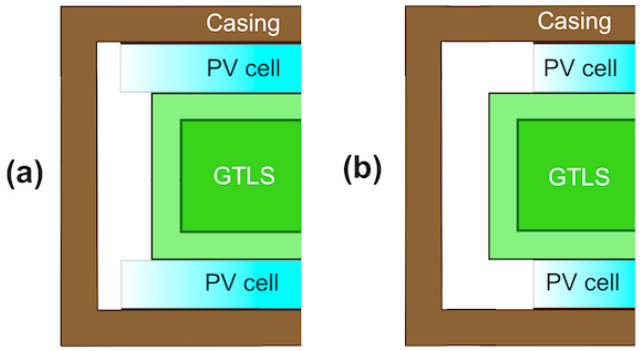



**Figure 6-13:** Layout of GTLSs, PV cells and casing relative to each other, (a) with the PV cells beyond the GTLSs, (b) with the GTLSs beyond the PV cells

Using the actual layout of the ICRB tested suggests that up to 17% of additional light may be reflected onto the PV cells for this configuration of twelve adjacent GTLSs (in contrast to the 2.3% previously predicted). This increase in light intensity may not map directly into a similar increase in power output of the battery. An additional explanation for the increase in power of the battery using barium sulphate is that these particular PV cells generate some power from light incident upon their reverse

side (something which is not always the case). This means that a greater percentage of reflected light would be available to generate power inside the PV cells. The effect of altering the theoretical model to incorporate this new geometry and then varying the number of GTLSs in the modelled ICRB is shown in Figure 6-14.

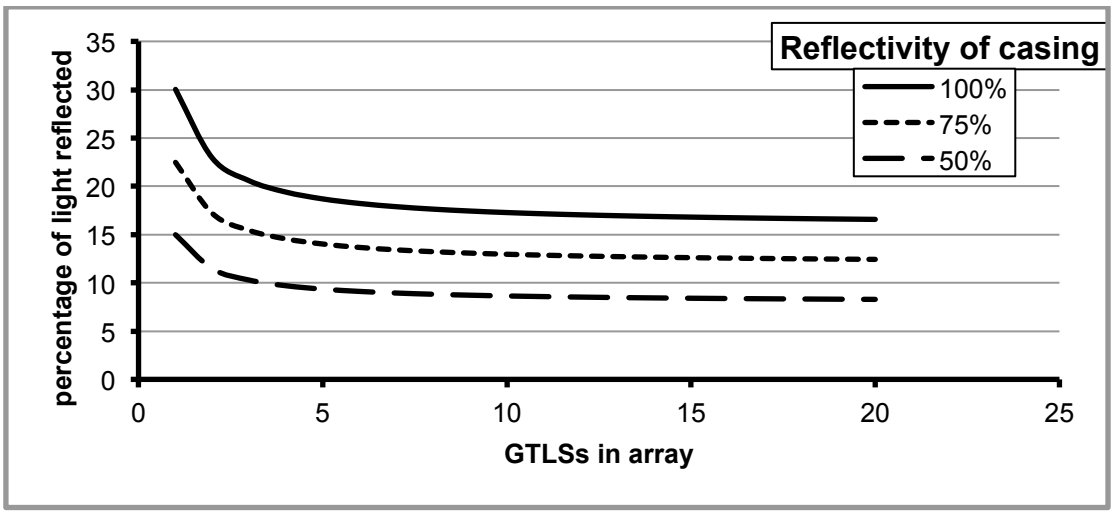



**Figure 6-14:** Revised effect of reflective material surrounding the ICRB dependent on the number of GTLSs in the ICRB array

Using this new model for a casing with 100% reflectivity gives a value of 17% extra light reflected back onto the PV cells, which is much closer to the experimental result of 26%. The increase in power found in the practical battery using barium sulphate is still greater than that predicted by this model and therefore further refinement is required to the theoretical model. Using gold as a reflective layer only increased the generated power by 10%, which is in line with a material of 50% reflectivity according to the model (as shown in Figure 6-14). This is also in accordance with the average reflectivity of gold across the range of the spectrum of light emitted from the GTLSs (460nm to 650nm) as shown in Figure 6-15.

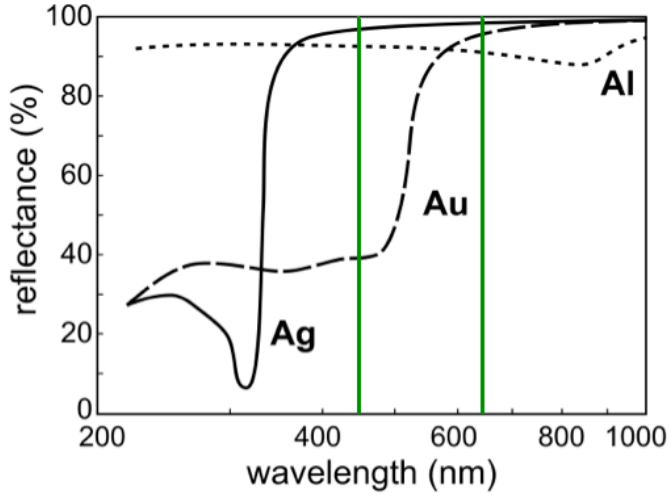



**Figure 6-15**: Reflectance of aluminium (Al), gold (Au) and silver (Ag) from 200nm to 1000nm (reproduced from [205])

#### 6.2.3.4 Effect of altering the medium between the GTLSs and the PV cells

Altering the refractive index of the medium surrounding the GTLS will affect the percentage of light which is reflected and the percentage transmitted. Considering a battery where only the medium between the GTLSs and the PV cells has been altered requires only the consideration of light transport between these two components. Losses from adjacent GTLSs into each other will remain similar as a percentage of the overall transmission of light from each GTLS as the geometry of the system has remained the same. Similarly, reflection from the casing back onto the PV cells will be largely similar since the positioning of the GTLSs relative to the PV cells and casing will not have changed. Since the geometry of the GTLSs themselves does not change it was decided to further simplify the model of the transport of light into a planar consideration, as shown in Figure 6-16, where light from the GTLSs must pass from the glass into the surrounding medium (air or index matching fluid) and then into the glass on the surface of the PV cell.

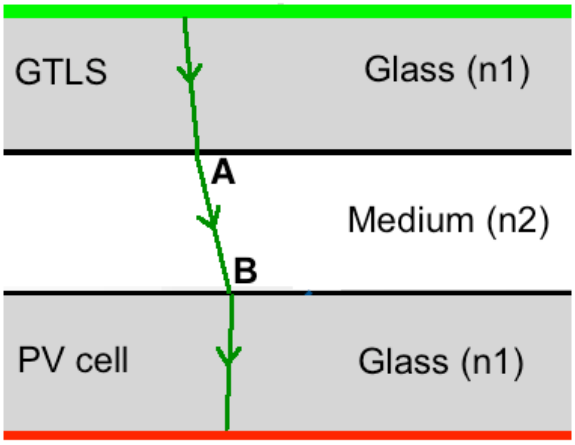



**Figure 6-16:** Transport of light between the GTLSs and PV cells

The glass surrounding the GTLSs is Schott-Duran® Borosilicate glass with a refractive index of 1.473 (from the manufacturer [230]). The behaviour of the photon transport was modelled using a medium between the glass of the GTLSs and the glass cover of the PV cells of either air (with a refractive index of 1) or an index matching fluid (with a refractive index of 1.52, which was the closest available to the refractive index of the glass). The glass covering the PV cell was modelled to be of the same type as that found around the GTLSs. Fresnel equation plots of the reflection of light at points A and B shown in Figure 6-16 generated from code in MATLAB® (see Appendix B.2.6) are presented in Figure 6-17 for a surrounding medium of air (refractive index 1). In these figures the green dashed lines are the reflected percentage of light in s and p polarities, while the red dotted line is the average of the other two lines. The solid blue line is then the average light reflected across the entire range of angles.

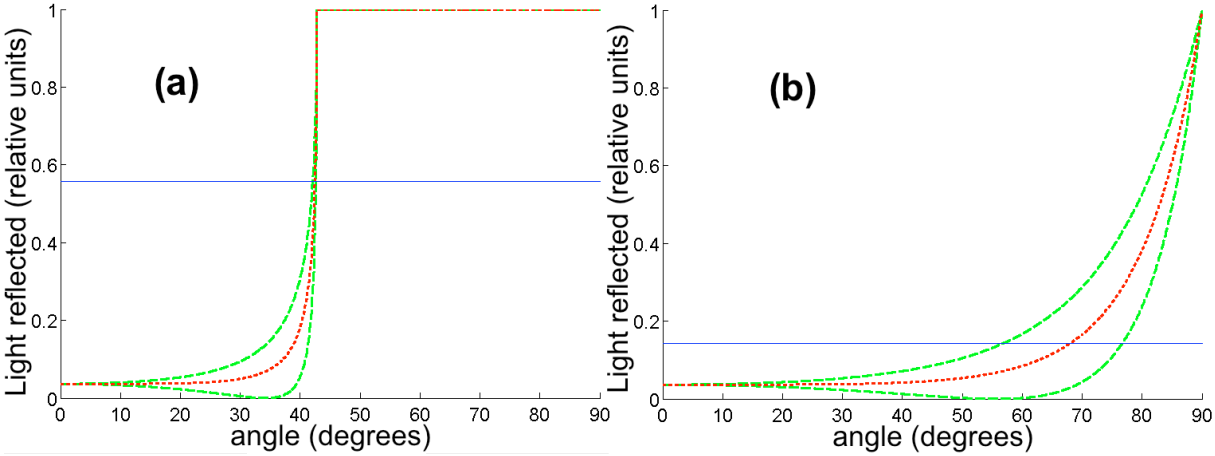



**Figure 6-17:** Transition graphs across the full range of incident angles as calculated using the Fresnel equations for light moving from (a) glass to air, (b) air to glass

Assuming light reflected at point A (Figure 6-16) will be incident on the phosphor layer of the GTLS and will then generate more light (at a 17.5% efficiency), it is possible to find the percentage of light transmitted from the GTLS into the PV cell in this planar geometry. This value is only 41.6%. Repeating the process with an index matching fluid of refractive index 1.52 between the GTLSs and PV cells produces the result shown in Figure 6-18 where the dotted, dashed and solid lines are representative of the same parameters as described for Figure 6-17.

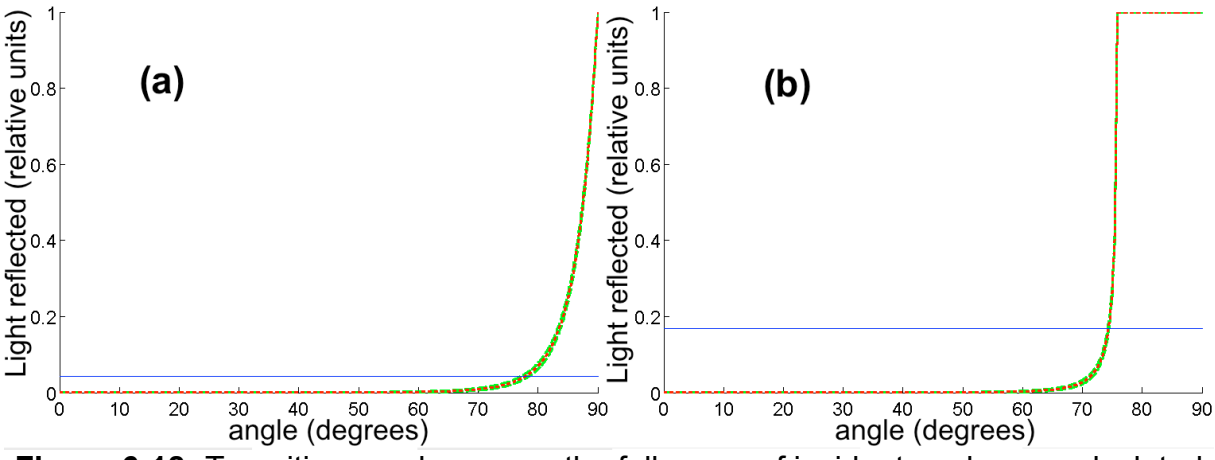



**Figure 6-18:** Transition graphs across the full range of incident angles as calculated using the Fresnel equations for light moving from (a) glass to index matching fluid, (b) index matching fluid to glass

The percentage of light transmitted into the PV cell from the GTLSs in this case is calculated to be 80.2%, which represents 93% greater intensity of light than in the case of air between the two components. If the electricity generated in the PV cell is assumed to be proportional to the intensity of light incident upon it (a reasonable assumption) then 93% more power should be generated in an ICRB using an index matching fluid of refractive index 1.52 than by using air.

Laboratory experimental investigation of the effect of the medium between PV cells and GTLSs was undertaken and compared with the theoretical modelling presented above. An ICRB consisting of ten 15mmX2.5mmØ GTLSs and two 12mmX2mmØ GTLSs sandwiched between two 29.6mmX11.7mm a-Si PV cells and surrounded by Mylar reflective material was constructed. The contacts of the PV cells were each connected to a 1000uF 25V aluminium electrolytic capacitor and the power of the ICRB was determined in the usual manner. The empty spaces within the ICRB were then filled with an index-matching fluid from Newport® Corporation [231] (refractive index of 1.52 at 589nm) and the power of the device was measured again. The results of these two tests are shown in Figure 6-19 and it can be seen that the ICRB using index-matching fluid performed better than the ICRB without.

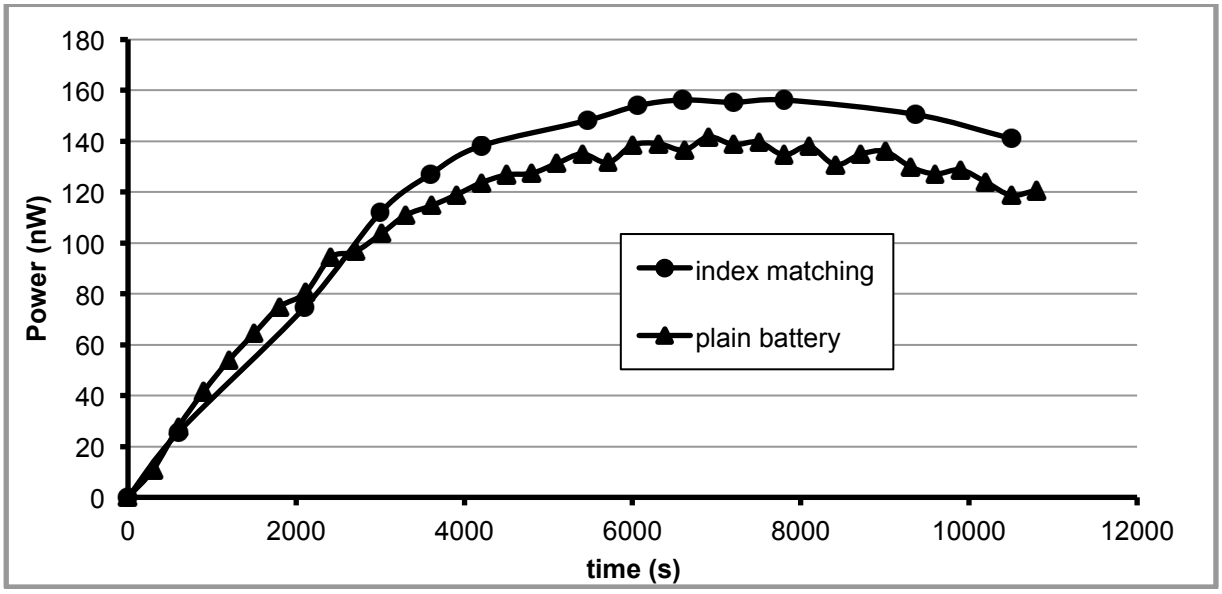



**Figure 6-19:** Effect of introducing an index matching fluid into an ICRB on the output power

The peak power from the ICRB with air between the GTLSs and PV cells was 141.7nW, while the peak power for the ICRB using index-matching fluid was 156.6nW. This represents a 9.5% increase in power generated by the ICRB and capacitor system. This is much lower than the 93% increase predicted by the theoretical modelling and may be due to a variety of factors. In reality, most PV cells have an anti-reflection coating (ARC) layer on top of the glass they are covered with. Anti-reflective coatings may be made from materials with indexes ranging between the index of air and that of the glass they are attached to, though layers between the glass and silicon of the PV cell with refractive indices between either material are also common [232-234]. Adding this effect to the model may alter the results in line with those discovered during experimentation, though the refractive index of the ARC on these PV cells is not known and so it is not possible to test this hypothesis.

Additionally the ARC on most PV cells is of a specific thickness in order to match a quarter of the wavelength of the most intense wavelength of light incident upon it (in

order that reflections beyond this layer will interact at a half wavelength with light about to enter the layer and hence cancel each other out leading to no reflectance). However, the wavelength of light alters depending on the medium it is travelling through and the thickness of the ARC designed for light travelling through air may well not be optimal for light travelling through the index matching fluid. This would result in additional reflections at the surface of the PV cell leading to a reduction in generated power. In the future, investigation of this area of ICRB design might look at the use of alternate index matching fluids of different refractive indices.

### 6.2.4 Efficiency of electricity generation by PV cells

Theoretical models of PV cells were generated using values gathered from laboratory experiments. These models were then run at different input illumination intensities with their outputs compared with the results of further laboratory experiments at these new illumination levels. Silicon PV cells of monocrystalline, polycrystalline and amorphous types were modelled and compared in this manner. First the photocurrent generated in the PV cells (as related to the intensity of illumination incident upon them) is modelled as a link between this section and Section 6.2.3. Then the operation of the model of the PV cells is explained. Finally the theoretical models are compared with the results of laboratory experiments.

#### 6.2.4.1 Calculation of photocurrent generated in PV cells

The photocurrent generated within a PV cell may be modelled using Equation (5-60) (with the assumption that the series resistance of the PV cell is lower than 10Ω and therefore the short circuit current is largely similar to the generated photocurrent).

$$I_{SC}(\lambda) = \frac{q.N_p.QE(\lambda)}{t} \quad \textbf{(5-60)}$$

In order to solve this equation it is necessary to know the quantum efficiency ($QE(\lambda)$) of the PV cell under consideration at the wavelengths of incident light. For illumination by GTLSs the light is considered to be monochromatic at a wavelength of 531nm (a simplifying assumption). At this wavelength a-Si PV cells have a $QE(531nm)$ of approximately 0.8 according to Escarre et al. [235], with their $QE(\lambda)$ graph shown in Appendix D.2. For the same wavelength of 531nm monocrystalline (m-Si) and polycrystalline (p-Si) have similar $QE(531nm)$ values of approximately 0.85 according to Choi et al. [236], with their $QE(\lambda)$ graph shown in Appendix D.2. For office lighting and direct sunlight all wavelengths of the visible spectrum should be considered and therefore an average $QE(\lambda)$ value will be used as a practical approximation. For a-Si PV cells the average $QE(\lambda)$ value is approximately 0.6, while for m-Si and p-Si PV cells the average $QE(\lambda)$ value is approximately 0.8.

For an ICRB consisting of two 72.3mmX15.0mm a-Si PV cells and 24 GTLSs of dimension 15mmX3mmØ the generated photocurrent modelled is 2.61μA. The efficiency of a-Si PV cells depends on the cell used and lies in the range of 8-12% [237]. Taking the best case scenario of an efficiency of 12% for the a-Si PV cells gives a short circuit current of 313nA for this theoretical ICRB. A laboratory experiment was conducted at these test conditions and the short circuit current recorded was in fact 260nA which means that the model overestimates the current generated by 20% in this instance. This may be due to using an efficiency of the a-Si PV cells which is too high. Using a 10% efficiency, for instance, results in a modelled short circuit current of 261nA, which is in line with the measured result.

### 6.2.4.2 Comparison of theoretical model with practical results

The theoretical model of PV cell behaviour is formed from empirical data and therefore is dependent upon laboratory experimentation. Hence it is not possible to conduct a simple comparison between theoretically generated results and experimentally generated ones. Instead, laboratory test results of PV cells will be shown and then the model which has been formed through the application of these results will be presented. The effect of altering the input light intensity on the model will then be shown followed by laboratory tests of the same PV cells exposed to the new light intensity. A comparison can then be made as to the usefulness of the model over a range of input light intensities.

Poly-crystalline silicon PV cells (in the form of two 49.8mmX19.9mm cells) were tested under illumination by direct sunlight (~100,000lux). .A theoretical model (Section 5.6.1.1) of these PV cells under this level of illumination was developed in MATLAB® (Appendix B.3), which generated an I-V and P-V output. The outputs of the practical experimentation and the theoretical model are shown in Figure 6-20, where the triangles and squares represent the experimental data and the solid lines the modelled behaviour.

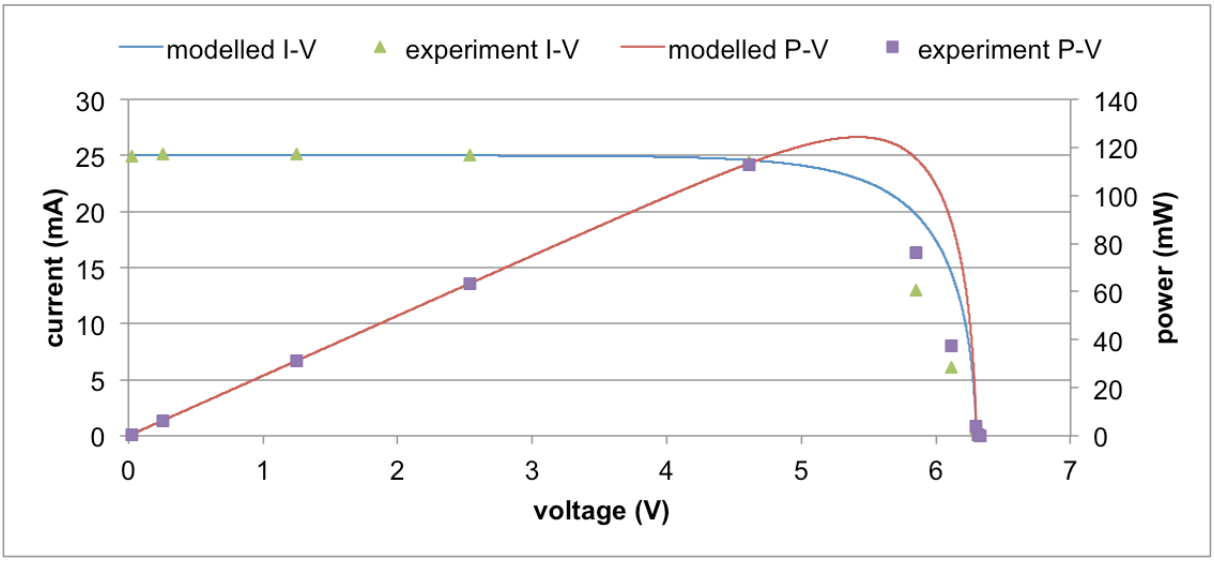



**Figure 6-20:** Experimental and modelled I-V and P-V curves of a p-Si PV cell illuminated by direct sunlight (~100,000lux)

Under direct sunlight (~100,000lux) the p-Si PV cells produced a smooth I-V curve with a current that was at first stable for increasing voltage before tailing off as the voltage approached open circuit level. The shape of the curve is typical of the behaviour of this class of PV cells under this level of illumination and was expected [238]. Initially the parallel resistance within the PV cell may be assumed to be infinite (in relation to the current being driven through the cell), which occurs for the period where the current does not decrease with increasing voltage. Eventually the current begins to decrease (as the voltage approaches the open circuit voltage) because at these voltage levels the current begins to recombine inside the PV cell.

Office lighting conditions of 134lux (measured with a light meter) were then applied to this model of the p-Si PV cells with the resulting I-V (solid blue line) and P-V (dashed green line) curves shown in Figure 6-21. The p-Si PV cells were tested under

exposure to office lighting conditions of 134lux with the results of this testing also shown in Figure 6-21.

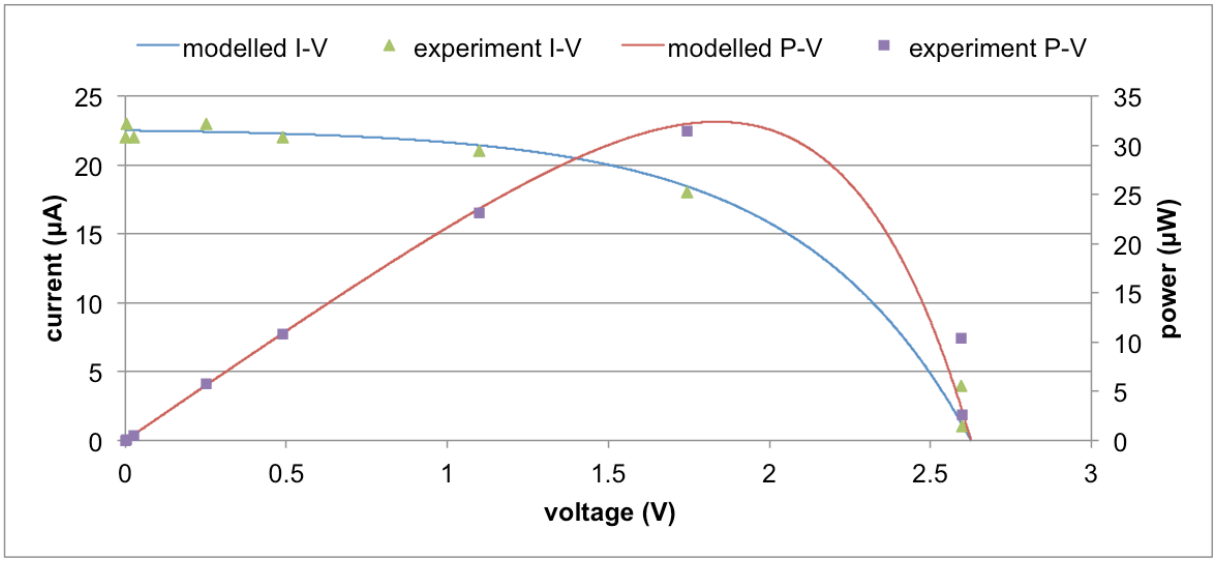



**Figure 6-21:** Experimental and modelled I-V and P-V curves of a p-Si PV cell illuminated by indoor lighting (~138lux)

The model provides a reasonable approximation of the p-Si PV cells under this intensity of illumination. It is also worth noting that the shape of the I-V curve has begun to change with no period of stable current as the voltage increases from zero. The parallel resistance of the PV cell may no longer be considered as infinite at lower intensity illumination levels. Instead, the fill factor of the PV cell at this level of illumination has decreased significantly, because p-Si PV cells of this type are not designed for optimal operation in such low light level environments.

An ICRB was constructed using the p-Si PV cells and fourteen 15mmX3mmØ GTLSs and was tested in the usual manner. The results of this testing are shown in Figure 6-22 where a peak power of 8.07nW at 0.08V is recorded. The shape of the I-V curve in this instance shows a nearly linear reduction in current levels as the voltage

increases. This suggests that the parallel resistance inside the PV cells is the dominant factor for this type of PV cell at this ultra low intensity of illumination.

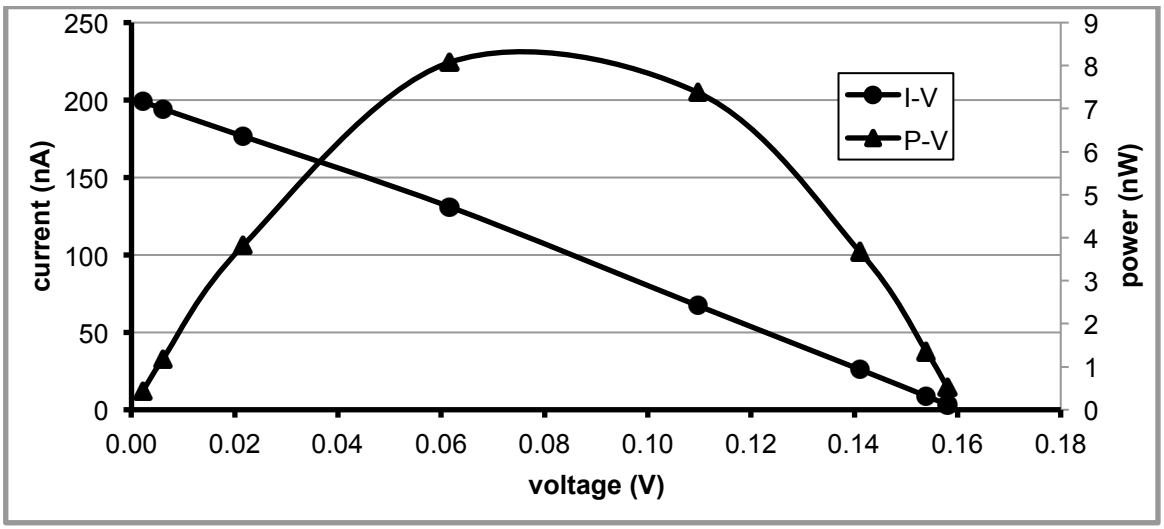



**Figure 6-22:** Experimental I-V and P-V curves for p-Si PV cells illuminated by GTLSs (3.8lux)

The light power incident upon the PV cells was calculated to be 6.9μW and the fill factor was 25%. This gives an efficiency of 0.12% for these p-Si PV cells under this level of illumination. This is far lower than was realised while the same PV cells were exposed to direct sunlight and is due to the way in which these types of PV cells are designed to operate. Polycrystalline PV cells consist of a number of p-n junctions set alongside each other and parallel to the surface of the PV cell. This structure is designed to convert directly incident and parallel beams of light into electricity, not light moving in random directions as is found indoors and (even more so) from the GTLSs.

The illuminance provided by the GTLSs onto the surface of the PV cells was described in Section 6.2.3 and is 0.55μW/cm$^2$ (3.8lux or 0.0000055 suns in the model) for the fourteen 15mmX3mmØ GTLSs used in this experiment (sandwiched

between two of the p-Si PV cells). The model was run again, this time with an incident illumination intensity of 3.8lux, and the I-V curve (solid blue line) and P-V curves (dashed green lines) generated shown in Figure 6-23.

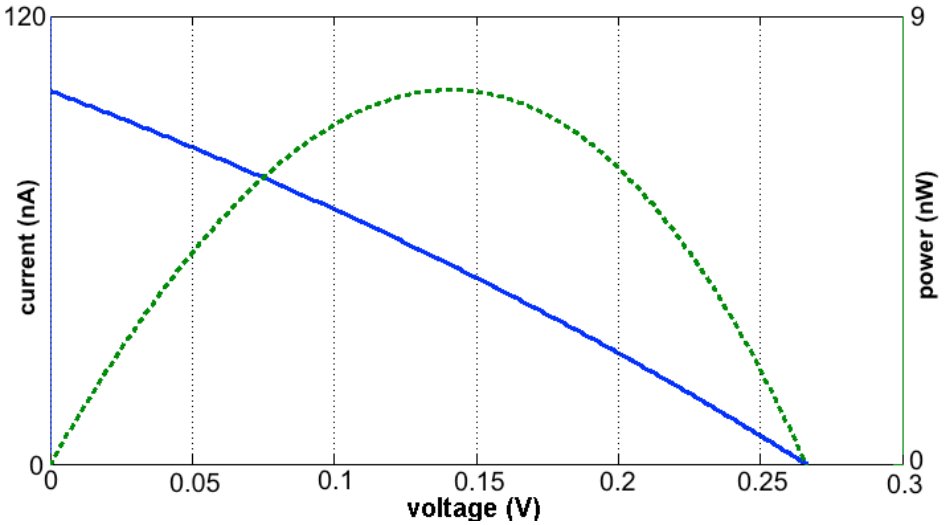



**Figure 6-23:** Modelled I-V and P-V curves for p-Si PV cells under illumination by GTLSs at 3.8lux

The model shows a degree of similarity to the results produced in laboratory experimentation, particularly in the shape of the I-V curve which is nearly a linear relationship. The modelled peak power of 7.6nW is also very similar to 8.02nW discovered during testing (a 5% underestimation of the true power). However, the short circuit current and open circuit voltage are not similar to the experimentally achieved results. The open circuit voltage is over-estimated in the model by 64% (0.263V instead of 0.16V) and the short circuit current is underestimated by 48% (105nA instead of 204nA). This lack of agreement between the model and the results achieved in laboratory testing is due to the simplicity of the MATLAB® model. The behaviour of monocrystalline and amorphous silicon PV cells was also modelled and compared to laboratory experimentation in the same way giving similar disparity at GTLS ultra-low illumination levels. In order to more accurately model the behaviour of the PV cells at these low illumination levels it would be necessary to more accurately

predict the behaviour of the parallel resistance in the cells. The parallel resistance values would then be included in the PV cell model (which they are not at present) and would therefore represent a more realistic approximation of reality. This investigation is recommended as future work in order to generate a more useful theoretical model of PV cell behaviour at the ultra low illuminations described here.

### 6.2.4.3 Modelling the efficiency of PV cells

The efficiency of a PV cell may be calculated by using Equation (3-15) (from Section 3.8.4) so long as all of the quantities are known.

$$\eta_{PV} = \frac{V_{oc}.I_{sc}.FF}{P_{in}} \quad \textbf{(3-15)}$$

An ICRB consisting of two 72.3mmX15.0mm a-Si PV cells and 24 GTLSs of dimension 15mmX3mmØ length was constructed and surrounded by a reflective layer of gold. The performance of the PV cells under illumination by these GTLSs was measured by the methodology described in Section 4.9.2, generating an I-V curve and a P-V curve as shown in Figure 6-24.

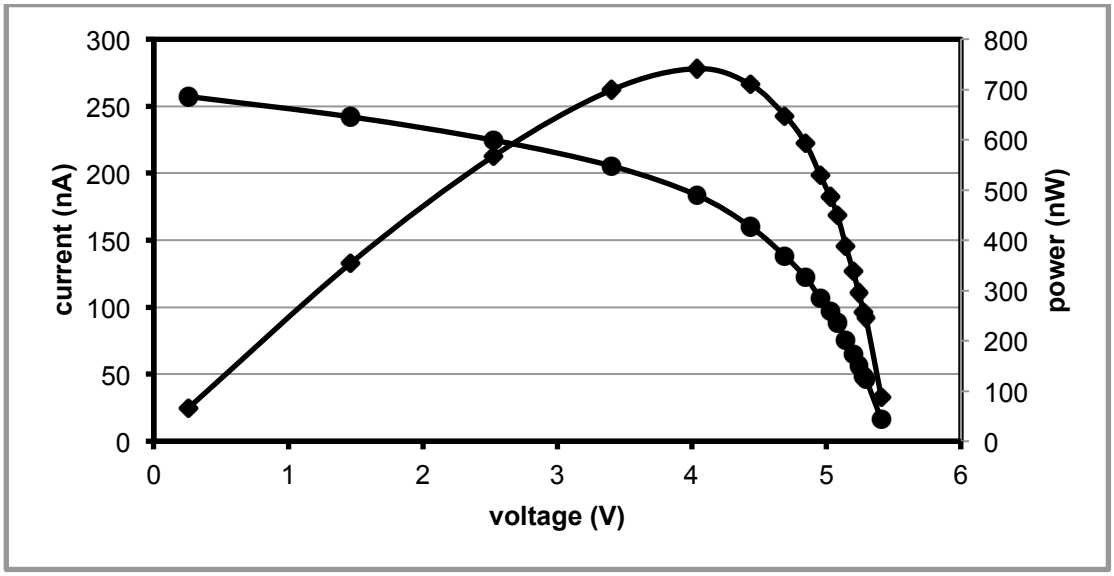



**Figure 6-24:** Power-voltage and current-voltage curves for an ICRB using a-Si PV cells and 24 15mmX3mmØ GTLSs (in a gold coated casing)

The peak power point in this configuration is 741.5nW reached at 4V and 187.5nA. The calculated fill factor of this I-V curve is 52.7%. The power of light incident on the PV cells from the GTLSs was calculated from Sections 6.2.1, 6.2.2 and 6.2.3 to give a value of 11.8μW. Application of these values to Equation (3-15) provides an efficiency of 6.27% for these PV cells under this level of illumination.

Calculation of a range of PV cell efficiencies is presented in Table 6-3. The peak electrical power measured to be generated by practical ICRB batteries containing the PV cells in question is also shown in this table along with the GTLSs that were used.

**Table 6-3:** Efficiency of selected PV cells under illumination by ultra-low brightness light from GTLSs

| PV cell type | PV cell dimensions | GTLSs | Light power flux (nW) | Electrical power (nW) | PV efficiency |
|---|---|---|---|---|---|
| | | | | | |
| **m-Si** | 59.9mmX30.0mm | 12<br>25mmX3mmØ | 9861 | 10.71 | 0.11% |
| **p-Si** | 49.8mmX19.9mm | 14<br>15mmX3mmØ | 6903 | 8.07 | 0.12% |
| **a-Si** | 72.3mmX15.0mm | 24<br>15mmX3mmØ | 11834 | 741.54 | 6.27% |
| **a-Si** | 107.7mmX28.0mm | 31<br>25mmX3mmØ | 25476 | 1726.56 | 6.78% |

From this experimentation it can be clearly seen that monocrystalline and polycrystalline silicon PV cells are very inefficient at converting light into electricity at the low light levels which GTLSs generate. This result can be extrapolated from the experimentation of Reich et al. which is presented in Figure 6-25 [239]. In their work a variety of PV cell types, including monocrystalline silicon (mc-Si), polycrystalline silicon (c-Si) and amorphous silicon (a-Si) were tested at different illumination levels with their efficiency of conversion of light calculated. These values of efficiency were

then plotted relative to the values of light conversion given under standard test conditions (STC) as shown in Figure 6-25.

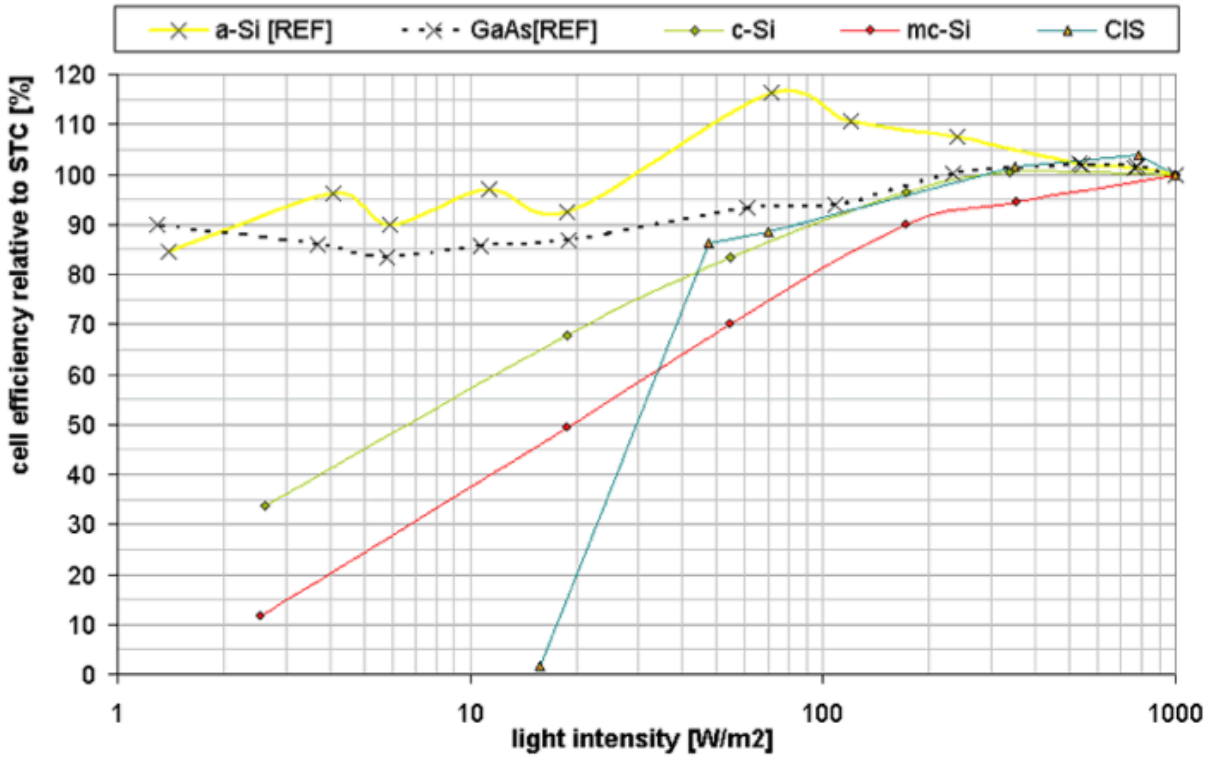



**Figure 6-25:** Comparison of efficiencies of selected PV cells to their STC at varying incident light intensity (reproduced from [239])

As the intensity of the light decreases it is shown that the efficiency of amorphous silicon PV cells (the yellow line with crosses) declines slowly while the efficiency of monocrystalline and polycrystalline silicon PV cells (the green line with large diamonds and the red line with small diamonds) drops away sharply. Experiments were not conducted at the ultra-low light intensities generated by GTLSs (around 0.5W/m$^2$), but this trend of reduced efficiency has been verified by the results presented in Table 6-3.

One additional reason for the disparity of performance of the a-Si PV cells relative to the crystalline (m-Si and p-Si) PV cells when exposed to green GTLS light is that the

spectral sensitivity of a-Si is greater at the wavelength of green light. This is shown in Figure 6-26 [240] where the solid blue line represents the spectral sensitivity of amorphous silicon and the dash-dot line represents the spectral sensitivity of crystalline silicon. The wavelength of green light is across the range of 495nm-570nm [241] and is therefore close to the peak spectral sensitivity of a-Si but only half the maximal spectral sensitivity of crystalline silicon.

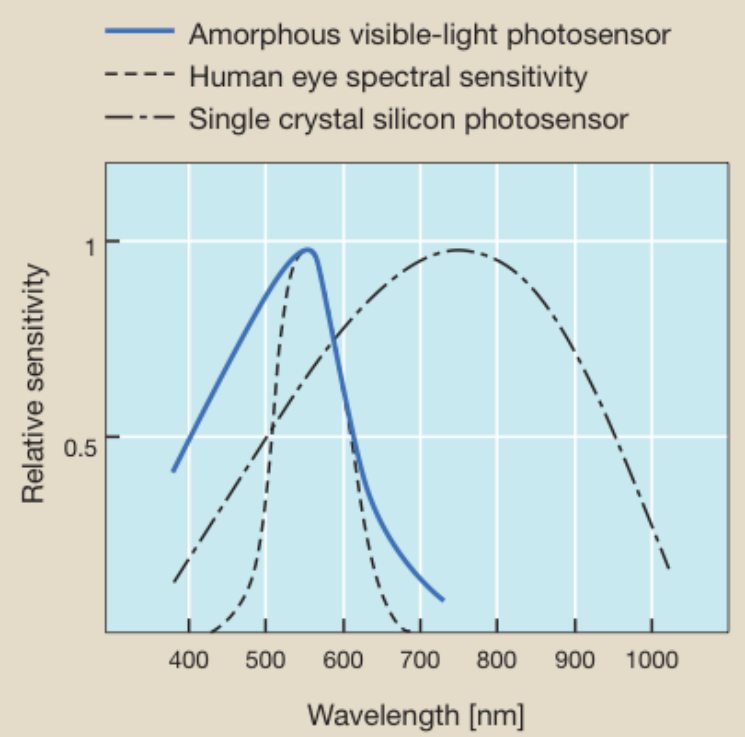



**Figure 6-26:** Spectral sensitivity of amorphous and crystalline silicon (reproduced from [240])

Overall laboratory experiments have demonstrated a broad agreement with modelled expectations of the behaviour of PV cells at various illumination intensities. The efficiency of PV cell conversion of light into electricity has been found to be greatly reduced in crystalline silicon PV cells at low light intensities. However, amorphous silicon PV cells have demonstrated similar efficiency of conversion of light into electricity at the ultra-low light intensities generated by GTLSs as at indoor light

intensities for which they were designed. The highest experimentally achieved efficiency of conversion of light into electricity by an a-Si PV cell was 6.78% with 107.7X28.0 PV cells.

### 6.2.5 Efficiency of capacitor charging

This section will explore the efficiency of charging a capacitor from an ICRB using both a theoretical model and experimental results. In addition, the performance of various capacitor types will be examined.

#### 6.2.5.1 Model of charging a capacitor

By treating a PV cell as a constant current source and through application of the equations found in Section 5.7.1 it is possible to model the efficiency of charging a capacitor, dependent on the length of time over which charging occurs. The characteristic of the capacitor which most impacts on this model is its parallel resistance and this resistance is related to the voltage to which the capacitor is charged, as demonstrated in Appendix B.4. The reason why the efficiency of charging does not begin at zero seconds but at 200 seconds instead is due to the simplicity of the relationship between capacitance and resistance as described by Equation (5-67).A more complex model would be necessary to model shorter periods of charging, however the charging of a capacitor by an ICRB is a lengthy process and therefore this model is of sufficient complexity for this particular task. As the charging duration increases so does the efficiency of charging until the increase in efficiency becomes negligible after 4000 seconds. For a 47μF capacitor that is charged to its peak voltage over a period of 4000 seconds the efficiency of charging is modelled to be 95.00%.

Experiments measuring the charging of capacitors connected to ICRBs located in the lightproof housing were conducted according to the regime discussed in Section 4.9.1.1. Comparing the results from these experiments with the results of laboratory experimentation measuring I-V and P-V curves directly from ICRBs, discussed in Section 6.2.4, reveals the effect of charging the capacitor on the generation of power. For the same ICRB (two 72.3mmX15.0mm a-Si PV cells and twenty four 15mmX3mmØ GTLSs) the difference between the two results at any measured voltage provides the efficiency for charging the capacitor (at that specific voltage), as is illustrated by Figure 6-27. The difference between the power measured to be entering the capacitor and the power measured to be generated by the ICRB represents loss in charging the capacitor. This loss can be calculated at any voltage in Figure 6-27 for the efficiency of charging the capacitor at that particular voltage.

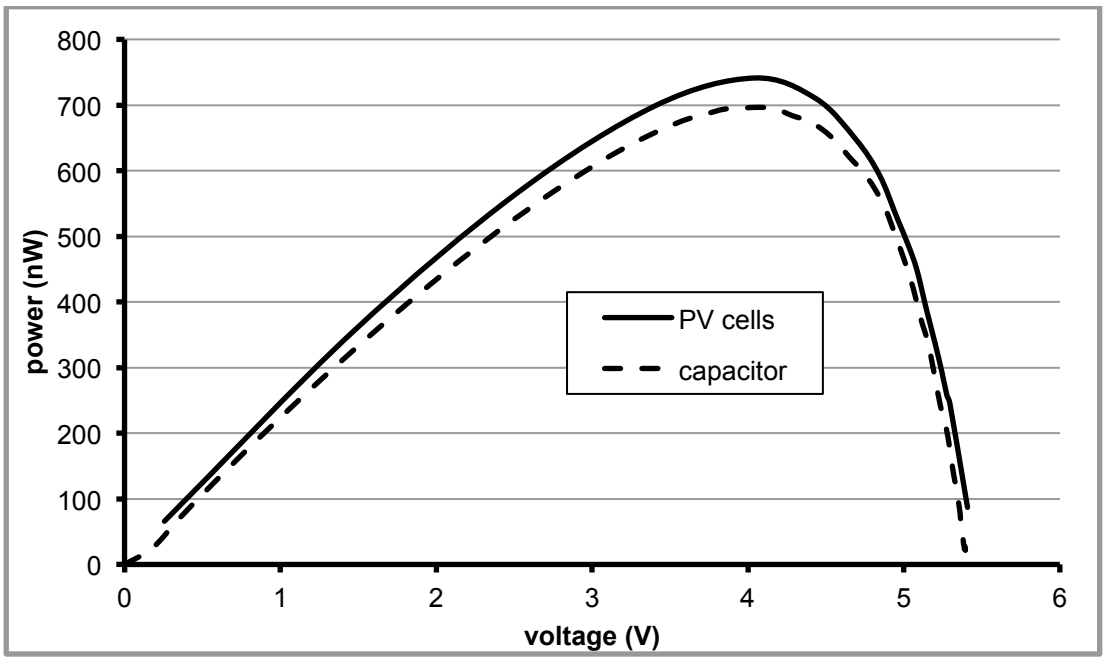



**Figure 6-27:** Power against voltage curves measured directly and charging a capacitor for an ICRB (using a-Si PV cells and twenty four 15mmX3mmØ GTLSs)

A 47μF 25V aluminium electrolytic capacitor was tested, with (at peak power, at 4.02V) the efficiency of charging is calculated to be 93.98%. The efficiency with which the capacitor accepts charge alters as the voltage within it changes.

The modelled efficiency of 95.00% is in broad agreement with this experimentally observed efficiency of 93.98% for the same capacitance of capacitor and the same duration of charging (4000 seconds).

The reason for the loss of energy (and hence power) during charging is due to leakage losses in the capacitor which are related to the parallel resistance of the device. This imperfect parallel resistance has multiple causes including moisture absorbtion in the dielectric, distorted polarization in the dielectric and impurities causing breakdown of the dielectric [242]. The higher the parallel resistance the lower the subsequent leakage losses. Factors affecting the parallel resistance of capacitors include the type of electrolyte, the age of the capacitor (leakage losses tend to increase as the capacitor ages) and the temperature at which the capacitor is operating – increased temperatures result in increased leakage losses.

### 6.2.5.2 Charging performance of different capacitor types

The relative performance of niobium oxide, tantalum, ceramic and aluminium electrolytic capacitors was investigated by connecting each type of capacitor in turn to an ICRB composed of ten 25mmX3mm and two 15mmX2.5mm GTLSs sandwiched between two arrays of three 54.5mmX4.5mm PV cells. The results of testing these arrangements are shown in Figure 6-28.

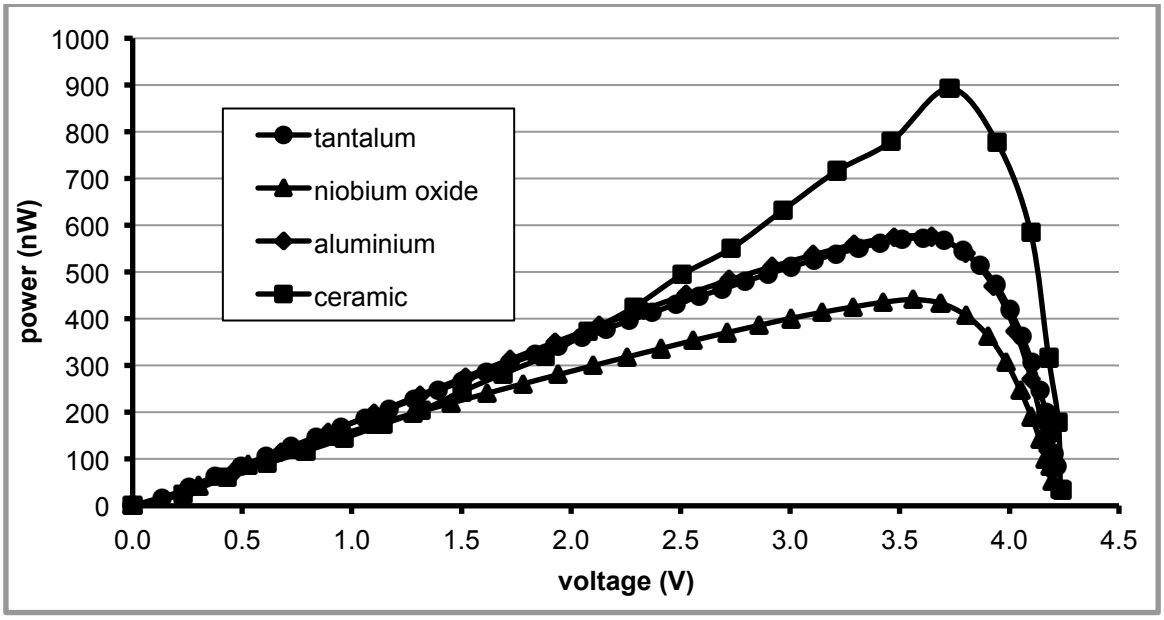



**Figure 6-28:** Power against voltage comparison of charging different capacitors by an ICRB

The most power was obtained when the ICRB was connected to the 47μF 10V ceramic capacitor and the least when connected to the 47μF 10V niobium oxide capacitor. The 100μF 16V tantalum and 47μF 25V aluminium electrolytic capacitors performed in a very similar manner during this experimentation. Examination of the shape of the power/voltage curves in Figure 6-28 reveals that the ceramic capacitor behaved abnormally to the rest. The rate of increase in power entering the capacitors dropped as the power approached its peak in all of the capacitor types except in ceramic, where the rate of increase in power actually rose towards the peak power point. Ceramic capacitors are susceptible to a phenomenon known as dc bias effect whereby the capacitance of the storage device is reduced if a dc voltage is applied within it. The reason for this effect is that the crystalline structure of the dielectric (often $BaTiO_3$) is itself polarized in its uncharged state, partly explaining the ability to generate such large capacitances in relatively small volumes. Applying a dc voltage to the dielectric results in de-polarization and therefore a decrease in capacitance

[243]. This decrease in capacitance is related to the type of ceramic capacitor and to the percentage of rated voltage to which the capacitor has been charged, as shown in Figure 6-29 [244] where the larger image models the behaviour of a 22μF 6.3V ceramic capacitor with a dc field applied to it.

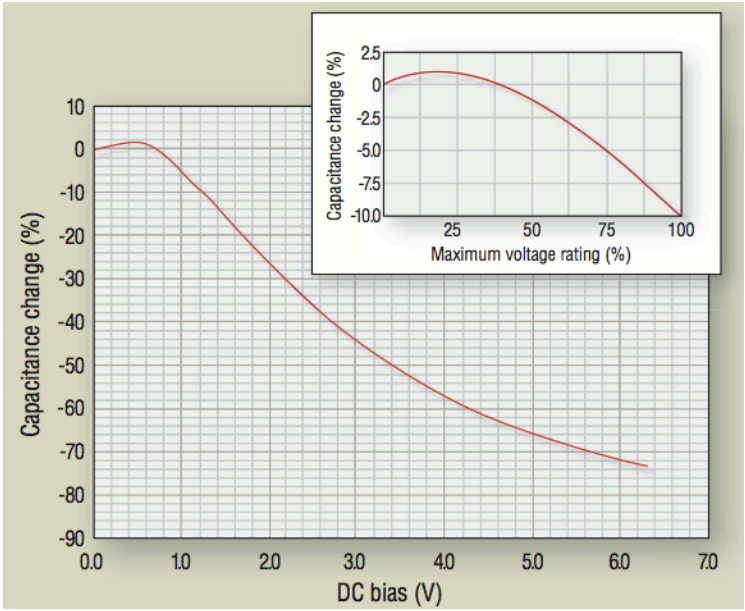



**Figure 6-29:** DC bias effect for X7R and X5R types of ceramic capacitor showing capacitance change set against applied DC voltage (reproduce from [244])

The dramatic changes in capacitance during charging by the ICRB rendered the measured charge stored in the ceramic capacitors at any given time highly inaccurate. Therefore further experimentation was limited to alternative types of capacitor such as aluminium electrolytic and tantalum capacitors. The following section investigates the mechanism of loss which affects these types of capacitor.

### 6.2.5.3 Investigation of leakage loss in capacitors

As leakage loss in capacitors has been shown to be important at the low powers found with ICRBs, selections of capacitors (aluminium electrolytic, tantalum and niobium oxide) were charged to a predetermined voltage and the decrease in their

voltage over time was then measured in order to ascertain their leakage power. The voltage (3.8V) was chosen to be slightly higher than the voltage at which the peak power had been observed to have driven charge into these capacitors from an ICRB, 3.6V, so that a full picture of leakage losses down to the key voltage could be produced. The leakage power generated over the time between readings was then calculated using Equation (4-1) and the leakage power at specific voltages of stored charge in the capacitors produced. The results of these tests are shown in Figure 6-30.

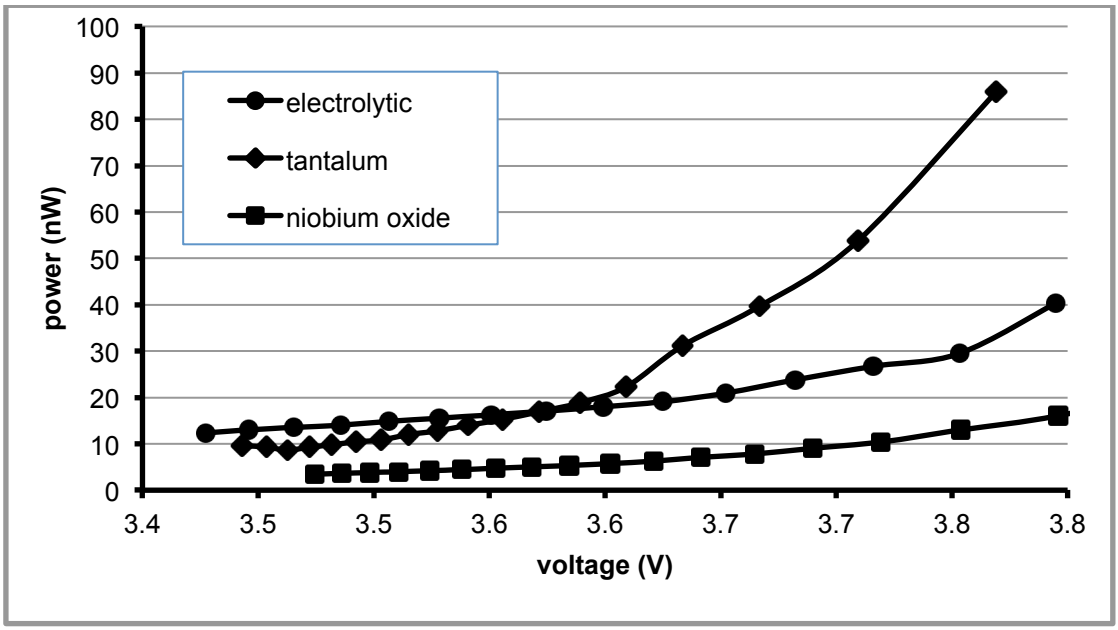



**Figure 6-30:** Comparison of leakage power in electrolytic, tantalum and niobium oxide capacitors

These tests show that, at the peak power voltage of 3.6V, the tantalum and aluminium electrolytic capacitors had a very similar leakage power of 18nW, while the niobium oxide capacitor had a far lower leakage power of only 8nW. It is to be expected that the aluminium electrolytic and tantalum capacitors would have a similar leakage loss at the peak power because their behaviour during charging by an ICRB (Figure 6-28) is markedly similar. However, the niobium oxide capacitors displayed a

much lower leakage power than the other types of capacitor, which is unexpected because the peak power during charging by an ICRB was lower than using the other types of capacitor. The slower rate of charge entering the niobium oxide capacitor (relative to the tantalum and aluminium electrolytic capacitors) may be explained by the higher equivalent series resistance (ESR) of the niobium oxide capacitor. ESR acts to prevent charge from entering a capacitor and for the niobium oxide capacitor it was 0.4Ω [245], while for the tantalum capacitor it was only 0.06Ω [246] and only 0.03Ω [247] for the aluminium electrolytic capacitor. These experiments were repeated with different size capacitors from different manufacturers with a similar result that aluminium electrolytic type had the lowest leakage power.

### 6.2.6 Overall efficiency of ICRB and capacitor system

The overall efficiency of the ICRB and capacitor system ($\eta_{total}$) is described by Equation (5-2).

$$\eta_{total} = \eta_{\beta} \times \eta_{p} \times \eta_{t} \times \eta_{pv} \times \eta_{c} \quad \textbf{(5-2)}$$

The efficiency of beta power flux ($\eta_{\beta}$) in a cylinder of gaseous tritium of radius 1.5mm was calculated to be approximately 82% (Section 6.2.1). The efficiency of photon generation and emission in the phosphor layer ($\eta_{p}$) was found to be 17.5% (Section 6.2.2). The efficiency of photon transport within the ICRB structure up to the PV cell ($\eta_{t}$) was calculated to be 54% (Section 6.2.3.4). Conversion of photons into electricity in the PV cell was calculated to have an efficiency of 6.78% for some of the a-Si PV cells (Section 6.2.4.3). The efficiency of charging a capacitor ($\eta_{c}$) from a constant current source (such as an ICRB) was practically demonstrated at 94% for a 47μF 25V aluminium electrolytic capacitor which is in broad agreement with the theoretical

model which predicted a 95% charging efficiency (Section 6.2.5.1). Inserting all of these efficiencies into Equation (5-2) generates an overall ICRB system efficiency of 0.5%.

The peak measured efficiency of an ICRB and capacitor system was found using 72.3mmX15.0mm a-Si PV cells with twenty four 15mmX3mmØ GTLSs and a 22μF 50V aluminium electrolytic capacitor. This experimentally achieved overall efficiency was 0.6% compared to the theoretically modelled efficiency of 0.5%. The model underestimated the efficiency of conversion of light into electricity in the PV cells, which accounts for the majority of the difference between these two values.

The areas where largest gains may be made regarding overall efficiency of the ICRB system are in the transport of light within the device and in the conversion of light into electricity in the PV cell. Further exploration of altering the medium between the GTLSs and PV cells may well result in gains in this regard and it may be advantageous to attempt to print the a-Si PV cells directly onto the outer surface of the GTLSs. This would remove two medium transitions for the pathway of light and have the added advantage of decreasing the volume of the overall device (and therefore increase the relative power density of the battery system). Alternative PV cells to silicon types may offer increased efficiencies of conversion at the ultra-low light intensities generated by GTLSs. GaN and AlGaAs PV cells (as explored by Andreev et al. [163]) may increase the overall efficiency of the battery. The efficiency of the a-Si PV cells is estimated to be 8% at present and with alternate PV cells it is feasible that this could be improved in future to nearer 30% efficiency. The potential therefore exists to treble the overall efficiency of the ICRB.

## 6.3 Power

This section describes the power generated by the ICRB system and analyses the amount of power generated by a variety of constructed ICRBs. The power generated is analysed whilst remembering the power required to power a WSN sensor node. In addition, the useful lifetime of an ICRB system is investigated through long-life buried testing with the results discussed.

### 6.3.1 Overall power in ICRB and capacitor system

When describing the power of the ICRB and capacitor system there are a number of ways to interpret the data. The units of the comparison between different battery systems can be in power per volume (power density), power per active surface area of the PV cells or in power per GBq of $^{3}H$ used.

When calculating the volume of the device, the volume of the PV cells and the distance between them (caused by the GTLS presence) was calculated, along with the volume of any reflective material used, and combined with the volume of the capacitor. The capacitor used in all cases was a 10μF 50V aluminium electrolytic capacitor of volume 0.25cm$^3$. The volume of the casing was neglected for these calculations because the operation of the batteries is not dependent upon the (variable) thickness of the container they are placed in. A comparison of selected batteries is presented in Table 6-4.

**Table 6-4:** Comparison of peak power of selected ICRB systems as a function of the activity, volume and active surface area of the PV cells in use.

| PV cell type | PV cell dimensions (mm) | Reflective coating | GTLSs (mm) | Peak power (nW) | Power (nW/GBq) | Power (nW/cm3) | Power (nW/cm2) |
|---|---|---|---|---|---|---|---|
| | | | | | | | |
| m-Si | 2 59.9 X 30.0 X 2.6 | none | 12 25X3Ø | 10.2 | 0.05 | 0.68 | 0.58 |
| p-Si | 2 49.8 X 19.9 X 2.6 | none | 14 15X3Ø | 7.7 | 0.10 | 0.92 | 0.63 |
| a-Si | 6 54.5 X 4.5 X 1.2 | gold | 10 25X3Ø + 2 15X3Ø | 575.1 | 3.18 | 123.28 | 39.08 |
| a-Si | 2 91.9 X 24.8 | none | 30 25X3Ø + 1 22.5X3Ø | 1606.2 | 3.06 | 126.90 | 35.24 |
| a-Si | 2 34.9 X 13.8 X 1.2 | none | 12 15X3Ø | 241 | 3.79 | 78.31 | 25.02 |
| a-Si | 2 34.9 X 13.8 X 1.2 | gold | 12 15X3Ø | 250.1 | 3.93 | 75.15 | 25.96 |
| a-Si | 2 34.9 X 13.8 X 1.2 | barium sulfate | 12 15X3Ø | 283.6 | 4.46 | 72.22 | 29.44 |
| a-Si | 2 72.3 X 15.0 X 1.2 | gold | 24 15X3Ø | 696.9 | 5.48 | 114.12 | 32.13 |
| a-Si | 2 103.1 X 15.5 X 1.2 | none | 34 15X3Ø | 786.2 | 4.36 | 88.54 | 24.60 |

It is clear that monocrystalline and polycrystalline silicon PV cells are highly inefficient at converting low intensity GTLS light into electricity and it was therefore expected that the power per GBq would be so low in the ICRBs using these types of PV cells compared to other ICRB types. It is interesting that the greatest power density does not always give the greatest power per activity and is due to the different activity density of the GTLSs used, where the 15mmX3mmØ GTLS had an activity of 5.3GBq and the 25mmX3mmØ GTLS had an activity of 17GBq.

A comparison of the generated peak powers per radioisotopic activity is particularly useful in the arena of radioisotopic batteries as this reveals the overall efficiency of the ICRB system in generating electrical power. In addition, there are regulations limiting the amount of radioisotope which may be used in any individual device (1000GBq for $^{3}H$). The radioisotope is also the most expensive component of the device which makes it desirable to minimise the quantity being used as much as possible. A comparison of manufactured ICRB systems reveals that the most efficient

devices use the 15mmX3mmØ GTLSs in combination with a-Si photovoltaic cells, with a reflective material increasing this efficiency further.

### 6.3.2 Long-life buried testing of ICRB

As described in Section 4.9.4, an ICRB was attached to a buried water pipe and then covered with soil with readings automatically taken, every 16 minutes, of the generated voltage over a two month time-period. The ICRB was composed of two 34.9mmX13.8mm a-Si PV cells and fourteen 14.5mmX2.5mmØ GTLSs, all contained in a casing without reflective coating. Immediately prior to installation the ICRB was measured to be generating 294.1nW at 1.8115V and 162.3nA. A prior experiment had shown that the voltage decreased broadly in line with the decrease in power. The results of the measurement of the ICRB voltage are shown in Figure 6-31.

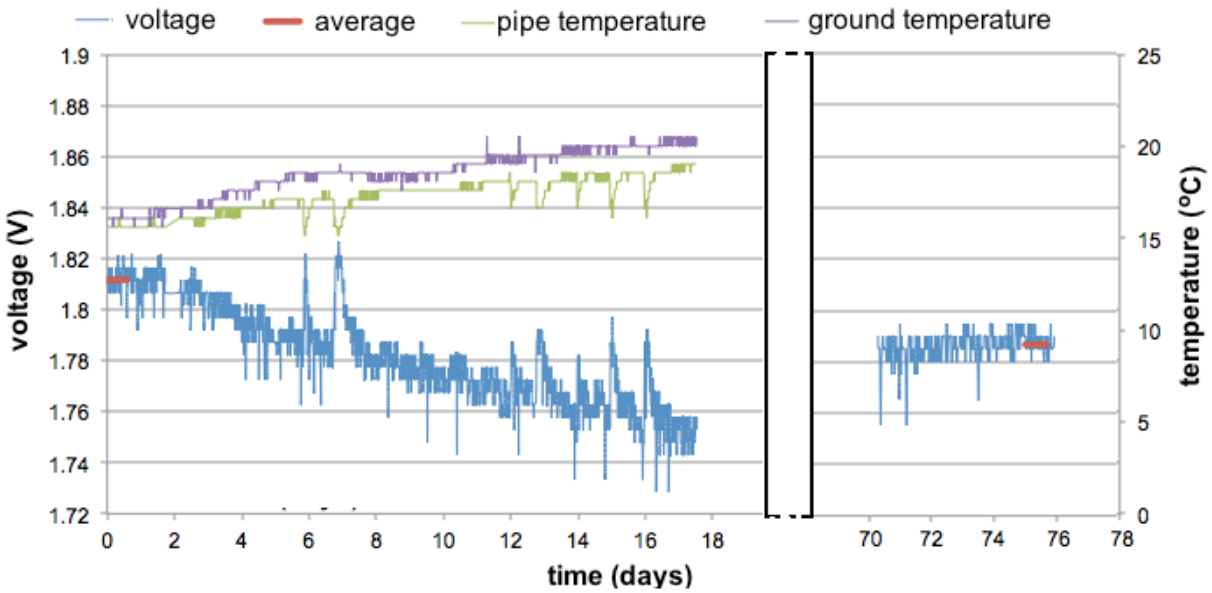



**Figure 6-31:** Voltage of buried ICRB measured over time and compared with the ground temperature and pipe temperature

The voltage (blue line) can be seen to have decreased slightly over time, though not in a linear manner. Meanwhile, the pipe temperature (green line) increased steadily

over the first 16 days before becoming highly erratic. There is a gap in recorded data due to the data logger being mistakenly turned off for an extended period of time. It is believed that the temperature sensor (thermistor) used to generate data became damaged after 20 days in the soil and began to provide unreliable readings.

There is a clear and immediate relationship between changes in the measured pipe temperature and changes in the measured voltage of the ICRB. This relationship is demonstrated most clearly by the "spiked" sudden drops in temperature that correspond in each instance to a spiked rise in the voltage. As the temperature decreases the voltage rises and vice versa. Meanwhile the ground temperature does not experience these spikes, which are unlikely to therefore be an artefact of measurement. Overall the temperature local to the ICRB was measured to have risen by 2.93°C over the period of 16.7 days while the voltage decreased by 43.91mV over the same period. Shaari et al. [248] explored the relationship between temperature and PV cell voltage output with their results shown in Figure 6-32.

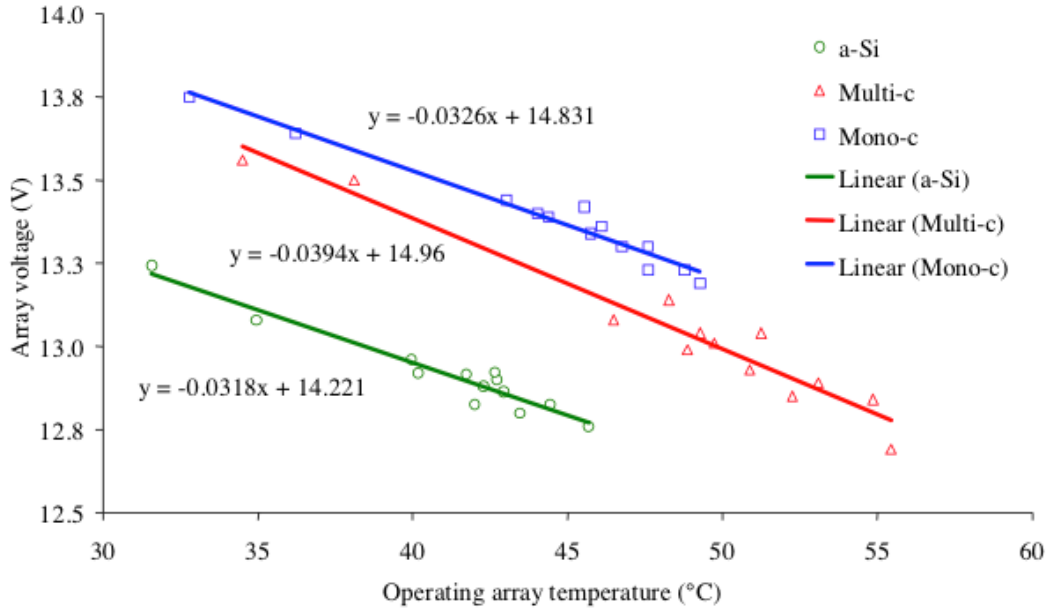



**Figure 6-32:** Measured values of voltage generated by a variety of PV cell array types at different temperatures, with the relationship between temperature and voltage modelled (reproduced from [248])

It is not possible to use the exact relationship between voltage and temperature for a-Si PV cells as described by Shaari et al. [248] to normalise the decrease in voltage over time displayed in Figure 6-31 because this ratio depends on the type of a-Si PV cells used.

From Figure 6-31 the ICRB voltage shows a decline over the period of 71 days of 24.4mV from a starting reading of 1.8115V. At this rate of change it would take 7.2 years for the voltage to be reduced to half of its starting value. The radioisotope used in this ICRB was tritium, which has a half-life of 12.3 years. Therefore, the voltage of the ICRB declines at a rate 1.7 times faster than the half-life of the radioisotope. This is primarily due to slow radiation damage of the phosphor layer through the creation of impurities and the ejection of phosphor atoms from the phosphor lattice. This figure of 7.2 years is similar to the predicted time for the halving of GTLS light intensity every 6.2 years as shown in Section 5.4.1. The difference is due to a small decrease in local temperature (resulting in a slightly higher voltage) for the later readings in Figure 6-31.

### 6.3.3 Suitability of ICRB system for powering a WSN sensor node

A WSN sensor node requiring ultra low power in order to function has been developed in parallel with this work (not described here) and is reported to require 1μW of continuous power in order to function. The greatest peak power generated in an ICRB during testing was 1.606μW (Table 6-4) using 91.9mmX24.8mm a-Si PV cells and thirty 25X3mmØ and one 22.5mmX3mmØ GTLSs. This ICRB is therefore capable of providing the power requirements of the WSN sensor node for a period of

4.24 years (assuming a half-life of the battery power of 6.2 years). The activity of $^{3}H$ contained in this device is 525GBq, which sits inside the limit proscribed by UK legislation [171]. In order to power the WSN sensor node for 20 years, as originally envisaged, the ICRB would need to produce 9.36μW at beginning of life and would therefore require 3058GBq of $^{3}H$ at the same efficiency for all parts of the ICRB. This activity of $^{3}H$ is greater than is allowed by UK legislation for a single device and therefore further efficiency gains would have to be made before this device could power a WSN sensor node for 20 years. A scaled version of the most efficient ICRB would be capable of providing more than 1μW for 15 years whilst still remaining within the 1000GBq regulation. A 20 year lifetime is therefore a feasible possibility.

## 6.4 Conclusions

This chapter has presented and compared the results of theoretical modelling with laboratory investigation and field trials. Theoretical results have been discussed in terms of their similarity or otherwise to the experimentally achieved measurements. Laboratory results have also been discussed in the context of their effect on the overall efficiency of the ICRB system.

Multiple ICRBs were manufactured and tested, with the results of only the most pertinent of these batteries presented here. The highest power generated by a manufactured ICRB was found to be 1.606μW, which is sufficient to power a WSN sensor node (shown to require only 1μW in research not presented in this thesis). The greatest overall efficiency achieved was found with 72.3mmX15.0mm a-Si PV cells and twenty four 15mmX3mmØ GTLSs and gave an efficiency of 0.60%. This compares with the work of Deus [1] who reported 0.17% overall efficiency using

GTLSs and a-Si PV cells. The use of reflective materials surrounding the ICRBs was found to improve the efficiency of the devices by up to 26% (depending on the geometry of the device). Following extensive testing it was found that aluminium electrolytic and tantalum capacitors are the most useful power storage options. Buried long-life testing of the ICRB system demonstrated its suitability to power applications for more than 7.2 years (dependent on the starting power of the device).

The theoretical model showed good convergence with practically achieved results in its modelling of the generation of light from GTLSs, and became more accurate in its prediction of efficiency gains in the total system stemming from the introduction of reflective materials with additional improvements. The model of PV cells was shown to be useful as was the model of the efficiency of capacitor charging, which showed a very good convergence with practical measurements.

Practical and theoretical investigation revealed transport of light within the ICRB and conversion of light into electricity in the PV cell as the two main areas where efficiency gains are most likely to be achieved in future research.

# 7 CONCLUSIONS

## 7.1 Thesis summary

Power supplies for buried wireless sensor network sensor nodes should be capable of providing useful power for the lifetime of the nodes. This consideration, along with the requirement to operate underground, limits the power options that are suitable for this application. A unique solution to the requirement is reported in this thesis. This research presents the design, modelling, manufacture and testing of an indirect conversion radioisotopic battery (ICRB) and capacitor system.

Gaseous tritum light sources (GTLSs) were used as the source of radioisotope due to their safety and the pre-existing UK legilslation allowing their use. Multiple ICRBs were constructed and tested in order to investigate the effect of altering a varity of parameters of the power source, such as capacitors, reflective materials, PV cells, GTLSs, etc. Long life buried testing of an ICRB was conducted on a water pipe in order to investigate the effect of burial and aging on the power source.

A comprehensive model was compiled for each of the individual stages of energy transport and conversion occurring within the ICRB and capacitor system. The results of this modelling were then compared with practical laboratory experimentation with conclusions drawn concerning the suitability of the model and the reasons behind variations in ICRB performance.

## 7.2 Key conclusions

The key conclusions of this research are:

- GTLSs sandwiched between two layers of PV cells were found to be the most efficient arrangement during initial testing.
- The overall modeled efficiency of an ICRB consisting of twenty four 15mmX3mmØ GTLSs, a-Si PV cells, no reflective coating and a 47μF 25V aluminium electrolytic capacitor was found to be 0.5%. The key parameters affecting this model are the efficiency of the phosphor layer generation of light, the transport of light within the ICRB and the efficiency of the PV cells.
- Comparison of theoretical models with laboratory measurements of ICRB and capacitor systems showed that the model worked well when modeling the generation of light in GTLSs, but it under-estimated performance when modeling the conversion of light into electricity in the PV cells. This was due to the PV cell model failing to model the effects of operation at the low light levels of GTLSs.
- Multiple prototype ICRBs were made with 0.6% recorded as the highest measured overall efficiency. This ICRB used two 72.3mmX15.0mm a-Si PV cells, no reflective coating and a 22μF 25V aluminium electrolytic capacitor.
- Barium sulfate was found to be the most effective reflective material for ICRBs and increased the peak power output of an ICRB by 26% (relative to no reflective coating being present).
- An ICRB was constructed which was measured to generate 1.6μW, sufficient to provide power to a wireless sensor network sensor node designed and

constructed in conjunction with this work (though not presented here) which required 1μW to provide readings once every day.

- Buried testing of an ICRB over a two month time period showed the robustness of the battery system to changes in temperature as well as its long-life capabilities in a buried environment.

## 7.3 Recommendations for future work

There are aspects of this research in which future investigation may prove beneficial, some of which are presented here. These areas involve practical and theoretical investigation of the power source as well as alternate methods of using the ICRB.

### 7.3.1 Battery design improvements

- Exploration of alternative non-silicon based PV cell types might result in efficiency gains for the system, particularly AlGaAs and GaP PV cells as their spectral efficiency is close to the spectral irradiance generated by the GTLSs under test. The use of such alternate PV cells offers the prospect of increasing the overall efficiency of ICRBs by as much as 300%.
- A further refinement of the ICRB design would be to “print” the PV cell directly onto the outside of the GTLSs [249]. In this way a significantly increased proportion of the light emitted by the GTLSs would be incident on the PV cells and therefore potentially be converted into electricity. An added benefit of this design would be to remove one layer of glass (on the surface of the a-Si PV cells) and, potentially, also the spaces between GTLSs. Using a single GTLS and surrounding it with a printed on PV cell, in this manner, would dramatically increase the power density of the device.

- Alternatively waveguides could be used to focus the light emitted from the GTLSs onto a smaller surface area PV cell. The higher intensity light might then be converted with greater efficiency into electricity within the PV cell.
- Alternative radioisotopes should also be considered for use in future batteries, particularly $^{63}$Ni and $^{241}$Am. $^{63}$Ni has a half-life of 101.2 years while the half-life of $^{241}$Am is even longer at 432.2 years. Such long half-lives should enable a future battery to operate for the 20 years envisaged in this report without having to increase the initial quantity of radioisotope present. Additionally both $^{63}$Ni and $^{241}$Am have far higher specific power than does $^{3}$H and therefore less of these radioisotopes would be required in order to generate the same power.
- In addition the use of alternative phosphors should be investigated with the aim of finding the most efficient generation of photons which can also be most efficiently converted into electricity by a PV cell.

### 7.3.2 Theoretical modelling

- The key area of theoretical modelling which could be improved is the model of PV cell conversion of light into electricity. Currently the model is useful for high or medium light levels (outdoor light or indoor office light levels) but is less useful at the ultra-low light levels of GTLSs. This is due to a simplifying assumption used in most PV cell models which is that the internal (parallel) resistance of the PV cell is infinite. This assumption is acceptable at high light levels as the impact of parallel resistance is negligible, however at low light levels this resistance becomes increasingly influential on the output of the PV cell. Therefore generating a model that included this parameter would improve the accuracy and usability of this aspect of modelling.

- In addition, future work should attempt to model the effect of alternate arrangements of PV cells, radioisotopes and phosphors. This modeling should attempt to simulate the effect of printing the PV cells onto the outside of the GTLSs

### 7.3.3 Alternative uses of the battery

- In addition to finding use as a power source for buried WSN sensor nodes, the ICRB described in this research could prove useful for monitoring other types of assets (such as bridges, buildings, planes, etc.).
- An ICRB may also find use as part of a hybrid system alongside another power source. One potential application of this idea would be to use an ICRB to overcome the leakage losses in a battery (or capacitor) whilst using an energy harvesting device to periodically charge the battery when an “event” occurs (such as a train passing over a section of railway track). In this way only a very small quantity of the radioisotope might be required (as the power necessary to overcome the leakage power would be very low).

# APPENDIX A: CALCULATION OF GTLS ACTIVITY

## A.1 Manufacturer data on GTLS activity levels

The activity level of the various GTLSs used during testing were calculated using Table A-1 with information regarding filling pressures and temperatures provided by the manufacturer (mb-microtec [217]).

**Table A-1:**Excel based method for calculating the activity of GTLSs

| | | | | | | | |
|---|---|---|---|---|---|---|---|
| | **CALCULATION OF GTLS TUBE ACTIVITY** | | | | | | |
| **Ac** | **Activity in GBq** | | | | | | |
| **To** | **Absolute Zero in Degrees Kelvin** | | | | | | |
| **Ta** | **Temperature at which GTLS Light Sources are filled at 77degrees Kelvin** | | | | | | |
| **V** | **Volume of tube in cm3 - if you insert mm accidentally remember to divide by 1000** | | | | | | |
| **FP** | **Filling Pressure in millibars** | | | | | | |
| **AP** | **Normal ambient pressure in millibars 1013** | | | | | | |
| **SpA/cm3** | **Specific Activity of 98% pure Tritium at NTP conversion from Ci/cm3 into GBq/cm3** | | | | | | |
| | **2.597** | **0.98** | **37** | | **94.16722** | | |
| | **Ci/cm3** | **Purity** | **GBq/Ci** | | **GBq/cm3** | | |
| **Example** | **For a 3 x 15mm GTLS Tube** | | | **Internal** | | | |
| | **Wall thickness 0.45mm** | | | **Radius therefore equals 1.5-0.45mm** | | | **1.05mm** |
| **Ac** | **V** | **To** | **FP** | **SpA** | | | |
| | | **Ta** | **AP** | | | | |
| | | | | | | **Activity of GTLS** | |
| | **0.048836646** | **273** | **330** | **94.167** | | **5.3** | **GBq** |
| | | **77** | **1013** | | | | |

# APPENDIX B: THEORETICAL MODELLING

## B.1 Stage 1: Kinetic energy of radioisotopic decay

The power flux per unit area at the outer surface of the cylinder of gaseous radioisotope was modelled using the point beta source dose function, as described in Section 5.3.2. The power flux at the ends of the cylinder is very similar to the flux on the sides of the same cylinder, and therefore Equation (3-9) was used to model this problem. A MATLAB® script was developed to model this equation.

$$\frac{dP_\beta}{dS_E} = \frac{3.7X10^{10}.d.A_m}{4\pi}\int_0^{\frac{\pi}{2}} cos\theta sin\theta \int_0^{C_2}\left[\varepsilon_{av} - \int_0^{\rho.d} 4\pi r^2.\varphi(r)dr\right]d\rho d\theta \quad \textbf{(3-9)}$$

where $C_2 = \frac{L}{cos\theta}$ if $0 \leq \theta \leq arccos\left(\frac{L}{\sqrt{R_c^2+L^2}}\right)$ or $C_2 = \frac{R_c}{sin\theta}$ if $arccos\left(\frac{L}{\sqrt{R_c^2+L^2}}\right) < \theta \leq \frac{\pi}{2}$

## B.1.1 Power flux per unit surface area from gas in cylindrical form

This is a three stage process. The first two integrals are solved symbolically, then the output equations are placed into a matrix form (with “dots” before multiplication and division symbols), and finally the remaining step of integration is undertaken numerically, using constants taken from

**Table 5-1**. The MATLAB® script for these stages is shown in the following subsections.

### B.1.1.1 Step 1: Two stages of symbolic integration

```
clear all
syms W L d v theta Eavg t k r ro Rc
syms t1 t2 t3 t4 t5 f2 f3 f4 f5 hi arc x Am J
```

```
% 1st integral
% dose function with respect to r
f1=(0.25*W)*(exp(-10*v*r));
beta1=int(f1,r,0,(d*ro));
f2=(0.75*W)*(exp(-2*v*r));
beta2=int(f2,r,0,(d*ro));
f3=(v*r)*((Eavg*v)-(0.4*W))*(exp(-v*r));
beta3=int(f3,r,0,(d*ro));

% result from integral 1 which is integral 2 input
t1=(Eavg-(beta1+beta2+beta3));

% 2nd integral
% dose function with respect to path length, ro

f4=(L/(cos(theta)));
beta4=int(t1,ro,0,f4);

f5=(Rc/(sin(theta)));
beta5=int(t1,ro,0,f5);

%3rd integral
%  geometrical component of equation
t2=((cos(theta))*(sin(theta))*beta4)
t3=((cos(theta))*(sin(theta))*beta5)
```

### B.1.1.2 Step 2: Equations converted to matrix form

```
clear all
syms W L d v phi theta Eavg t k m Rc

k=(-cos(theta)*sin(theta)*((61*W)/(100*d*v^2)     -     (2*Eavg)/(d*v)     +
(Eavg*L*exp(-(L*d*v)/cos(theta)))/cos(theta)        +         (2*Eavg*exp(-
(L*d*v)/cos(theta)))/(d*v)   -   (4*W*exp(-(L*d*v)/cos(theta)))/(5*d*v^2)   +
(3*W*exp(-(2*L*d*v)/cos(theta)))/(16*d*v^2)           +           (W*exp(-
(10*L*d*v)/cos(theta)))/(400*d*v^2)             -             (2*L*W*exp(-
(L*d*v)/cos(theta)))/(5*v*cos(theta))));
j=1;
dd=k;
k=char(zeros(1,size(dd)+10));
dd=char(dd);
for i=1:size(dd,2)
    k(j)=dd(i);
    if dd(i)=='*'
        k(j)='.';
        j=j+1;
        k(j)='*';
    end
        if dd(i)=='/'
            k(j)='.';
            j=j+1;
            k(j)='/';
        end
            j=j+1;
end
k

m=(-cos(theta)*sin(theta)*((61*W)/(100*d*v^2)     -     (2*Eavg)/(d*v)     +
```

```
(2*Eavg*exp(-(Rc*d*v)/sin(theta)))/(d*v)          +          (Eavg*Rc*exp(-
(Rc*d*v)/sin(theta)))/sin(theta)                 -              (4*W*exp(-
(Rc*d*v)/sin(theta)))/(5*d*v^2)                 +              (3*W*exp(-
(2*Rc*d*v)/sin(theta)))/(16*d*v^2)                +               (W*exp(-
(10*Rc*d*v)/sin(theta)))/(400*d*v^2)             -            (2*Rc*W*exp(-
(Rc*d*v)/sin(theta)))/(5*v*sin(theta))));
h=1;
ee=m;
m=char(zeros(1,size(ee)+10));
ee=char(ee);
for q=1:size(ee,2)
    m(h)=ee(q);
    if ee(q)=='*'
        m(h)='.';
        h=h+1;
        m(h)='*';
    end
        if ee(q)=='/'
            m(h)='.';
            h=h+1;
            m(h)='/';
        end
            h=h+1;
end
m
```

### B.1.1.3 Step 3: Solve final integral numerically

```
clear all
syms theta f1 arc


L=2;
W=56.6;
pres=[0:0.01:3];
v=15000;
Eavg=5700;
Rc=;
Am=9700;
J=0.00000000000000001602;

d=(0.000016.*6.*760.*pres.*0.6)./(273+20);

arc=acos(L./(sqrt((Rc.^2)+(L.^2))));

dtheta=0.001;
thetaint=arc;
thetamax=pi/2;

i=0;
for theta=0:dtheta:(thetaint-dtheta)

i=dtheta.*(-cos(theta).*sin(theta).*((61.*W)./(100.*d.*v.^2)             -
(2.*Eavg)./(d.*v)  +  (Eavg.*L.*exp(-(L.*d.*v)./cos(theta)))./cos(theta)  +
(2.*Eavg.*exp(-(L.*d.*v)./cos(theta)))./(d.*v)        -        (4.*W.*exp(-
(L.*d.*v)./cos(theta)))./(5.*d.*v.^2)            +            (3.*W.*exp(-
(2.*L.*d.*v)./cos(theta)))./(16.*d.*v.^2)          +            (W.*exp(-
(10.*L.*d.*v)./cos(theta)))./(400.*d.*v.^2)       -       (2.*L.*W.*exp(-
```

```
(L.*d.*v)./cos(theta))).(5.*v.*cos(theta))))+i;

end

i;

j=0;
for theta=thetaint: dtheta:(thetamax-dtheta)

j=dtheta.*(-cos(theta).*sin(theta).*((61.*W)./(100.*d.*v.^2)              -
(2.*Eavg)./(d.*v)   +   (2.*Eavg.*exp(-(Rc.*d.*v)./sin(theta))).(d.*v)   +
(Eavg.*Rc.*exp(-(Rc.*d.*v)./sin(theta))).(sin(theta)     -     (4.*W.*exp(-
(Rc.*d.*v)./sin(theta))).(5.*d.*v.^2)            +            (3.*W.*exp(-
(2.*Rc.*d.*v)./sin(theta))).(16.*d.*v.^2)           +           (W.*exp(-
(10.*Rc.*d.*v)./sin(theta))).(400.*d.*v.^2)       -       (2.*Rc.*W.*exp(-
(Rc.*d.*v)./sin(theta))).(5.*v.*sin(theta))))+j;

end

j;

x=i+j;
powerflux=((37000000000.*d.*Am.*x)./(4.*pi));
answer=powerflux.*J.*1000000;

maximum=max(answer);
norm=answer/maximum;
plot(pres, norm)
%plot(Rc, answer)
```

### B.1.2 Efficiency of power flux for gas in cylindrical form

The efficiency of power flux from the gas of radioisotope to the surface of the cylinder of gas may be calculated by application of Equation (5-5). A modified version of the above MATLAB® code is utilized for these calculations.

## B.2 Stage 3: Efficiency of light transport in ICRB

This stage describes the loss of light within the inner geometry of the ICRB between its generation and transmission into to PV cell.

## B.2.1 Derivation of Equation (5-8)

Equation (6-16) is derived through the following methodology. Analysis of Figure B-1(b) reveals that Equation (B-1) is valid. Similarly analysis of Figure B-1(c) shows that Equation (B-2) is correct.

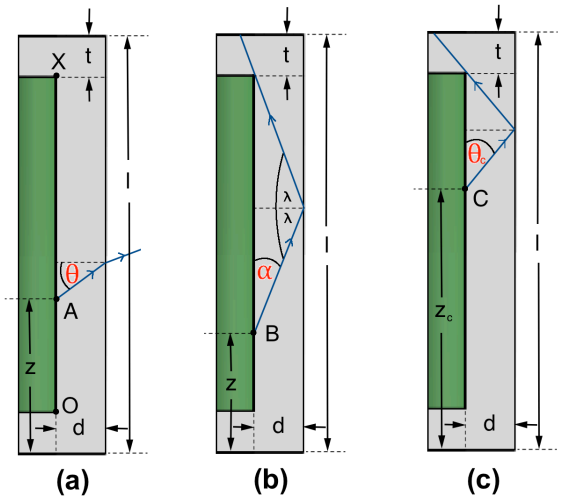



**Figure B-1:** 'x-y' plane of Section X showing (a) transmission through the side, (b) reflection and transmission through the end, and (c) point of maximum reflective transmission

$$\tan\lambda = \frac{2d}{(l-z-t)} \rightarrow \lambda = \tan^{-1}\left(\frac{2d}{l-z-t}\right) \quad \textbf{(B-1)}$$

$$\tan\theta_c = \frac{2d}{(l-z_c-t)} \rightarrow z_c = l - t - \frac{2d}{\tan\theta_c} \quad \textbf{(B-2)}$$

For $t \leq z < z_c$ all of $\alpha$ is able to be transmitted. Therefore for transmission out of the end up to the maximum angle of $\alpha$ from $t \rightarrow z_c$ use Equation (B-3).

$$T_{e1} = \frac{1}{(z_c - t)} \int_t^{z_c} \frac{1}{(\alpha)} \int_{\left(\frac{\pi}{2} - \alpha\right)}^{\frac{\pi}{2}} (1 - R_{A\alpha}) d\alpha dz \quad \textbf{(B-3)}$$

Where $R_{A\alpha}$ is Equation (5-7) (the Fresnel equations) but using $\alpha$ in place of $\theta$.

From $z_c \leq z \leq (l - t)$ the value of $\alpha$ grows beyond $\theta_c$, however any values beyond $\theta_c$ will not be transmitted. Therefore it is necessary to limit this value to $\theta_c$ by subsitituting it into the previous equation, giving Equation (B-4).

$$T_{e2} = \frac{1}{(l - t - z_c)} \int_{z_c}^{(l-t)} \frac{1}{\theta_c} \int_{\left(\frac{\pi}{2} - \theta_c\right)}^{\frac{\pi}{2}} \left(1 - R_{A\theta_c}\right) d\theta dz \quad \textbf{(B-4)}$$

Where $R_{A\theta_c}$ is Equation (5-7) (the Fresnel equations) but using $\theta_c$ in place of $\theta$.

## B.2.2 Simulink model of transmission losses from a single GTLS

Further block diagrams of the Simulink simulation developed to model the loss of light due to reflection and absorbtion in a single GTLS are presented here. The top diagram is shown in Figure 5-18 in Section 5.5.1.5 and is not reproduced here. The workings behind the block titled “efficiency of light transmitted from cap” is shown in Figure B-2 and the diagram behind the block “efficiency of light transmitted from cylinder walls” is shown in Figure B-3 with the “average percentage transmission efficiency” block from this diagram expanded in Figure B-4.

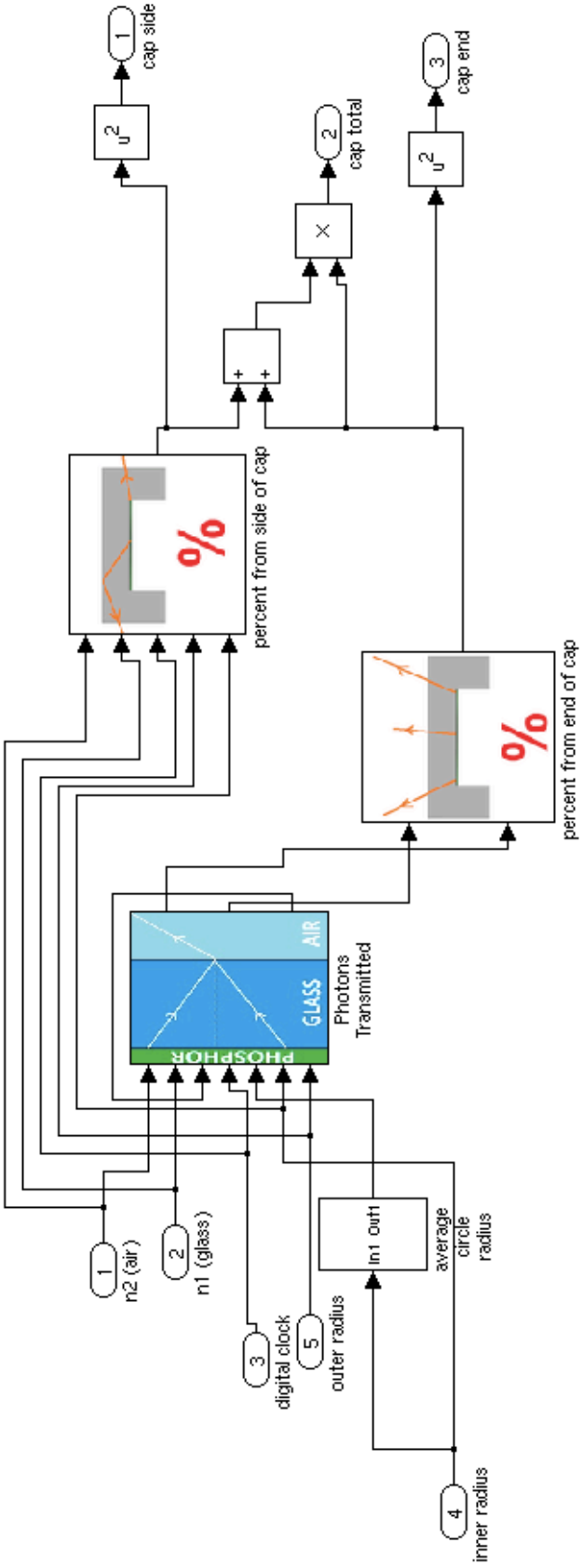



**Figure B-2:** Simulink block diagram: “efficiency of light transmitted from cap”

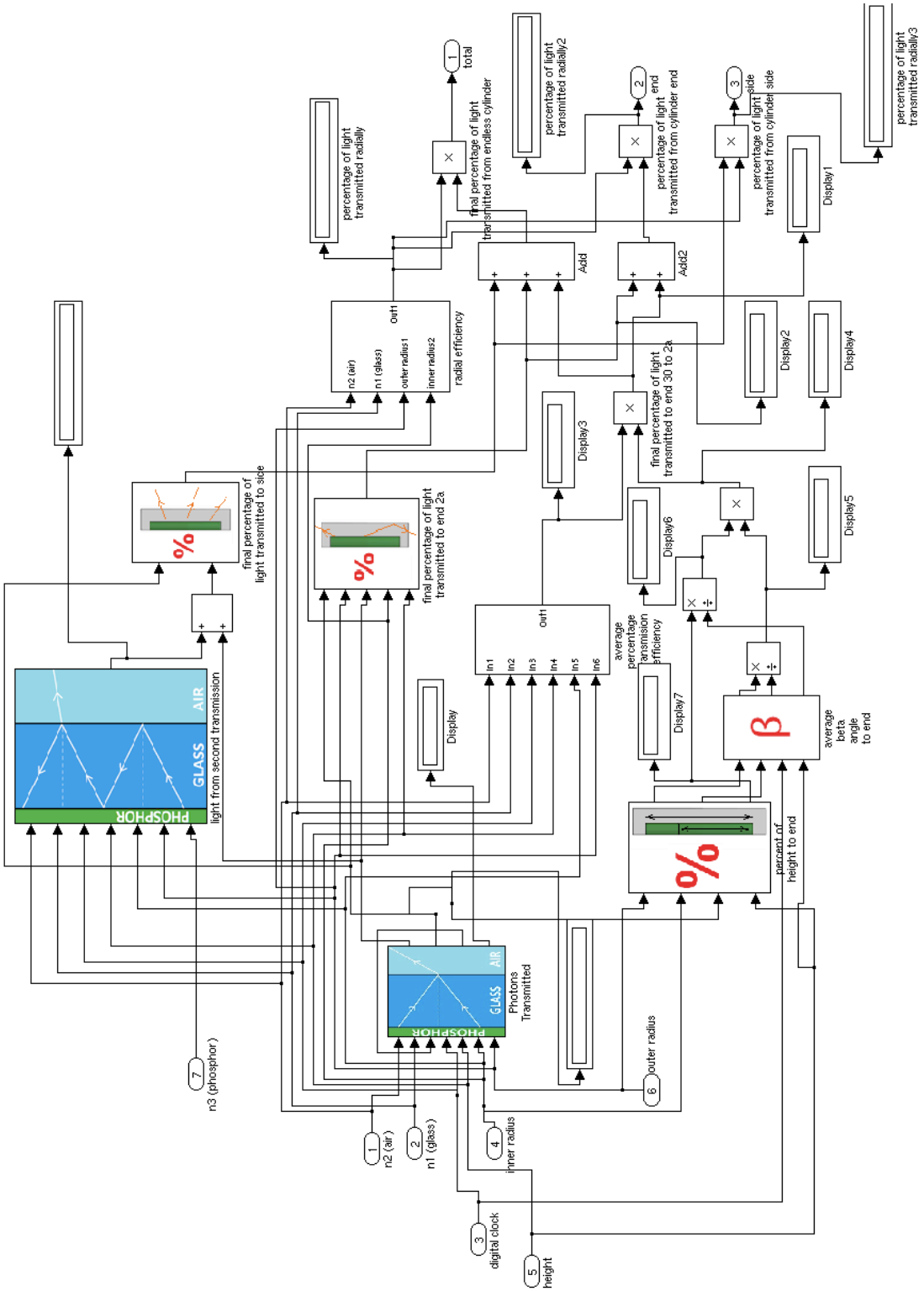



**Figure B-3:** Simulink block diagram: “efficiency of light transmitted from cylinder walls”

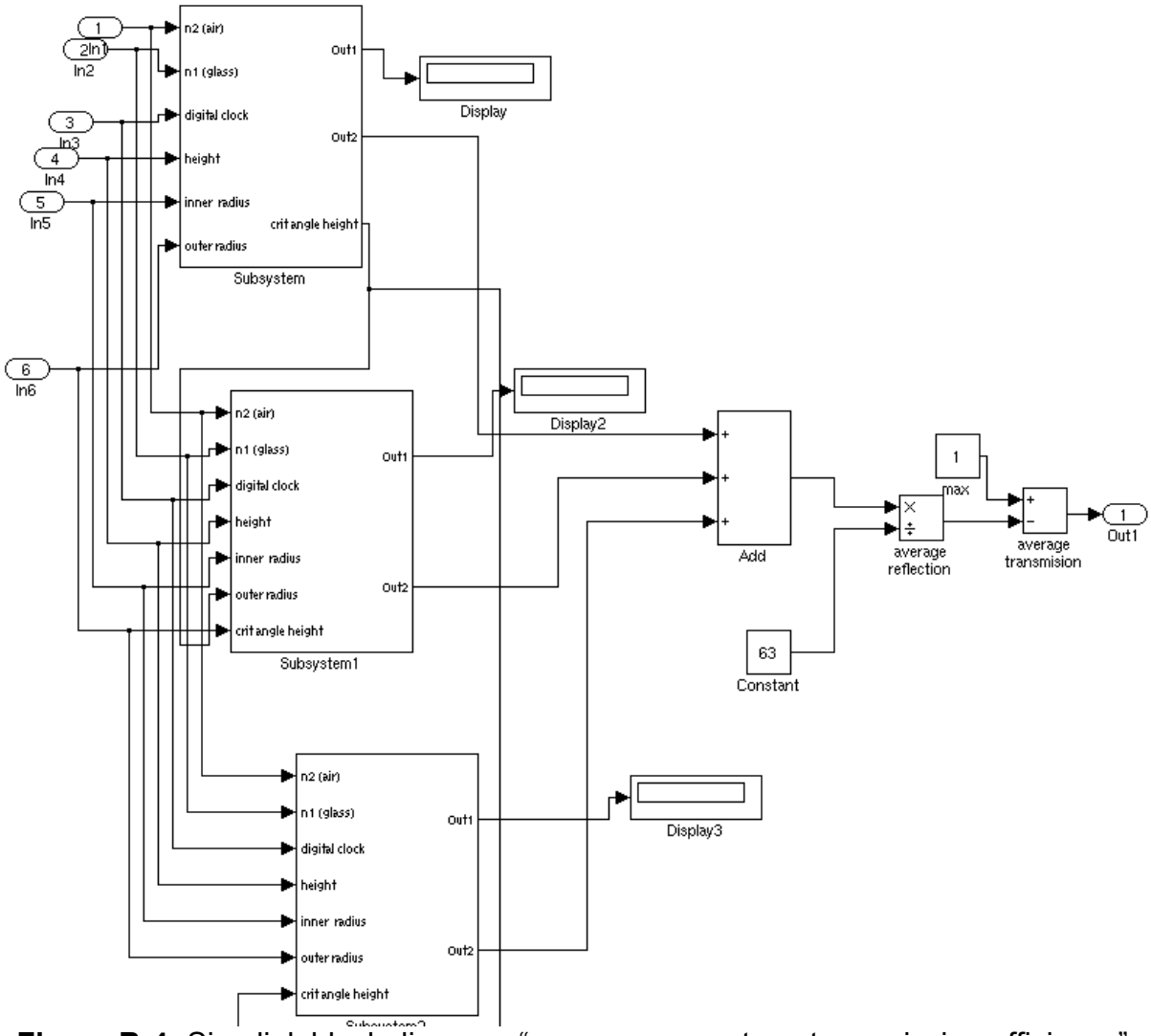



**Figure B-4:** Simulink block diagram: “average percentage transmission efficiency”

One of the “subsystems” from Figure B-4 is shown in expanded form in Figure B-5. In addition the “photons transmitted” block is presented in Figure B-6 in expanded forum, which shows the blocks which contain diagrams modelling the Fresnel equations (a block diagram of which is shown in **Figure 5-17**). Further minor blocks are not presented here.

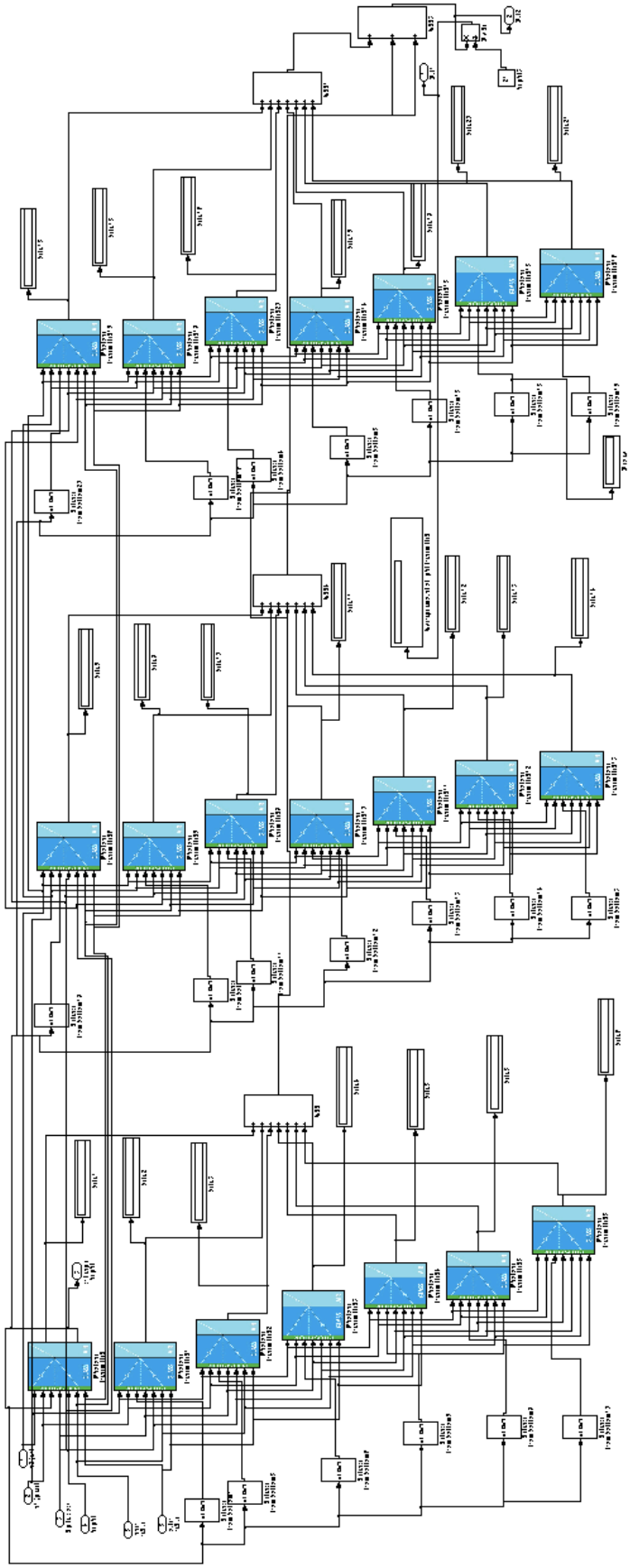


**Figure B-5:** Simulink block diagram: “subsystem”

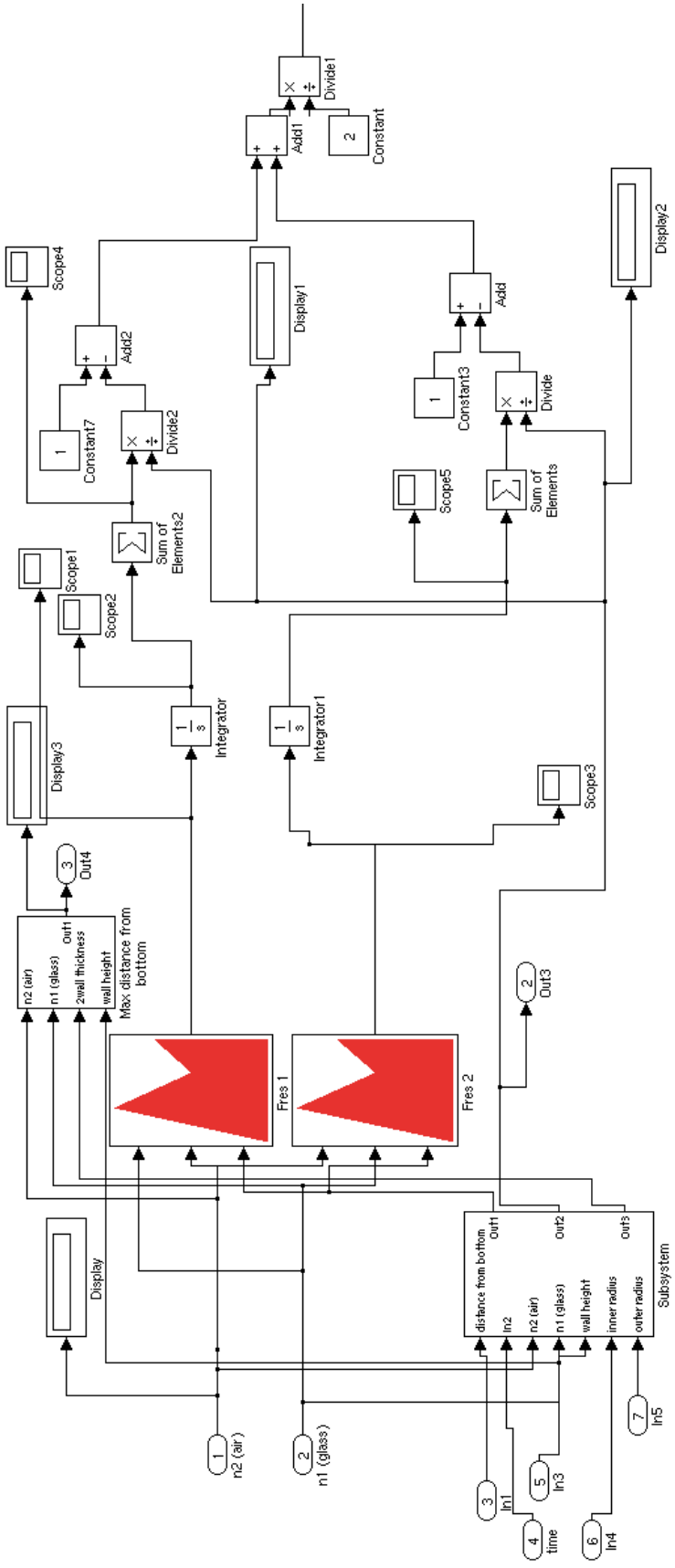



**Figure B-6:** Simulink block diagram: “photons transmitted”

### B.2.3 Transmission losses between GTLSs

This is the MATLAB® code used to model the losses experienced by one GTLS into an immediately adjacent GTLS of the same dimensions.

The m-file which controls the function is shown here:

```
% solving equation 5-6 from phosphors_b

clear all


r1=input('r1 is what?');
%r2=input('r2 is what?');
r2=1.495;
thetaint=pi/1800;


[ ktheta1, ktotalloss, ktheta2, ktotalloss2, ktheta3, ktotalloss3, ktheta4,
ktotalloss4,  ktheta5,  ktotalloss5,  t1,  t2,  t3,  t4,  t5  ]=loss(  r1,  r2,
thetaint);

% averages of each angle segment
ans1=mean((100*ktotalloss)/pi);
ans2=mean((100*ktotalloss2)/pi);
ans3=mean((100*ktotalloss3)/pi);
ans4=mean((100*ktotalloss4)/pi);
ans5=mean((100*ktotalloss5)/pi);

% total average for the full range of theta
 ans6=((ans1*t1)+(ans2*(t2-t1))+(ans3*(t3-t2))+(ans4*(t4-t3))+(ans5*(t5-
t4)))/(t5)

% total average without stage 3
%ans6=((ans1*t1)+(ans2*(t2-t1))+(ans4*(t4-t3))+(ans5*(t5-t4)))/(t5)


hold all

plot ( ktheta1, (100*ktotalloss)/pi, 'r')
plot ( ktheta1, ans1, 'b')
plot ( ktheta2, (100*ktotalloss2)/pi, 'r')
plot ( ktheta2, ans2, 'b')
plot ( ktheta3, (100*ktotalloss3)/pi, 'r')
plot ( ktheta3, ans3, 'b')
plot ( ktheta4, (100*ktotalloss4)/pi, 'r')
plot ( ktheta4, ans4, 'b')
```

```
plot ( ktheta5, (100*ktotalloss5)/pi, 'r')
plot ( ktheta5, ans5, 'b')
plot ( ktheta1, ans6, 'g')
plot ( ktheta2, ans6, 'g')
plot ( ktheta3, ans6, 'g')
plot ( ktheta4, ans6, 'g')
plot ( ktheta5, ans6, 'g')
```

This controls the function (labelled loss.m) shown here:

```
function [   thetaA, totalloss, thetaB, totalloss2a, thetaD, totalloss3a,
thetaE, totalloss4a,  thetaF, totalloss5a, theta1, theta2, theta3, theta4,
theta5 ] = loss( r1, r2, thetaint )

% refractive indicies

n1=1.5;
n2=1;


theta1=acos(r1./(2.*r2));
theta=0:thetaint:theta1;

% critical angle

thetaC=asin(n2/n1);


% limits of theta when equations will change


theta1=acos(r1./(2.*r2));
theta2=acos(r1./r2);
theta3=acos(((r2.*sin(thetaC))+r1)./(2.*r2));
theta4=acos((r1+r2)./(2.*r2));
theta5=pi/2;

% worst case scenario percentage loss over all of the transmission at each
% value of theta
%loss=alfie/pi;

% loss in first section of theta (zero to theta4)
theta4=acos((r1+r2)./(2.*r2));
thetaA=0:thetaint:theta4;

g1= (r1.*(sin(thetaA))).^2;

g2= ((2.*r2)-(r1.*(cos(thetaA)))).^2;

g=sqrt(g1+g2);


loss1=asin(r1./g);
loss2=asin(r1./g);
loss3=asin(r2./g)-asin(r1./g);
```

```
loss4=asin(r2./g)-asin(r1./g);
gain3=((r2.*sin(thetaC))./g)-asin(r1./g);
gain4=((r2.*sin(thetaC))./g)-asin(r1./g);
totalloss=loss1+loss2+loss3+loss4-gain3-gain4;

% loss in second section of theta (theta4 to theta3)
theta4=acos((r1+r2)./(2.*r2));
theta3=acos(((r2.*sin(thetaC))+r1)./(2.*r2));
thetaB=theta4:thetaint:theta3;

g1= (r1.*(sin(thetaB))).^2;

g2= ((2.*r2)-(r1.*(cos(thetaB)))).^2;

g=sqrt(g1+g2);

mu=(pi./2)-thetaB-asin((r1.*sin(thetaB))./g)-asin(r2./g);


loss1=asin(r1./g);
loss2=asin(r1./g);
loss3=asin(r2./g)-asin(r1./g);
loss4=asin(r2./g)-asin(r1./g);
gain3=((r2.*sin(thetaC))./g)-asin(r1./g);
gain4=((r2.*sin(thetaC))./g)-asin(r1./g);
totalloss2=loss1+loss2+loss3+loss4-gain3-gain4;
totalloss2a=loss1+loss2+loss3+loss4-gain3-gain4+mu;

% loss in third section of theta (theta3 to theta2)
theta2=acos(r1./r2);
theta3=acos(((r2.*sin(thetaC))+r1)./(2.*r2));
thetaD=theta3:thetaint:theta2;

g1= (r1.*(sin(thetaD))).^2;

g2= ((2.*r2)-(r1.*(cos(thetaD)))).^2;

g=sqrt(g1+g2);

mu=(pi./2)-thetaD-asin((r1.*sin(thetaD))./g)-asin(r2./g);


loss1=asin(r1./g);
loss2=asin(r1./g);
loss3=asin(r2./g)-asin(r1./g);
loss4=asin(r2./g)-asin(r1./g);
gain3=((r2.*sin(thetaC))./g)-asin(r1./g);
gain4=((r2.*sin(thetaC))./g)-asin(r1./g);
totalloss3=loss1+loss2+loss3+loss4-gain3-gain4;
totalloss3a=loss1+loss2+loss3+loss4-gain3-gain4+mu;

% loss in fourth section of theta (theta2 to theta1)
theta1=acos(r1./(2.*r2));
theta2=acos(r1./r2);
thetaE=theta2:thetaint:theta1;

g1= (r1.*(sin(thetaE))).^2;
```

```
g2= ((2.*r2)-(r1.*(cos(thetaE)))).^2;

g=sqrt(g1+g2);

mu=(pi./2)-thetaE-asin((r1.*sin(thetaE))./g)-asin(r2./g);

loss1=asin(r1./g);
loss2=asin(r1./g);
loss3=asin(r2./g)-asin(r1./g);
loss4=asin(r2./g)-asin(r1./g);
gain3=((r2.*sin(thetaC))./g)-asin(r1./g);
gain4=((r2.*sin(thetaC))./g)-asin(r1./g);
totalloss4=loss1+loss2+loss3+loss4-gain3-gain4;
totalloss4a=loss1+loss2+loss3+loss4-gain3-gain4+mu;

% loss in fifth section of theta (theta1 to pi/2)
theta1=acos(r1./(2.*r2));
thetaF=theta1:thetaint:(pi/2);

g1= (r1.*(sin(thetaF))).^2;

g2= ((2.*r2)-(r1.*(cos(thetaF)))).^2;

g=sqrt(g1+g2);

mu=(pi./2)-thetaF-asin((r1.*sin(thetaF))./g)-asin(r2./g);

loss1=asin(r1./g);
loss2=asin(r1./g);
loss3=asin(r2./g)-asin(r1./g);
loss4=asin(r2./g)-asin(r1./g);
gain3=((r2.*sin(thetaC))./g)-asin(r1./g);
gain4=((r2.*sin(thetaC))./g)-asin(r1./g);
totalloss5=loss1+loss2+loss3+loss4-gain3-gain4;
totalloss5a=loss1+loss2+loss3+loss4-gain3-gain4+mu;

end
```

## B.2.4 Derivation of Equation (5-50)

Equation (5-50) may be formed by considering the dot product of vectors $\underset{HG}{\rightarrow}$ and $\underset{OG}{\rightarrow}$ and the equation of the circle with origin at point O. There is a right angle between the two vectors, and therefore their dot product is equal to zero, as shown in Equation (B-5).

$$\overrightarrow{HG}.\overrightarrow{OG} = 0 \quad \textbf{(B-5)}$$

The two vectors are defined as shown in Equation (B-6).

$$\overrightarrow{HG} = (x_1 - r_o)\,\underline{i} + (y_1 - y)\underline{j}$$
$$\overrightarrow{OG} = (x_1)\,\underline{i} + (y_1)\underline{j} \quad \textbf{(B-6)}$$

Where $x_1$ and $y_1$ are distances along the x and y axis of the vectors.

Substituting Equation (B-6) into Equation (B-5) gives Equation (B-7).

$$x_1^2 - r_o x_1 + y_1^2 - y_1 y = 0 \quad \textbf{(B-7)}$$

However any point 'G' is along the outside of the circle of the GTLS and must therefore conform to the equation of a circle as shown in Equation (B-8).

$$x_1^2 + y_1^2 = r_o^2 \quad \textbf{(B-8)}$$

This equation may be rearranged into Equation (B-9).

$$x_1 = \sqrt{r_o^2 - y_1^2} \quad \textbf{(B-9)}$$

Substituting Equation (B-7) into Equation (B-9) gives Equation (B-10).

$$r_o^2 - r_o\sqrt{r_o^2 - y_1^2} - y_1 y = 0 \quad \textbf{(B-10)}$$

Separating terms, squaring both sides of the equation and then multiplying through gives Equation (5-50).

## B.2.5 Light reflected from GTLSs onto casing and then to PV cells

The percentage of light transmitted from GTLSs onto the ICRB casing and then reflected onto the PV cells is modelled by the MATLAB® script shown below.

### B.2.5.1 For region 1 and from the GTLS to the casing

```
clear all

%  inputs
% outer radius of GTLS (mm)
r0 = 1.5;
% gap between solar cells and end of casing (mm)
c = 0.6;
% thickness of solar cells (mm)
d = 1.1;
% intermediate value of theta
thetaL = atan((r0+d)./(r0-c));
interval = pi/1800;
thetamax = pi/2;
% first values of theta
theta1 = 0:interval:(thetaL);
theta2 = (thetaL):(interval):(thetamax);

% define angle mu1 from the two vectors
top1=((r0.*cos(theta1)).*((r0.*cos(theta1))-
r0+c))+((r0.*sin(theta1)).*((r0.*sin(theta1))-r0-d));
bottom1=r0.*(sqrt((((r0.*cos(theta1))-r0+c).^2)+(((r0.*sin(theta1))-r0-
d).^2)));
mu1=acos(top1./bottom1);
beta1=(3*pi/2)-mu1;
average1=mean(beta1)

% define angle mu2 from the two vectors
top2=((-r0.*cos(theta2)).*((-r0.*cos(theta2))+r0-c))+((-
r0.*sin(theta2)).*((-r0.*sin(theta2))+r0+d));
bottom2=r0.*(sqrt((((-r0.*cos(theta2))+r0-c).^2)+(((-
r0.*sin(theta2))+r0+d).^2)));
mu2=acos(top2./bottom2);
beta2=(mu2-(pi/2));
average2=mean(beta2)

total = ((thetaL * average1)+(((pi/2)-thetaL) * average2))/thetamax

% percentage incident on casing in this quadrant of end GTLS
perc_incident=100.*(total./pi)
% percentage directly into solar cell in this quadrant
perc_solarcell=100-perc_incident

hold all

  plot (theta1,beta1)
  plot (theta2,beta2)
```

```
  plot (theta1,average1)
  plot (theta2,average2)
  plot (theta1,total, 'r')
  plot (theta2,total, 'r')

%n1=input('n1 is what?');
%n2=input('n2 is what?');
%[first, second]=fresnels(theta, n1, n2);

%average=0.5.*(first+second);
```

## B.2.5.2 For region 1 and from the casing to the PV cell

```
clear all

%  inputs
% outer radius of GTLS (mm)
r0 = 1.5;
% gap between solar cells and end of casing (mm)
c = 0.3;
% thickness of solar cells (mm)
d = 1.1;
% values of "y" along the vertical reflective surface
ymax = r0+d;
ystart=0.001;
yint = 0.001;
y = [ystart:yint:r0];
ys = [r0:yint:ymax];

% define angle phi from the two vectors

x1 = sqrt((r0.^2)-(((2.*y.*(r0.^2))./(((y.^2)+r0.^2))).^2));
y1 = (2.*y.*(r0.^2))./(((y.^2)+(r0.^2)));

top3 = (y-y1).*(y-r0-d);
bottom3 = (y-r0-d).*(sqrt(((r0-x1).^2)+((y-y1).^2)));

phi = pi - acos(top3./bottom3);

% find the angle of incidence with solar cell past y = r0

phi2 = pi/2;

% define angle delta to the top casing wall

delta = atan (c./(r0+d-y));
delta2 = atan (c./(r0+d-ys));
ans1=phi - delta;
ans2=phi2 - delta2;
avans1=mean(ans1)
avans2=mean(ans2)

aver=((avans1.*r0)+(avans2.*d))./ymax

% percentage of light reflected back to solar cell
```

```
perc3=100*(aver/(pi))

hold all

plot (y,ans1)
plot (ys,ans2)
plot (y,avans1)
plot (ys,avans2)
plot (y, aver, 'r')
plot (ys, aver, 'r')
```

## B.2.5.3 For region 2 from the GTLS to the casing

```
clear all

%  inputs
% outer radius of GTLS (mm)
r0 = 1.5;
% gap between solar cells and end of casing (mm)
c = 0.3;
% thickness of solar cells (mm)
d = 1.1;
% gap between end of solar cell and end of GTLS (mm)
f = 0.1;
% values of "s" along the vertical end of the GTLS
smax=2*r0;
intervals=r0/200;
s=[0:intervals:smax];

% light lost according to angle and position
bet=atan(f./((2*r0)+d-s));
gam=atan(f./(d+s));
incident=pi-bet-gam;
avinc=mean(incident)

% percentage of light from GTLS incident on casing
perc4=100.*(avinc/pi)

% percentage of light from GTLS directly incident on solar cell
perc5=100-perc4

hold all

plot (s,bet)
plot (s,gam)
plot (s,incident)
% plot (ys,ans2)
% plot (y,avans1)
% plot (ys,avans2)
% plot (y, aver, 'r')
% plot (ys, aver, 'r')
```

## B.2.5.4 For region 2 from the casing to the PV cell

```
clear all
```

```
%  inputs
% outer radius of GTLS (mm)
r0 = 1.5;
% gap between solar cells and end of casing (mm)
c = 0.3;
% thickness of solar cells (mm)
d = 1.1;
% gap between end of solar cell and end of GTLS (mm)
f = 0.1;
% gap between end of solar cell and casing (mm)
l = 0.1;
% values of "w" along the vertical end of the casing
wmax=d;
w1max=(2.*r0)+d;
w2max=(2.*r0)+(2.*d);
intervalw=0.002;

w=[0:intervalw:wmax];
w1=[wmax:intervalw:w1max];
w2=[w1max:intervalw:w2max];

% light incident on solar cell according to position up vertical side of
% casing

bet1=(pi./2).*(w/w);
bet2=atan((l+f)./(w1-d));
bet3=atan((l+f)./(w2-d));


bet4=atan((l+f)./((2.*r0)+d-w));
bet5=atan((l+f)./((2.*r0)+d-w1));
bet6=(pi./2).*(w2./w2);

om1=atan(l./w);
om2=atan(l./w1);
om3=atan(l./w2);
om4=atan(l./(w2max-w));
om5=atan(l./(w2max-w1));
om6=atan(l./(w2max-w2));

tor1=bet1-om1;
tor2=bet2-om2;
tor3=bet3-om3;
tor4=bet4-om4;
tor5=bet5-om5;
tor6=bet6-om6;

av1=mean(tor1);
av2=mean(tor2);
av3=mean(tor3);
av4=mean(tor4);
av5=mean(tor5);
av6=mean(tor6);

avtot1=((av1*wmax)+(av2*(w1max-wmax))+(av3*(w2max-w1max)))/w2max

% percentage of light reflecting onto solar cell
```

```
perc8=100.*(avtot1./pi)

% percentage of light reflecting onto GTLS

perc9=100-perc8


% aver=((avans1.*r0)+(avans2.*d))./ymax

% percentage of light reflected back to solar cell

% perc3=100*(aver/(pi/2))

hold all

plot (w,av1)
%plot (w,om1)
plot (w,tor1)
plot (w1,av2)
%plot (w1,om2)
plot (w1,tor2)
plot (w2,av3)
%plot (w2,om3)
plot (w2,tor3)
%plot (w,av4)
%plot (w,om4)
plot (w,tor4)
%plot (w1,av5)
%plot (w1,om5)
plot (w1,tor5)
%plot (w2,av6)
%plot (w2,om6)
plot (w2,tor6)
%plot (w2,bet3)
%plot (w,bet4)
%plot (w1,bet5)
%plot (w2,bet6)
plot (w, avtot1)
plot (w1, avtot1)
plot (w2, avtot1)
```

## B.2.6 Fresnel equations for refractive index changes

The control program in MATLAB® is:

```
clear all
theta=0:(pi/1800):(pi/2);
n1=1.473;
n2=1.0;
n3=2.3
[first, second, third, fourth]=fresnels2(theta, n1,n2, n3);
deg=theta*(180./pi);
average1=0.5.*(first+second);
```

```
ans1=mean(average1);

average2=0.5.*(third+fourth);
ans2=mean(average2);

total=(1-ans1).*(1-ans2)
```

The program which this runs (fresnels2) is:

```
function [ reflect, reflect2, reflect3, reflect4 ] = fresnels2( theta,

n1,n2, n3 )



% 1st interface of light transport


out1=(n1.*cos(theta));
out2=(n1./n2).*(sin(theta));
out3=sqrt(1-(out2.^2));
top=(out1-(n2.*out3));
bottom=out1+(n2.*out3);
reflect=abs(top./bottom).^2;

out2=(n1./n2).*(sin(theta));
out3=sqrt(1-(out2.^2));
out4=n2.*cos(theta);
top2=(n1.*out3)-out4;
bottom2=(n1.*out3)+out4;
reflect2=abs(top2./bottom2).^2;

% 2nd interface of light transport

out5=(n2.*cos(theta));
out6=(n2./n3).*(sin(theta));
out7=sqrt(1-(out6.^2));
top3=(out5-(n3.*out7));
bottom3=out5+(n3.*out7);
reflect3=abs(top3./bottom3).^2;

out6=(n2./n3).*(sin(theta));
out7=sqrt(1-(out6.^2));
out8=n3.*cos(theta);
top4=(n2.*out7)-out8;
bottom4=(n2.*out7)+out8;
reflect4=abs(top4./bottom4).^2;

end
```

## B.3 Stage 4: Model of PV cells

The operation of PV cells in modeled by use of the MATLAB® code presented here.

First is the control m-file:

```
clear all
Va=[0:0.001:6.3];
Ill=input('Illumination is what?');
[first]=solar_poly_5020_0_001sun(Va, Suns, TaC);
p=Va.*first;

hold all
plotyy (Va,first, Va,p)
```

This controls the function (titled solar) shown here:

```
function Ia=solar(Va,Suns,TaC)
k = 1.38e-23;
q = 1.60e-19;
n=1.2;

Vg = 1.12;

Ns=17;

T1 = 273 + 25;
Voc_T1 = 6.3 /Ns;
Isc_T1 = 0.025;
TaK = 273 + 25;
IL_T1 = Isc_T1 * Ill;
IL = IL_T1;
I0_T1=Isc_T1/(exp(q*Voc_T1/(n*k*T1))-1);
I0= I0_T1*(TaK/T1).^(3/n).*exp(-q*Vg/(n*k).*((1./TaK)-(1/T1)));
Xv = I0_T1*q/(n*k*T1) * exp(q*Voc_T1/(n*k*T1))
dVdI_Voc = - 2.3/Ns;

Rs = - dVdI_Voc - 1/Xv

Vt_Ta = n * k * TaK / q;
Vc = Va/Ns;
Ia = zeros(size(Vc));
% Newton Rapheson Method
for j=1:0.1:5;
    Ia=Ia-(IL-  Ia  -  I0.*(  exp((Vc+Ia.*Rs)./Vt_Ta)  -1))./(-1  -  (I0.*(
exp((Vc+Ia.*Rs)./Vt_Ta))).*Rs./Vt_Ta);
end
```

## B.4 Stage 5: Efficiency of charging a capacitor

The voltage of a *1000μF 25V* capacitor discharging due to leakage was measured over time [250], with power loss calculated through application of Equation (4-1). Resistance relative to voltage at any given time was calculated by means of Equation 3-19, and also by curve fitting. The results were plotted in a Microsoft Excel® program, as shown in Figure B-1, Figure B-2 and Figure B-3.

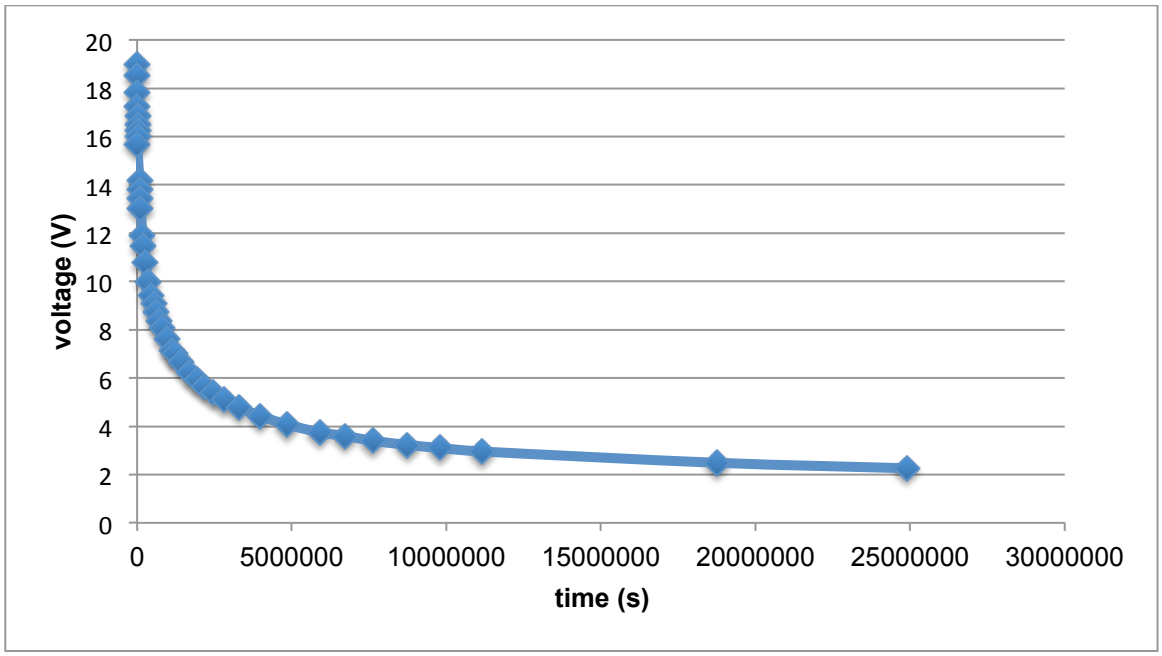



**Figure B-1:** Discharge voltage of a *1000μF 25V* aluminium electrolyte capacitor

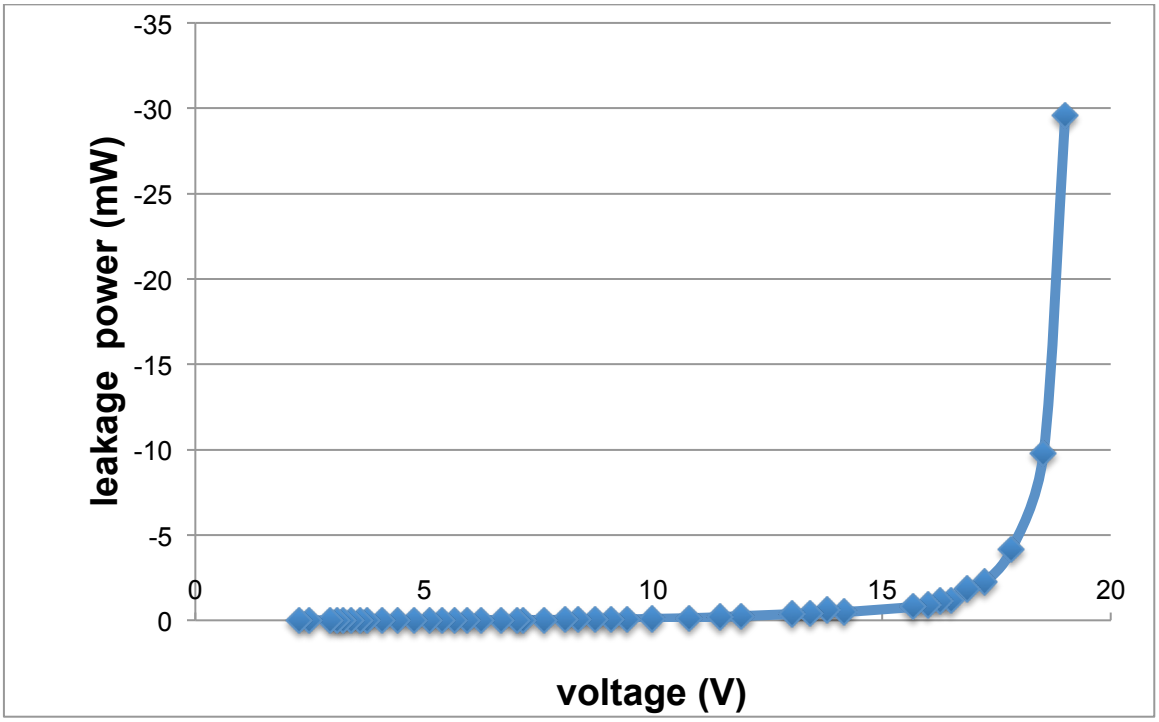



**Figure B-2:** Leakage power vs Voltage for *1000μF 25V* capacitor

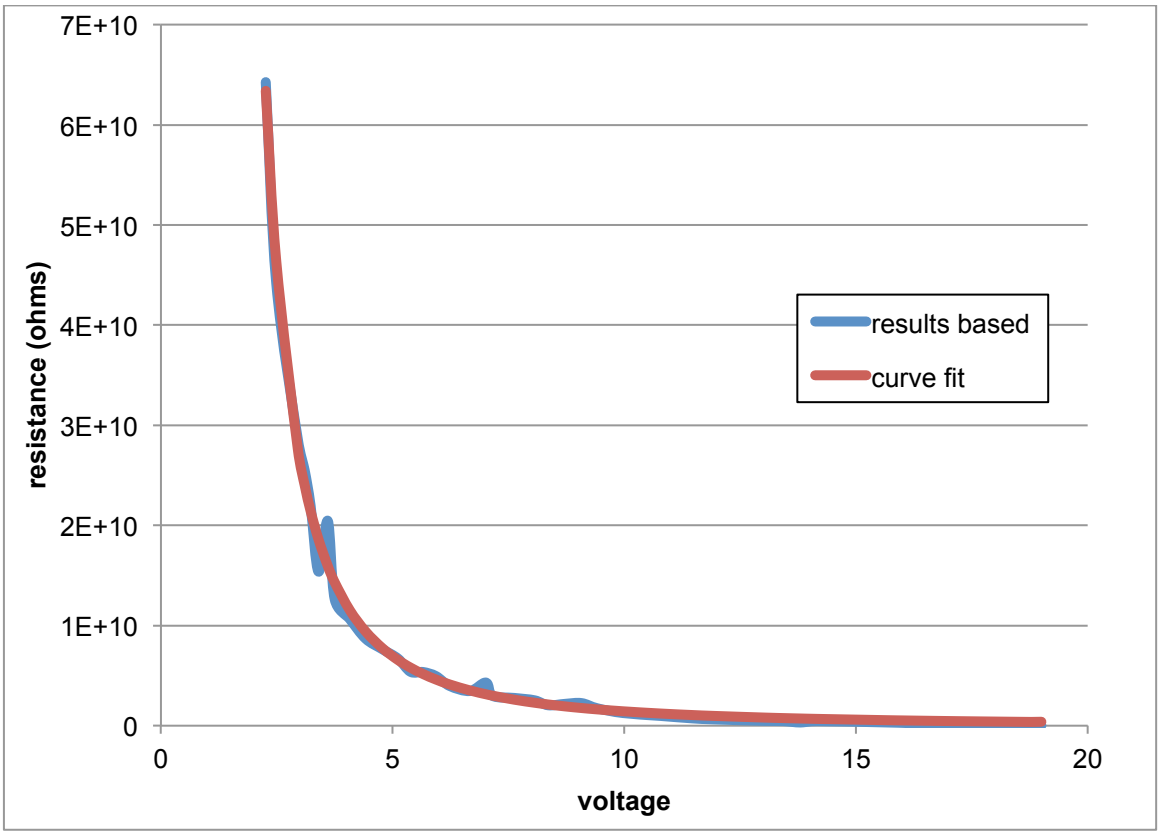



**Figure B-3:** Resistance vs voltage for a discharging *1000μF 25V* capacitor

## B.4.1 MATLAB® code for curve fit of power loss during discharge

The following code models the power loss of a 47µF 25V aluminium electrolytic capacitor during leakage, while the formula for the resistance (*R*) has been generated by curve fitting the resistance from a measured discharging capacitor.

```
clear all
syms  R

C=0.000047;
V0=3.8;
t=100;
deltat=1;

% 1000uF curve expert pro (mac) equation for R, from leakage test results

% R=108560719923.*((V0-0.94727852293759).^(-1.965771619))

% 47uF curve expert (windows)equation for R

R=(1.805951885e+11)+((-
1.51011967479e+11).*V0)+((4.26375310329e+10).*V0.*V0)+((-
4.04708141564e+9).*V0.*V0.*V0)

V1=V0.*(exp((-t)./(R.*C)));
deltat=1;
E0=0.5.*C.*V0.*V0;
V1=V0;
E1=E0;
i=0;
q=zeros(2,3600);
for t=101:1:3600
i=t-100;


V2=V0.*(exp((-t)./(R.*C)));
E2=0.5.*V2.*V2.*C;
P=((E1-E2).*1000000000)./deltat;
q(1,i)=V2;
q(2,i)=P;


R=(1.805951885e+11)+((-
1.51011967479e+11).*V2)+((4.26375310329e+10).*V2.*V2)+((-
4.04708141564e+9).*V2.*V2.*V2);

V1=V2;
E1=E2;
end
plot(q(1,10:3500),q(2,10:3500))
```

### B.4.1.1 Results of power loss discharging capacitor code

Measured and modelled graphs of power loss as the 47μF 25V aluminium electrolytic capacitor discharges are shown in Figure B-4.

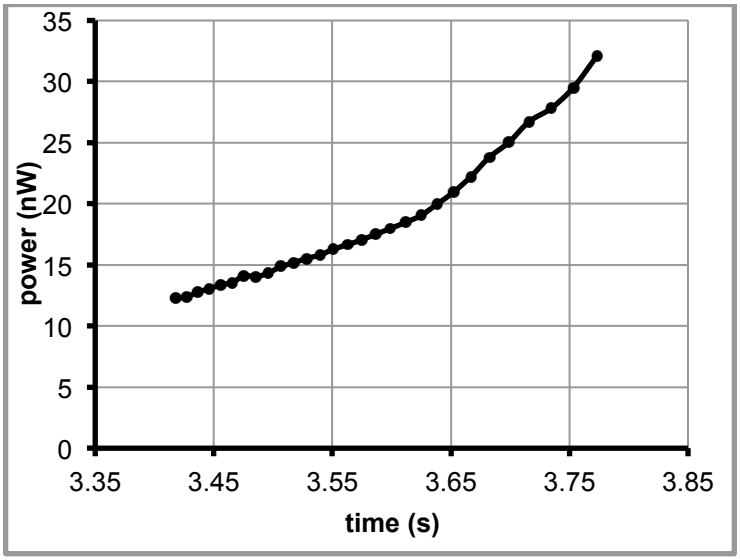



**Figure B-4:** Leakage power from capacitor discharging calculated in Excel®

## B.4.2 MATLAB® code for efficiency of charging a capacitor

The following code to be used in MATLAB® models the efficiency of charging a 47μF 25V aluminium electrolytic capacitor at a range of charging times (200s to 4000s). The parallel resistance of the capacitor is assumed to be related to the capacitance via Equation 5-67.

```
clear all

C=0.000047;
V0=5;

t=[200:1:4000];
R=100./(C);
f1=0.5*C*V0*V0
X=(2.*R.*C)./t;
percent=(1-X).*100;
plot(t, percent)
```

# APPENDIX C: DESIGN, FABRICATION AND TESTING

## C.1 Automated testing using LabVIEW

The block diagram which controls the experimental test circuitry, processes input signal data and generates the graphical user interface is displayed in Figure C-1.

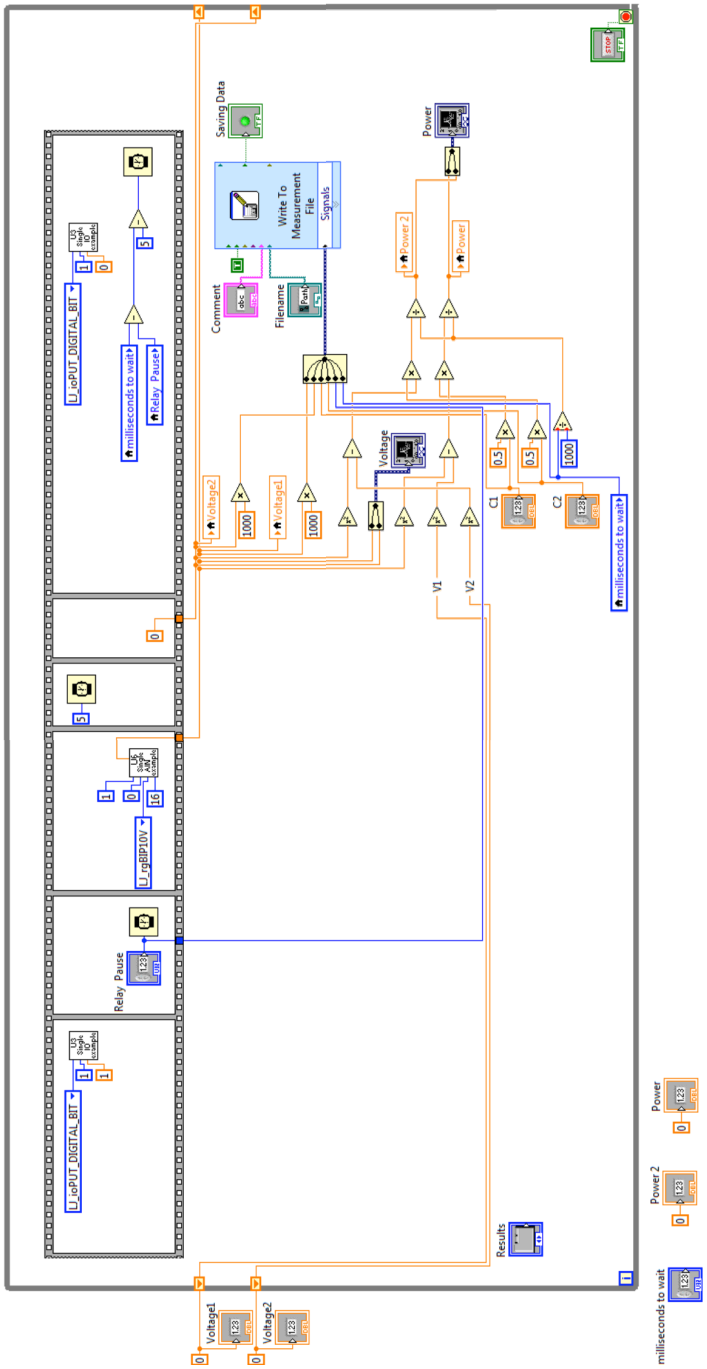



**Figure C-1**: LabVIEW block diagram for low power ICRB measurement

## C.2 Buried testing

Addition photographs of the burial of an indirect conversion radioisotopic battery are shown in Figure C-2 through to Figure C-6.

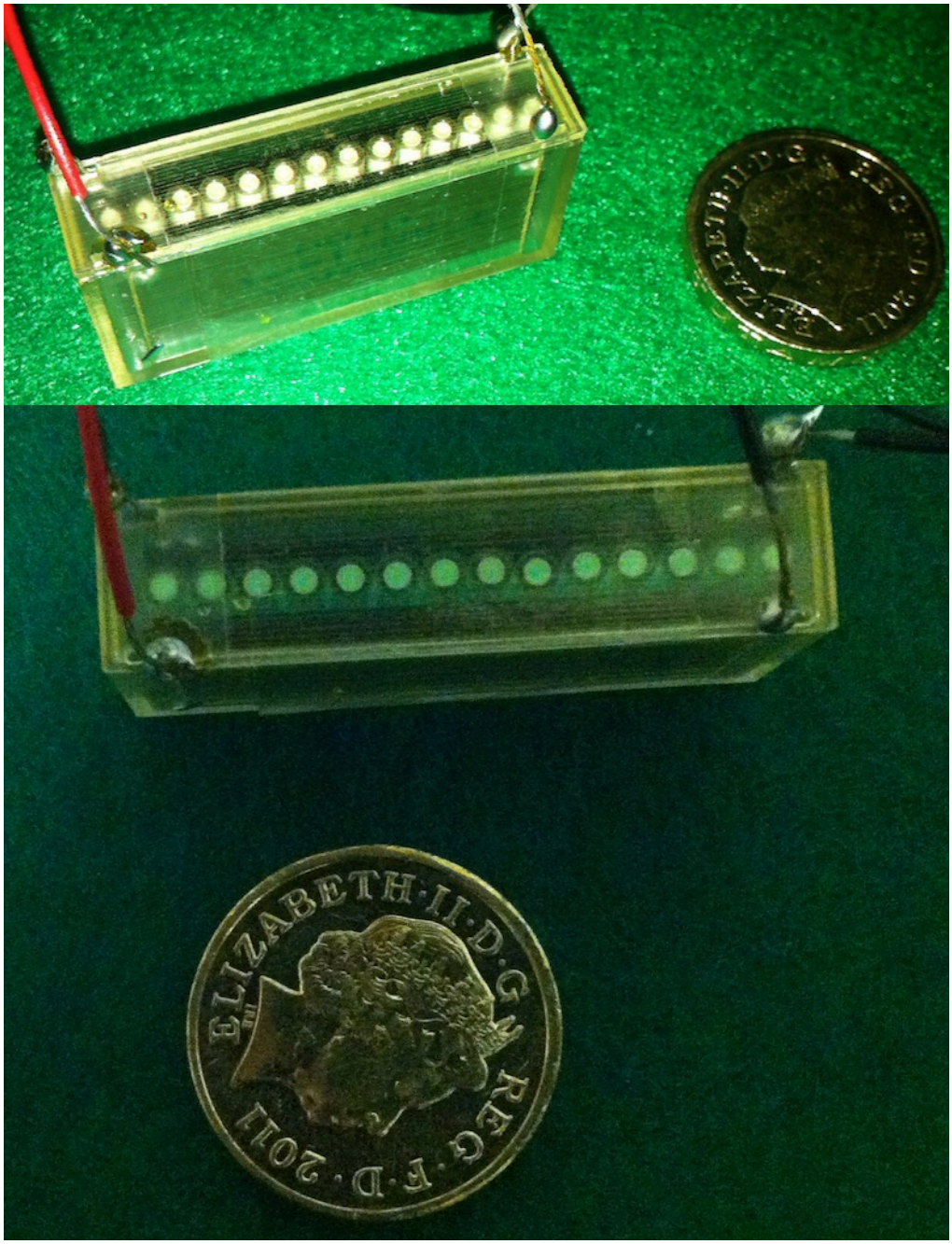



**Figure C-2:** ICRB for burial on water pipe, various views

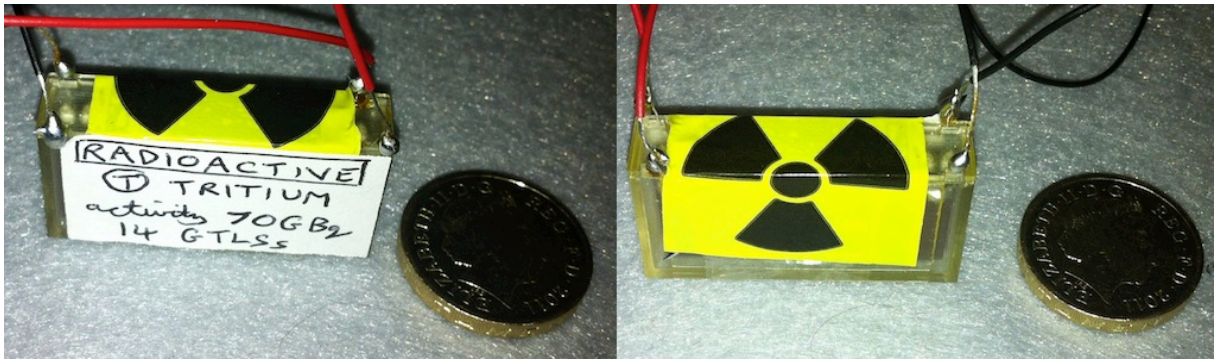



**Figure C-3:** ICRB labelled according to UK legislative requirements



**Figure C-4:** Water pipe immediately following exposure (no ICRB attached)



**Figure C-5:** ICRB in enclosure affixed to the water pipe



**Figure C-6:** Above ground container of sensor node, in situ directly above ICRB which has been buried on the pipe

# APPENDIX D: RESULTS

## D.1 PV cell test results

Additional I-V and P-V curves are shown here for monocrystalline silicon PV cells under illumination by direct sunlight (Figure D-1), indoor lighting (Figure D-2) and GTLSs (Figure D-3).

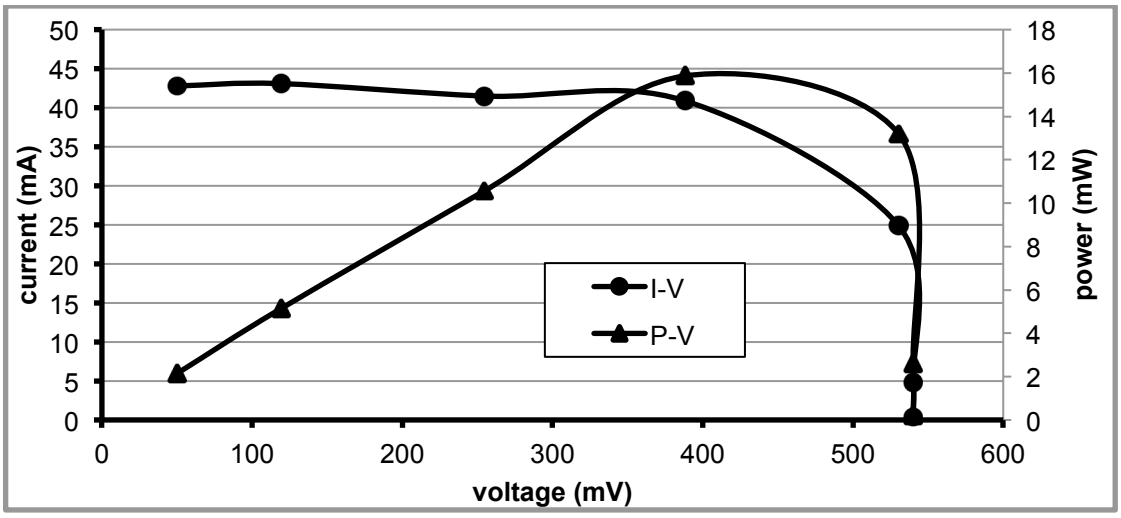



**Figure D-1:** Power-voltage and current-voltage curves for m-Si PV cells under illumination by direct sunlight

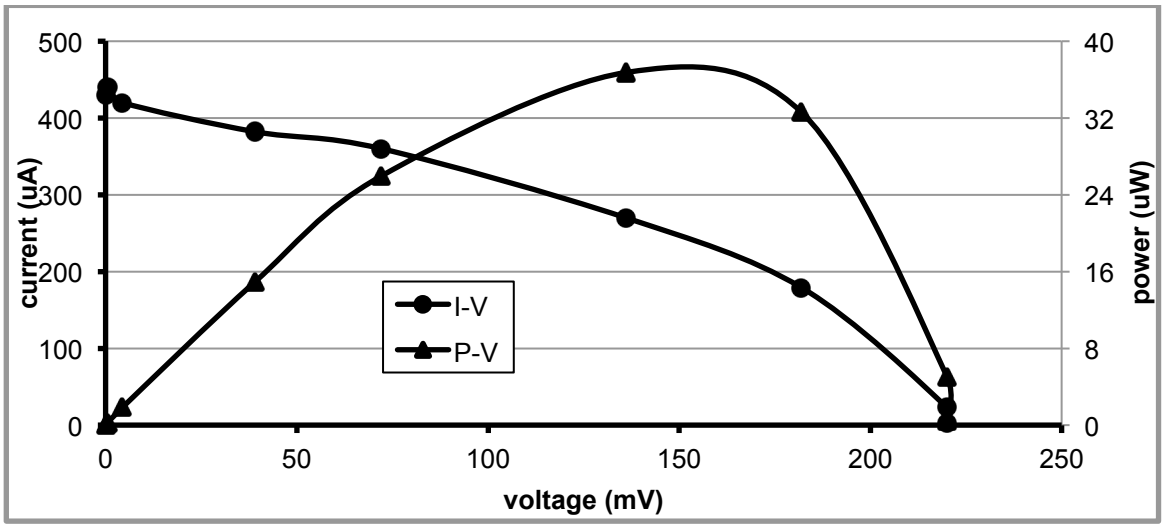



**Figure D-2:** Power-voltage and current-voltage curves for m-Si PV cells illuminated indoors at 138lux

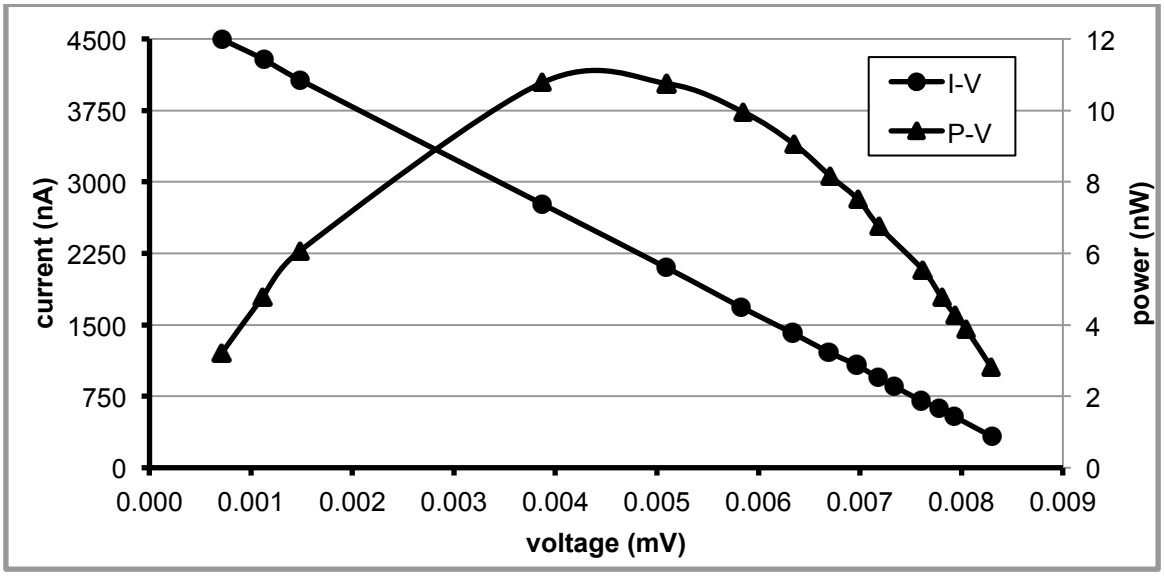



**Figure D-3:** Power-voltage and current-voltage curves for an ICRB using m-Si PV cells and 12 25mmX3mmØ GTLSs

## D.2 PV cell characteristics

The external quantum efficiency of an a-Si PV cell for the range of wavelengths covering the visible spectrum is shown in Figure D-4.

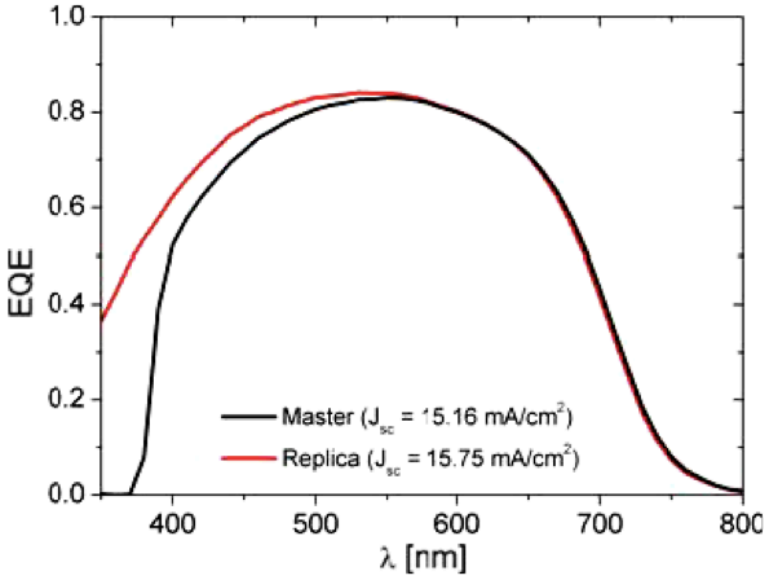



**Figure D-4:** External quantum efficiency of two manufactured a-Si PV cells (black line the original, red line a replica) (reproduced from [235])

The external quantum efficiency of m-Si and p-Si PV cells across a wide range of wavelengths is shown in Figure D-5.

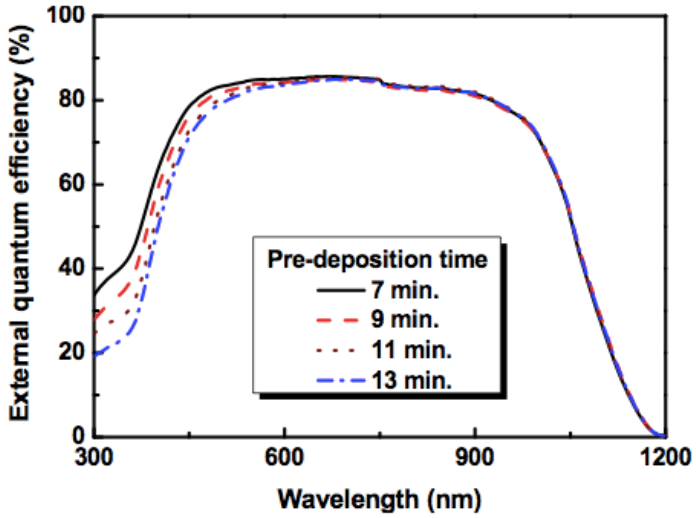



**Figure D-5:** External quantum efficiency of crystalline silicon PV cells with different pre-deposition times (reproduced from [236])

# REFERENCES


[1] S. Deus, "Tritium-powered betavoltaic cells based on amorphous silicon," in *Proceedings of 28th IEEE Photovoltaic Specialists Conference, 15-22 Sept. 2000*, Piscataway, NJ, USA, 2000, pp. 1246-9.

[2] Z. Shiwei and Z. Haitao, "A review of wireless sensor networks and its applications," in *2012 IEEE International Conference on Automation and Logistics (ICAL), 15-17 Aug. 2012*, Piscataway, NJ, USA, 2012, pp. 386-9.

[3] S. Singhal, A. K. Gankotiya, S. Agarwal, and T. Verma, "An investigation of wireless sensor network: A distributed approach in smart environment," in *2012 Second International Conference on Advanced Computing & Communication Technologies (ACCT 2012), 7-8 Jan. 2012*, Los Alamitos, CA, USA, 2012, pp. 522-9.

[4] Z. G. Wan, Y. K. Tan, and C. Yuen, "Review on energy harvesting and energy management for sustainable wireless sensor networks," in *2011 IEEE 13th International Conference on Communication Technology (ICCT), 25-28 Sept. 2011*, Piscataway, NJ, USA, 2011, pp. 362-7.

[5] M. Shinozuka, P. H. Chou, K. Sehwan, K. Hong Rok, Y. Eunbae, H. Mustafa, D. Karmakar, and S. Pul, "Nondestructive Monitoring of a Pipe Network using a MEMS-Based Wireless Network," in *Nondestructive Characterization for Composite Materials, Aerospace Engineering, Civil Infrastructure, and Homeland Security 2010, 8-11 March 2010*, USA, 2010, p. 76490P (12 pp.).

[6] W. S. Wang, R. O'Keeffe, N. Wang, M. Hayes, B. O'Flynn, and S. C. O'Mathuna, "Practical wireless sensor networks power consumption metrics for building energy management applications," in *23rd European Conference Forum Bauinoformatik*, Cork, Ireland, 2011.

[7] Texas Instruments Inc., "Zigbee CC2420 chip 2.4GHz," ed: [Available: http://www.ti.com/product/cc2420 ], [Accessed on 11th September 2013].

[8] G. V. Merrett, N. R. Harris, B. M. Al-Hashimi, and N. M. White, "Energy managed reporting for wireless sensor networks," *Sensors & Actuators: A. Physical,* vol. 142, pp. 379-89, 2008.

[9] G. W. Challen, J. Waterman, and M. Welsh, "IDEA: Integrated distributed energy awareness for wireless sensor networks," in *8th Annual International Conference on Mobile Systems, Applications and Services, MobiSys 2010, June 15, 2010 - June 18, 2010*, San Francisco, CA, United states, 2010, pp. 35-48.

[10] R. Walton, A. M. Sadeghioon, N. Metje, D. Chapman, and M. Ward, "Smart pipes: The future for proactive asset management," in *International Conference on Pipelines and Trenchless Technology 2011: Sustainable Solutions for Water, Sewer, Gas, and Oil Pipelines, ICPTT 2011, October 26, 2011 - October 29, 2011*, Beijing, China, 2011, pp. 1512-1523.

[11] N. Metje, D. N. Chapman, R. Walton, A. M. Sadeghioon, and M. Ward, "Real time condition monitoring of buried water pipes," *Tunnelling and Underground Space Technology,* vol. 28, pp. 315-320, 2012.

[12] A. Dementyev, S. Hodges, S. Taylor, and J. Smith, "Power consumption analysis of Bluetooth Low Energy, ZigBee and ANT sensor nodes in a cyclic sleep scenario," in *2013 IEEE International Wireless Symposium (IWS), 14-18 April 2013*, Piscataway, NJ, USA, 2013, p. 4 pp.

[13] S. J. Roundy, "Energy scavenging for wireless sensor nodes with a focus on vibration to electricity conversion," PHD thesis, Berkley: University of California, 2003.
[14] P. D. Mitcheson, T. C. Green, E. M. Yeatman, and A. S. Holmes, "Architectures for vibration-driven micropower generators," *Journal of Microelectromechanical Systems,* vol. 13, pp. 429-440, 2004.
[15] J. Yang, *An introduction to the theory of piezoelectricity* vol. 9 of Advances in mechanics and mathematics: Boston: Springer, 2005.
[16] Physik Instrumente Ltd., "Physik Instrumente Ltd. company webstite," ed: [Available from: http://www.physikinstrumente.co.uk/ ], [Accessed on 6th March 2013].
[17] Microstrain Inc., "Microstrain Inc. company website," ed: [Available from: http://www.microstrain.com/ ], [Accessed on 6th March 2013].
[18] A. Khalatkar, V. K. Gupta, and R. Haldkar, "Modeling and simulation of Cantilever Beam for optimal placement of piezoelectric actuators for maximum energy harvesting," in *Smart Nano-Micro Materials and Devices, December 5, 2011 - December 7, 2011*, Hawthorn, VIC, Australia, 2011, p. Swinburne University of Technology.
[19] N. M. Wereley, W. Gang, and A. Chaudhuri, "Demonstration of uniform cantilevered beam bending vibration using a pair of piezoelectric actuators," *Journal of Intelligent Material Systems and Structures,* vol. 22, pp. 307-316, 2011.
[20] P. Smithmaitrie, "Vibration theory and design of piezoelectric energy harvesting structures," *Materials Science Foundations,* vol. 72, pp. 57-79, 2011.
[21] Y. C. Shu and I. C. Lien, "Efficiency of energy conversion for a piezoelectric power harvesting system," *Journal of Micromechanics and Microengineering,* vol. 16, pp. 2429-38, 2006.
[22] C. Zhengjun and L. Lijie, "Design and characterisation of a piezoelectric scavenging device with multiple resonant frequencies," *Sensors and Actuators: A Physical,* vol. 162, pp. 82-92, 2010.
[23] S. Beeby and N. White, *Energy Harvesting for Autonomous Systems*: Artech House, 2010.
[24] I. A. Henslee, D. A. Miller, and T. Tempero, "Fatigue life characterization for piezoelectric macrofiber composites," *Smart Materials and Structures,* vol. 21, p. 105037 (7 pp.), 2012.
[25] A. Kubba, "Wireless tyre condition monitoring system self-powered by means of energy harvesting," PHD Thesis, University of Birmingham, 2012.
[26] P. M. Whelan and M. J. Hodgeson, *Essential principles of physics*, 2nd Edition ed.: John Murray, 1978.
[27] C. B. Williams and R. B. Yates, "Analysis of a micro-electric generator for microsystems," in *Proceedings of the International Solid-State Sensors and Actuators Conference - TRANSDUCERS '95, 25-29 June 1995*, Stockholm, Sweden, 1995, pp. 369-72.
[28] Perpetuum Ltd., "Perpetuum Ltd. Company website," ed: [Available from: http://www.perpetuum.com/ ], [Accessed on 6th March 2013].

[29] P. Jong Cheol and P. Jae Yeong, "A Bulk Micromachined Electromagnetic Micro-Power Generator for an Ambient Vibration-energy-harvesting System," *Journal of the Korean Physical Society,* vol. 58, pp. 1468-73, 2011.
[30] S. Roundy, P. K. Wright, and J. Rabaey, "A study of low level vibrations as a power source for wireless sensor nodes," *Computer Communications,* vol. 26, pp. 1131-1144, 2003.
[31] D. Maurath, P. F. Becker, D. Spreemann, and Y. Manoli, "Efficient Energy Harvesting With Electromagnetic Energy Transducers Using Active Low-Voltage Rectification and Maximum Power Point Tracking," *IEEE Journal of Solid-State Circuits,* vol. 47, pp. 1369-80, 2012.
[32] J. E. Shigley, *Mechanical Engineering Design*: McGraw-Hill Australia, 1986.
[33] E. Bouendeu, A. Greiner, P. J. Smith, and J. G. Korvink, "A Low-Cost Electromagnetic Generator for Vibration Energy Harvesting," *IEEE Sensors Journal,* vol. 11, pp. 107-13, 2011.
[34] S. Meninger, J. O. Mur-Miranda, R. Amirtharajah, A. Chandrakasan, and J. H. Lang, "Vibration-to-electric energy conversion," *IEEE Transactions on Very Large Scale Integration (VLSI) Systems,* vol. 9, pp. 64-76, 2001.
[35] S. W. Liu, S. W. Lye, and J. M. Miao, "Sandwich structured electrostatic/electrets parallel-plate power generator for low acceleration and low frequency vibration energy harvesting," in *2012 IEEE 25th International Conference on Micro Electro Mechanical Systems (MEMS), 29 Jan.-2 Feb. 2012*, Piscataway, NJ, USA, 2012, pp. 1277-80.
[36] K. A. Cook-Chennault, N. Thambi, and A. M. Sastry, "Powering MEMS portable devices-a review of non-regenerative and regenerative power supply systems with special emphasis on piezoelectric energy harvesting systems," *Smart Materials and Structures,* vol. 17, p. 043001 (33 pp.), 2008.
[37] S. Roundy, P. K. Wright, and J. M. Rabaey, *Energy Scavenging for Wireless Sensor Networks: With Special Focus on Vibrations*: Kluwer Academic Publishers, 2004.
[38] C. Knight, J. Davidson, and S. Behrens, "Energy Options for Wireless Sensor Nodes," *Sensors,* vol. 8, pp. 8037-8066, 2008.
[39] D. M. Rowe, *Thermoelectrics Handbook: Macro to Nano*: CRC/Taylor & Francis, 2006.
[40] Micropelt GmbH, "Micropelt GmbH company website," ed: [Available from: http://www.micropelt.com/ ], [Accessed on 6th March 2013].
[41] Nextreme Thermal Solutions Inc., "Nextreme Thermal Solutions Inc. company website," ed: [Available from: http://www.nextreme.com/ ], [Accessed on 6th March 2013].
[42] Thermo Life® Energy Corp., "Thermo Life® Energy Corp company website," ed: [Available from: http://www.poweredbythermolife.com/ ], [Accessed on 6th March 2013].
[43] "Thermoelectric materials, phenomena, and applications: A bird's eye view," *MRS Bulletin,* vol. 31, pp. 188-194, 2006.
[44] N. S. Hudak and G. G. Amatucci, "Small-scale energy harvesting through thermoelectric, vibration, and radiofrequency power conversion," *Journal of Applied Physics,* vol. 103, pp. 101301-1, 2008.

[45] B. I. Ismail and W. H. Ahmed, "Thermoelectric power generation using waste-heat energy as an alternative green technology," *Recent Patents on Electrical Engineering,* vol. 2, pp. 27-39, 2009.
[46] M. Kishi, H. Nemoto, T. Hamao, M. Yamamoto, S. Sudou, M. Mandai, and S. Yamamoto, "Micro thermoelectric modules and their application to wristwatches as an energy source," in *Eighteenth International Conference on Thermoelectrics. Proceedings, ICT'99, 29 Aug.-2 Sept. 1999*, Piscataway, NJ, USA, 1999, pp. 301-7.
[47] Z. Li, Q. Sun, X. D. Yao, Z. H. Zhu, and G. Q. Lu, "Semiconductor nanowires for thermoelectrics," *Journal of Materials Chemistry,* vol. 22, pp. 22821-22831, 2012.
[48] W. Wong-Ng, N. Lowhorn, J. Martin, P. Zavalij, H. Joress, Q. Huang, Y. Yan, A. N. Mansour, E. L. Thomas, J. Yang, and M. L. Green, "Bi2Te3 and Bi2Te3-xS x for thermoelectric applications," in *Advances and Applications in Electroceramics II - Materials Science and Technology 2011 Conference and Exhibition, MS and T 2011*, Columbus, OH, United states, 2012, pp. 31-42.
[49] C. B. Vining, "An inconvenient truth about thermoelectrics," *Nature Materials,* vol. 8, pp. 83-85, 2009.
[50] G. W. Taylor, J. R. Burns, S. M. Kammann, W. B. Powers, and T. R. Welsh, "The energy harvesting Eel: A small subsurface ocean/river power generator," *IEEE Journal of Oceanic Engineering,* vol. 26, pp. 539-547, 2001.
[51] L. A. Weinstein, M. R. Cacan, P. M. So, and P. K. Wright, "Vortex shedding induced energy harvesting from piezoelectric materials in heating, ventilation and air conditioning flows," *Smart Materials and Structures,* vol. 21, 2012.
[52] Y. Qi, N. T. Jafferis, K. Lyons Jr, C. M. Lee, H. Ahmad, and M. C. McAlpine, "Piezoelectric ribbons printed onto rubber for flexible energy conversion," *Nano Letters,* vol. 10, pp. 524-525, 2010.
[53] D.-A. Wang, C.-Y. Chiu, and H.-T. Pham, "Electromagnetic energy harvesting from vibrations induced by Karman vortex street," Langford Lane, Kidlington, Oxford, OX5 1GB, United Kingdom, 2012, pp. 746-756.
[54] J. A. R. Azevedo and F. E. S. Santos, "Energy harvesting from wind and water for autonomous wireless sensor nodes," *IET Circuits, Devices & Systems,* vol. 6, pp. 413-20, 2012.
[55] R. T. Deam, E. Lemma, B. Mace, and R. Collins, "On scaling down turbines to millimeter size," *Journal of Engineering for Gas Turbines and Power,* vol. 130, 2008.
[56] "Theory of the tesla turbine," *Engineering,* vol. 99, p. 423, 1915.
[57] V. G. Krishnan, Z. Iqbal, and M. M. Maharbiz, "A micro Tesla turbine for power generation from low pressure heads and evaporation driven flows," in *TRANSDUCERS 2011 - 2011 16th International Solid-State Sensors, Actuators and Microsystems Conference, 5-9 June 2011*, Piscataway, NJ, USA, 2011, pp. 1851-4.
[58] S. Roundy and P. K. Wright, "A piezoelectric vibration based generator for wireless electronics," *Smart Materials and Structures,* vol. 13, pp. 1131-1142, 2004.
[59] T. B. Reddy, *Linden's handbook of batteries*, Fourth ed.: McGraw-Hill, 2011.
[60] M. Nathan, D. Golodnitsky, V. Yufit, E. Strauss, T. Ripenbein, I. Shechtman, S. Menkin, and E. Peled, "Three-dimensional thin-film Li-ion microbatteries for

autonomous MEMS," *Journal of Microelectromechanical Systems,* vol. 14, pp. 879-885, 2005.
[61] Y. K. Tan and S. K. Panda, in *Sustainable wireless sensor networks*, W. Seah and Y. K. Tan, Eds., ed: InTech, 2010.
[62] B.-P. GmbH, "mobile synergy Batteries for TPMS," ed.
[63] Y. Ju and K. Maruta, "Microscale combustion: Technology development and fundamental research," *Progress in Energy and Combustion Science,* vol. 37, pp. 669-715, 2011.
[64] C. Lee, S. Arslan, and L. G. Frechette, "Design Principles and Measured Performance of Multistage Radial Flow Microturbomachinery at Low Reynolds Numbers," *Journal of Fluids Engineering,* vol. 130, pp. 111103-11, 2008.
[65] C. J. Teo, L. X. Liu, H. Q. Li, L. C. Ho, S. A. Jacobson, F. F. Ehrich, A. H. Epstein, and Z. S. Spakovszky, "High-speed operation of a gas-bearing supported MEMS-air turbine," *Journal of Tribology,* vol. 131, pp. 1-9, 2009.
[66] A. Mehra, X. Zhang, A. A. Ayon, I. A. Waitz, M. A. Schmidt, and C. M. Spadaccini, "Six-wafer combustion system for a silicon micro gas turbine engine," *Journal of Microelectromechanical Systems,* vol. 9, pp. 517-527, 2000.
[67] C. H. Lee, K. C. Jiang, P. Jin, and P. D. Prewett, "Design and fabrication of a micro Wankel engine using MEMS technology," in *Micro and Nano Engineering 2003, September 22, 2003 - September 25, 2003*, Cambridge, United kingdom, 2004, pp. 529-534.
[68] K. Fu, A. J. Knobloch, B. A. Cooley, D. C. Walther, C. Fernandez-Pello, D. Liepmann, and K. Miyaska, "Microscale combustion research for applications to MEMS rotary IC engine," in *2001 National Heat Transfer Conference (NHTC2001), June 10, 2001 - June 12, 2001*, Ananheim, CA, United states, 2001, pp. 613-618.
[69] H. T. Aichlmayr, D. B. Kittelson, and M. R. Zachariah, "Micro-HCCI combustion: Experimental characterization and development of a detailed chemical kinetic model with coupled piston motion," *Combustion and Flame,* vol. 135, pp. 227-248, 2003.
[70] F. Takei, N. F. Cooray, K. Yoshida, H. Yoshida, K. Ebisu, S. Suzuki, and N. Sawatari, "Development of prototype micro fuel cells for mobile electronics," *Fujitsu Scientific and Technical Journal,* vol. 41, pp. 191-200, 2005.
[71] Y. Yamazaki, "Application of MEMS technology to micro fuel cells," 2004, pp. 663-666.
[72] K. Reifsnider and X. Huang, "Engineering Durability of Micro-Miniature Fuel Cells," in *Mini-Micro Fuel Cells*, S. Kaka√ß, A. Pramuanjaroenkij, and L. Vasiliev, Eds., ed: Springer Netherlands, 2008, pp. 75-86.
[73] E. Zakrisson, "The effect of start/stop strategy on PEM fuel cell degradation characteristics," Masters Thesis, Department of Applied Physics, Chalmers University of Technology, Gothenburg, 2011.
[74] C. Cheng, G. Levitin, D. W. Hess, and T. F. Fuller, "XPS investigation of Nafion membrane degradation," *Journal of Power Sources,* vol. 169, pp. 288-95, 2007.
[75] H. G. J. Moseley, "Attainment of high potentials by the use of radium," *Proceedings of the Royal Society of London, Series A (Mathematical and Physical Sciences),* vol. 88, pp. 471-476, 1913.

[76] K. S. Krane, *Introductory Nuclear Physics*: John Wiley & Sons, 1987.
[77] R. Colle, B. E. Zimmerman, P. Cassette, and L. Laureano-Perez, "63Ni, its half-life and standardization: Revisited," *Applied Radiation and Isotopes,* vol. 66, pp. 60-68, 2008.
[78] P. B. Koeneman, I. J. Busch-Vishniac, and K. L. Wood, "Feasibility of micro power supplies for MEMS," *Journal of Microelectromechanical Systems,* vol. 6, pp. 355-62, 1997.
[79] R. L. Cataldo and G. L. Bennett, *Radioisotopes - Applications in Physical Sciences* vol. Chapter 22: U.S. Space Radioisotope Power Systems and Applications: Past, Present and Future: InTech, 2011.
[80] G. R. Schmidt, T. J. Sutliff, and L. A. Dudzinski, *Radioisotopes - Applications in Physical Sciences* vol. Chapter 20: Radioisotope Power - A Key Technology for Deep Space Exploration: InTech, 2011.
[81] G. L. Bennett, J. J. Lombardo, R. J. Hemler, G. Silverman, C. W. Whitmore, W. R. Amos, E. W. Johnson, A. Schock, R. W. Zocher, T. K. Keenan, J. C. Hagan, and R. W. Englehart, "Mission of daring: The general-purpose heat source radioisotope thermoelectric generator," in *4th International Energy Conversion Engineering Conference, June 26, 2006 - June 29, 2006*, San Diego, CA, United states, 2006, pp. 720-742.
[82] L. C. Olsen, "ADVANCED BETAVOLTAIC POWER SOURCES," pp. 754-762, 1974.
[83] W. R. Corliss and D. G. Harvey, *Radioisotopic power generation*: Prentice-Hall, 1964.
[84] "Nuclide Safety Data Sheet Hydrogen-3 (Tritium)," N. C. H. P. Society, Ed., ed.
[85] "Environmental protection, England and Wales, The environmental permitting (England and Wales) (amendment) regulations 2011," ed. UK, 2011, pp. 32-33.
[86] V. Raghunathan and P. H. Chou, "Design and power management of energy harvesting embedded systems," in *ISLPED'06 - 11th ACM/IEEE International Symposium on Low Power Electronics and Design, October 4, 2006 - October 6, 2006*, Tegernsee, Bavaria, Germany, 2006, pp. 369-374.
[87] F. Simjee and P. H. Chou, "Everlast: long-life, supercapacitor-operated wireless sensor node," in *ISLPED'06 Proceedings of the 2006 International Symposium on Low Power Electronics and Design, 4-6 Oct. 2006*, Piscataway, NJ, USA, 2006, pp. 197-202.
[88] L. Chao, V. Raghunathan, and K. Roy, "Micro-scale energy harvesting: a system design perspective," in *2010 15th Asia and South Pacific Design Automation Conference (ASP-DAC 2010), 18-21 Jan. 2010*, Piscataway, NJ, USA, 2010, pp. 89-94.
[89] D. Wei, F. Hengchang, L. Meijiao, and W. Zhangqi, "Dynamic analysis and simulation of flat spiral spring in elastic energy storage device," in *2012 IEEE PES Asia-Pacific Power and Energy Engineering Conference (APPEEC), 27-29 March 2012*, Piscataway, NJ, USA, 2012, p. 4 pp.
[90] F. A. Hill, T. F. Havel, and C. Livermore, "Modeling mechanical energy storage in springs based on carbon nanotubes," *Nanotechnology,* vol. 20, p. 255704 (12 pp.), 2009.

[91] J. Liley, *Nuclear physics: Principles and applications*: John Wiley & Sons, 2001.
[92] M. M. Be, V. Chiste, C. Dulieu, X. Mougeot, E. Browne, C. Baglin, V. P. Chechev, A. Egorov, N. K. Kuzmenko, V. O. Sergeev, F. G. Kondev, A. Luca, M. Galan, X. Huang, B. Wang, R. G. Helmer, E. Schonfeld, R. Dersch, A. L. Nichols, T. D. Macmahon, A. Pearce, A. Arinc, K. B. Lee, and S. C. Wu, "Table of radionuclides (Comments on evaluation)," vol. 5, Bureau International des Poids et Measures (BIPM), ed, 2010.
[93] J. E. Strain and G. W. Leddicotte, "The preparation, properties and uses of americium-214 alpha, gamma and neutron sources," Oak Ridge National Laboratory1962.
[94] G. F. Knoll, *Radiation detection and measurement*, 3rd ed.: John Wiley & Sons, 2000.
[95] C. E. Land, "Do gamma rays and alpha particles cause different types of lung cancer? a comparison between atomic bomb survivors and uranium miners," in *Radiobiology and Dosimetry of Inhaled Radionuclides, 9-10 Nov. 1993*, UK, 1995, pp. 279-85.
[96] M. Goldman, R. C. Nelson, L. Bollinger, M. D. Hoover, W. Templeton, and L. Anspaugh, "Potential health risks from postulated accidents involving the Pu-238 RTG on the Ulysses solar exploration mission," in *Eighth Symposium on Space Nuclear Power Systems, 6-10 Jan. 1991*, USA, 1991, pp. 152-64.
[97] A. Lal, R. Duggirala, and H. Li, "Pervasive power: a radioisotope-powered piezoelectric generator," *IEEE Pervasive Computing,* vol. 4, pp. 53-61, 2005.
[98] U. Government, "JSP 392: Radiation safety Handbook, Leaflet 19:Gaseous tritium light sources (GTLSs) and gaseous tritium light devices (GTLDs)," vol. 2, ed: UK Government, 2011.
[99] Ministry_of_Defence, "Smoke detectors containing americium-241," in *JSP 392: Radiation safety handbook volume 2*, ed, 2011.
[100] F. H. Attix, *Introduction to Radiological Physics and Radiation Dosimetry*: Wiley-VCH, 1991.
[101] G. L. Bennett, J. J. Lombardo, R. J. Hemler, G. Silverman, C. W. Whitmore, W. R. Amos, E. W. Johnson, R. W. Zocher, J. C. Hagan, and M. S. El-Genk, "The general-purpose heat source radioisotope thermoelectric generator: a truly general-purpose space RTG," in *Space Technology and Applications International FORUM-STAIF 2008: 12th Conference on Thermophysics Applications in Microgravity, 10-14 Feb. 2008*, USA, 2008, pp. 663-71.
[102] NASA, "Close-up of the RTG from the south.," ed: Online, [Available: http://www.hq.nasa.gov/alsj/a16/AS16-113-18371HR.jpg] , [Accessed on: 29 May 2013].
[103] F. Ritz and C. E. Peterson, "Multi-mission radioisotope thermoelectric generator (MMRTG) program overview," in *2004 IEEE Aerospace Conference Proceedings, 6-13 March 2004*, Piscataway, NJ, USA, 2004, pp. 2950-7.
[104] T. E. Hammel, R. Bennett, W. Otting, and L. Gard, "Multi-Mission Radioisotope Thermoelectric Generator (MMRTG) Engineering Unit (EU) testing," in *Nuclear and Emerging Technologies for Space 2011, NETS-2011, February 7, 2011 - February 10, 2011*, Albuquerque, NM, United states, 2011, pp. 529-36.

[105] Y. V. Lazarenko, V. V. Gusev, and A. A. Pustovalov, "Basic parameters of a radionuclide thermoelectric generator," *Soviet atomic energy,* vol. 64, pp. 131-36, 1988.
[106] A. A. Sarkisov and V. A. Yakimov, "Principal scientific and engineering problems of development of thermo-electrical generators with nuclear heat sources," *Applied Energy: Russian Journal of Fuel, Power and Heat Systems,* vol. 33, pp. 1-15, 1995.
[107] NASA, JPL-Caltech, and MSSS, "Curiosity Self-Portrait at 'John Klein'," ed: Online, [Available: http://www.nasa.gov/mission_pages/msl/multimedia/pia16937.html] , [Accessed on: 28 May 2013].
[108] M. I. Rylov and M. N. Tikhonov, "Problemy radiatsionnoi bezopasnosti," in *Atomnaya Strategiya*, St Petersburg, Russia, June 2003, p. 32.
[109] J. Warrick, "Makings of a 'Dirty Bomb'. Radioactive Devices Left by Soviets Could Attract Terrorists.," in *Washington Post, USA*, ed, 19/03/2002.
[110] M. Alais, R. Berger, R. Boucher, J. D. Hixson, P. Laurens, and A. Piwnica, "The french nuclear-powered pacemaker program," *Nuclear News,* vol. 13, pp. 42-6, 1970.
[111] V. Parsonnet, J. Driller, D. Cook, and S. A. Rizvi, "Thirty-One Years of Clinical Experience with "Nuclear-Powered" Pacemakers," *Pace-pacing and Clinical Electrophysiology,* vol. 29, pp. 195-200, 2006.
[112] ARCO, "ARCO Medical Products Company promotional material," ed, 1974.
[113] O. Lastres, D. Chandler, J. J. Jarrell, and G. I. Maldonado, "Studies of Plutonium-238 Production at the High Flux Isotope Reactor," *Transactions of the American Nuclear Society,* vol. 104, pp. 716-18, 2011.
[114] L. Cordingley, T. Rice, M. J. Sarsfield, K. Stephenson, and T. Tinsley, "241Americium as a potential power source for space missions," in *9th European Space Power Conference, 6-10 June 2011*, Noordwijk, Netherlands, 2011.
[115] R. C. O'Brien, R. M. Ambrosi, N. P. Bannister, S. D. Howe, and H. V. Atkinson, "Safe radioisotope thermoelectric generators and heat sources for space applications," *Journal of Nuclear Materials,* vol. 377, pp. 506-21, 2008.
[116] I. Klotz, "U.S. starts making plutonium " in *Discovery News*, ed: Online, [Available: http://news.discovery.com/space/nasa-plutonium-production-space-fuel-130314.htm%5D, [Accessed on: 03 June, 2013], 14 March 2013.
[117] V. V. Gusev, A. A. Pustovalov, N. N. Rybkin, L. I. Anatychuk, B. N. Demchuk, and I. Y. Ludchak, "Milliwatt-Power Radioisotope Thermoelectric Generator (RTG) Based on Plutonium-238," *Journal of Electronic Materials,* vol. 40, pp. 807-11, 2011.
[118] J. Chan, D. Hill, T. Hoye, and D. Leland, "Development of advanced Stirling Radioisotope Generator for planetary surface and deep space missions," in *6th International Energy Conversion Engineering Conference, IECEC, July 28, 2008 - July 30, 2008*, Cleveland, OH, United states, 2008.
[119] J. Chan, J. G. Wood, and J. G. Schreiber, "Development of advanced stirling radioisotope generator for space exploration," presented at the Space Technology and Applications International Forum, Albuquerque, New Mexico, USA, 2007.

[120] E. J. Lewandowski and J. G. Schreiber, "Testing to characterize the Advanced Stirling Radioisotope Generator engineering unit," in *8th Annual International Energy Conversion Engineering Conference, July 25, 2010 - July 28, 2010*, Nashville, TN, United states, 2010.
[121] D. J. Anderson, W. A. Wong, and K. L. Tuttle, "An overview and status of NASA's Radioisotope Power Conversion Technology NRA," in *3rd International Energy Conversion Engineering Conference, August 15, 2005 - August 18, 2005*, San Francisco, CA, United states, 2005, pp. 1681-1689.
[122] W. A. Wong, "Advanced radioisotope power conversion technology research development," in *Collection of Technical Papers - 2nd International Energy Conversion Engineering Conference, August 16, 2004 - August 19, 2004*, Providence, RI, United states, 2004, pp. 119-125.
[123] V. L. Teofilo, P. Choong, J. Chang, Y. L. Tseng, and S. Ermer, "Thermophotovoltaic energy conversion for space," *Journal of Physical Chemistry C,* vol. 112, pp. 7841-5, 2008.
[124] J. R. Lee, B. Ulmen, and G. H. Miley, "Honeycomb betavoltaic battery for space applications," in *Space Technology and Applications International FORUM-STAIF 2008: 12th Conference on Thermophysics Applications in Microgravity, 10-14 Feb. 2008*, USA, 2008, pp. 557-69.
[125] E. G. Linder and S. M. Christian, "The use of radioactive material for the generation of high voltage," *Journal of Applied Physics,* vol. 23, pp. 1213-1216, 1952.
[126] J. Braun, L. Fermvik, and A. Stenback, "Theory and performance of a tritium battery for the microwatt range," *Journal of Physics E (Scientific Instruments),* vol. 6, pp. 727-31, 1973.
[127] A. Kavetskiy, G. Yakubova, Q. Lin, D. Chan, S. M. Yousaf, K. Bower, J. D. Robertson, A. Garnov, and D. Meier, "Promethium-147 capacitor," *Applied Radiation and Isotopes,* vol. 67, pp. 1057-1062, 2009.
[128] G. N. Yakubova, "Nuclear batteries with tritium and promethium-147 radioactive sources," PhD, Department of Nuclear, Plasma and Radiological Engineering, University of Illinois, UIrbana-Champaign, 2010.
[129] Texas Instruments, "LM5019 100V 100mA Constant On-Time Synchronous Buck Regulator," vol. Online, [Available: http://www.ti.com/ww/en/analog/power_management/high-voltage-point-of-load.html%5D, [Accessed: 03 June, 2013], ed.
[130] R. Duggirala, R. G. Polcawich, M. Dubey, and A. Lal, "Radioisotope thin-film fueled microfabricated reciprocating electromechanical power generator," *Journal of Microelectromechanical Systems,* vol. 17, pp. 837-49, 2008.
[131] R. Duggirala, L. Hui, and A. Lal, "High efficiency radioisotope energy conversion using reciprocating electromechanical converters with integrated betavoltaics," *Applied Physics Letters,* vol. 92, pp. 154104-1, 2008.
[132] R. J. Walko, C. S. Ashley, C. J. Brinker, S. T. Reed, C. L. Renschler, T. J. Shepodd, R. E. Ellefson, J. T. Gill, and L. E. Leonard, "Electronic and photonic power applications," in *Radioluminescent Lighting Technology*, Annapolis, Maryland, USA, 1990, pp. 13-1 - 13-14.
[133] S. M. Sze, *Physics of semiconductor devices: Chapter 2*, 3rd Edition ed.: Wiley-Blackwell, 2006.

[134] P. Cabauy, L. Olsen, B. Elkind, and T. Adams, "Micropower betavoltaic hybrid sources," in *44th Power Sources Conference*, Las Vegas, Nevada, USA, 2010.
[135] C. Canali, M. Martini, G. Ottaviani, and A. Alberigi Quaranta, "Measurements of the average energy per electron-hole pair generation in silicon between 5-320K," *IEEE Transactions on Nuclear Science,* vol. NS-19, pp. 9-19, 1972.
[136] Y. Shulin, S. Zijun, W. Xiang, S. Haisheng, and Y. Yuxi, "Design and simulation of betavoltaic battery using large-grain polysilicon," *Applied Radiation and Isotopes,* vol. 70, pp. 2388-94, 2012.
[137] X. Tang, D. Ding, Y. Liu, and D. Chen, "Optimization design and analysis of Si-63Ni betavoltaic battery," *Science in China Series E: Technological Sciences,* vol. 55, pp. 990-6, 2012.
[138] P. Rappaport, J. J. Loferski, and E. G. Linder, "The electron-voltaic effect in germanium and silicon p-n junctions," *RCA Review,* vol. 17, pp. 100-128, 1956.
[139] H. Flicker, J. J. Loferski, and T. S. Elleman, "Construction of a promethium-147 atomic battery," *IEEE Transactions on Electron Devices,* vol. ED-11, pp. 2-8, 1964.
[140] L. C. Olsen, "Review of betavoltaic energy conversion," in *Proceedings of the 12th Space Photovoltaic Research and Technology Conference - SPRAT 12, Oct 20 - 22 1992*, Cleveland, OH, USA, 1993, pp. 256-256.
[141] L. Olsen, D. Serralta, and P. Cabauy, "Betavoltaic batteries: a historical review," ed: Online, [Available: Thesis_11_02_2014.docx, [Accessed: 11 April, 2013], 2010.
[142] L. C. Olsen, P. Cabauy, and B. J. Elkind, "Betavoltaic power sources," *Physics Today,* vol. 65, pp. 35-8, 2012.
[143] M. V. S. Chandrashekhar, C. I. Thomas, H. Li, M. G. Spencer, and A. Lal, "Demonstration of a 4H SiC betavoltaic cell," *Materials Science Forum,* vol. 527-529, pp. 1351-4, 2006.
[144] W. Sun, N. P. Kherani, K. D. Hirschman, L. L. Gadeken, and P. M. Fauchet, "A three-dimensional porous silicon p-n diode for betavoltaics and photovoltaics," *Advanced Materials,* vol. 17, pp. 1230-1233, 2005.
[145] G. Hang and A. Lal, "Nanopower betavoltaic microbatteries," in *IEEE International Solid-State Sensors and Actuators Conference, 8-12 June 2003*, Piscataway, NJ, USA, 2003, pp. 36-9.
[146] T. Kosteski, N. P. Kherani, P. Stradins, F. Gaspari, W. T. Shmayda, L. S. Sidhu, and S. Zukotynski, "Tritiated amorphous silicon betavoltaic devices," *IEE Proceedings-Circuits, Devices and Systems,* vol. 150, pp. 274-81, 2003.
[147] Z. Cheng, Z. Zhao, H. San, and X. Chen, "Demonstration of a GaN betavoltaic microbattery," in *6th IEEE International Conference on Nano/Micro Engineered and Molecular Systems, NEMS 2011, February 20, 2011 - February 23, 2011*, Kaohsiung, Taiwan, 2011, pp. 1036-1039.
[148] C. J. Eiting, V. Krishnamoorthy, S. Rodgers, T. George, J. D. Robertson, and J. Brockman, "Demonstration of a radiation resistant, high efficiency SiC betavoltaic," *Applied Physics Letters,* vol. 88, 2006.
[149] V. M. Andreev, A. G. Kevetsky, V. S. Kaiinovsky, V. P. Khvostikov, V. R. Larionov, V. D. Rumyantsev, M. Z. Shvarts, E. V. Yakimova, and V. A. Ustinov, "Tritium-powered betacells based on AlxGa1-xAs," in *Proceedings of*

*28th IEEE Photovoltaic Specialists Conference, 15-22 Sept. 2000*, Piscataway, NJ, USA, 2000, pp. 1253-6.
[150] City Labs Inc, "City Labs Homepage," ed: [Available: http://www.citylabs.net/%5D, [Accessed on: 05 June 2013].
[151] C. Veiga, "Homestead's City Labs makes first commercial tritium battery," in *The Miami Herald*, ed, 26/07/2012.
[152] J. Koetsier. (14/08/2012). *Hello, Spider Man 2: first commerical tritium battery for sale - with a 20-year life span*. Available: http://venturebeat.com/2012/08/14/tritium-battery-first/
[153] P. Ridden. (15/08/2012, Accessed on: 06/05/2013). *Commerically available nanotritium battery can power microelectronics for 20+ years*. Available: http://www.gizmag.com/city-labs-nanotritium-betavoltaic-battery/23720/
[154] R. Bogue, "Powering tomorrow's sensor: a review of technologies - Part 1," *Sensor Review,* vol. 30, pp. 182-6, 2010.
[155] Widetronix, "Widetronix Products," ed: [Available: http://www.widetronix.com/products ], [Accessed on: 05 June 2013].
[156] City Labs Inc., "NanoTritium P100 battery," ed: [Available: http://www.citylabs.net/index.php?option=com_wrapper&view=wrapper&Itemid=25 ], [Accessed on: 05 June 2013].
[157] C. Honsberg, W. A. Doolittle, M. Allen, and C. Wang, "GaN betavoltaic energy converters," in *Conference Record of the Thirty-First IEEE Photovoltaic Specialists Conference, 3-7 Jan. 2005*, Piscataway, NJ, USA, 2005, pp. 102-5.
[158] R. J. Walko, C. S. Ashley, C. J. Brinker, S. T. Reed, C. L. Renschler, T. J. Shepodd, R. E. Ellefson, J. T. Gill, and L. E. Leonard, "Electronic and photonic power applications," in *Radioluminescent Lighting Conference* Washington, DC, USA, 1990, pp. 13-1.
[159] M. Arneson, P. Bilhuber, E. F. Divers, and R. S. Rivenburg, "Power source using a photovoltaic array and self-luminous microspheres," US Patent, 1995.
[160] K. Bower, Y. A. Barbanel, Y. Shreter, and G. Bohnert, "Chapter 1: Conversion of Radioactive Decay Energy into Electricity," in *Polymers, Phosphors, and Voltaics for Radioisotope Microbatteries*, A. G. Kavetsky, S. P. Meleshkov, and M. M. Sychov, Eds., ed: CRC Press, 2002.
[161] "Atomic Battery," *Chemical & Engineering News Archive,* vol. 35, p. 84, 1957/02/11 1957.
[162] M. Sychov, A. Kavetsky, G. Yakubova, G. Walter, S. Yousaf, L. Qian, D. Chan, H. Socarras, and K. Bower, "Alpha indirect conversion radioisotope power source," *Applied Radiation and Isotopes,* vol. 66, pp. 173-7, 2008.
[163] V. M. Andreev, "Nuclear Batteries Based on III-V Semiconductors," in *Polymers, Phosphors and Voltaics for Radioisotope Microbatteries*, K. E. Bower, Y. A. Barbanel, Y. G. Shreter, and G. W. Bohnert, Eds., ed: CRC Press LLC, 2002.
[164] E. V. Steinfelds and J. S. Tulenko, "Development and testing of a nanotech nuclear battery for powering MEMS devices," *Nuclear Technology,* vol. 174, pp. 119-23, 2011.
[165] C. L. Renschler, J. T. Gill, R. J. Walko, C. S. Ashley, T. J. Shepodd, S. T. Reed, G. M. Malone, L. E. leonard, R. E. Ellefson, and R. L. Clough, "Solid state radioluminescent lighting," *Radiation Physics and Chemistry,* vol. 44, pp. 629-644, 1994.

[166] D. G. Guthrie, "Self-powered emergency signs," *Lighting Equipment News,* vol. 6, pp. 8-10, 1972.
[167] The Exit Store, "Self-Luminous exit signs," ed: [Available: http://www.theexitstore.com/self-luminous-exit-signs.html ], [Accessed on: 06 June 2013].
[168] Nite International Ltd., "Nite Hawk T100," ed: [Availabe: http://www.nitewatches.com ], [Accessed on: 06 June 2013].
[169] TruGlu Inc., "TruGlo's Brite.Site Handgun series," ed: [Available: http://www.truglo.com/ ], [Accessed on: 06 June 2013].
[170] Ministry of Defence, "Nuclear Lamps (Gaseous Tritium Light Sources): Defence Standard," vol. 62-4/Issue 4, ed, 1992.
[171] *Environmental Protection, England and Wales: The Environmental Permitting (England and Wales) (Amendment) Regulations 2011,* U. K. government No. 2043, 2011.
[172] J. A. Tompkins, L. E. Leonard, G. A. Jenson, and R. J. Traub, "Radiation safety of tritium lights," in *Radioluminescent Lighting Conference*, Washington, DC, USA, 1990, pp. 14-1.
[173] V. E. Lewis, "Beta decay of tritium," *Nuclear Physics A,* vol. A151, pp. 120-8, 1970.
[174] D. P. Gregory and D. A. Landsman, "Average decay energy of tritium," *Physical Review,* vol. 109, p. 2091, 1958.
[175] K. E. Bower, Y. A. Barbanel, Y. G. Shreter, and G. W. Bohnert, *Polymers, Phosphors, and Voltaics for Radioisotope Microbatteries*: Taylor & Francis, 2002.
[176] V. V. Bochkarev, G. B. Radzievsky, L. V. Timofeev, and N. A. Demianov, "Distribution of absorbed energy from a point beta-source in a tissue-equivalent medium," *International Journal of Applied Radiation and Isotopes,* vol. 23, pp. 493-504, 1972.
[177] S. Shionoya, T. Koda, K. Era, and H. Fujiwara, "Nature of luminescence transitions in ZnS crystals," *Journal of the Physical Society of Japan,* vol. 19, pp. 1157-1167, 1964.
[178] W. M. Yen, S. Shionoya, and H. Yamamoto, *The Phosphor Handbook*, Second ed.: CRC Press 2006.
[179] D. J. Robbins, "On predicting the maximum efficiency of phosphor systems excited by ionizing radiation," *Journal of the Electrochemical Society,* vol. 127, pp. 2694-2702, 1980.
[180] V. D. Meyer, "Measurements of the absolute radiative efficiency of cathodoluminescent phosphors," *Journal of the Electrochemical Society,* vol. 119, pp. 920-6, 1972.
[181] G. W. Ludwig and J. D. Kingsley, "The efficiency of cathode-ray phosphors. I. Measurement," *Journal of the Electrochemical Society,* vol. 117, pp. 348-53, 1970.
[182] G. Alexander, P. Ramakrishnan, T. K. Mukherjee, and K. S. V. Nambi, "Measurement of quantum and cathodoluminescent efficiencies of inorganic powder phosphors using silicon photodiode detector," *Indian Journal of Pure and Applied Physics,* vol. 31, pp. 531-8, 1993.

[183] A. Bril, *Luminescence of organic and inorganic materials: Absolute efficiencies of phosphors with ultra-violtet and cathode-ray excitation*: John Wiley & Sons Inc., 1962.
[184] E. Hecht, *Optics*, 4th ed.: Pearson, 2003.
[185] Lambda Research Corporation, "TracePro," ed: [Available from: http://www.lambdares.com/?gclid=CNbDz5mQmbkCFVDItAodQh0AOg ], [Accessed on 25th August 2013].
[186] Science Lab Software, "Optics lab optical ray tracing software," ed: [Available from: http://www.optics-lab.com/ ], [Accessed on 25th August 2013].
[187] Pixar, "Renderman Studio 18," ed: [Available from: http://renderman.pixar.com/view/renderman ], [Accessed on 6th March 2013].
[188] Persistence of vision raytracer Pty. Ltd., "POV-Ray," ed: [Available from: http://www.povray.org ], [Accessed on 6th March 2013].
[189] S. D. Roth, "Ray Casting for Modeling Solids," *Computer Graphics and Image Processing,* vol. 18, pp. 109-114, 1982.
[190] A. Luque and S. Hegedus, *Handbook of photovoltaic science and engineering*, 2nd ed.: Wiley & Sons, 2011.
[191] Squirmymcphee. (2008, Accessed on 28/06/2013). *Equivalent circuit of a solar cell*. Available: http://upload.wikimedia.org/wikipedia/commons/c/c4/Solar_cell_equivalent_circuit.svg
[192] G. Farivar and B. Asaei, "Photovoltaic module single diode model parameters extraction based on manufacturer datasheet parameters," in *2010 IEEE International Conference on Power and Energy (PECon 2010), 29 Nov.-1 Dec. 2010*, Piscataway, NJ, USA, 2010, pp. 929-34.
[193] J. D. Servaites, M. A. Ratner, and T. J. Marks, "Practical efficiency limits in organic photovoltaic cells: Functional dependence of fill factor and external quantum efficiency," *Applied Physics Letters,* vol. 95, 2009.
[194] M. Rahman and S. Khan, "Modelling electrical characteristics of a pn-junction silicon solar cell using pspice," *Smart Grid and Renewable Energy,* vol. 3, pp. 133-138, 2012.
[195] M. Alonso and E. J. Finn, *Funamental university physics: quantum and statistical physics v.3*: Addison Wesley, 1968.
[196] R. L. Spyker and R. M. Nelms, "Classical equivalent circuit parameters for a double-layer capacitor," *IEEE Transactions on Aerospace and Electronic Systems,* vol. 36, pp. 829-36, 2000.
[197] E. Hecht, *Physics*: Pacific Grove, Brooks/Cole, 1994, pp. 648-649.
[198] Cornell Dubilier, "Aluminum electrolytic capacitor application guide," ed: Online, [Available: http://www.cde.com/catalogs/AEappGUIDE.pdf%5D, [Accessed on: 11 April, 2013].
[199] Dassault Systemes Solidworks Corp., "Solidworks standard edition," ed: [Available from: http://www.solidworks.co.uk/ ], [Accessed on 11th July 2013].
[200] Stratasys Ltd., "Stratasys Design Series: Objet250," ed: [Available from: http://www.stratasys.com/3d-printers/design-series ], [Accessed on 24th June 2013].
[201] Applied Rapid Technolgies, "High-performance materials: The specifics: Rigids: FullCure 720," ed: [Available from: http://www.artcorp.com/material.html ], [Accessed on 24th June 2013].

[202] C. Starr, *Biology: Concepts and Applications*: Thomson Brooks/Cole, 2005.
[203] J. M. Palmer, *The handbook of optics, Chapter 25: The measurement of transmission, absorption, emissionand reflection*, Second ed. NY: McGraw-Hill, 1994.
[204] K. M. McCord, D. A. Klinglesmith, C. A. Jurgenson, E. J. Bakker, R. A. Schmell, D. Gartner, A. Jaramillo, K. Romero, A. Rael, and J. Lewis, "Characterization of silver and aluminum custom mirror coatings for the MRO interferometric telescopes," in *Optical Materials and Structures Technologies IV, 2-3 Aug. 2009*, USA, 2009, p. 74250V (9 pp.).
[205] M. Bartek, J. H. Correia, and R. F. Wolffenbuttel, "Silver-based reflective coatings for micromachined optical filters," *Journal of Micromechanics and Microengineering,* vol. 9, pp. 162-165, 1999.
[206] Pro-Lite Technology Ltd, "Pro-Lite Water-Based Barium Sulphate Coating," ed: [Available from: http://www.pro-lite.uk.com/File/Pro-Lite Barium Sulphate Coating Specifications & Ordering Guide.pdf ] , [Accessed on 20th August 2013].
[207] J. B. Schutt, J. F. Arens, C. M. Shai, and E. Stromberg, "Highly reflecting stable white paint for the detection of ultraviolet and visible radiations," *Applied Optics,* vol. 13, pp. 2218-21, 1974.
[208] W. Smith, *Modern optical engineering*, Third ed.: McGraw-Hill, 2000.
[209] LabJack Corporation, "LabJack U6-PRO ", ed: [Availabe from: http://labjack.com/u6 ], [Accessed on 11th July 2013].
[210] National Instruments Corporation, "LabVIEW system design software," ed: [Available from: http://www.ni.com/labview/ ], [Accessed on 11th July 2013].
[211] J. C. Kuenen and G. C. M. Meijer, "Measurement of dielectric absorption of capacitors and analysis of its effects on VCOs," *IEEE Transactions on Instrumentation and Measurement,* vol. 45, pp. 89-97, 1996.
[212] R. A. Pease, "Understand capacitor soakage to optimize analog systems," *EDN,* vol. 27, pp. 125-9, 1982.
[213] Cornell Dubilier, "Aluminium electrolytic capacitor application guide," ed: [Available from: http://www.cde.com/catalogs/AEappGUIDE.pdf ], [Accessed on 10th July 2013].
[214] Severn Trent Water, "Severn Trent Water company information," ed: [Available from: http://www.stwater.co.uk/ ], [Accessed on 11th July 2013].
[215] H. K. Wentworth Limited, "Electrolube Resins: UR5562 - (Water white) ", ed: [Available from: http://www.electrolube.com/docs/resinsmain.asp?id=50 ], [Accessed on 2nd July 2013].
[216] L Robinson & co, "Jubilee clips," ed: [Available from: http://www.jubileeclips.co.uk/ ], [Accessed on 11th July 2013].
[217] mb-microtec ag, "Products: trigalight(r) sources," ed: [Available: http://www.mbmicrotec.com/en/products/trigalight-sources ], [Accessed on: 12th September 2013].
[218] *Nuclear lamps defence standard,* M. o. D. o. GB Standard 62-4/Issue 2, 1972.
[219] *SH3.R05 and Sh3.R06 Type radioluminescent light sources, Technical specifications*, 1997.
[220] N. E. Brese, C. L. Rohrer, and G. S. Rohrer, "Brightness degradation in electroluminescent ZnS:Cu," *Solid State Ionics, Diffusion & Reactions,* vol. 123, pp. 19-24, 1999.

[221] O. A. Trykov, "High-intensity autonomous light sources based on radioluminescent principle of conversion of the nuclear particle energy to electromagnetic optical radiation in the visible range," 1998.
[222] (Accessed on 26/06/2013). *Matlab*. Available: http://www.mathworks.co.uk/products/matlab/
[223] M. R. Spiegel, S. Lipschutz, and D. Spellman, *Vector Analysis*, 2nd ed.: Schaum's outlines, 2009.
[224] K. E. Atkinson, *An introduction to numerical analysis*: John Wiley & Sons, Inc., 1989.
[225] F. M. González-Longatt, "Model of photovoltaic module in Matlab," presented at the 2do congreso iberoamericano d estudiantes de ingenieria electrica, electronica y computacion (II CIBELEC), 2005.
[226] C. P. Navathe and S. Nigam, "Numerical evaluations of different methods used for charging capacitor banks in pulsed power applications," *Physics Education,* pp. 31-46, April-June 2006.
[227] R. A. Millikan and E. S. Bishop, *Elements of electricity: A practical discussion of the fundamental laws and phenomena of electricity and their practical appliations in the business and industrial world*: American Technical Society, 1917.
[228] Cornell Dubilier, "Type 300/301 –55 oC to 105 oC Long-Life, Switching Power Grade Radial," vol. Online, [Available: http://www.cde.com/catalogs/300-301.pdf%5D, [Accessed: 11 April, 2013], ed.
[229] W. M. Yen, S. Shionoya, and H. Yamamoto, *Phosphor Handbook*, 2nd Edition ed.: CRC Press, 2006.
[230] SCHOTT AG, "SCHOTT Technical Glasses: Physical and technical properties," ed: [Available: http://www.schott.com/tubing/english/download/schott-tubing_brochure_technical-glasses_english.pdf ], [Accessed on: 7th October 2013].
[231] Newport Corporation, "Index-matching fluid," ed: [Available from: http://www.newport.com/Index-Matching-Fluid/835182/1033/info.aspx ], [Accessed on: 31 July 2013].
[232] G. A. Neuman, "Anti-reflective coatings by APCVD using graded index layers," in *Coating on Glass. First International Conference. Advanced Technologies and Future Trends for High Volume and/or Large Areas, 27-31 Oct. 1997*, Netherlands, 1997, pp. 92-9.
[233] D. N. Wright, E. S. Marstein, and A. Holt, "Double layer anti-reflective coatings for silicon solar cells," in *Conference Record of the Thirty-First IEEE Photovoltaic Specialists Conference, 3-7 Jan. 2005*, Piscataway, NJ, USA, 2005, pp. 1237-40.
[234] Y. Xing, D. J. Poxson, C. Jaehee, R. E. Welser, A. K. Sood, K. Jong Kyu, and E. F. Schubert, "Enhanced Omnidirectional Photovoltaic Performance of Solar Cells Using Multiple-Discrete-Layer Tailored- and Low-Refractive Index Anti-Reflection Coatings," *Advanced Functional Materials,* vol. 23, pp. 583-90, 2013.
[235] J. Escarre, C. Battaglia, K. Soderstrom, C. Pahud, R. Biron, O. Cubero, F. J. Haug, and C. Ballif, "UV imprinting for thin film solar cell application," *Journal of Optics,* vol. 14, 2012.

[236] S. J. Choi, G. J. Yu, G. H. Kang, J. C. Lee, D. Kim, and H.-E. Song, "The electrical properties and hydrogen passivation effect in mono crystalline silicon solar cell with various pre-deposition times in doping process," *Renewable Energy,* vol. 54, pp. 96-100, 2013.
[237] Y. Yamauchi, H. Takatsuka, M. Fukagawa, K. Kawamura, and N. Yamashita, "Development of a-Si/microcyrstalline-Si tandem-type photovoltaic solar-cells," *Energy,* vol. 56, pp. 46-52, 2006.
[238] M. A. Green, K. Emery, Y. Hishikawa, W. Warta, and E. D. Dunlop, "Solar cell efficiency tables (version 42)," *Progress in Photovoltaics: Research and Applications,* vol. 21, pp. 827-837, 2013.
[239] N. H. Reich, S. Y. Kan, W. G. J. H. v. Sark, E. A. Alsema, S. Silvester, A. S. H. v. d. Heide, R. W. Lof, and R. E. I. Schropp, "Weak light performance and spectral response of different solar cell types," in *20th European Photovoltaic Solar Energy Conference and Exhibition* Barcelona, Spain, 2005.
[240] SANYO Semiconductor Co. Ltd., "Amorphous silicon solar cells / amorphous photosensors," ed: [Available: http://www.panasonic.net/energy/amorton/en/pdf/EP120B.pdf ], [Accessed on: 13th August 2013].
[241] T. J. Bruno and P. D. N. Svoronos, *CRC Handbook of Fundamental Spectroscopic Correlation Charts*: CRC Press, 2005.
[242] Nichicon Corporation, "General descriptions of aluminium electrolytic capacitors," ed: [Available from: http://www.nichicon.co.jp/english/products/pdf/aluminum.pdf ], [Accessed on 22nd July 2013].
[243] T. Vogt, "Effects of temperature and of DC bias on ceramic capacitors," *Elektronik Praxis,* pp. 54-7, 2009.
[244] S. M. Sandler and C. E. Hymowitz, "Capacitor values: don't believe the label," *Power Electronics Technology,* vol. 33, pp. 22-5, 2007.
[245] AVX Corporation, "Oxicap NOJ series, niobium oxide capacitor," ed: [Available: http://www.avx.com/docs/catalogs/noj.pdf ], [Accessed on: 23 July 2013].
[246] AVX Corporation, "TPS series, low ESR," ed: [Available: http://www.avx.com/docs/catalogs/tps.pdf ], [Accessed on: 23 July 2013].
[247] Nichicon Corporation, "Conductive polymer aluminium solid electrolytic capacitors, LF series," ed: [Available: http://www.nichicon.co.jp/english/products/pdfs/e-lf.pdf ], [Accessed on: 23 July 2013].
[248] S. Shaari, K. Sopian, N. Amin, and M. N. Kassim, "The temperature dependence coefficients of amorphous silicon and crystalline photovoltaic modules using Malaysian field test investigation," *American Journal of Applied Sciences,* vol. 6, pp. 586-93, 2009.
[249] H. Hannebauer, T. Falcon, R. Hesse, T. Dullweber, and R. Brendel, "18.9 %-Efficient screen-printed solar cells applying a print-on-print process," in *26th European International Conference on Photovoltaic Solar Energy, 5-9 Sept. 2011*, Munich, Germany, 2011, pp. 1607-10.
[250] A. Kubba, "Wireless tyre condition monitoring system self-powered by means of energy harvesting," PhD, School of Mechanical Engineering, The University of Birmingham, 2012.